A stochastic approach to the modelling of cosmic rays in the heliosphere

JL Raath



orcid.org / 0000-0003-3965-0636

Thesis accepted for the degree *Doctor of Philosophy in Space Physics* at the North-West University

Promoter:	Prof SES Ferreira
Co-promoter:	Dr A Kopp

Graduation May 2020

20368879

Wisdom fears no thing, but still bows humbly to its own source, with its deeper understanding, loves all things, for it has seen the beauty, the tenderness, and the sweetness which underlie Life's Mystery.

- Manly Palmer Hall

To my mother

Stephanie Suzan Raath *née* **Graham**

and in loving memory of my father

Jan Louis Raath

(1950 - 2012)

Abstract

A spatially three-dimensional numerical modulation model based on solving a set of stochastic differential equations, corresponding to the Parker transport equation, is employed to study the galactic proton spectra measured by the PAMELA instrument during January 2010 (solar minimum) to January 2014 (solar maximum). The model is able to reproduce these spectra well and various sets of values are determined for the modulation parameters required to do so, for different assumptions of the solar magnetic polarity and drift coefficient. A consideration central to the theme of this thesis is the scaling down of drifts with turbulence, i.e. towards solar maximum conditions, and a simple scaling function is introduced to incorporate this solar activity dependent suppression of drift effects. It is indicated that the difference in modulation between successive six-monthly averaged spectra cannot be accounted for by merely changing the tilt angle and magnetic field magnitude as function of time, but that an additional change in the magnitude of the diffusion coefficient is necessary; an increase in the rigidity dependence of the diffusion coefficient below 4.2 GV may also be required towards solar maximum conditions. The drift properties of this modulation model are investigated by making use of its illustrative capabilities so that contour plots are produced showing particle entry positions and energies. It is found that energy losses increase when drifts are turned on, a fact which could be explained by considering contour plots indicating the regions in modulation space where these particles spend most time during the modulation process. Finally, it is indicated that the model produces charge-sign dependent modulation that is consistent with those of other authors and that it can be used in future studies to reproduce data.

Keywords: solar modulation, cosmic rays, stochastic differential equations, drift coefficient, drift reduction/scaling/suppression, diffusive processes, heliospheric current sheet, heliospheric magnetic field, solar activity, magnetic polarity cycles, solar turbulence, charge-sign dependent.

Nomenclature

Listed below are the acronyms and abbreviations used in the text.

ACE	Advanced Composition Explorer
AMS	Alpha Magnetic Spectrometer
AU	Astronomical Unit[1]
ACR	Anomalous Cosmic Ray
CR	Cosmic Ray
CRN	Carrington Rotation Number
eV	Electron Volt[2]
GCR	Galactic Cosmic Ray
HCS	Heliospheric Current Sheet
HMF	Heliospheric Magnetic Field
HP	Heliopause
ISM	Interstellar Medium
LIS	Local Interstellar Spectrum
MFP	Mean Free Path
MHD	Magneto-hydrodynamic
NLGC	Non-Linear Guiding Center
NM	Neutron Monitor
PAMELA	Payload for Antimatter Matter Exploration and Light-nuclei Astrophysics
QLT	Quasi-Linear Theory
SDE	Stochastic Differential Equation
SEP	Solar Energetic Particle
SW	Solar Wind
TPE	Transport Equation
TS	Termination Shock

[1] The average distance between the Earth and the Sun, 1 AU = 1.49×10^8 km;
[2] 1 eV = 1×6^{-19} J (10^3 eV = 1 keV, 10^6 eV = 1 MeV, 10^9 eV = 1 GeV).

Table of contents

1 Introduction **1**

2 Modelling Cosmic Ray Transport in the Heliosphere **9**

2.1 Introduction . . . 9
2.2 The Parker Transport Equation . . . 10
2.3 The Transport Equation in Spherical Coordinates . . . 13
2.4 Particle Drifts . . . 16
2.4.1 The Drift Coefficient . . . 17
2.4.2 Drift Velocities . . . 21
2.4.3 The Global Drift Pattern . . . 22
2.5 Particle Diffusion . . . 23
2.5.1 Parallel Diffusion . . . 24
2.5.2 Perpendicular Diffusion . . . 25
2.6 The Numerical Model . . . 27
2.6.1 Stochastic Differential Equations . . . 28
2.6.2 Models Based on Stochastic Differential Equations . . . 29
2.6.3 SDE Formulation for the TPE . . . 31
2.6.4 Boundary Conditions . . . 34
2.7 Summary . . . 35

3 Galactic Proton Modulation in the Inner Heliosphere **37**

3.1 Introduction . . . 37
3.2 The Proton Local Interstellar Spectrum . . . 37
3.3 PAMELA Proton Spectra from 2010 to 2014 . . . 40
3.4 Solar Activity during Solar Cycle 24 . . . 45
3.5 Modelling the PAMELA Proton Spectra . . . 49
3.5.1 Half-Yearly Averaged Spectra . . . 49
3.5.2 Numerically Reproduced Spectra: Results . . . 53
3.5.3 Numerically Reproduced Spectra: Discussion . . . 59
3.6 Summary . . . 64

4 The Properties of Drifts and its Effect on Cosmic Rays in the Heliosphere 67
4.1 Introduction . . . 67
4.2 Cosmic Ray Drift over a Solar Cycle . . . 67
4.3 The Drift Scaling Function . . . 71
4.4 PAMELA Proton Spectra . . . 72
4.5 Drift Properties of the Model . . . 75
4.5.1 Altering of Drift Effects towards Solar Maximum . . . 75
4.5.2 Diffusion and Drift Effects . . . 83
4.5.3 Drift Effects as Function of Energy . . . 89
4.6 Summary . . . 98

5 Charge-Sign Dependent Modulation 101
5.1 Introduction . . . 101
5.2 Positron and Electron Modulation . . . 101
5.3 Positron Fraction as Function of Energy . . . 105
5.4 Positron to Electron Ratios as Function of Solar Activity . . . 107
5.5 Future Research . . . 115
5.5.1 The Drift Scaling Down Function . . . 115
5.5.2 A More Realistic Time Dependence . . . 117
5.5.3 Observations . . . 121
5.6 Summary . . . 124

6 Summary and Conclusions 126

References 131

Chapter 1

Introduction

The heliosphere can be defined as the local region of interstellar space that is influenced by the Sun. It is formed as a result of the interaction between the outblowing solar wind (SW) plasma and the interstellar medium (ISM). The boundary between the SW plasma and the ISM is referred to as the heliopause (HP). See Fichtner and Scherer [2000] for an overview. The Sun goes through an $\sim$ 11-year solar activity cycle: it is characterised by high (low) solar activity, referred to as solar maximum (minimum) conditions, every $\sim$ 11 years. This cycle is reflected in the SW and heliospheric magnetic field (HMF) as well as in the global structure of the heliosphere and therefore also in the consequent modulation of cosmic rays (CRs) within the heliosphere. See Scherer et al. [2000] for a review of the heliosphere.

Cosmic rays are energetic particles which, after being accelerated to very high velocities, propagate throughout the galaxy; for a review see e.g. Simpson [1998]. CRs that reach Earth are mainly composed of $\sim$ 98% atomic nuclei (most of which are protons) and $\sim$ 2 % electrons, positrons, and anti-protons, along with small abundances of heavier nuclei (e.g. Longair [1990]; Simpson [1992]). CRs are generally classified into a number of major populations, according to their origin; see e.g. Heber and Potgieter [2006] and Potgieter [2008] for reviews.

The focus in this work is on the modulation of Galactic cosmic rays (GCRs). These particles originate from far outside the solar system. They are accelerated by supernova explosions and, during this process, distributed over energies ranging from a few hundred keV to energies larger than 10^{20} eV (e.g. Koyama et al. [1995]; Tanimori [1998]). It was already suggested in 1969 that GCRs may originate not only from supernova explosions, but also from supernova remnants which may include neutron stars (Ginzburg and Syrovatskii [1969]. Non-thermal radio, X-ray and gamma-ray radiation also provides direct evidence of particle acceleration in supernova remnants (e.g. Ptuskin [2005]). The energy spectrum of GCRs takes on the form of a power law $j \propto E^{-\gamma}$; here, the spectral index is defined $\gamma \approx 2.7$ (in mid-energy range only), E is the kinetic energy per nucleon (MeV/nucleon), and j is the differential intensity (particles/m^2/sr/s/MeV). Because solar modulation effects become more and more important at lower energies, the GCR spectrum measured

at Earth will have a spectral index different from $\gamma \approx 2.7$; Strauss and Potgieter [2014*b*] indicated that this deviation from $\gamma \approx 2.7$ started at about ∼30 GeV.

Solar energetic particles (SEPs) form the second group of CRs. These particles originate from regions close to the Sun, including the solar corona, and are related to coronal mass ejections and solar flares (e.g. Forbush [1946]). Shocks in the interplanetary medium can also produce SEPs (e.g. Cliver [2000]; Reames [2013]). These particles have energies at the lower end of the spectrum up to several hundred MeV. For the purposes of this thesis these particles are not important.

Anomalous cosmic rays (ACRs) form a third population of CRs. These particles enter the heliosphere as neutral interstellar atoms and are therefore initially unaffected by the HMF. Closer to the Sun they become singly ionised through photo-ionisation (Pesses et al. [1981]) or through charge-exchange occuring mainly in the heliosheath (Fahr et al. [2000]). The heliosheath is the region between the termination shock (TS) and the HP, where the TS is the boundary between supersonic and subsonic SW flows. After ionisation or charge-exchange, the resulting ions are 'picked up' by the HMF and transported to the TS where they are accelerated up to energies of $\sim$ 100 MeV through a process of first order Fermi acceleration, gaining energy by multiple crossings of the TS. See e.g. Fichtner [2001] for a review; see also Strauss [2010]. This component of CRs also does not feature prominently in this thesis and is only mentioned where applicable.

The fourth population of CRs consists of electrons originating from the magnetosphere of Jupiter and are called Jovian electrons. These particles were discovered in 1973 by Pioneer 10 and it is well known that the magnetosphere of Jupiter is a relatively strong source of electrons at energies $\sim$ 30 MeV (e.g. Simpson et al. [1974], Chenette et al. [1974]). For a detailed study of the transport of Jovian electrons in the heliosphere, see Ferreira [2002]. Due to their low energies, Jovian electrons are not important for the purposes of this study.

The solar wind profile assumed in this study is relatively simple and is directed radially outwards. It is assumed that the radial and latitudinal dependencies can be written independently from each other (e.g. Hattingh [1998], Langner [2004], Moeketsi [2004]) so that

$$\vec{V}_{\rm sw}(r,\theta) \equiv V_{\rm sw}(r,\theta)\vec{\rm e}_r = V_0 V_r(r) V_\theta(\theta)\vec{\rm e}_r, \tag{1.1}$$

where r is the radial distance from the Sun in astronomical units (AUs) and θ is the polar angle or co-latitude, where $\theta = 90^\circ$ defines the equatorial plane; $\vec{\rm e}_r$ is the unit vector in the radial direction and $V_0 = 400$ km/s. The SW latitude dependence is based on observations by Ulysses (e.g. Phillips et al. [1995]) and is written as

$$V_\theta(\theta) = 1.475 \mp 0.4 \tanh\left[6.8\left(\theta - \frac{\pi}{2} \pm \varphi\right)\right], \tag{1.2}$$

where the top and bottom signs correspond to the Northern (for $0 \leq \theta \leq \pi/2$) and Southern (for $\pi/2 \leq \theta \leq \pi$) hemispheres, respectively. The quantity $\varphi = 45^\circ$ for all values

of α where α is the tilt angle of the neutral heliospheric current sheet (HCS), i.e. the angle between the rotational and magnetic axes of the Sun. Similar approaches to modelling the SW were followed by e.g. Langner [2004], Strauss [2010], Vos [2011], Manuel [2013], Raath [2015], Prinsloo [2016] and Mohlolo [2016].

Inside of the TS, the radial dependence of the SW speed $V_r(r)$ is modelled as

$$V_r(r) = 1 - \exp\left[\frac{40}{3}\left(\frac{r_\odot - r}{r_0}\right)\right], \tag{1.3}$$

where $r_\odot = 0.005$ AU is the solar radius and $r_0 = 1$ AU. This equation is in accordance with measurements by Sheeley et al. [1997] who showed that the SW accelerates within the first 0.1 AU from the Sun and, on average, maintains a constant radial speed after 0.3 AU.

To account for the TS, i.e. simulate the decrease in V_{sw} that occurs at the radial position of the shock r_{TS}, the expression for the SW speed is modified by

$$V_{\text{sw}}(r,\theta) = V_{\text{sw}}(r_{\text{TS}},\theta)\frac{s+1}{2s} - V_{\text{sw}}(r_{\text{TS}},\theta)\frac{s-1}{2s}\tanh\left(\frac{r - r_{\text{TS}}}{L}\right), \tag{1.4}$$

(le Roux et al. [1996]) where the shock scale length is given by $L = 1.2$ AU and the shock compression ratio by $s = 2.5$; this compression ratio is defined in terms of the SW speed in the upstream region V_1 and in the downstream region V_2, i.e. $s = V_1/V_2$. See e.g. Li et al. [2008] for a discussion on the properties of the TS. See also e.g. Marsch et al. [2003] for a review on the SW.

In this work, the Smith-Bieber (Smith and Bieber [1991]) modified Parker HMF is employed. The unmodified Parker HMF (Parker [1958]) is given by

$$\vec{B} = B_0\left[\frac{r_0}{r}\right]^2\left(\vec{\text{e}}_r - \frac{\Omega(r - r_\odot)\sin\theta}{V_{\text{sw}}}\vec{\text{e}}_\phi\right) \tag{1.5}$$

where $\vec{\text{e}}_r$ and $\vec{\text{e}}_\phi$ are unit vectors in the radial and azimuthal directions respectively. B_0 is a normalization value which is related to the HMF magnitude at Earth B_{E} through

$$B_0 = B_{\text{E}}\left[1 + \left(\frac{\Omega r_0}{V_{\text{sw}}}\right)^2\right]^{-1/2}, \tag{1.6}$$

and $\Omega = 2.66 \times 10^{-6}$ rad/s is the average angular rotation speed of the Sun. Equation (1.5) is valid for $r > r_\odot$ and is written more compactly as

$$\vec{B} = B_0\left[\frac{r_0}{r}\right]^2\left(\vec{\text{e}}_r - \tan\psi\vec{\text{e}}_\phi\right), \tag{1.7}$$

where ψ is the Parker spiral angle or "garden hose" angle; this angle is defined as the angle between the radial direction and the direction of the average HMF at any given position

and is expressed as

$$\tan\psi = \frac{\Omega(r - r_\odot)}{V_{\rm sw}} \sin\theta. \tag{1.8}$$

The spiral angle ψ is an indication of how tightly winded the HMF lines are and, in the equatorial plane at Earth, is typically 45°; it increases with radial distance to 90° at $r \gtrsim 10$ AU.

The HMF magnitude follows directly from Equation (1.7), and is given by

$$B = B_0 \left[\frac{r_0}{r}\right]^2 \sqrt{1 + \tan^2\psi}. \tag{1.9}$$

The unmodified Parker HMF leads to an over-estimation of drift effects in the polar regions. In this work, such exaggerated drift velocities are reduced by modifying the HMF. It has, however, been demonstrated by Moloto et al. [2019] that observed larger turbulence levels over the poles could also act so as reduce drift effects in these regions even in the presence of an unmodified Parker HMF.

The modification to the HMF is implemented as by Smith and Bieber [1991] through the expression for the spiral angle so that

$$\tan\psi = \frac{\Omega(r - b)\sin\theta}{V_{\rm sw}(r,\theta)} - \frac{r}{b}\frac{V_{\rm sw}(b,\theta)}{V_{\rm sw}(r,\theta)}\left(\frac{B_{\rm T}(b)}{B_{\rm R}(b)}\right) \tag{1.10}$$

where $B_{\rm T}(b)/B_{\rm R}(b)$ is the ratio of the azimuthal to the radial magnetic field components at a position b near the solar surface, here taken as $b = 20r_\odot$. Smith and Bieber [1991] showed that the value of $B_{\rm T}(b)/B_{\rm R}(b)$ is approximately -0.02. The net effect is an average magnetic field magnitude that is larger in the polar regions than in the regions further away from the poles. See Haasbroek [1993] for an implementation of the Smith-Bieber modification.

There are also other modifications to the HMF that address the overly large drift velocities in the polar regions, the most notable of these being the Jokipii-Kóta modification (Jokipii and Kóta [1989]) and the modification by Moraal [1990]. For applications of the Jokipii-Kóta modification, see e.g. Haasbroek and Potgieter [1995], Jokipii et al. [1995], Hattingh [1998], Potgieter and Ferreira [1999] and Potgieter [2000]. For a comparison between the Smith-Bieber and Jokipii-Kóta modifications, as well as the respectively resulting drift velocities, see Raath [2015] and Raath et al. [2016].

An alternative model for the HMF was proposed by Fisk [1996]. This modification was based on the argument that the Sun does not rotate rigidly, but rather differentially with the poles rotating slower than the solar equator (e.g. Snodgrass [1983]). The implementation of this HMF, however, lies beyond the scope of this study. For more information, see e.g. Kóta and Jokipii [1997], Giacalone and Jokipii [1999], Burger and Hattingh [2001], Burger and Hitge [2004], Krüger [2005], Engelbrecht [2008], Burger et al.

[2008] and Sternal et al. [2011]. See also Steyn [2016] for an investigation into a generalized Fisk-type heliospheric magnetic field.

The modulation model featured in this study contains a wavy HCS (Strauss et al. [2012]). The HCS is a major co-rotating structure in the heliosphere and defines the magnetic equator in that it divides the HMF into hemispheres of opposite polarities. The existence of the HCS, separating the two regions of oppositely directed magnetic field lines, is a requirement of Maxwell's equations (e.g. Smith [2001]). The result is a jump in polarity across the HCS that was first observed by the early Pioneer missions (Smith [1989]). Observations furthermore suggest that the HCS can cover the entire extent of the heliosphere during the course of the solar activity cycle (e.g. Burlaga and Ness [1993]). For a detailed review of the HCS, see Smith [2001]. The misalignment between the rotational and magnetic axes of the Sun, separated by the tilt angle α (e.g. Hoeksema [1992]) causes the HCS to be warped rather than flat. As will be discussed in later chapters, the tilt angle varies as function of solar activity, ranging from minimum values at solar minimum conditions to maximum values at solar maximum conditions (see Figure 3.6) and therefore the waviness of the HCS varies with solar activity. The HCS tilt angle is most often used as a proxy for solar activity in modulation models and, in this work, also features prominently in this capacity (see Chapters 3 to 5).

The expression that will be used for the HCS latitudinal extent in this work is equivalent to that obtained by Kóta and Jokipii [1983] and Pogorelov et al. [2007]

$$\theta^{'} = \frac{\pi}{2} - \tan^{-1}\left[\tan\alpha \sin\left(\phi + \frac{\Omega(r - r_{\odot})}{V_{\rm sw}}\right)\right]. \tag{1.11}$$

This expression was used by e.g. Langner [2004] who showed that it was generally valid up to tilt angles as large as 75°. See also Raath et al. [2015].

In order to incorporate the HCS into the HMF, Equation (1.7) must be modified to

$$\vec{B} = A_c B_0 \left[\frac{r_0}{r}\right]^2 (\vec{\rm e}_r - \tan\psi \vec{\rm e}_\phi)\left[1 - 2H(\theta - \theta^{'})\right] \tag{1.12}$$

where $A_{\rm c} = \pm 1$ and $H(\theta - \theta^{'})$ is the Heaviside step function. The constant A_c determines the polarity of the HMF with $A_{\rm c} \equiv +1$ for the $A > 0$ polarity cycle and $A_{\rm c} \equiv -1$ for the $A < 0$ polarity cycle. The $A > 0$ polarity cycle has been defined as periods when the magnetic lines are directed outward in the northern hemisphere of the Sun and inward in the southern hemisphere; the direction of these lines is reversed during the $A < 0$ polarity cycle. The Heaviside step function is given by

$$H(\theta - \theta^{'}) \equiv \begin{cases} 0 & \text{when} \quad \theta < \theta^{'} \\ \\ 1 & \text{when} \quad \theta > \theta^{'} \end{cases} \tag{1.13}$$

and causes the HMF polarity to change across the HCS.

All of these aspects, as well as suitable CR transport parameters, are incorporated into a numerical modulation model to simulate CR modulation for varying solar activity and different polarity cycles; in particular, the simulations are compared to measurements from the PAMELA instrument. The acronym "PAMELA" stands for "Payload for Antimatter Matter Exploration and Light-nuclei Astrophysics"; see Casolino et al. [2008] and references therein for technical information on this instrument. The primary scientific goal of PAMELA is to study the antimatter component of the cosmic radiation at Earth (Picozza et al. [2007]). The detector is, however, of particular interest in this study for its measurement of the GCR proton spectra at Earth, specifically for the time interval 2010 to 2014. For a review of the PAMELA mission and its accomplishments, see Adriani et al. [2014] and Galper and Spillantini [2018].

The theory of CR transport in the heliosphere and the physical processes by which CRs are modulated are discussed in the first sections of **Chapter 2**, introducing the Parker transport equation (TPE); see Parker [1965], Gleeson and Axford [1967]. The important modulation processes of drifts and diffusion are discussed. In the discussion of particle drifts, much emphasis is placed on the scaling down of drifts due to turbulence, though the theory of turbulence is not considered in detail. An expression that includes this suppression due to turbulence is defined for the drift coefficient, and expressions are obtained for the drift velocities.

The final sections of Chapter 2 discuss the numerical model that is featured in this study in the necessary detail, giving a brief introduction to stochastic differential equations (SDEs) and discussing such models. The SDE formulation for the TPE is then presented, and the basis for the numerical model is established; the relevant boundary conditions are also defined.

In **Chapter 3**, the SDE-based numerical modulation model described in Chapter 2 is applied to study the solar modulation of GCR protons over the time period spanning January 2010 to January 2014. Data from the PAMELA experiment measured over this period of time is used for comparison (Martucci et al. [2018]). The model that is employed in this thesis was applied to the January 2010 and January 2014 GCR proton spectra in Martucci et al. [2018] and, in this chapter, the relevant results of that study are revisited, providing further insights. Next, a number of eight half-yearly averaged spectra, falling in between January 2010 and 2014, are calculated from the PAMELA data and the model is applied to reproduce these spectra so that the modulation over this entire range of time is studied effectively in increments of six months.

In **Chapter 4** the scaling down of drift effects towards solar maximum conditions forms the central topic. To this end, a function $f_{\mathrm{d}}(\alpha)$ is introduced to scale down drift effects towards solar maximum conditions. The scaling down function is defined in terms of the tilt angle and the approach is purely phenomenological; see e.g. Ferreira [2002] and Ndiitwani et al. [2005]. The reproductions of the PAMELA proton data (Martucci et al. [2018]) that were obtained in Chapter 3 are reconsidered, so that a new set of parameters

is obtained to account for the additional scaling down of drifts towards solar maximum. A large part of this chapter is also devoted to a discussion of the drift properties of the model. The illustrative capability of the SDE-based model is exploited to yield some valuable insights into the mechanisms of modulation and drifts in particular. Different ways in which drifts can be scaled down, as well as the energy dependence of drift effects, are illustrated and discussed.

It is mentioned, at this point, that measurements of the CR proton flux taken by AMS-02 (Alpha Magnetic Spectrometer) between May 2011 and May 2017 in the rigidity range 1 to 60 GV is also available (Aguilar et al. [2018]). The study of this thesis is, however, restricted to the observations from the PAMELA instrument and no attempts are made to compare AMS-02 and PAMELA data - that is the topic of another study. For modelling done on this AMS-02 data, see e.g. Tomassetti et al. [2018] and Corti et al. [2019].

In **Chapter 5**, particle drift effects are illustrated in terms of the charge-sign dependent modulation of cosmic ray positrons e^+ and electrons e^-. The energy dependence of the e^+ fraction, $e^+/(e^+ + e^-)$, calculated by the model employed in this study is presented and the results are shown to be in agreement with the qualitative picture provided by observations from the PAMELA spacecraft (Galper and Spillantini [2018]). The e^+ to e^- ratio, e^+/e^-, is then considered as function of solar activity and it is again illustrated that the model yields results that are in qualitative agreement with the work of other authors (e.g. Burger and Potgieter [1999]). New in this chapter is that cases with and without the inclusion of the drift scaling function $f_{\mathrm{d}}(\alpha)$ are considered. The final section of this chapter is devoted to providing a glimpse of research that can be done in future, using this model, to investigate drift effects. Specifically, it is illustrated how different scaling functions $f_{\mathrm{d}}(\alpha)$ can influence the e^+/e^- ratio as a function of solar activity and also how the inclusion of a time-dependent magnetic field magnitude can affect the intensity versus solar activity profiles. Though the aim of this chapter is not to reproduce data, it is motivated that the model should be ideally suited to reproduce observations such as e^+/e^- ratios and the e^+ fraction in future studies.

Chapter 6 gives a summary of this thesis and presents all of the significant conclusions drawn during the course of this study.

A nomenclature is provided defining most of the relevant abbreviations and acronyms used in this study. However, for the sake of easy readability, when a concept is referred to for the first time, it is written out in full and the abbreviation or acronym given in brackets. Acronyms are written out in full only the first time they occur, while abbreviations are written out in full when they are used the first time in each chapter; abbreviations are also written out in full when used for the first time in the summary sections of each chapter.

Aspects of this work were presented at the following conferences and workshops:

- The 2014 National Meeting of the Centre for High Performance Computing (CHPC) in Skukuza, South Africa (December 2014).
- The 60th annual Conference of the South African Institute of Physics (SAIP) in Port Elizabeth, South Africa (July 2015).
- Workshop held in Potchefstroom, South Africa (March 2017).
- The 35th biannual International Cosmic Ray Conference (ICRC) in Busan, South Korea (July 2017).
- The 42nd biannual General Assembly of the Committee on Space Research (COSPAR) in Pasadena, California, USA (July 2018).

Extracts from this thesis were published in

- Martucci, M., R. Munini, M. Boezio, V. Di Felice, O. Adriani, G.C. Barbarino, G.A. Bazilevskaya, R. Bellotti, et al., *Proton fluxes measured by the PAMELA experiment from the minimum to the maximum solar activity for solar cycle 24*, The Astrophysical Journal Letters, 854, L2, 2018.

Chapter 2

Modelling Cosmic Ray Transport in the Heliosphere

2.1 Introduction

When Galactic cosmic rays (GCRs) enter the heliosphere, their differential intensity and distribution, as specified by the relevant local interstellar spectrum (LIS) at the boundary of the modulation space, are altered as function of energy, position and time. There are a number of important physical processes involved in this modulation that cosmic rays (CRs) experience in the heliosphere, viz. particle drifts and diffusion, adiabatic energy changes and convection via the solar wind (SW); Parker [1958]. Not only must all of these processes be taken into account, but they must be understood as comprehensively as possible in order to construct the most realistic modulation models. In this work, the processes of drift and diffusion are of main concern and are therefore discussed in the necessary detail. The above mentioned modulation processes are all accounted for in the Parker transport equation (TPE) (Parker [1965]; Gleeson and Axford [1967]). As such, the TPE forms the basis for discussion in this chapter. In order to construct the numerical modulation model, which approximates the heliosphere as spherical in geometry, the TPE is converted to spherical coordinates, after which the set of stochastic differential equations (SDEs) corresponding to the TPE is derived. This results in the SDE-based numerical modulation model, consisting of three spatial dimensions and energy (rigidity).

Chapter 2 is primarily concerned with the theoretical background that is essential for the research presented in Chapters 3 to 5 and therefore borrows from existing literature, in particular Strauss [2013], Raath [2015] and Strauss and Effenberger [2017].

2.2 The Parker Transport Equation

The TPE was originally derived by Parker [1965] and re-derived by Gleeson and Axford [1967]. It can be expressed as

$$\frac{\partial f}{\partial t} = -\left(\vec{V}_{\rm sw} + \langle \vec{v}_{\rm d} \rangle\right) \cdot \nabla f + \nabla \cdot \left(\mathbf{K}^{(\rm s)} \cdot \nabla f\right) + \frac{1}{3}\left(\nabla \cdot \vec{V}_{\rm sw}\right) \frac{\partial f}{\partial \ln p} + Q', \tag{2.1}$$

in terms of the omni-directional CR distribution function $f\left(\vec{r}, p, t\right)$, where $\vec{r}$ is the position, p the particle momentum, and t is the time.

This form of the TPE accounts for all the relevant transport phenomena. The terms, from left to right, respectively represent time-dependent changes, outward convection via the SW flow $\vec{V}_{\rm sw}$, CR drifts in terms of the pitch-angle averaged guiding centre drift velocity $\langle \vec{v}_{\rm d} \rangle$, spatial diffusion through the symmetric diffusion tensor $\mathbf{K}^{(\rm s)}$, adiabatic energy changes through the solar wind divergence $\nabla \cdot \vec{V}_{\rm sw}$, and any possible sources of CRs inside the heliosphere $Q'(\vec{r}, p, t)$ such as Jovian electrons. See e.g. Fisk [1999] and Potgieter [1998, 2011, 2013] for overviews of all the heliospheric transport processes.

The model employed in this work does not account for diffusive shock acceleration (Fermi I acceleration), but does provide for a 'simulated' heliosheath and termination shock (TS) established entirely through Equation (1.4) by which the $\vec{V}_{\rm sw}$ drops to lower values over the TS at $r = r_{\rm TS}$; this will effectively also incorporate corresponding changes in the magnetic field and transport coefficients; see also Ferreira and Scherer [2005]. This is sufficient for the purposes of the current study, since the focus here is on the modulation of high-energy GCRs and these effects would only become important when, for example, the anomalous component of cosmic rays (ACRs) was considered. For a description of a TPE that includes an additional term to describe Fermi II acceleration (stochastic acceleration), derived from a more general Fokker-Planck equation, see e.g. Schlickeiser [2002] and Strauss [2010]. For details on the further refinement of the TPE, see Gleeson and Axford [1968], Jokipii and Parker [1970] and Schlickeiser [2002].

Although the TPE is written in terms of momentum, it is usually solved in terms of rigidity, defined as

$$\begin{aligned} P &\equiv \frac{pc}{Q} \\ &= \frac{mvc}{Ze}, \end{aligned} \tag{2.2}$$

with $p = mv$ the particle's momentum, $Q = Ze$ its signless charge, and c the speed of light.

The total energy of a relativistic particle can be written as

$$\begin{aligned} E_{\mathrm{p}}^2 &= p^2c^2 + m_0^2c^4 \\ &= \left(T_{\mathrm{p}} + E_{0,\mathrm{p}}\right)^2, \end{aligned} \tag{2.3}$$

where m_0 is the particle rest-mass and T_{p} and $E_{0,\mathrm{p}}$ are the total kinetic energy and total rest energy of the particle respectively. Then, in terms of rigidity, the total energy is

$$E_{\mathrm{p}}^2 = P^2(Ze)^2 + E_{0,\mathrm{p}}^2. \tag{2.4}$$

For data comparison purposes, these quantities are rewritten in terms of the total energy per nucleon E_{n} and the total kinetic energy per nucleon T_{n}, as

$$\begin{aligned} A^2E_{\mathrm{n}}^2 &= P^2(Ze)^2 + A^2E_0^2 \\ &= (AT_{\mathrm{n}} + AE_0)^2, \end{aligned} \tag{2.5}$$

where A is the mass number and E_0 the rest-energy of a single nucleon. The total kinetic energy per nucleon can be written in terms of particle rigidity as

$$T_{\mathrm{n}} = \sqrt{P^2\left(\frac{Ze}{A}\right)^2 + E_0^2} - E_0, \tag{2.6}$$

or, conversely, the rigidity can be written in terms of the kinetic energy per nucleon

$$\begin{aligned} P &= \left(\frac{A}{Ze}\right)\sqrt{\left(T_{\mathrm{n}} + E_0\right)^2 - E_0^2} \\ &= \left(\frac{A}{Ze}\right)\sqrt{T_{\mathrm{n}}\left(T_{\mathrm{n}} + 2E_0\right)}. \end{aligned} \tag{2.7}$$

From these expressions, another useful quantity is defined, namely the ratio of the particle speed to the speed of light, β_c, given by

$$\begin{aligned}\beta_c &= \frac{v}{c} \\ &= \frac{pc}{mc^2} \\ &= \frac{PZe}{AE} \\ &= \frac{PZe}{\sqrt{P^2\left(Ze\right)^2 + A^2E_0^2}} \\ &= \frac{P}{\sqrt{P^2 + \left(\frac{A}{Ze}\right)^2 E_0^2}}\end{aligned} \tag{2.8}$$

in terms of rigidity or

$$\begin{aligned}\beta_c &= \frac{v}{c} \\ &= \frac{pc}{mc^2} \\ &= \frac{\sqrt{E_{\mathrm{p}}^2 - E_{0,\mathrm{p}}^2}}{E_{\mathrm{p}}} \\ &= \frac{\sqrt{E^2 - E_0^2}}{E} \\ &= \frac{\sqrt{T_{\mathrm{n}}(T_{\mathrm{n}} + 2E_0)}}{T_{\mathrm{n}} + E_0},\end{aligned} \tag{2.9}$$

in terms of kinetic energy. From this equation, the relation between rigidity, kinetic energy, and β_c is

$$\begin{aligned}P &= \frac{A}{Z}\sqrt{T_{\mathrm{n}}(T_{\mathrm{n}} + 2E_0)} \\ &= \left(\frac{A}{Z}\right)\beta_c(T_{\mathrm{n}} + E_0).\end{aligned} \tag{2.10}$$

Furthermore, the density of particles within a region d^3r with a momentum between $\vec{p}$ and $\vec{p} + d\vec{p}$ is related to the full CR distribution function through

$$\begin{aligned}n &= \int F\left(\vec{r}, \vec{p}, t\right) d^3p \\ &= \int_p p^2 \left[\int_\Omega F\left(\vec{r}, \vec{p}, t\right) d\Omega\right] dp,\end{aligned} \tag{2.11}$$

where the relation $d^3p = p^2 dp d\Omega$ was used. Also, the differential particle density U_p is related to n by

$$n \equiv \int U_p\left(\vec{r}, p, t\right) dp, \tag{2.12}$$

resulting in

$$U_p\left(\vec{r},p,t\right)=\int_\Omega p^2F\left(\vec{r},\vec{p},t\right)d\Omega. \tag{2.13}$$

The omni-directional (or pitch angle) average of $F\left(\vec{r},\vec{p},t\right)$, as used in this study, can be calculated as

$$\begin{aligned} f\left(\vec{r},p,t\right) &\equiv \frac{\int_\Omega F\left(\vec{r},\vec{p},t\right)d\Omega}{\int_\Omega d\Omega} \\ &= \frac{1}{4\pi}\int_\Omega F\left(\vec{r},\vec{p},t\right)d\Omega, \end{aligned} \tag{2.14}$$

leading to the relation

$$U_p\left(\vec{r},p,t\right)=4\pi p^2f\left(\vec{r},p,t\right). \tag{2.15}$$

The differential intensity, in units of particles/unit area/unit time/unit momentum/unit solid angle, is defined as

$$\begin{aligned} j_p\left(\vec{r},p,t\right) &= \frac{vU_p\left(\vec{r},p,t\right)}{\int_\Omega d\Omega} \\ &= \frac{vU_p\left(\vec{r},p,t\right)}{4\pi} \\ &= vp^2f\left(\vec{r},p,t\right). \end{aligned} \tag{2.16}$$

The particle speed can be eliminated from this equation by noting that

$$\frac{\partial p}{\partial E}=\frac{1}{v}, \tag{2.17}$$

and by using the relation $jdE=j_pdp$, it follows that

$$\begin{aligned} j\left(\vec{r},p,t\right) &= \frac{v}{4\pi}U_p\frac{dp}{dE} \\ &= \frac{1}{4\pi}U_p \\ &= p^2f\left(\vec{r},p,t\right), \end{aligned} \tag{2.18}$$

in units of particles/unit area/unit time/unit kinetic energy per nucleus/unit solid angle. See also Potgieter [1984] and Strauss [2010].

2.3 The Transport Equation in Spherical Coordinates

For the purposes of the numerical model, discussed in Section 2.6, the TPE is solved in a spherical coordinate system. While the heliosphere is here simply assumed to be spherical in geometry, some models based on magneto-hydrodynamic (MHD) input assume different geometries e.g. Luo et al. [2013]. Consider a coordinate system which has one axis parallel to the mean heliospheric magnetic field (HMF), i.e. $\vec{B}=B_0\vec{e}_z$ in the $r\phi$-plane ($\vec{e}_{||}$); it

has another axis perpendicular to the first in the $\vec{e}_\theta$-direction ($\vec{e}_1$), and a third axis ($\vec{e}_2$) perpendicular to both the first two axes in the $r\theta$-plane so that it forms a right-handed HMF-aligned coordinate system. Within this coordinate system, a tensor $\mathbf{K}$ can be set up, consisting of the sum of the symmetric tensor $\mathbf{K}^{(s)}$ (as it occurs in Equation (2.1)) and an antisymmetric part $\mathbf{K}^{(a)}$, i.e.

$$\begin{aligned}
\mathbf{K} &= \mathbf{K}^{(s)} + \mathbf{K}^{(a)} \\
&= \begin{bmatrix} \kappa_{||} & 0 & 0 \\ 0 & \kappa_{\perp\theta} & 0 \\ 0 & 0 & \kappa_{\perp r} \end{bmatrix} + \begin{bmatrix} 0 & 0 & 0 \\ 0 & 0 & \kappa_A \\ 0 & -\kappa_A & 0 \end{bmatrix} \\
&= \begin{bmatrix} \kappa_{||} & 0 & 0 \\ 0 & \kappa_{\perp\theta} & \kappa_A \\ 0 & -\kappa_A & \kappa_{\perp r} \end{bmatrix},
\end{aligned} \tag{2.19}$$

so that the diffusion coefficients are contained in the symmetric part of the tensor, while the drift coefficient is accounted for in the antisymmetric part. This tensor then contains the necessary diffusion and drift coefficients that determine the extent of particle modulation in the heliosphere: $\kappa_{||}$ is the diffusion coefficient parallel to the HMF, $\kappa_{\perp\theta}$ is the diffusion coefficient perpendicular to the HMF in the $\vec{e}_\theta$-direction, and $\kappa_{\perp r}$ is the diffusion coefficient perpendicular to the HMF in the $\vec{e}_r$-direction; κ_A is the drift coefficient. See e.g. Gleeson [1969], Forman et al. [1974] and Burger and Hattingh [1998].

Now the TPE of Equation (2.1) can be written in a more compact form,

$$\frac{\partial f}{\partial t} = -\vec{V}_{sw} \cdot \nabla f + \nabla \cdot (\mathbf{K} \cdot \nabla f) + \frac{1}{3}(\nabla \cdot \vec{V}_{sw}) \frac{\partial f}{\partial \ln p}, \tag{2.20}$$

where the average guiding center drift velocity $\langle \vec{v}_d \rangle$ is included in the tensor $\mathbf{K}$ and the source term Q' has has been set to zero.

The HMF-aligned coordinate system is related to the spherical coordinate system through

$$\begin{aligned}
\vec{e}_{||} &= \cos\psi \vec{e}_r - \sin\psi \vec{e}_\phi \\
\vec{e}_1 &= \vec{e}_\theta \\
\vec{e}_2 &= \vec{e}_{||} \times \vec{e}_1 = \sin\psi \vec{e}_r + \cos\psi \vec{e}_\phi,
\end{aligned} \tag{2.21}$$

where ψ is the spiral angle, defined as the angle between the parallel component of the magnetic field (in the $\vec{e}_{||}$ direction) and the radial direction $\vec{e}_r$. By specifying an appropriate transformation matrix $\mathbf{T}$, with $\det(\mathbf{T}) = 1$, the tensor $\mathbf{K}$ can be written in

terms of heliocentric spherical coordinates. This transformation matrix is given by

$$\mathbf{T} = \begin{bmatrix} \cos\psi & 0 & \sin\psi \\ 0 & 1 & 0 \\ -\sin\psi & 0 & \cos\psi \end{bmatrix}, \tag{2.22}$$

so that the tensor $\mathbf{K}$ in spherical coordinates is

$$\begin{aligned} \mathbf{K} &= \mathbf{T}\mathbf{K}\mathbf{T}^T \\ &= \begin{bmatrix} \cos\psi & 0 & \sin\psi \\ 0 & 1 & 0 \\ -\sin\psi & 0 & \cos\psi \end{bmatrix} \begin{bmatrix} \kappa_{||} & 0 & 0 \\ 0 & \kappa_{\perp\theta} & \kappa_{\mathrm{A}} \\ 0 & -\kappa_{\mathrm{A}} & \kappa_{\perp r} \end{bmatrix} \begin{bmatrix} \cos\psi & 0 & -\sin\psi \\ 0 & 1 & 0 \\ \sin\psi & 0 & \cos\psi \end{bmatrix} \\ &= \begin{bmatrix} \kappa_{||}\cos^2\psi + \kappa_{\perp r}\sin^2\psi & -\kappa_{\mathrm{A}}\sin\psi & (\kappa_{\perp r} - \kappa_{||})\cos\psi\sin\psi \\ \kappa_{\mathrm{A}}\sin\psi & \kappa_{\perp\theta} & \kappa_{\mathrm{A}}\cos\psi \\ (\kappa_{\perp r} - \kappa_{||})\cos\psi\sin\psi & -\kappa_{\mathrm{A}}\cos\psi & \kappa_{||}\sin^2\psi + \kappa_{\perp r}\cos^2\psi \end{bmatrix} \\ &= \begin{bmatrix} \kappa_{rr} & \kappa_{r\theta} & \kappa_{r\phi} \\ \kappa_{\theta r} & \kappa_{\theta\theta} & \kappa_{\theta\phi} \\ \kappa_{\phi r} & \kappa_{\phi\theta} & \kappa_{\phi\phi} \end{bmatrix}. \end{aligned} \tag{2.23}$$

The above transformation assumes a Parker field geometry. Note that the Smith-Bieber modified field still has a Parker field geometry since it does not contain a θ-component. See also Alania and Dzapiashvili [1979], Kobylinski [2001] and Alania [2002] for more on this transformation. For a transformation assuming a more general heliospheric magnetic field model, see e.g. Burger et al. [2008], Moloto [2015] and Engelbrecht and Burger [2015*b*].

The TPE in Equation (2.20) can now be written in terms of spherical coordinates as

$$\begin{aligned}
\frac{\partial f}{\partial t} &= \overbrace{\left[\frac{1}{r^2}\frac{\partial}{\partial r}(r^2\kappa_{rr}) + \frac{1}{r\sin\theta}\frac{\partial \kappa_{\phi r}}{\partial \phi}\right]\frac{\partial f}{\partial r} + \left[\frac{1}{r^2\sin\theta}\frac{\partial}{\partial\theta}(\kappa_{\theta\theta}\sin\theta)\right]\frac{\partial f}{\partial\theta}}^{\text{diffusion}} \\
&+ \overbrace{\left[\frac{1}{r^2\sin\theta}\frac{\partial}{\partial r}(r\kappa_{r\phi}) + \frac{1}{r^2\sin^2\theta}\frac{\partial\kappa_{\phi\phi}}{\partial\phi}\right]\frac{\partial f}{\partial\phi}}^{\text{diffusion}} \\
&+ \overbrace{\kappa_{rr}\frac{\partial^2 f}{\partial r^2} + \frac{\kappa_{\theta\theta}}{r^2}\frac{\partial f^2}{\partial\theta^2} + \frac{\kappa_{\phi\phi}}{r^2\sin^2\theta}\frac{\partial^2 f}{\partial\phi^2} + \frac{2\kappa_{r\phi}}{r\sin\theta}\frac{\partial^2 f}{\partial r\partial\phi}}^{\text{diffusion}} \\
&+ \overbrace{[-\langle\vec{v}_{\mathrm{d}}\rangle_r]\frac{\partial f}{\partial r} + \left[-\frac{1}{r}\langle\vec{v}_{\mathrm{d}}\rangle_\theta\right]\frac{\partial f}{\partial\theta} + \left[-\frac{1}{r\sin\theta}\langle\vec{v}_{\mathrm{d}}\rangle_\phi\right]\frac{\partial f}{\partial\phi}}^{\text{drift}} \\
&- \overbrace{V_{\mathrm{sw}}\frac{\partial f}{\partial r}}^{\text{convection}} \\
&+ \overbrace{\frac{1}{3r^2}\frac{\partial}{\partial r}(r^2 V_{\mathrm{sw}})\frac{\partial f}{\partial\ln p}}^{\text{adiabatic energy losses}}.
\end{aligned} \tag{2.24}$$

Here it is assumed that the SW is axis-symmetrical and consists only of a radial component, i.e. $\vec{V}_{\mathrm{sw}} = V_{\mathrm{sw}}\vec{e}_r$. The TPE was rearranged so that the various terms that are responsible for each of the modulation processes respectively were isolated. The first three lines contain the terms that describe diffusion, while the fourth line accounts for the terms that describe particle drift motions; the terms of the fifth and sixth lines represent convection and adiabatic energy losses respectively; see also e.g. Hattingh [1998], Ferreira [2002], Vos [2011], Strauss [2013] and Raath [2015].

2.4 Particle Drifts

During modulation in the heliosphere, CRs will be affected by drifts through the gradient and curvature of the large scale HMF, as well as current sheet drifts at the magnetic equator due to the switch in magnetic polarity across the neutral heliospheric current sheet (HCS) (e.g. Burger and Potgieter [1989]). Even though included in the original derivation of the TPE by Parker [1965], the effect of drifts was neglected in modulation models until Jokipii et al. [1977] showed that this modulation mechanism may, in fact, play a significant role in CR modulation; see also Jokipii and Levy [1977] and Jokipii and Thomas [1981]. Kóta [2016] showed that the effect of drifts was important even in the heliosheath.

Drift effects explain the observed HMF polarity dependent CR observations (e.g. Jokipii and Kopriva [1979]; Potgieter and Moraal [1985]; Webber et al. [2005]) and also lead to a strong dependence of cosmic ray intensity on the solar tilt angle (Lockwood and Webber [2005]). The drift process also has a significant influence on global cosmic ray modulation phenomena such as observed latitude gradients (Heber et al. [1996], Zhang [1997], de Simone et al. [2011]) and may also be important for the study of solar energetic particles (Dalla et al. [2013]).

With the development of more realistic numerical models for the modulation of CRs, (e.g. Kóta and Jokipii [1983]; Potgieter and Moraal [1985]; Hattingh and Burger [1995]) it became clear that drift effects for CRs of low to intermediate energies had to be suppressed in order to account for observations (e.g. Potgieter et al. [1989]). The suppression of drift effects by turbulence has been indicated theoretically and by means of numerical test-particle simulations; see e.g. Burger [1990], Jokipii [1993], Fisk and Schwadron [1995], Candia and Roulet [2004], Minnie et al. [2007], Tautz and Shalchi [2012], Engelbrecht and Burger [2015*a*] and Engelbrecht et al. [2017].

2.4.1 The Drift Coefficient

In the most general case the pitch-angle averaged guiding center drift velocity is given by

$$\langle \vec{v}_{\rm d} \rangle = \frac{pv}{3Q} \frac{(\omega\tau_{\rm d})^2}{1+(\omega\tau_{\rm d})^2} \nabla \times \frac{\vec{B}}{B^2}, \tag{2.25}$$

where the suppression of drifts by turbulence (scattering) is included via the term containing $\omega\tau_{\rm d}$; see Minnie et al. [2007] and references therein for a more complete treatment of the matter. Here, ω is the particle gyro-frequency and $\tau_{\rm d}$ is a time scale defined by scattering; $\vec{B}$ and B are the magnetic field vector and magnitude respectively.

Using a simple vector identity, Equation (2.25) can be written as

$$\begin{aligned} \langle \vec{v}_{\rm d} \rangle &= \nabla \times \frac{pc}{Q}\frac{v}{c}\frac{1}{3B}\frac{(\omega\tau_{\rm d})^2}{1+(\omega\tau_{\rm d})^2}\frac{\vec{B}}{B} \\ &= \nabla \times \frac{P\beta_c}{3B}\frac{(\omega\tau_{\rm d})^2}{1+(\omega\tau_{\rm d})^2}\frac{\vec{B}}{B} \\ &= \nabla \times \frac{v}{3} r_{\rm L} \frac{(\omega\tau_{\rm d})^2}{1+(\omega\tau_{\rm d})^2}\vec{e}_B \\ &= \nabla \times \kappa_{\rm A}\vec{e}_B, \end{aligned} \tag{2.26}$$

where r_L is the maximal Larmor radius, i.e. for a 90° pitch angle,

$$\begin{aligned} r_{\rm L} &= \frac{mv}{QB} \\ &= \frac{P}{Bc}, \end{aligned} \tag{2.27}$$

and where $\vec{e}_B = \vec{B}/B$ is a unit vector directed along $\vec{B}$; in the last step, the drift coefficient $\kappa_{\rm A}$ has been defined as

$$\kappa_{\rm A} = \frac{v}{3} r_{\rm L} \frac{(\omega\tau_{\rm d})^2}{1+(\omega\tau_{\rm d})^2}, \tag{2.28}$$

as it occurs in Bieber and Matthaeus [1997] where this expression was obtained considering the effects of transverse turbulent fluctuations on unperturbed particle orbits.

The assumption of weak scattering, i.e. assuming that a particle undergoes a large number of gyrations before being scattered, leads to a drift velocity taking on its maximal weak scattering value and therefore

$$(\omega\tau_{\rm d})^{\rm ws} \gg 1. \tag{2.29}$$

With this assumption, Eq. (2.26) reduces to

$$\begin{aligned} \langle \vec{v}_{\rm d} \rangle^{\rm ws} &= \nabla \times \frac{v}{3} r_{\rm L} \vec{e}_B \\ &= \nabla \times \kappa_{\rm A}^{\rm ws} \vec{e}_B, \end{aligned} \tag{2.30}$$

with the weak scattering drift coefficient given by

$$\kappa_{\rm A}^{\rm ws} = \frac{v}{3} r_{\rm L}. \tag{2.31}$$

Note that for very strong scattering $(\omega\tau_{\rm d})^{\rm ss} \to 0$, and it follows that $\kappa_{\rm A}^{\rm ss} \to 0$ so that no particle drift is present.

The exact form of the suppression factor on $\kappa_{\rm A}$ continues to be studied, e.g. Visser [2009], Burger and Visser [2010], Engelbrecht and Burger [2015*a*], Ngobeni and Potgieter [2015] and Engelbrecht et al. [2017]. In this study the approach of Burger et al. [2000, 2008] is followed, where it is assumed that $(\omega\tau_{\rm d}) \sim P$, resulting in

$$\kappa_{\rm A} = \kappa_{\rm A,0} \frac{v}{3} r_{\rm L} \frac{(P/P_0)^2}{1+(P/P_0)^2}, \tag{2.32}$$

with $P_0 = 0.16$ GV, following Vos [2011]. It is clear that $\kappa_{\rm A} \to \kappa_{\rm A}^{\rm ws}$ if $P_0 \to 0$. An increase in the value of P_0 will imply a smaller $\kappa_{\rm A}$ and decreased drift effects, while the converse applies for a decrease in P_0; see Engelbrecht [2008].

The parameter $\kappa_{\rm A,0} \in [0,1]$ is used to scale the drift from zero ($\kappa_{\rm A,0} = 0$) to one hundred ($\kappa_{\rm A,0} = 1$) percent. The need to introduce this parameter follows from Potgieter et al. [1989], who showed that full drifts at all energies were not plausible and that $\kappa_{\rm A,0}$ needed to be reduced in order to reproduce CR observations (Webber et al. [1990]). Furthermore, Ferreira and Potgieter [2004] showed that $\kappa_{\rm A,0} \in [0.0, 0.1]$ was needed to reproduce solar maximum observations; see also Ferreira [2002], Ndiitwani et al. [2005], Manuel et al. [2011] and Siluszyk et al. [2011] for modelling where drifts were scaled down towards solar

maximum. Nel [2015] has also indicated that drift effects showed a clear dependence on solar activity.

The drift coefficient is related to the so-called drift scale through

$$\lambda_{\mathrm{A}} = \frac{3}{v}\kappa_{\mathrm{A}}, \tag{2.33}$$

which, in this work, is presented in astronomical units (AUs). For the weak-scattering scenario, the drift scale becomes $\lambda_{\mathrm{A}}^{\mathrm{ws}} = r_{\mathrm{L}}$.

Figure 2.1 shows the rigidity and radial dependencies of the drift scale λ_{A}, employing a Smith-Bieber modified magnetic field as explained in Chapter 1. The top panel of Figure 2.1 shows the rigidity dependence of λ_{A} at Earth. The dashed red and blue lines show the cases where drifts have been modified according to Equation (2.32), for values of $P_0 = P_{0,1} = 0.16$ GV and $P_0 = P_{0,2} = 2.0$ GV respectively. These two values for P_0 are indicated by the vertical dashed lines. The weak scattering limit for λ_{A} is also shown by the solid black line. It is clear from this figure that, for the modified form of κ_{A}, λ_{A} is significantly reduced when $P < P_0$, and drifts at low energies can therefore be neglected, i.e. at rigidities $P \ll P_0$.

The radial dependence of λ_{A} in the equatorial plane at 1 GV is shown in the bottom panel of Figure 2.1, using $P_0 = P_{0,1} = 0.16$ GV. The vertical dashed line now indicates the position of the TS, being set at a radial distance of $r_{\mathrm{TS}} = 90$ AU. From the top panel of Figure 2.1, it is clear that the modified and weak scattering values of κ_{A} are comparable at this rigidity and, as such, the bottom panel also shows r_{L} indirectly. From the expressions presented earlier, the radial dependence of λ_{A} is seen to be essentially governed by B which, in turn, is dependent on the magnitude of $\vec{V}_{\mathrm{sw}}$ through Equations (1.9) and (1.10). The drift scale is therefore seen to decrease sharply over the TS. The current profile assumed beyond the TS is sufficient for the purposes of this study; for a discussion of different $\vec{V}_{\mathrm{sw}}$ profiles in the heliosheath, see e.g. Langner et al. [2006] and Strauss [2010].

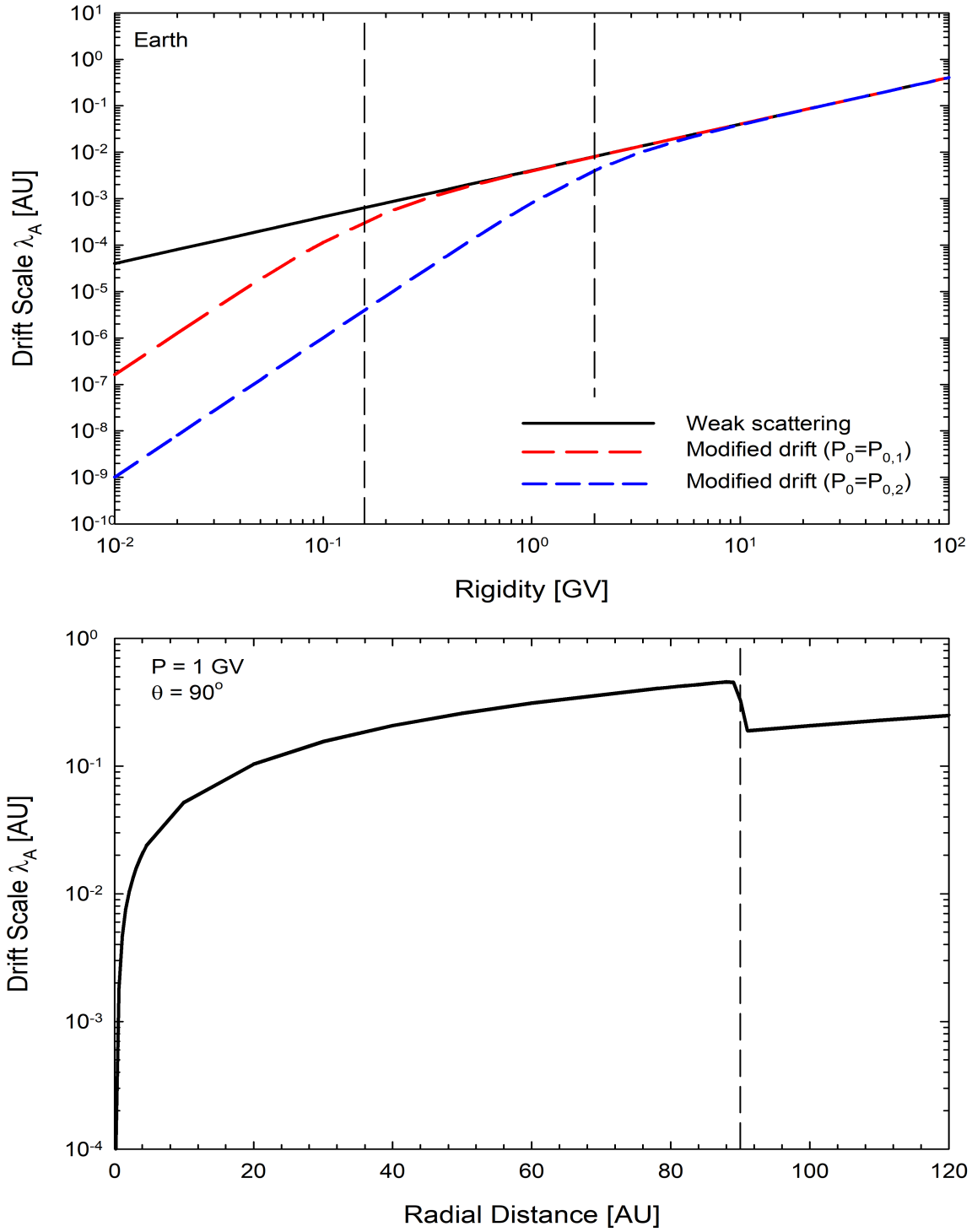


Fig. 2.1 *The top panel shows the drift scale* λ_A *as a function of rigidity at the position of the Earth for the weak scattering case (solid black line) and for the scattering modified approximation assuming* $P_0 = P_{0,1} = 0.16$ *GV (dashed red line) and* $P_0 = P_{0,2} = 2.0$ *GV (dashed blue line), respectively. The vertical lines indicate these values of* P_0 *for each of the two cases respectively. The bottom panel shows the radial dependence of* λ_A *with the position of the assumed TS fixed at* $r_{TS} = 90$ *AU (vertical dashed line).*

2.4.2 Drift Velocities

The components of the gradient and curvature drift velocity, as they occur in Equation (2.24), are given by e.g. Hattingh [1998] as

$$\begin{aligned}
\langle \vec{v}_{\rm d} \rangle_r &= -\frac{q^{'} A_{\rm c}}{r \sin\theta} \frac{\partial}{\partial \theta} \left(\sin\theta \kappa_{\theta r} \right) \\
&= -\frac{q^{'} A_{\rm c}}{r \sin\theta} \frac{\partial}{\partial \theta} \left(\kappa_{\rm A} \sin\theta \sin\psi \right) \\
\langle \vec{v}_{\rm d} \rangle_\theta &= -\frac{q^{'} A_{\rm c}}{r} \left[\frac{1}{\sin\theta} \frac{\partial}{\partial \phi} \left(\kappa_{\phi\theta} \right) + \frac{\partial}{\partial r} \left(r \kappa_{r\theta} \right) \right] \\
&= \frac{q^{'} A_{\rm c}}{r} \frac{\partial}{\partial r} \left(\kappa_{\rm A} r \sin\psi \right) \\
\langle \vec{v}_{\rm d} \rangle_\phi &= -\frac{q^{'} A_{\rm c}}{r} \frac{\partial}{\partial \theta} \left(\kappa_{\theta\phi} \right) \\
&= -\frac{q^{'} A_{\rm c}}{r} \frac{\partial}{\partial \theta} \left(\kappa_{\rm A} \cos\psi \right), \qquad (2.34)
\end{aligned}$$

in terms of the drift coefficient $\kappa_{\rm A}$ after substitution from Equation (2.23). In these expressions, $A_{\rm c}$ is as defined in Equation (1.12) and $q^{'}$ is the sign of the particle charge q. Note that, in the expression for $\langle \vec{v}_{\rm d} \rangle_\theta$, the derivative to $\partial/\partial\phi$ was assumed to be zero.

A derivation for the drift velocity along the HCS was presented by e.g. Raath [2015] (see also Raath et al. [2015]), following the same basic approach as that of Strauss et al. [2012]. Only the most important assumptions and results of this derivation are repeated here.

The drift velocity along the HCS, $\vec{v}_{\rm ns}$, is directed parallel to the HCS and perpendicular to the HMF (Burger et al. [1985], Burger and Potgieter [1989]) and is given by

$$\vec{v}_{\rm ns} = v_{\rm ns} F(P) \{ \cos(\pm\beta) \sin\psi \vec{\rm e}_r + \sin(\pm\beta) \vec{\rm e}_\theta + \cos(\pm\beta) \cos\psi \vec{\rm e}_\phi \} \cdot q A_{\rm c}, \qquad (2.35)$$

where

$$F(P) = \kappa_{\rm A,0} \frac{(P/P_0)^2}{1 + (P/P_0)^2} \qquad (2.36)$$

makes provision for the scaling down by turbulence and $A_{\rm c}$ indicates the magnetic polarity cycle; $\beta(r, \theta, \phi, \alpha) \in (-180°, 180°)$ is the angle between a vector parallel to the HCS

$$\vec{h} = \cos(\pm\beta) \vec{\rm e}_r + \sin(\pm\beta) \vec{\rm e}_\theta + \cos(\pm\beta) \vec{\rm e}_\phi, \qquad (2.37)$$

and the radial direction $\vec{e}_r$, defined by

$$\tan(\pm\beta) = \pm\left[1 - R\frac{\partial V_{\rm sw}}{\partial r}\right] R\frac{\sqrt{\tan^2\alpha - \cot^2\theta'}}{\cot^2\theta' + 1}, \tag{2.38}$$

where θ' is the latitudinal extent of the HCS, given by Equation (1.11); see Burger [2012]. Equation (2.38) is valid in the case of a Parker HMF geometry; the reader is reminded of the fact that the Smith-Bieber modified field still contains a Parker geometry, as explained earlier. In Equation (2.38), R has been defined as

$$R := \frac{\Omega(r - r_\odot)}{V_{\rm sw}}. \tag{2.39}$$

The correct sign of β is determined through

$$\begin{aligned} \frac{\partial\theta'}{\partial r} < 0 \quad &\Rightarrow \quad \beta > 0 \\ \frac{\partial\theta'}{\partial r} > 0 \quad &\Rightarrow \quad \beta < 0. \end{aligned} \tag{2.40}$$

In Equation (2.35), $\nu_{\rm ns}$ is given by the approximation of Burger et al. [1985]

$$\nu_{\rm ns} = \left\{0.457 - 0.412\frac{|L|}{r_{\rm L}} + 0.0915\frac{|L|^2}{r_{\rm L}^2}\right\}\nu. \tag{2.41}$$

Here L is the smallest distance from the CR's current position to the HCS. This expression was derived for a locally flat HCS, i.e. CRs are assumed to interact with only a single fold of the HCS at a given time; this assumption has, however, been challenged by the simulations of Florinski [2011].

Equation (2.35) is applied when

$$|L| \leq 2r_{\rm L}, \tag{2.42}$$

i.e. when the particle is within two gyro-radii or less from the HCS. The method in which L is calculated was explained by Strauss et al. [2012] where it was also indicated that the condition $\nabla \cdot \vec{\nu}_{\rm d} = 0$ is automatically satisfied. For the most recent developments on the subject of drift velocities along the HCS, see e.g. Engelbrecht et al. [2019].

2.4.3 The Global Drift Pattern

Figure 2.2 depicts a meridional cut of the heliosphere. Defining $d\vec{l}$ as a line element in spherical coordinates and solving for $d\vec{l} \times \langle\vec{\nu}_{\rm d}\rangle = \vec{0}$, streamlines of the drift velocity can be obtained. The arrowed lines in Figure 2.2 show these streamlines for positively charged

particles (Helium in this case) during the $A > 0$ magnetic polarity cycle as obtained from Pesses et al. [1981]; protons will exibit the same qualitative drift pattern. Similar diagrams

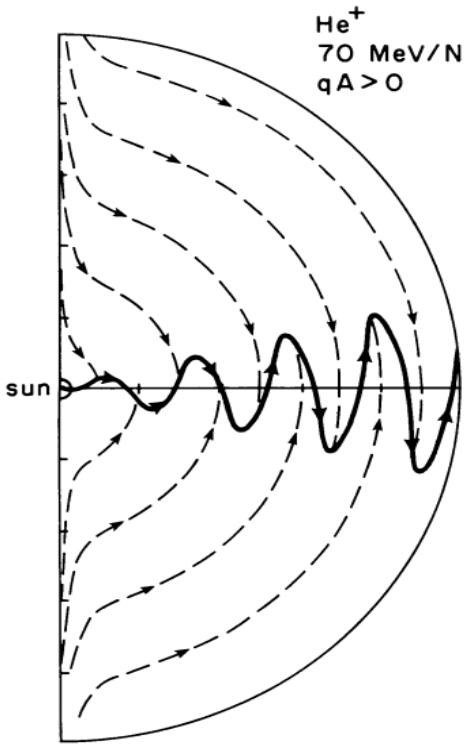


Fig. 2.2 *Average drift velocity streamlines in the meridional plane of the heliosphere for positive particles (Helium in this case) in the $A > 0$ magnetic polarity cycle. The drift directions will reverse for negatively charged particles, as well as for the $A < 0$ polarity cycle. This figure was taken from Pesses et al. [1981]; note that similar diagrams were presented by Jokipii and Thomas [1981].*

were presented earlier by Jokipii and Thomas [1981] and more recently by Dunzlaff et al. [2008] as well as Moloto [2015]. It is clear that, during such a polarity cycle, positive particles drift primarily from the polar regions down towards the equatorial plane, and outwards along the HCS. For negatively charged particles, this behaviour will be reversed. The drift directions during the $A < 0$ polarity cycle are reversed again. This overall drift pattern is referred to as the 'global drift pattern' throughout this work. See also Potgieter [1984], Burger [1987] and Hattingh [1998].

2.5 Particle Diffusion

As a result of fluctuations in the HMF, CRs propagate through the heliosphere by means of a diffusive process known as pitch angle scattering or "random walk". This process can be described by weak turbulence quasi-linear theory (QLT), introduced by Jokipii [1966]. The process may be interpreted as waves (e.g. Schlickeiser [1988]) or as dynamical turbulence (e.g. Bieber and Matthaeus [1991]). Cosmic ray diffusion is included in Equation (2.1)

through the elements of the symmetric diffusion tensor, written in HMF-aligned coordinates in Equation (2.19).

Each element of this tensor, i.e. $\kappa_{||}$, $\kappa_{\perp\theta}$ and $\kappa_{\perp r}$, is called a diffusion coefficient and is related to the corresponding mean free path (MFP) through

$$\kappa = \frac{v}{3}\lambda. \tag{2.43}$$

In this work, λ is given in astronomical units (AU); this produces a variable that is more readily understood on an intuitive level.

A comprehensive study of CR diffusion as well as the underlying turbulence theory is beyond the scope of this study and, in the following sections, only the necessary details are discussed. See e.g. Hattingh [1998], Minnie [2002, 2006], Shalchi [2009] and Engelbrecht [2008, 2012] for in-depth studies.

2.5.1 Parallel Diffusion

The pitch-angle averaged parallel diffusion coefficient $\kappa_{||}$ is related to the pitch-angle Fokker-Planck coefficient $D_{\mu\mu}(\mu)$ through

$$\kappa_{||} = \frac{v^2}{8}\int_{-1}^{1}\frac{(1-\mu^2)^2}{D_{\mu\mu}(\mu)}d\mu, \tag{2.44}$$

which relates the interaction between particles and turbulence (e.g. Schlickeiser [2002], Stawicki [2003], Shalchi and Schlickeiser [2004]).

This coefficient, $D_{\mu\mu}(\mu)$, therefore depends on the turbulence model and theory which is adopted. The calculation of $D_{\mu\mu}(\mu)$ requires a power spectrum of magnetic field fluctuations; an example of such a spectrum is shown in Figure 2.3. The spectrum is clearly divisible into three distinct ranges: (1) the energy range at low wavenumbers where the power spectrum variation is independent of the wavenumber k; (2) the inertial range at intermediate wavenumbers where the variation is proportional to $k^{-5/3}$; (3) the dissipation range at high wavenumbers where the variation is proportional to k^{-3} (e.g. Bieber et al. [1994]). Teufel and Schlickeiser [2003] presented a derivation of piecewise continuous expressions for the parallel MFPs from QLT for a full turbulence spectrum; see also Engelbrecht and Burger [2010, 2013*a*,*b*].

In this study, a much more simplified approach is followed (Vos [2011]), and the parallel diffusion coefficient is given by

$$\kappa_{||} = \kappa_{||,0}\beta_c\frac{B_0}{B}\left[\frac{\left(\frac{P}{P_0'}\right)^c + \left(\frac{P_k}{P_0'}\right)^c}{1+\left(\frac{P_k}{P_0'}\right)^c}\right]^{\frac{b-a}{c}}\left(\frac{P}{P_0'}\right)^a, \tag{2.45}$$

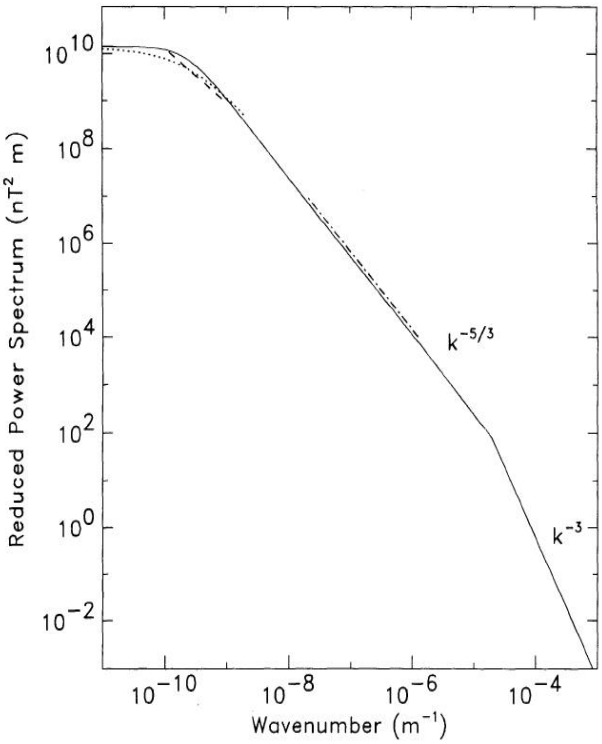


Fig. 2.3 *A typical slab turbulence power spectrum model (solid line) for the heliosphere at Earth compared to observations (dashed and dotted lines). This figure was taken from Bieber et al. [1994].*

where $\kappa_{||,0}$ is a constant in units of 1×10^{22} cm^2/s, with $P_0' = 1$ GV and $B_0 = 1$ nT added on dimensional grounds. Here a and b are dimensionless constants and determine the slope of the rigidity dependence below and above a rigidity P_k respectively. The quantity c is another dimensionless constant and determines the smoothness of the transition between the two slopes P^a and P^b at P_k. The rigidity dependence is therefore essentially a double power-law (see Figure 3.20). In this work, $P_\mathrm{k} = 4.2$ GV is used in later chapters, following Vos [2011]. Note that the spatial dependence of $\kappa_{||}$ is therefore assumed to be inversely proportional to the magnitude of the magnetic field B. See Langner [2004], Vos [2011], Raath [2015] and Vos [2016] for similar approaches; see also Ferreira et al. [2001*b*]. More complicated rigidity dependences are discussed by e.g. Engelbrecht [2008].

2.5.2 Perpendicular Diffusion

The gyrocentres of particles can be displaced transverse to the mean HMF through scattering or due to the random walk of magnetic field lines, leading to diffusion perpendicular to the HMF field lines. These processes are accounted for in numerical modulation models in a collective fashion, through the perpendicular diffusion coefficient $\kappa_\perp$. This coefficient is subdivided into two possibly independent coefficients $\kappa_{\perp r}$ and $\kappa_{\perp\theta}$, which describe the perpendicular diffusion in the radial and polar directions respectively. The importance of

perpendicular diffusion in modulation studies has been discussed by e.g. Potgieter [1996, 2000], Potgieter and Ferreira [1999] and Ferreira et al. [2000]. See e.g. Jokipii [2001] for theoretical work related to perpendicular diffusion.

The pure field line random walk scenario, however, gives an insufficient description of perpendicular diffusion. A process by which particles sometimes retrace their paths after backscattering had not been taken into account until the nonlinear guiding centre (NLGC) theory of Matthaeus et al. [2003]. According to NLGC theory, the process of perpendicular diffusion is a combination of field line random walk, backscattering from parallel diffusion, and the transfer of particles across field lines due to the perpendicular complexity of the magnetic field. For a general discussion of NLGC theory and comparison with observations, see Bieber et al. [2004].

The NLGC theory of Matthaeus et al. [2003] provides an integral equation for the perpendicular MFP. Shalchi et al. [2004] presented analytical solutions of this equation in the case of magnetostatic turbulence; from this work, expressions for the perpendicular MFP were adapted by Engelbrecht and Burger [2010] and incorporated into a numerical modulation model. Zank et al. [2004] obtained an approximate solution to the integral equation which was indicated to be in excellent agreement with the exact solution and also readily amenable into numerical modulation models. However, demonstrating important shortcomings of the NLGC theory, Shalchi [2006] presented an extended theory which included the relevant improvements. Engelbrecht and Burger [2013*a*] derived expressions for the perpendicular MFP based on the extended NLGC theory, forming part of an *ab initio* model for CR modulation; see also Engelbrecht and Burger [2013*b*].

In this work, a simple approach by which $\kappa_\perp$ is scaled as $\kappa_{||}$ is followed. The ratio of $\kappa_\perp/\kappa_{||}$ was found to be between 0.02 and 0.04 by Giacalone and Jokipii [1999]. Kóta and Jokipii [1995] proposed the concept of anisotropic perpendicular diffusion with $\kappa_{\perp\theta} > \kappa_{\perp r}$ in the off-equatorial regions (e.g. Potgieter [1996], Burger et al. [2000]) after Ulysses observations revealed that the latitude dependence of CR protons was significantly less than predicted by classical drift models (Potgieter and Haasbroek [1993]). To account for such anisotropic perpendicular diffusion, this work follows e.g. Langner [2000], Vos [2011] and Raath [2015] so that

$$\kappa_{\perp r} = \kappa^0_{\perp r}\kappa_{||} \tag{2.46}$$

and

$$\kappa_{\perp\theta} = f(\theta)\kappa^0_{\perp\theta}\kappa_{||}, \tag{2.47}$$

where $\kappa^0_{\perp r} = \kappa^0_{\perp\theta} = 0.02$ are dimensionless constants, and

$$f(\theta) = A^+ + A^- \tanh\left[\frac{1}{\Delta\theta}\left(\widetilde{\theta} - \frac{\pi}{2} + \theta_{\mathrm{F}}\right)\right]. \tag{2.48}$$

Here $A^{\pm} = \dfrac{d \pm 1}{2}$, $\Delta\theta = 1/8$, with

$$\widetilde{\theta} = \begin{cases} \theta & \text{for} \quad \theta \geq \dfrac{\pi}{2} \\ \\ \pi - \theta & \text{for} \quad \theta < \dfrac{\pi}{2}, \end{cases} \tag{2.49}$$

and

$$\theta_{\mathrm{F}} = \begin{cases} \dfrac{-35^{\circ}\pi}{180^{\circ}} & \text{for} \quad \theta \geq \dfrac{\pi}{2} \\ \\ \dfrac{35^{\circ}\pi}{180^{\circ}} & \text{for} \quad \theta < \dfrac{\pi}{2}, \end{cases} \tag{2.50}$$

where $d = 3.0$ (Vos [2011], Raath [2015]) is a dimensionless constant that determines the enhancement factor of $\kappa_{\perp\theta}$ from its value in the equatorial plane towards the poles, with respect to $\kappa_{||}$. Other than these expressions, the concept of anisotropic perpendicular diffusion is not pursued in any more detail in this work. See e.g. Ferreira et al. [2000] and Strauss et al. [2016] for studies related to anisotropic perpendicular diffusion.

It must be mentioned that to select the same rigidity dependence for the perpendicular and parallel diffusion coefficients is a simplification, since both turbulence theory and observations predict a different rigidity dependence; see e.g. Burger et al. [2000] where it was indicated that $\kappa_{\perp\theta}$ should have a flatter rigidity dependence than $\kappa_{||}$.

See also Zhao et al. [2018], where the solar cycle dependence of CR diffusion has been discussed in much detail. In this thesis, however, the solar cycle dependence of the diffusion coefficient is initially included only through its $1/B$ dependence in Equation (2.45), while further solar activity related changes are made manually in Chapters 3 and 4 where the value of $\kappa_{||,0}$ is adjusted so as to reproduce proton data from PAMELA.

2.6 The Numerical Model

The numerical model featured in this work is formulated from a set of SDEs, derived for the TPE. The model is time-stationary and spatially three-dimensional, including energy as a fourth dimension. It is based on the model introduced by Strauss et al. [2011*a*] and, in Chapters 3 to 5, is applied to the modulation of GCRs. This model has been benchmarked and implemented extensively, e.g. Strauss et al. [2011*a*,*b*, 2012], Strauss [2013], Raath [2015], Raath et al. [2015, 2016] and Raath and Potgieter [2017].

This section presents a brief introduction to SDEs in Section 2.6.1; the introduction was reprinted from the work of Strauss [2013] and Raath [2015]. Section 2.6.2 provides an overview of SDE-based numerical modulation models and their application in CR modulation studies; the overview was constructed from the work of Strauss and Effenberger [2017]. Sections 2.6.3 and 2.6.4 respectively present the SDE formulation of the TPE and

the relevant boundary conditions; these two sections were also reprinted from Strauss [2013] and Raath [2015].

2.6.1 Stochastic Differential Equations

Stochastic calculus is a well developed field and, in this work, only the most essential principles are discussed. For any further reading on this topic, the reader is referred to several standard texts on SDEs (e.g. Gardiner [1983, 2009]; Kloeden et al. [1994]; Kloeden and Platen [1999]; Øksendal [2003]).

For the purposes of this work, it is sufficient to define a SDE as any equation that can be cast into the general form

$$\frac{\partial x(t)}{\partial t} = \mu(x,t) + \sigma(x,t)\zeta(t), \tag{2.51}$$

for the one-dimensional case where $\mu(x,t)$ and $\sigma(x,t)$ are continuous functions, while $\zeta(t)$ represents a rapidly varying stochastic function, also referred to as the noise term. The first and second terms on the right hand side of Equation (2.51) are referred to as the *drift* and *diffusion* terms respectively. These terms are not to be confused with the physical drift and diffusive terms present in the TPE. Moreover, only SDEs of the Itō type are considered, where Equation (2.51) can be rewritten as

$$dx(t) = \mu(x,t)dt + \sigma(x,t)dW(t), \tag{2.52}$$

where $dW(t)$ represents the Wiener process. This is a time stationary stochastic Levy process where the time increments have a Normal distribution with a mean of zero (i.e. a Gaussian distribution) and a variance of dt; $dW(t) = W(t) - W(t-dt) \sim \mathcal{N}(0, dt)$.

Equation (2.52) can be integrated as

$$x(t) = x_0 + \int_0^t \mu(x,t')dt' + \int_0^t \sigma(x,t')dW(t'), \tag{2.53}$$

where the first integral is a normal (Riemann or Lebesgue) integral, while the second is an Itō type stochastic integral. Since analytical solutions for SDEs are only available for a limited few scenarios, Equation (2.53) is usually integrated numerically. In this work, the SDEs are integrated by using the Euler-Maruyama numerical scheme (Maruyama [1955]), where a finite time step Δt is chosen and Equation (2.52) is solved iteratively

$$x^{t+\Delta t} = x^t + \mu(x,t)\Delta t + \sigma(x,t)\Delta W(\Delta t), \tag{2.54}$$

from an initial position $x = x_0$ at time $t = 0$ and continued until the boundary is reached at $x = x_\mathrm{e}$ at $t = t_\mathrm{e}$, or until a temporal integration limit is reached at $t = t^\mathrm{N}$; in this work, $\Delta t = 0.001$ PUs, i.e. program units, corresponding to a few days of modulation time. The

Wiener process is discretised as

$$\Delta W(\Delta t) = \sqrt{\Delta t} \cdot \Lambda(t), \tag{2.55}$$

where $\Lambda(t)$ is a simulated Gaussian distributed pseudo-random number. The temporal evolution of x forms a trajectory through phase space, which is generally referred to as the trajectory of a pseudo-particle. Integrating Equation (2.54) for a single pseudo-particle has no significance, as integration must be carried out over all possible trajectories, so that Equation (2.54) is usually integrated $N \gg 1$ times; this is also referred to as tracing N pseudo-particles.

A normalised (conditional) probability density $\rho^{'}(x,t)$ can be calculated from the pseudo-particle trajectories, such that

$$\int_{\Omega} \rho^{'}(x,t) d\Omega = 1, \tag{2.56}$$

where Ω denotes the entire integration space. Numerically this is done by dividing e.g. x into a series of bins, e.g. $N^{'}$ intervals, and calculating the number of pseudo-particles ending up in each bin, i.e. bin i has N_i particles, and dividing by N. The discretised version of Equation (2.56) thus reads

$$\sum_{i=1}^{N^{'}} \rho_i^{'}(x,t) = \sum_{i=1}^{N^{'}} \frac{N_i}{N} = 1. \tag{2.57}$$

Note that at $t = 0$, $\rho^{'}(x,t) = \delta(x - 0, t - 0)$, where δ presents a Dirac-delta function, while at later times, the distribution becomes Gaussian.

2.6.2 Models Based on Stochastic Differential Equations

Yamada et al. [1998] presented the first SDE-based model for GCR modulation, in a one-dimensional case; this model was applied to GCR proton modulation and the validity of the SDE-approach was illustrated by successfully benchmarking this approach to a traditional finite difference scheme. After Zhang [1999] successfully applied SDEs to study CR modulation in the heliosphere, the use of such models has become increasingly popular; this author implemented a three-dimensonal case including particle drifts for a flat (i.e. a tilt angle of 0°) HCS. Later models applied essentially the same SDE formulation, applied to GCR protons, electrons and Jovian electrons, most including extensive benchmarking studies (e.g. Gervasi et al. [1999], Bobik et al. [2008], Pei et al. [2010], Strauss et al. [2011*a*,*b*, 2012]).

The first SDE-based model to implement a wavy HCS in three dimensions was presented by Miyake and Yanagita [2005]. A detailed methodology in two dimensions was given by Alanko-Huotari et al. [2007] and in three dimensions by Pei et al. [2012] and Strauss et al. [2012]. The inclusion of a wavy HCS enabled effective illustration of the drift process

by means of exit positions and trajectories for pseudo-particles. For details on this, see Strauss et al. [2012]; see also the modelling done by Raath et al. [2015, 2016]. In Chapters 4 and 5 of this work, drift properties are again under consideration. The effectiveness of SDE-based models in modelling and reproducing drift effects have led to these models being increasingly applied to model charge-sign dependent modulation effects (see Chapter 5), e.g. Della Torre et al. [2012], Bobik et al. [2012] and Maccione [2013].

The SDE formulation also makes it possible to calculate propagation times and energy losses suffered by GCRs; see Chapter 4 for more on energy losses. Strauss et al. [2011*b*] showed that these quantities, calculated numerically via the SDE-based model, compared well with earlier analytical models. See e.g. Florinski and Pogorelov [2009] and Bobik et al. [2011] for studies related to these two quantities. Note that it is not yet conclusively established how these quantities are related to CR intensities or observations, since it must always be kept in mind that pseudo-particles are not identical to actual (physical) particles; see e.g. Strauss et al. [2013], Vogt et al. [2015].

Hybrid CR modulation models have also been created. Such models use relevant input from MHD models, such as information regarding the heliosphere geometry and solar wind flow. It then couples the TPE and MHD input to solve the TPE using an essentially test- or pseudo-particle approach. The first of these models was presented by Ball et al. [2005], whereafter the approach was followed by Florinski and Pogorelov [2009], Strauss et al. [2013], Luo et al. [2013], Guo and Florinski [2014*a*,*b*] and Kopp et al. [2017].

The numerical approach to integrating SDEs is time dependent, per definition. However, most of the above-mentioned work considered only the steady-state solution in which pseudo-particles were integrated until they reached a boundary. Some work that has focused on time-dependent solutions, meaning that a time dependence was incorporated into the transport coefficients and that no stationary solution existed, is however available, e.g. Yamada et al. [1999], Luo et al. [2011], Guo and Florinski [2014*b*], Wawrzynczak et al. [2015*a*,*b*] and Wawrzynczak and Modzelewska [2016]. For a recent study that makes use of a simulated time dependence, using the stochastic approach outlined by Engelbrecht and Burger [2015*b*], see Moloto et al. [2018]. See also Qin and Shen [2017].

SDE-based models have also been applied in modulation studies pertaining to solar energetic particles (SEPs), e.g. Dröge et al. [2010, 2014, 2016, 2018], Dresing et al. [2012], and Laitinen et al. [2013, 2016, 2018]. Some models of pick-up ion transport in the heliosphere, like Chalov et al. [1995] and Fichtner et al. [1996], also employ SDE methods which are related to SEP transport models. Since neither SEPs nor pick-up ions form an important part of this study, these models are not discussed.

There are numerous advantages to adopt an SDE-based numerical scheme above the more traditional finite difference methods. These are summarised in Strauss and Effenberger [2017]: (1) the SDE numerical scheme is unconditionally stable, although it does not imply numerical accuracy; (2) because of the numerical stability, the model can handle large gradients, but care has to be taken in the choice of the time-step; (3)

the SDE-approach does not calculate solutions on a specific grid, but at a number of discrete phase-space positions so that there is no need to store unnecessary information, saving computational memory and making computations in higher dimensions possible; (4) each solution is completely independent, making it possible to perform calculations on parallel computational environments (see e.g. Moloto et al. [2019]) and even graphics processing units (e.g. Dunzlaff et al. [2015]), significantly speeding up calculations; (5) the SDE-approach allows one to visualise more of the physical processes included in the transport equation under investigation.

2.6.3 SDE Formulation for the TPE

The TPE is solved by means of SDEs in a so-called *time backward* fashion. The time backward and time forward approaches are equivalent (e.g. Bobik et al. [2016]), but for CR modulation, the former approach is numerically easier to handle and also computationally much faster. An *observational point* is chosen $(\vec{x}^0, s^0)$, i.e. the phase space position where the CR intensity will be calculated, and the trajectory of a pseudo-particle is then integrated time backwards until a modulation boundary is reached at $(\vec{x}^{\mathrm{e}}, s^{\mathrm{N}})$. Here, s is the time backward parameter, related to t by

$$s = t^{\mathrm{N}} - t, \tag{2.58}$$

i.e. in the normal time forward scenario, integration is performed in the time domain $t = 0 \longrightarrow t = t^{\mathrm{N}}$, while in the time backward case, this becomes $s = 0(t = t^{\mathrm{N}}) \longrightarrow s = s^{\mathrm{N}}(t = 0)$. In both cases, however, the temporal integration domain remains constant, i.e. $t^{\mathrm{N}} = s^{\mathrm{N}}$. Furthermore, $\vec{x}$ represents any set of phase space coordinates. From Equation (2.58) it follows that

$$\frac{\partial}{\partial t} = -\frac{\partial}{\partial s}. \tag{2.59}$$

For an n dimensional set of SDEs, the general formulation becomes

$$dx_i = \mu_i(x_i, s)ds + \sum_{j=1}^{n} \sigma_{ij}(x_i, s) \cdot dW_i(s), \tag{2.60}$$

where $\vec{\mu}$ is an n-dimensional vector and $\boldsymbol{\sigma}$ is an $n \times n$ matrix. When time backward integration is performed, Equation (2.60) is equivalent to the following Fokker-Planck equation (also referred to as the time backward Kolmogorov equation)

$$-\frac{\partial \rho'(x_i, s)}{\partial s} = \sum_{i=1}^{n} \mu_i(x_i, s)\frac{\partial \rho'(x_i, s)}{\partial x_i} + \frac{1}{2}\sum_{i=1}^{n}\sum_{j=1}^{n} C_{ij}(x_i, s)\frac{\partial^2 \rho'(x_i, s)}{\partial x_i \partial x_j}. \tag{2.61}$$

For a detailed discussion on how the time forward and backward SDE formulations are related to different Fokker-Planck equations, see Kopp et al. [2012] and Bobik et al. [2016].

In Equation (2.61),

$$C_{ij}(x_i, s) \equiv \left(\sigma_{ij}(x_i, s) \cdot \sigma_{ij}(x_i, s)^T\right). \tag{2.62}$$

The TPE can therefore be cast into the form of Equation (2.61), the quantities $\vec{\mu}$ and $\boldsymbol{\sigma}$ obtained, and the equivalent SDE formulation for CR transport emerges naturally. The n-dimensional TPE is therefore transformed into a set of $n-1$, two-dimensional SDEs, with the latter being much easier to handle numerically.

Equivalent to Equation (2.24), the TPE in spherical coordinates can be written as

$$\begin{aligned}
\frac{\partial f}{\partial t} &= \left[\frac{1}{r^2}\frac{\partial}{\partial r}\left(r^2\kappa_{rr}\right) + \frac{1}{r\sin\theta}\frac{\partial}{\partial\theta}\left(\kappa_{\theta r}\sin\theta\right) + \frac{1}{r\sin\theta}\frac{\partial\kappa_{\phi r}}{\partial\phi} - V_r\right]\frac{\partial f}{\partial r} \\
&+ \left[\frac{1}{r^2}\frac{\partial}{\partial r}\left(r\kappa_{r\theta}\right) + \frac{1}{r^2\sin\theta}\frac{\partial}{\partial\theta}\left(\kappa_{\theta\theta}\sin\theta\right) + \frac{1}{r^2\sin\theta}\frac{\partial\kappa_{\phi\theta}}{\partial\phi} - \frac{1}{r}V_\theta\right]\frac{\partial f}{\partial\theta} \\
&+ \left[\frac{1}{r^2\sin\theta}\frac{\partial}{\partial r}\left(r\kappa_{r\phi}\right) + \frac{1}{r^2\sin\theta}\frac{\partial\kappa_{\theta\phi}}{\partial\theta} + \frac{1}{r^2\sin^2\theta}\frac{\partial\kappa_{\phi\phi}}{\partial\phi} - \frac{1}{r\sin\theta}V_\phi\right]\frac{\partial f}{\partial\phi} \\
&+ \kappa_{rr}\frac{\partial^2 f}{\partial r^2} + \frac{\kappa_{\theta\theta}}{r^2}\frac{\partial^2 f}{\partial\theta^2} + \frac{\kappa_{\phi\phi}}{r^2\sin^2\theta}\frac{\partial^2 f}{\partial\phi^2} + \frac{2\kappa_{r\phi}}{r\sin\theta}\frac{\partial^2 f}{\partial r\partial\phi} + \frac{2\kappa_{r\theta}}{r}\frac{\partial^2 f}{\partial r\partial\theta} \\
&+ \frac{2\kappa_{\theta\phi}}{r^2\sin\theta}\frac{\partial^2 j}{\partial\phi\partial\theta} + \frac{p}{3}\left(\nabla\cdot\vec{V}_{\rm sw}\right)\frac{\partial f}{\partial p},
\end{aligned} \tag{2.63}$$

where $\vec{V} = \vec{V}_{\rm sw} + \vec{v}_{\rm d}$ was introduced. Assuming that $f(\vec{x}, t) \propto \rho'(\vec{x}, t)$ and using Equation (2.59), it follows that

$$\begin{aligned}
\mu_r &= \frac{1}{r^2}\frac{\partial}{\partial r}\left(r^2\kappa_{rr}\right) + \frac{1}{r\sin\theta}\frac{\partial}{\partial\theta}\left(\kappa_{\theta r}\sin\theta\right) + \frac{1}{r\sin\theta}\frac{\partial\kappa_{\phi r}}{\partial\phi} - V_r \\
\mu_\theta &= \frac{1}{r^2}\frac{\partial}{\partial r}\left(r\kappa_{r\theta}\right) + \frac{1}{r^2\sin\theta}\frac{\partial}{\partial\theta}\left(\kappa_{\theta\theta}\sin\theta\right) + \frac{1}{r^2\sin\theta}\frac{\partial\kappa_{\phi\theta}}{\partial\phi} - \frac{1}{r}V_\theta \\
\mu_\phi &= \frac{1}{r^2\sin\theta}\frac{\partial}{\partial r}\left(r\kappa_{r\phi}\right) + \frac{1}{r^2\sin\theta}\frac{\partial\kappa_{\theta\phi}}{\partial\theta} + \frac{1}{r^2\sin^2\theta}\frac{\partial\kappa_{\phi\phi}}{\partial\phi} - \frac{1}{r\sin\theta}V_\phi \\
\mu_p &= \frac{p}{3}\left(\nabla\cdot\vec{V}_{\rm sw}\right),
\end{aligned} \tag{2.64}$$

and

$$\mathbf{C} = \begin{bmatrix}
\kappa_{rr} & \frac{\kappa_{r\theta}}{r} & \frac{\kappa_{r\phi}}{r\sin\theta} \\
\frac{\kappa_{r\theta}}{r} & \frac{\kappa_{\theta\theta}}{r^2} & \frac{\kappa_{\theta\phi}}{r^2\sin\theta} \\
\frac{\kappa_{r\phi}}{r\sin\theta} & \frac{\kappa_{\theta\phi}}{r^2\sin\theta} & \frac{\kappa_{\phi\phi}}{r^2\sin\theta}
\end{bmatrix}, \tag{2.65}$$

and the multi-dimensional Wiener process

$$d\vec{W} = [dW_r, dW_\theta, dW_\phi]\,. \tag{2.66}$$

Because only spatial diffusion is taken into account, $\boldsymbol{\sigma}$ can be reduced from a 4×4 matrix to a 3×3 matrix (see also the discussion by Kopp et al. [2012]). To calculate $\boldsymbol{\sigma}$, the square root of $\mathbf{C}$ must be calculated. As discussed by e.g. Johnson et al. [2002], the magnitude and form of $\boldsymbol{\sigma}$ may not be unique, but all of these $\boldsymbol{\sigma}$'s will be mathematically equivalent. Here, $\sigma_{\theta r} = \sigma_{\phi r} = \sigma_{\phi\theta} = 0$, while the other elements of $\boldsymbol{\sigma}$ are given by

$$\begin{aligned}
\sigma_{rr} &= \sqrt{\frac{\kappa_{\phi\phi}\kappa_{r\theta}^2 - 2\kappa_{r\phi}\kappa_{r\theta}\kappa_{\theta\phi} + \kappa_{rr}\kappa_{\theta\phi}^2 + \kappa_{\theta\theta}\kappa_{r\phi}^2 - \kappa_{rr}\kappa_{\theta\theta}\kappa_{\phi\phi}}{\kappa_{\theta\phi}^2 - \kappa_{\theta\theta}\kappa_{\phi\phi}}} \\
\sigma_{r\theta} &= \frac{\kappa_{r\phi}\kappa_{\theta\phi} - \kappa_{r\theta}\kappa_{\phi\phi}}{\kappa_{\theta\phi}^2 - \kappa_{\theta\theta}\kappa_{\phi\phi}} \sqrt{\kappa_{\theta\theta} - \frac{\kappa_{\theta\phi}^2}{\kappa_{\phi\phi}}} \\
\sigma_{r\phi} &= \frac{\kappa_{r\phi}}{\sqrt{\kappa_{\phi\phi}}} \\
\sigma_{\theta\theta} &= \frac{1}{r}\sqrt{\kappa_{\theta\theta} - \frac{\kappa_{\theta\phi}^2}{\kappa_{\phi\phi}}} \\
\sigma_{\theta\phi} &= \frac{\kappa_{\theta\phi}}{r\sqrt{\kappa_{\phi\phi}}} \\
\sigma_{\phi\phi} &= \frac{\sqrt{\kappa_{\phi\phi}}}{r\sin\theta}.
\end{aligned} \tag{2.67}$$

The set of SDEs governing CR transport therefore becomes

$$\begin{aligned}
dr &= \mu_r \cdot ds + \sigma_{rr} \cdot dW_r + \sigma_{r\theta} \cdot dW_\theta + \sigma_{r\phi} \cdot dW_\phi \\
d\theta &= \mu_\theta \cdot ds + \sigma_{\theta\theta} \cdot dW_\theta + \sigma_{\theta\phi} \cdot dW_\phi \\
d\phi &= \mu_\phi \cdot ds + \sigma_{\phi\phi} \cdot dW_\phi \\
dp &= \mu_p \cdot ds,
\end{aligned} \tag{2.68}$$

which can be integrated relatively easily by means of the Euler-Maruyama scheme mentioned earlier. Note that the momentum SDE can also be rewritten in terms of kinetic energy as

$$dE = \frac{1}{3}\left(\nabla \cdot \vec{V}_{\rm sw}\right)\Gamma E \cdot ds, \tag{2.69}$$

with

$$\Gamma \equiv \frac{E + 2E_0}{E + E_0}, \tag{2.70}$$

where E_0 is the rest mass energy.

2.6.4 Boundary Conditions

The Outer Modulation Boundary

A Dirichlet boundary condition is specified at the HP for GCRs as the LIS. In general it can be handled by using the Green's function interpretation of the conditional probability density $\rho^{'}(\vec{x},t)$ (e.g. Webb and Gleeson [1977]),

$$f(\vec{x}^0,t^0) = \int_0^{t^0} \int_{\vec{x}\in\Omega_\mathrm{b}} f_\mathrm{b}(\vec{x},t)\rho^{'}(\vec{x},t)d\Omega dt + \int_\Omega f_\mathrm{a}(\vec{x},0)\rho^{'}(\vec{x},0)d\Omega, \tag{2.71}$$

where $f_\mathrm{b}(\vec{x},t)$ represents the boundary condition (i.e. the LIS); $f(\vec{x}^0,t^0)$ is the phase space position where the intensity is calculated, i.e. the observational point. In the last term on the right hand side, $f_\mathrm{a}(\vec{x},0)$ represents the initial condition, which for CR modulation is usually set to zero; this corresponds to a heliosphere initially empty of CRs. The boundary of the integration domain is represented by Ω_b and $\vec{x} = \{r,\theta,\phi,p\}$. For the purposes of this work, only steady state solutions of the TPE are considered, where $t \longrightarrow \infty$ (no temporal restriction on the time), reducing Equation (2.71) to

$$f(\vec{x}^0) = \int_{\vec{x}\in\Omega_\mathrm{b}} f_\mathrm{b}(\vec{x})\rho^{'}(\vec{x})d\Omega. \tag{2.72}$$

For CRs, the boundary values are only momentum dependent so that only integration over momentum space is performed, i.e. $d\Omega \longrightarrow dp$,

$$f(\vec{x}^0) = \int_0^p f_\mathrm{b}(p^{'})\rho(\vec{x})dp^{'}\Big|_{\vec{x}\in\Omega_\mathrm{b}}, \tag{2.73}$$

which is essentially a convolution of the boundary condition and the probability distributions.

An approach that is numerically easy is used to incorporate this boundary condition. The weighted value of $f(\vec{x}^0)$ is calculated for each pseudo-particle individually, whereupon it is normalised to the correct magnitude at the end of the integration process. For a single pseudo-particle, reaching a momentum dependent boundary with $p_i = p_i^\mathrm{e}$ (where i labels the pseudo-particles),

$$\rho_i^{'}(\vec{x}) = \delta(p_i - p_i^\mathrm{e})|_{\vec{x}\in\Omega_\mathrm{b}}, \tag{2.74}$$

because of the normalisation condition. This implies that

$$f_i(\vec{x}^0) = f_\mathrm{b}(p_i^\mathrm{e}), \tag{2.75}$$

so that each pseudo-particle traced to the boundary makes some weighted contribution to the total solution. Repeating for $N \gg 1$ pseudo-particles, the numerical solution of the

TPE can be calculated as

$$f(\vec{x}^0) = \frac{1}{N}\sum_{i=1}^{N} f_{\rm b}(p_i^{\rm e}), \tag{2.76}$$

which follows from Equations (2.57) and (2.73).

The Inner Modulation Boundary

The inner modulation boundary is a Neumann boundary condition. Generally, all models assume a boundary condition at small values of r. This is mainly done because some of the heliospheric parameters, e.g. the HMF, is undefined at $r = 0$. Here, a reflecting inner boundary condition is assumed at $r_{\rm in} = 0.1$ AU,

$$\left.\frac{\partial f(\vec{x})}{\partial r}\right|_{r=r_{\rm in}} = 0. \tag{2.77}$$

For SDEs, this means that a pseudo-particle penetrating this boundary is again placed into the computational domain by reflection at the boundary

$$r < r_{\rm in} : r \longrightarrow 2r_{\rm in} - r. \tag{2.78}$$

Other Boundary Related Conditions

Although the SDE-approach does not have to prescribe boundary conditions at the computational domains of the angular coordinates, the angular position of the pseudo-particles needs to be renormalised so that $\theta \in [0, \pi]$ and $\phi \in [0, 2\pi]$. This is done by specifying the following conditions:

$$\begin{aligned}
\phi < 0 \quad &: \quad \phi \longrightarrow \phi + 2\pi \\
\phi > 2\pi \quad &: \quad \phi \longrightarrow \phi - 2\pi \\
\theta < 0 \quad &: \quad \theta \longrightarrow |\theta|; \phi \longrightarrow \phi \pm \pi \\
\theta > \pi \quad &: \quad \theta \longrightarrow 2\pi - \theta; \phi \longrightarrow \phi \pm \pi,
\end{aligned} \tag{2.79}$$

which occur when the pseudo-particle either propagates around the ecliptic plane or crosses the solar poles.

2.7 Summary

Chapter 2 was concerned primarily with the theoretical background that would be essential for the research presented in Chapters 3 to 5. As such, much of the content of this chapter was borrowed from existing literature, in particular Strauss [2013], Raath [2015] and Strauss and Effenberger [2017].

The Parker transport equation (TPE) was introduced in Section 2.2, given by Equation (2.1). This equation was indicated to account for all of the relevant transport phenomena, i.e. physical modulation processes, in the heliosphere. All the relations needed for the implementation of the TPE were explained, including relations between particle energy and rigidity, and between the omni-directional distribution function and particle density.

In Section 2.3, the TPE was solved in spherical coordinates to yield Equation (2.24), in which each term is associated with a physical modulation process. In this section, the diffusion tensor $\mathbf{K}$ was defined in field-aligned coordinates with elements giving the diffusion coefficients parallel and perpendicular to the heliospheric magnetic field (HMF) as well as the drift coefficient. The tensor $\mathbf{K}$ was then cast into spherical coordinates in Equation (2.23) to establish the relations between the coefficients in the field-aligned and spherical coordinate systems respectively.

As one of the major physical modulation processes in the heliosphere - and one that is of particular interest in this study - particle drifts were discussed in Section 2.4. The drift coefficient was defined in Equation (2.32) where much emphasis was placed on the suppression of drift effects due to turbulence. The relation between the drift coefficient and the drift scale was given in Equation (2.33) and the top and bottom panels of Figure 2.1 presented the rigidity and radial profiles of the drift scale respectively. Gradient and curvature drift velocities were defined in Equation (2.34) in terms of the drift coefficient, while drift velocities along the neutral heliospheric current sheet (HCS) were defined by Equations (2.35) to (2.42). Finally, the global drift pattern was explained with the help of Figure 2.2.

Particle diffusion was discussed in Section 2.5 and it was indicated that the diffusion coefficient depends on the turbulence model and theory which is adopted, requiring a power spectrum of magnetic field fluctuations as input; an example of such a spectrum was shown in Figure 2.3. The mean free path (MFP) was related to the diffusion tensor through Equation (2.43). The expression for the parallel diffusion coefficient was given by Equation (2.45), while the perpendicular diffusion coefficients were defined through Equations (2.46) to (2.50).

Section 2.6 considered the numerical modulation model featured in this work and is divided into four parts. Section 2.6.1 served as a brief introduction to the essential principles of stochastic differential equations (SDEs), while a discussion of SDE-based CR modulation models was presented in Section 2.6.2. The numerical scheme on which the model is based was illustrated in Section 2.6.3, where the SDE formulation of the TPE was presented. Finally, in Section 2.6.4, the relevant boundary conditions of the model were considered.

Chapter 3

Galactic Proton Modulation in the Inner Heliosphere

3.1 Introduction

In this chapter, the numerical modulation model described in Chapter 2 is applied to study the solar modulation of galactic cosmic ray (GCR) protons over the time period spanning January 2010 (01/2010) to January 2014 (01/2014). Data from the PAMELA experiment measured over this period of time is used for comparison. This data has been presented and discussed by Martucci et al. [2018] and, in that publication, the modulation model featured in this thesis was applied to model the 01/2010 and 01/2014 proton energy spectra, each averaged over one Carrington Rotation. In this chapter, the relevant results of that study are presented and further insights are provided into the total modulation difference between 01/2010 and 01/2014. The larger part of this chapter, however, is devoted to the study of the heliospheric modulation conditions in between these two periods and, to this end, a number of eight half-yearly averaged energy spectra are calculated from the data. Suitable averages for the relevant modulation parameters, i.e. the tilt angle α and magnetic field magnitude at Earth B_{E}, are calculated and the spectra are then reproduced by determining compatible values for the transport coefficients. Chapter 3, in this way, offers insight into the modulation processes that were prevalent in the heliosphere from 01/2010 (solar minimum) to 01/2014 (solar maximum), in steps of six months.

3.2 The Proton Local Interstellar Spectrum

The local interstellar spectrum (LIS) for protons is the spectrum in the local interstellar medium (LISM), before it is affected by solar modulation in the heliosphere. This modulation starts at the outer modulation boundary, where the different modulation processes alter the LIS to yield a modulated spectrum at a given position in the heliosphere. In this work, the outer modulation boundary is assumed to be located at the position of

the heliopause (HP); see e.g. Guo and Florinski [2014*b*], Kóta and Jokipii [2014], Zhang et al. [2015]. For work done on the modulation of GCRs in the outer heliosheath, i.e. beyond the HP, see e.g. Scherer et al. [2011], Herbst et al. [2012], Florinski et al. [2013], Strauss et al. [2013] and Luo et al. [2015]. In this work, the LIS serves as the primary input spectrum or boundary condition in the numerical modulation model. As such, a proper knowledge of the exact shape of the LIS is very important in modulation studies; e.g. Moskalenko and Strong [1998], Moskalenko et al. [2002], Bisschoff and Potgieter [2016], Boschini et al. [2017] and Bisschoff et al. [2019]. See also Potgieter [2014].

To determine such a LIS is a difficult task, with limited *in situ* measurements available at lower energies. Before the HP crossing of the Voyager spacecraft, and at energies relevant to modulation studies, neither the absolute flux nor the spectral shape could be determined to adequate precision (e.g. Menn et al. [2000]). Because the solar modulation of protons is negligible above about 30 GeV (Strauss and Potgieter [2014*b*]), it was possible to confine the LIS above these energies, making use of CR proton measurements from e.g. PAMELA (Picozza et al. [2007]). Below 30 GeV, however, the effects of solar modulation become more pronounced and therefore the low energy part of the proton LIS remained significantly uncertain.

This matter was improved greatly after the crossing of the HP by Voyager 1. The first indications of such a crossing came on July 28th of 2012, when the spacecraft was at about 121 AU. It detected an abrupt decrease in the intensities of termination shock particles (TSPs) as well as anomalous cosmic rays (ACRs), which was coincided with an increase in GCR intensities (Webber et al. [2012], Webber and McDonald [2013], Krimigis et al. [2013]). The increase in GCR intensities was consistent with a crossing of the HP. If TSPs and ACRs are the most prevalent charged particles in the heliosheath (Stone et al. [2005], Decker et al. [2005]), the implication would be that the decreases in these intensities were also indicative of a HP crossing. Gurnett et al. [2013] studied observations of electron plasma oscillations by Voyager 1 and presented further strong evidence that the crossing of the HP had indeed occurred on or about August 25, 2012. Having crossed the HP, Voyager 1 had thus started to register direct measurements of the LIS. The crossing of the HP by the Voyager 2 spacecraft in November 2018 at about 119 AU (Dialynas et al. [2019]) should also impose further restrictions on the proton LIS.

The origin of the proton LIS used in this study is in that of Langner and Potgieter [2004], which was based on the computations of Moskalenko et al. [2002]. The LIS was improved by Vos [2011] and Potgieter et al. [2014], taking into account measurements from PAMELA at energies between 30 and 50 GeV. This LIS is shown by the solid black line in Figure 3.1 and is labelled LIS_1. The LIS_1 was further improved after Voyager 1 crossed the HP, taking into account new observations in the lower energy range (see Potgieter [2014]); Voyager 1 measurements from Stone et al. [2013] are shown by the green diamonds. The

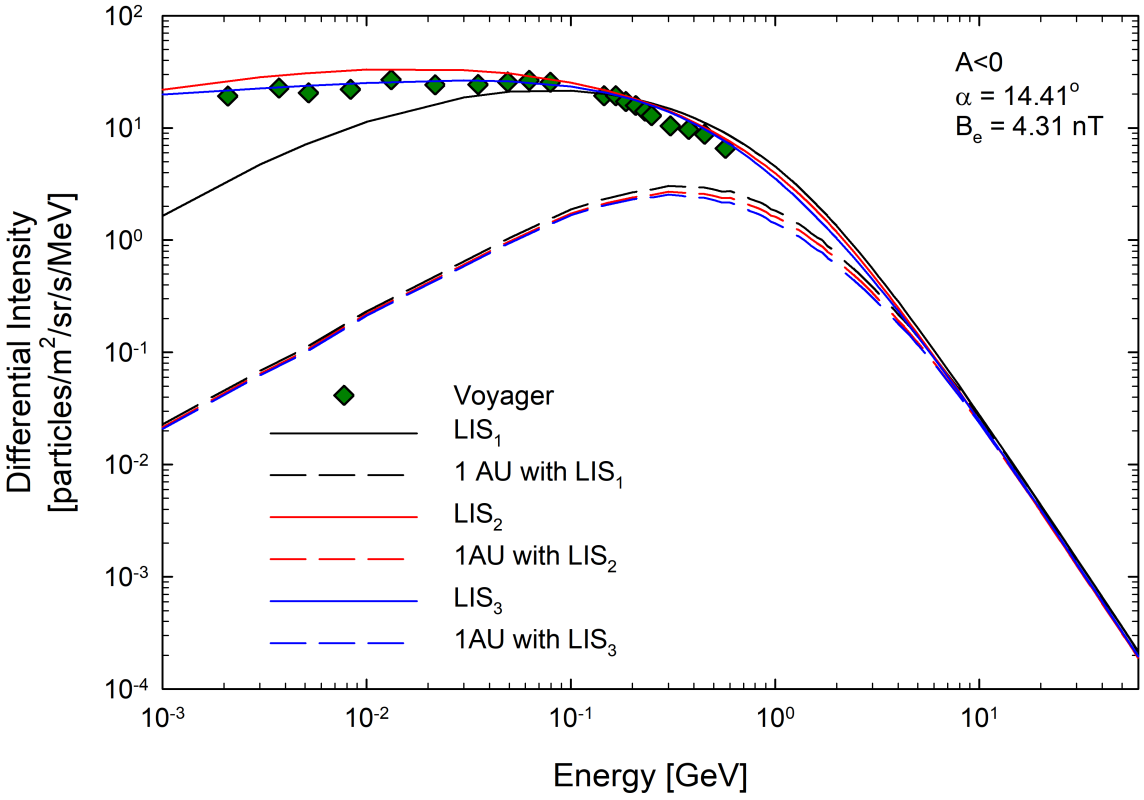


Fig. 3.1 *The proton LIS used in this study is indicated by LIS_3 and represented by the solid blue line. Two earlier LISs, i.e. the LIS_1 and LIS_2, are shown by the solid black and red lines respectively. The data from Voyager is indicated by the green diamonds. The black, red and blue dashed lines present the modulated spectra at Earth, assuming LIS_1, LIS_2, and LIS_3 respectively. The computed spectra at Earth represent $A < 0$ solar minimum conditions with the tilt angle $\alpha = 14.41°$ and the magnetic field magnitude at Earth $B_E = 4.31$ nT.*

LIS resulting from these modifications is defined by two expressions below and above 1.4 GV respectively and was used by e.g. Raath et al. [2016]; this LIS is shown by the solid red line and is labelled LIS_2. A single expression for the LIS was obtained and used by Vos and Potgieter [2015] as well as Potgieter and Vos [2017], and is given by

$$j = 2.70 \frac{\xi^{1.12}}{\beta_c^2} \left(\frac{\xi + 0.67}{1.67} \right)^{-3.93}, \tag{3.1}$$

in units of particles/m^2/sr/s/MeV; $\xi = E/1\text{GeV}$ where E is given in GeV and divided by 1 GeV in order to obtain a dimensionless quantity ξ. This LIS, shown by the solid blue line in Figure 3.1 is denoted LIS_3 and is the LIS used in this work.

The respective LISs differ from each other below $\sim$ 10 GeV. Above $\sim$ 200 MeV, LIS_1 is higher than LIS_2, which is approximately the same as LIS_3 up to energies of $\sim$ 700 MeV where LIS_2 becomes slightly higher than LIS_3. Below $\sim$ 200 MeV the LIS_1 is progressively lower than both the LIS_2 and LIS_3 towards lower energies. The LIS_3 is lower than the LIS_2 and is a slightly better representation of the Voyager 1 data at energies below $\sim$ 100 MeV.

Table 3.1 This table relates selected CRNs to their corresponding dates over the period January 2010 to January 2014.

Date	**CRNs**
01/2010	2092/3
01/2011	2105/6
01/2012	2118/9
01/2013	2132/3
01/2014	2145/6

The modulated spectra at Earth, while using the same modulation parameters and assuming as primary input (boundary condition) each of the LIS_1, LIS_2 and LIS_3 in turn, are also indicated (black, red and blue dashed lines respectively). These spectra are computed for the $A < 0$ polarity cycle with the tilt angle $\alpha = 14.41°$ and the magnetic field magnitude at Earth $B_E = 4.31$ nT. The spectrum at Earth that assumes LIS_1 is significantly higher than the spectrum assuming LIS_2 only down to energies of $\sim$ 100 MeV; in the same way, the spectrum using LIS_2 is higher than the spectrum using LIS_3. Around $\sim$ 100 MeV the spectra become about equal and all three is bent into the shape which is characteristic of the dominating effects of adiabatic cooling at these low energies.

3.3 PAMELA Proton Spectra from 2010 to 2014

Galactic proton observations from the PAMELA spacecraft spanning the time period 01/2010 to 01/2014 is discussed in this section, i.e. the data that was recorded during the first four years of Solar Cycle 24. The focus of this section is on the overall variation in modulation from solar minimum conditions in 01/2010 to solar maximum conditions in 01/2014; this corresponds to Carrington Rotation numbers (CRNs) 2092/3 to 2145/6. Table 3.1 relates the CRNs and dates which are included in the period 01/2010 to 01/2014.

Figure 3.2 shows a plot of these proton spectra, which were averaged over one Carrington Rotation or $\sim$27 days; different colours are used to indicate the spectra for each of eight consecutive periods of six months, as indicated in the legend. Data from CRNs 2095 to 2102 are missing due to a system shut-down for satellite maintenance operations, while data from CRNs 2113, 2115, 2121, 2123, 2125, 2126, 2135, 2136, 2137, 2143, and 2145 are also not represented due to the presence of solar energetic particles (SEPs); see Martucci et al. [2018].

Most apparently, there is an overall decrease in the levels of intensity, decreasing from higher values in 2010 to lower values in 2014, as solar activity increases. It is evident that intensities in the lower energy ranges experienced the largest decreases. Reading the values directly from the data, the highest intensity was recorded in January 2010, peaking at around 300 MeV, where it reached levels of $\sim$ 2.7 particles/m^2/sr/s/MeV. These levels

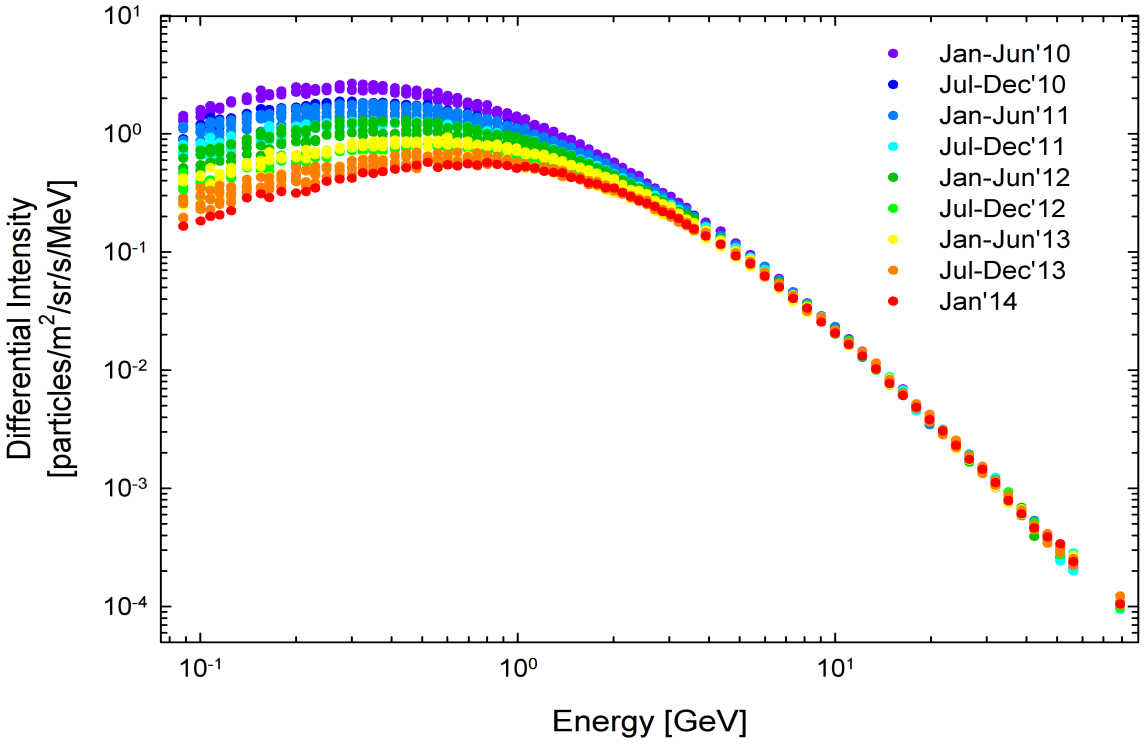


Fig. 3.2 *The PAMELA proton data for January 2010 to 2014 are presented, using the colours given in the legend. These spectra were averaged over one Carrington Rotation ∼27 days. The data is as published by Martucci et al. [2018].*

dropped to a maximum of ∼ 0.6 particles/m^2/sr/s/MeV in January of 2014, represented by a factor decrease of ∼ 4.5; the peak of the spectrum had also shifted to ∼ 520 MeV.

In Figure 3.3 the ratios of the consecutively Carrington Rotation averaged spectra relative to January 2010 are shown. It is clear that particle intensities at the lower end of the energy spectrum experienced the largest decreases. The largest decrease relative to the January 2010 spectrum was by a factor of ∼8.2 in January 2014 around 110 MeV. This is consistent with what was found by Martucci et al. [2018] who reported a factor decrease of nearly 10.0. Proton intensities in the region around 150 MeV decreased by a factor of ∼7.7 from 01/2010 to 01/2014.

The extremities presented by this data, i.e. the 01/2010 and 01/2014 spectra, were modelled by Martucci et al. [2018] employing the SDE-model featured in this thesis. The LIS as used by Vos and Potgieter [2015] and Potgieter and Vos [2017], i.e. LIS_3, was assumed and the HP was located at a radial distance of $r_{\mathrm{HP}} = 122$ AU. Over the four years spanning 01/2010 to 01/2014, changes in the HCS tilt angle α as well as the magnetic field magnitude B_{E} as observed at Earth were taken into account. These parameters changed from $\alpha = 10.19°$ and $B_{\mathrm{E}} = 3.98$ nT in 01/2010 to $\alpha = 65.54°$ and $B_{\mathrm{E}} = 5.20$ nT in 01/2014. These values were averaged over the preceding 15 months, as an estimation of prevailing

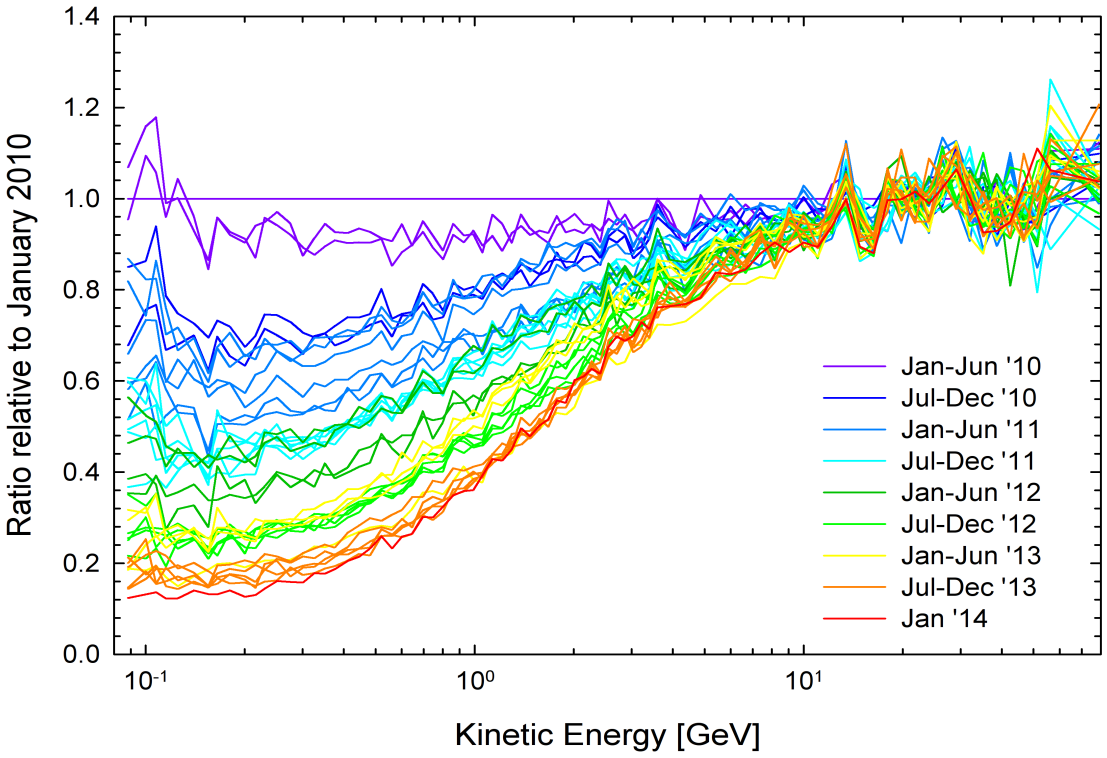


Fig. 3.3 *The ratios of consecutive proton spectra from PAMELA with respect to January 2010. Different colours are used to indicate the ratios for the different time periods, as indicated in the legend and also in Figure 3.2.*

conditions in the heliosphere at that time; assuming a constant solar wind speed $V_{sw} = 430$ km/s, it takes an estimated 15 months for the frozen-in magnetic field and the HCS tilt angles to propagate from the sun outwards to fill the whole heliosphere (e.g. Vos [2016]). The diffusion coefficients, parallel and perpendicular to the global magnetic field were then constructed; the perpendicular coefficient consisted of two components in the radial and polar directions respectively. These coefficients as well as the drift coefficient were assumed to scale inversely with the magnetic field (HMF) magnitude, i.e. $1/B$. Its rigidity dependence was fixed through Equations (2.32) and (2.45). For more on possible rigidity dependencies for the diffusion coefficients as well as implementations, see e.g. Ferreira et al. [2001*a*], Engelbrecht [2008] and Manuel et al. [2013]. The study of Martucci et al. [2018] therefore followed the same basic modelling approach described earlier in Chapter 2; see also Potgieter et al. [2015].

The results of Martucci et al. [2018] are shown in Figure 3.4; take note that intensities are given in units of particles/m^2/sr/s/GeV and therefore differs from Figure 3.2 where intensities were given in units of particles/m^2/sr/s/MeV. Figure 3.4 shows the computed spectra for 01/2010 and 01/2014 respectively, with the corresponding observations from PAMELA. The model reproduces the features of these two spectra well over this entire

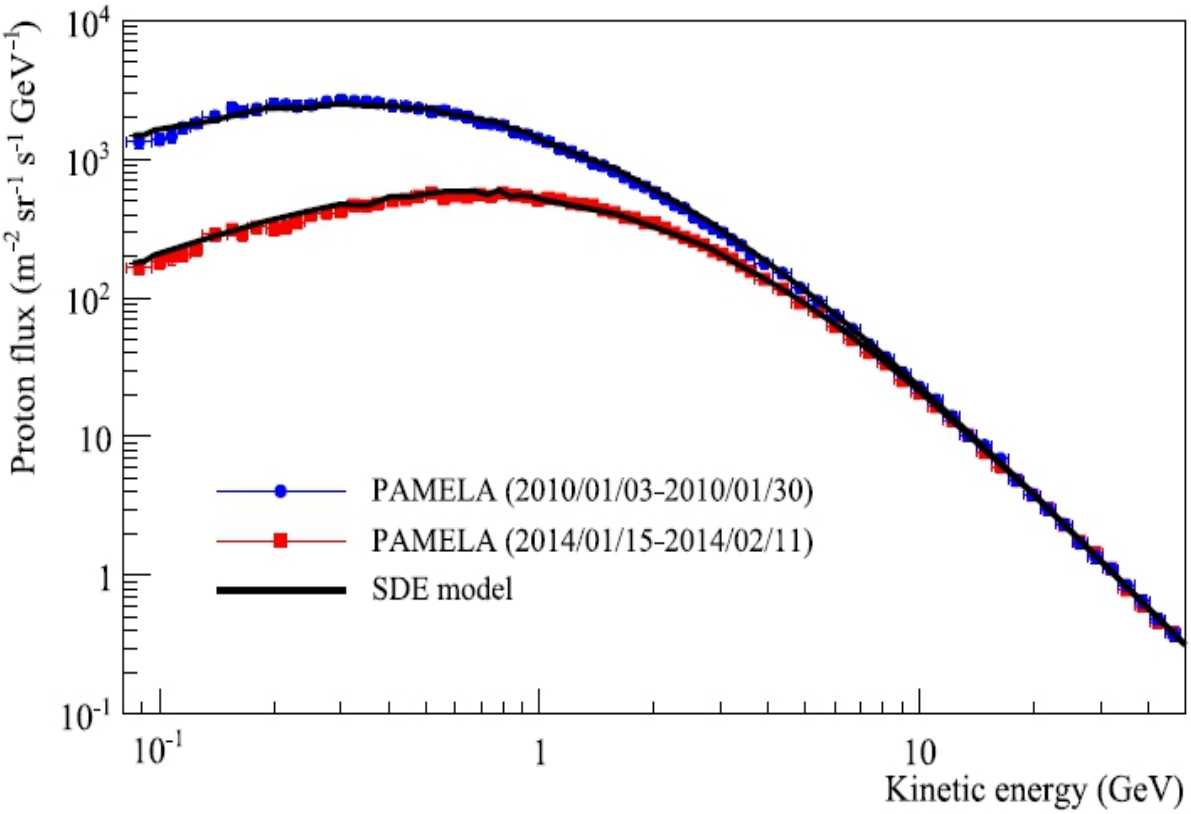


Fig. 3.4 *Proton spectra from PAMELA measured during two Carrington Rotations for January 2010 (blue circles) and 2014 (red squares), respectively. The SDE-model reproductions for these two spectra are shown by the black lines. The parameter settings for these two reproductions are shown in Table 3.2. This figure was taken from Martucci et al. [2018].*

range of energy, in particular when considering the values of intensity where the spectra peak and how this peak shifts to higher energies, while the spectrum decreases with increased modulation.

To reproduce the 01/2010 spectrum, which was during an $A < 0$ polarity cycle, only minor changes to the modulation parameters used by Raath et al. [2016] were required. However, reproducing the 01/2014 spectrum, which was assumed to be during an $A > 0$ polarity cycle, the diffusion coefficients had to be decreased by a factor of 2.0 with respect to the values in 01/2010; refer to the values of $\kappa_{||,0}$ in Table 3.2. In addition to the smaller absolute value of diffusion, the rigidity dependence of the diffusion coefficients below $P_{\mathrm{k}} = 4.2$ GV had to be changed from a $P^{0.95}$ dependence in 01/2010 to a $P^{1.15}$ dependence in 01/2014, which indicates a hardening in the spectra towards 01/2014; above $P_{\mathrm{k}} = 4.2$ GV, the rigidity dependence was set at $P^{1.95}$, with P_{k} as defined in Equation (2.45). Additionally, the drift coefficient had to be reduced to only 10% of the value at solar minimum, i.e. the value of $\kappa_{\mathrm{A},0}$ in Equation (2.32) was set to $\kappa_{\mathrm{A},0}$ =0.1 instead of 1.0. Without these alterations to diffusion and drift, intensity levels would have remained

Table 3.2 Values of parameters used to reproduce the PAMELA proton spectra for January of 2010 and 2014 respectively, employed by Martucci et al. [2018]. The parameters $\kappa_{||,0}$, P_{k}, a, b, and c are as they occur in Equation (2.45); the values d, $\kappa^0_{\perp r}$ and $\kappa^0_{\perp\theta}$ are as defined by equations (2.46) to (2.50), while $P_{\mathrm{A},0}$ is as in Equation (2.32).

Parameter	**2010**	**2014**
α [deg]	10.19	65.54
B_{E} [nT]	3.98	5.20
$\kappa_{\|\|,0}$ [1×10^{22} cm^2/s]	18.40	9.20
$\kappa^0_{\perp r}$, $\kappa^0_{\perp\theta}$	0.02	0.02
$\kappa_{A,0}$	1.00	0.10
a	0.95	1.15
b	1.95	1.95
c	3.00	3.00
d	3.00	3.00
$P_{\mathrm{A},0}$ [GV]	0.16	0.16
P_{k} [GV]	4.20	4.20

far too high. The parameters used for the 01/2010 and 01/2014 model reproductions are shown in Table 3.2.

It will now be illustrated further that to make up this modulation difference between the spectra of 01/2010 and 01/2014, changing only the values of α and B_{E} as a function of solar activity is not sufficient and that the diffusion coefficients must be changed, both in terms of magnitude and in terms of its rigidity dependence. In Figure 3.5 the ratio of the 01/2014 to the 01/2010 PAMELA data is shown by the white circles; this indicates the total difference in modulation between the 2014 and 2010 spectra at energies between 100 MeV and 80 GeV. The red line shows the ratio of the 01/2014 to 01/2010 model reproduced spectra from Martucci et al. [2018], i.e. the case where the diffusion and drift coefficients as well as the polarity cycle were changed in addition to the solar activity dependent changes in α and B_{E}. This indicates that the fit was better at higher energies, starting to deviate from the data-ratio from about 1 GeV downwards; nevertheless, the reproduction was sufficient at these lower energies. The blue line shows the ratio when merely both α and B_{E} were changed from their values in 01/2010 to their values in 01/2014, with the drift and diffusion coefficients left other-wisely unchanged. This ratio is far higher than that shown by the data at all energies below $\sim$10 GeV. It is therefore obvious that a change of α and B_{E} alone does not account for the difference in modulation between 01/2010 and 01/2014. The green line shows the ratio where α has been increased to its maximum value $\alpha = 75°$, with B_{E} at its 2014 value, and the ratio is still not comparable to that given by the data. The violet line shows the ratio where $\alpha = 75°$ and B_{E} was increased to an unrealistic value of $B_{\mathrm{E}} = 10.00$ nT; it is clear that the ratio given by the data will not be reproduced in this way: the model reproduction is now higher than the

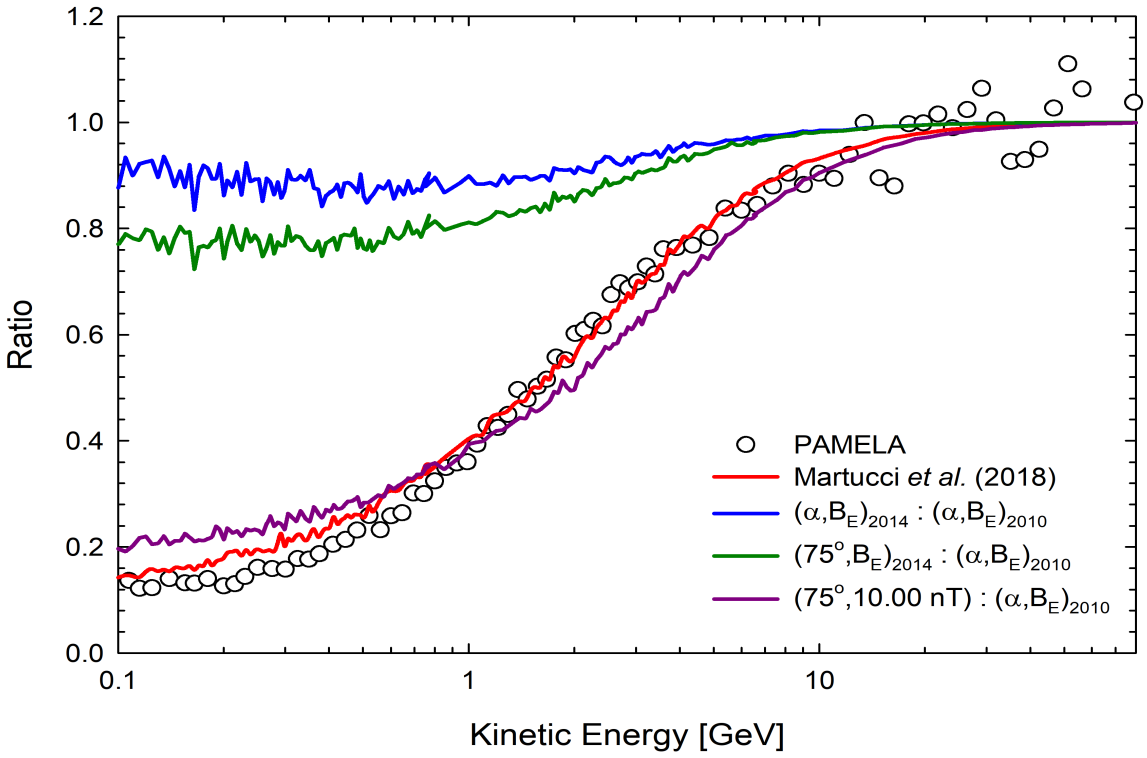


Fig. 3.5 *The white circles show the ratio of the 01/2014 to 01/2010 proton spectra from PAMELA. It is overlaid by the ratio of the 01/2014 to 01/2014 intensities as computed by Martucci et al. [2018], shown by the red line. The blue line shows the ratio resulting from only changing the values of α and B_E from their values in 01/2010 to those in 01/2014. The green line shows this ratio, but with α for the 01/2014 spectrum now increased to the maximum of 75°. The violet line shows the ratio with the value of $B_E = 10.00$ nT now increased to an unrealistically high value.*

data below ∼1 GeV and lower than the data above this energy up to ∼ 10 GeV. Therefore, additional changes to the diffusion coefficients, as indicated in Table 3.2, are necessary.

3.4 Solar Activity during Solar Cycle 24

The prolonged solar minimum period of Solar Cycles 23/24 ended in 2009 with record levels of CR intensities (Heber et al. [2009], Mewaldt et al. [2010], Strauss and Potgieter [2014*a*], Zhao et al. [2014]), after which solar activity began to increase again steadily, but appeared weak in terms of e.g. sunspot number and number of solar events (Aslam and Badruddin [2015], Schröder et al. [2017]). This increase in solar activity is evident in the decreasing intensities occuring in the spectra of the previous section, i.e. Figures 3.2 and 3.3.

The three panels of Figure 3.6 show the evolution of Solar Cycle 24 toward solar maximum, indicating a number of solar activity parameters starting at 2008.5 and ending at 2014.5, i.e. overlapping the time period during which the data considered in this chapter

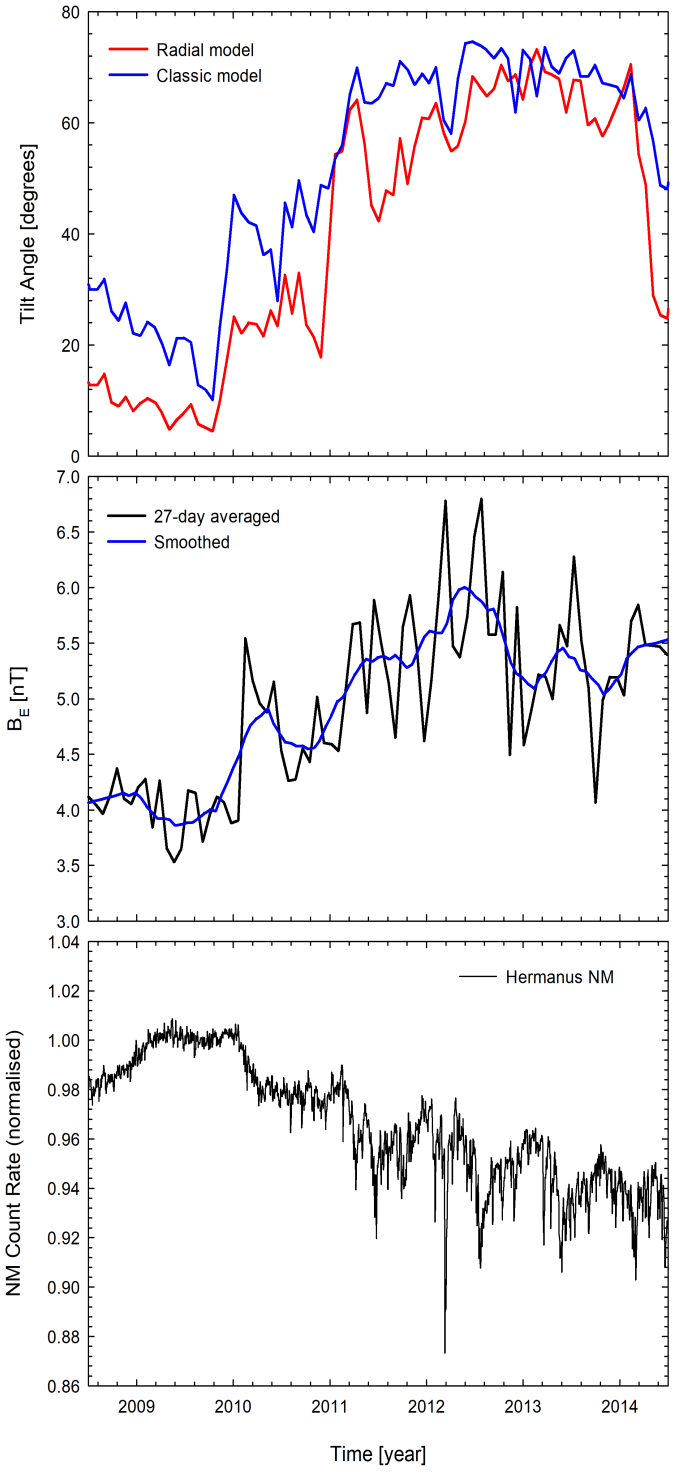


Fig. 3.6 *This figure shows the evolution of solar activity conditions towards the solar maximum of Solar Cycle 24. In the top panel, the tilt angles according to the Radial and Classic models are represented by the red and blue lines respectively;* `http://wso.stanford.edu/Tilts.html`. *In the middle panel, the black line shows the 27-day averaged HMF magnitude at Earth, while the blue line shows the smoothed version;* `https://omniweb.gsfc.nasa.gov`. *In the bottom panel, the black line shows the monthly averaged count rate from the Hermanus NM, normalised to one on 1 January of 2010;* `http://natural-sciences.nwu.ac.za/neutron-monitor-data`.

was recorded. The top panel shows the values of α computed according to the Radial (red line) en Classic (blue line) models respectively; these were obtained from the website of the Wilcox Solar Observatory `http://wso.stanford.edu/Tilts.html`. The middle panel shows the 27-day averaged values for B_{E} measured by the Advanced Composition Explorer or ACE (black line), together with the smoothed data (blue line); data obtained from `https://omniweb.gsfc.nasa.gov`. The bottom panel shows the Hermanus neutron monitor (NM) count rate, normalised to a value of one on 1 January 2010; data obtained from `http://natural-sciences.nwu.ac.za/neutron-monitor-data`.

Comparing the values of α computed by the Radial and Classic models respectively, the tilt angles of both these models show a marked increase at the end of 2009. It then flattens off again in 2010 (especially the Radial model) and starts increasing again at the end of 2010. The recovery of α computed by the Classic model is more gradual, with that of the Radial model showing an abrupt increase at this point in time. The Radial model intensities do, however, decrease significantly again just after the start of 2011 and attain a more gradual increase thereafter. After the initial increase at the end of 2010, the α computed by the Classic model stays between about 60° and 75°; the Radial model only maintains these levels about a year later from the start of 2012. The tilt angles computed by both models drop sharply just after the start of 2014.

Concerning the value of the HMF magnitude at Earth, the middle panel of Figure 3.6 shows that B_{E} remained below ∼4.5 nT up to the end of 2009 where it started increasing. Except for an initial increase up to ∼5.5 nT, B_{E} varies between ∼4.0 nT and ∼5.0 nT until the end of 2010. After this point, the values of B_{E} remain above ∼5.0 nT with the 27-day averaged values reaching levels above ∼6.5 nT.

The monthly averaged NM count rate in the bottom panel of Figure 3.6, which was normalised to one on 1 January 2010, shows the first decrease in intensities at about the end of 2009 and then keeps on decreasing in a step-like fashion towards solar maximum in 2014. This step-like behaviour is a property of short-term modulation where structures such as global merged interaction regions (GMIRs) are accounted for (e.g. Ferreira [2002]) and therefore not reproduced by the model of this study which considers only long-term modulation. The decrease in the NM count rate is, however, clearly anti-correlated with the behaviour of α and B_{E} in the sense that it decreases towards solar maximum in 2014, while the former two parameters show an increase instead. See Iskra et al. [2019] for an in detail study of delay times between various parameters characterising solar activity and GCR intensity.

The evolution of the solar magnetic polarity cycle was less clear, e.g. it was not exactly clear when the shift in magnetic polarity from $A < 0$ to $A > 0$ had occurred; this issue was handled in various ways by different authors (see e.g. Sun et al. [2015], Adriani et al. [2016]; Chowdhury et al. [2016]; Kalinin et al. [2017]). At the maximum of Solar Cycle 24, the polarity would change from $A < 0$ to $A > 0$. In the top panel of Figure 3.7 the North

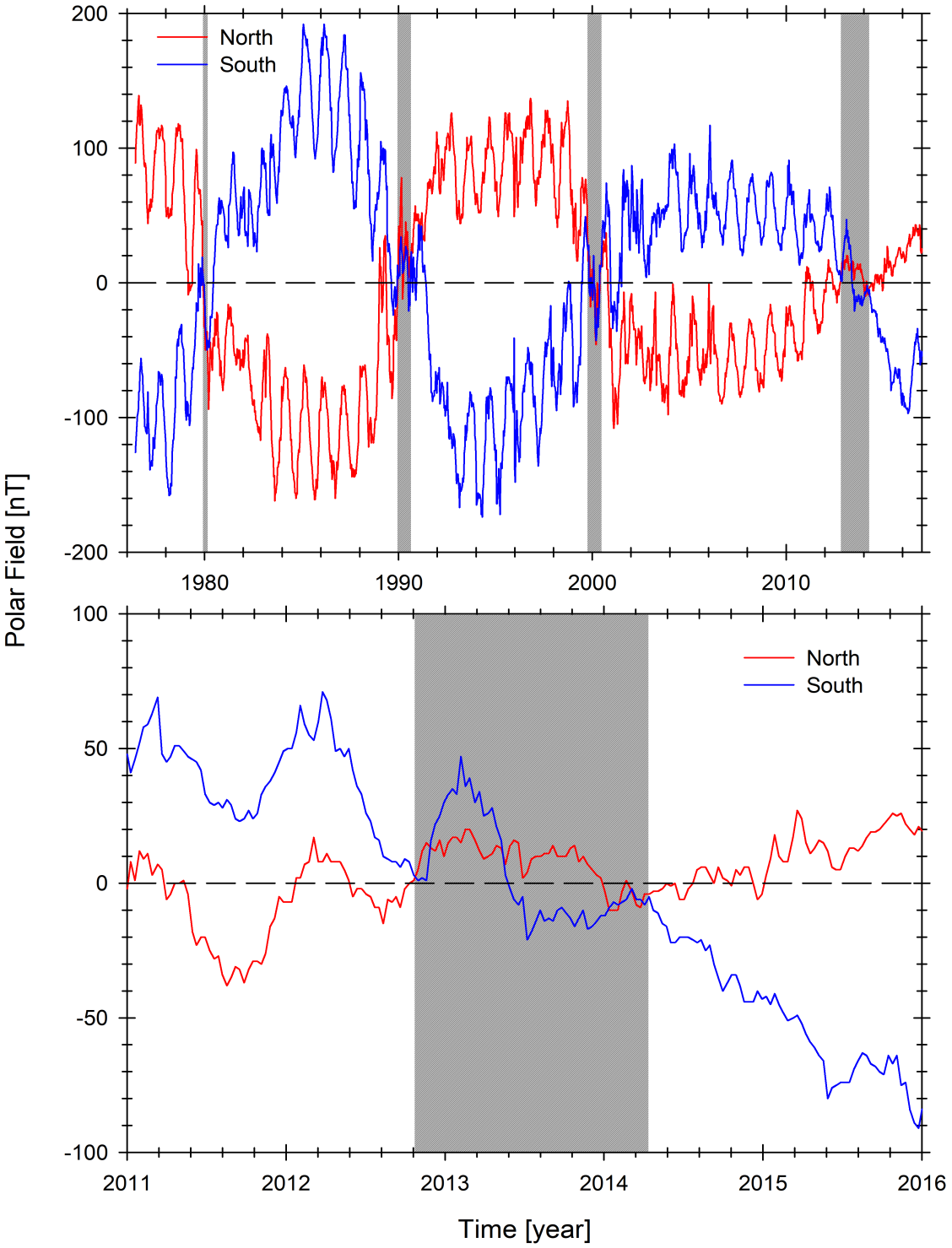


Fig. 3.7 *The top panel shows the North (red line) and South (blue line) polar magnetic fields of the Sun over the period 1976 to 2017. The transition region of Solar Cycle 24 as well as that of three previous polarity switches are indicated by the shaded regions. The bottom panel zooms in on the transition period of Solar Cycle 24, stretching from 2012.81 to 2014.28. This data is obtained from* `wso.stanford.edu`.

(red lines) and South (blue lines) polar fields of the Sun over the period 1976 to 2017 are shown; `wso.stanford.edu`. In the bottom panel it is zoomed in on the period of time 2011 to 2016 and it is evident that, between September 2012 (∼2012.81) and March 2014 (∼2014.28), it was quite uncertain what the status of the polarity was. The period from 2012.81 (CRNs 2127/8) to 2014.28 (CRNs 2147/8) was, in this thesis, defined as the 'transition period' for the solar magnetic polarity cycle. During this time the polarity could have been either $A < 0$ or $A > 0$ or even zero-drift, owing to the suppression of drift effects during solar maximum (see the discussions in Chapters 2 and 4). This transition period as well as three earlier ones are indicated by the shaded regions and it is noteworthy that the last transition period was significantly longer than the previous ones, spanning more than one and a half years, where the previous periods were only between three and nine months each.

3.5 Modelling the PAMELA Proton Spectra

3.5.1 Half-Yearly Averaged Spectra

In this section a number of eight half-yearly averaged proton spectra are calculated from the Carrington Rotation averaged PAMELA data discussed earlier. The first of these eight spectra is for the first six months of 2010, i.e. January 1st to June 30th of 2010; it is henceforth denoted by 2010a. The second six-monthly averaged spectrum is that for the second half of 2010, i.e. July 1st to December 31st of 2010 and is denoted by 2010b. This denotation is used throughout for the first and second halves of 2011, 2012 and 2013 as well. The eight spectra are shown in Figure 3.8 where the energy range has been restricted to between 100 MeV and 10 GeV in order to better illustrate the spread of the spectra with increasing solar activity. The decrease in proton intensity from solar minimum to maximum, as well as the upward shift of the energy at which the peak in intensity is measured, are clearly evident.

A picture of the global modulation conditions in the heliosphere has been sketched in Section 3.4. In this section, the information is used to calculate the average conditions prevailing in the heliosphere, applicable to each of the eight half-yearly averaged spectra, i.e. averages for both α and B_{E} are obtained. Assuming that the HMF is frozen into the solar wind (SW) and that all changes in the HMF and α are therefore propagated at the speed of the SW, the period of averaging for both these parameters was chosen as 15 months; this was explained in Section 3.3.

The 15-month averaged tilt angles were obtained from the values calculated by the Radial and Classic models, respectively indicated by α_{R} and α_{C}. The top panel of Figure 3.9 shows the Radial model calculations, with the 15-month running average shown by the red line. The middle panel does the same, but for the case of the Classic model. The bottom panel shows the 15-month running averages of both the calculations by the Radial

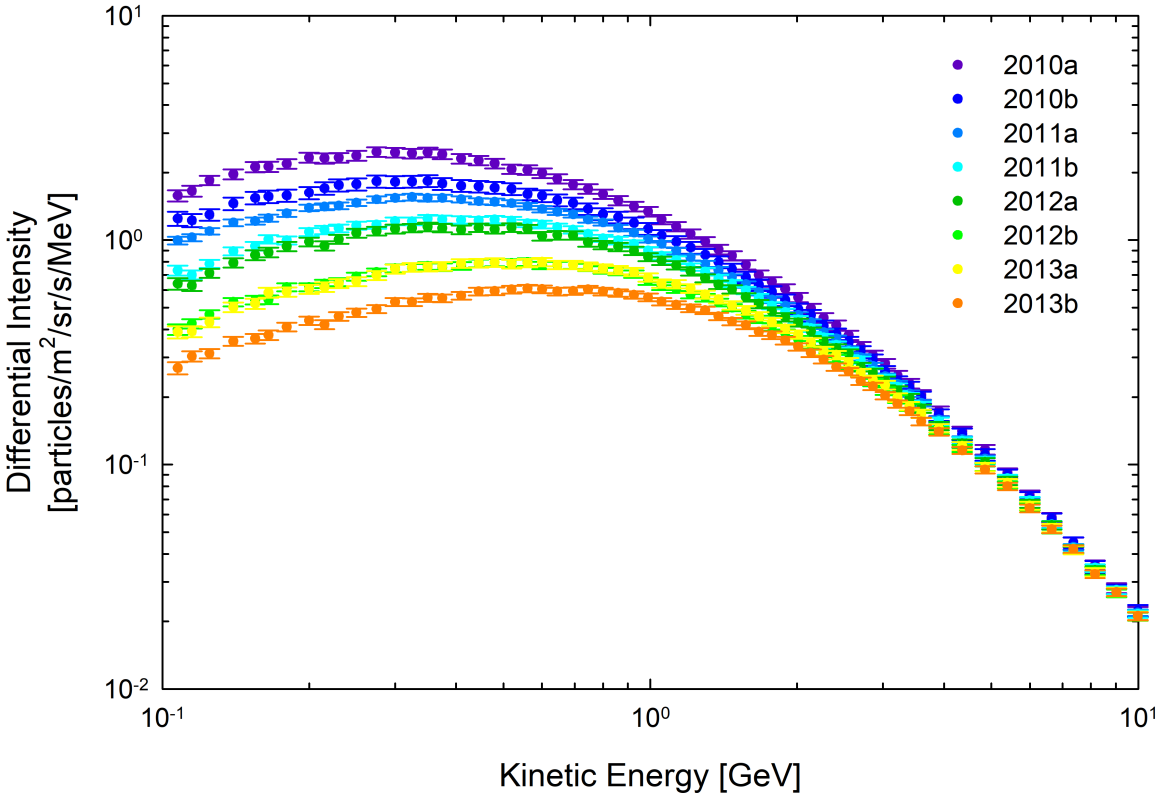


Fig. 3.8 *The eight half-yearly averaged proton energy spectra calculated from the PAMELA data. The spectra labelled with a and b are the half-yearly averages for the periods January to June and July to December respectively, for each of the indicated years. A different colour is used for each spectrum, as indicated in the legend.*

and Classic models (red and blue lines respectively), as well as for the average α_A of the two models (green line); the 15-month averaged values of α for each of the half-yearly averaged spectra are indicated by the dots and the 15-month period over which the first average was calculated is indicated by the shaded region. The average values of the tilt angle for the eight half-yearly averaged spectra from January 2010 to December 2013 are indicated in Table 3.3. From 2010a to 2013b, as solar activity evolves from minimum to maximum conditions, α_A increases gradually over each of the six-month intervals from 18.65° to 25.71°, 38.79°, 48.71°, 58.72°, 63.27°, 67.02°, and 68.78° respectively. It is notable that this increase became progressively smaller towards solar maximum, as the tilt angle obtained its maximum values. Note that the average values α_A were determined by calculating a profile representative of the average of Radial and Classic models and then taking a 15-month running average of this profile; consequently, the average value α_A employed in the model is not identical to $(\alpha_R + \alpha_C)/2$.

In the same way, average values for the HMF magnitude at Earth were calculated, using the 27-day averaged data shown in the middle panel of Figure 3.6 and described in

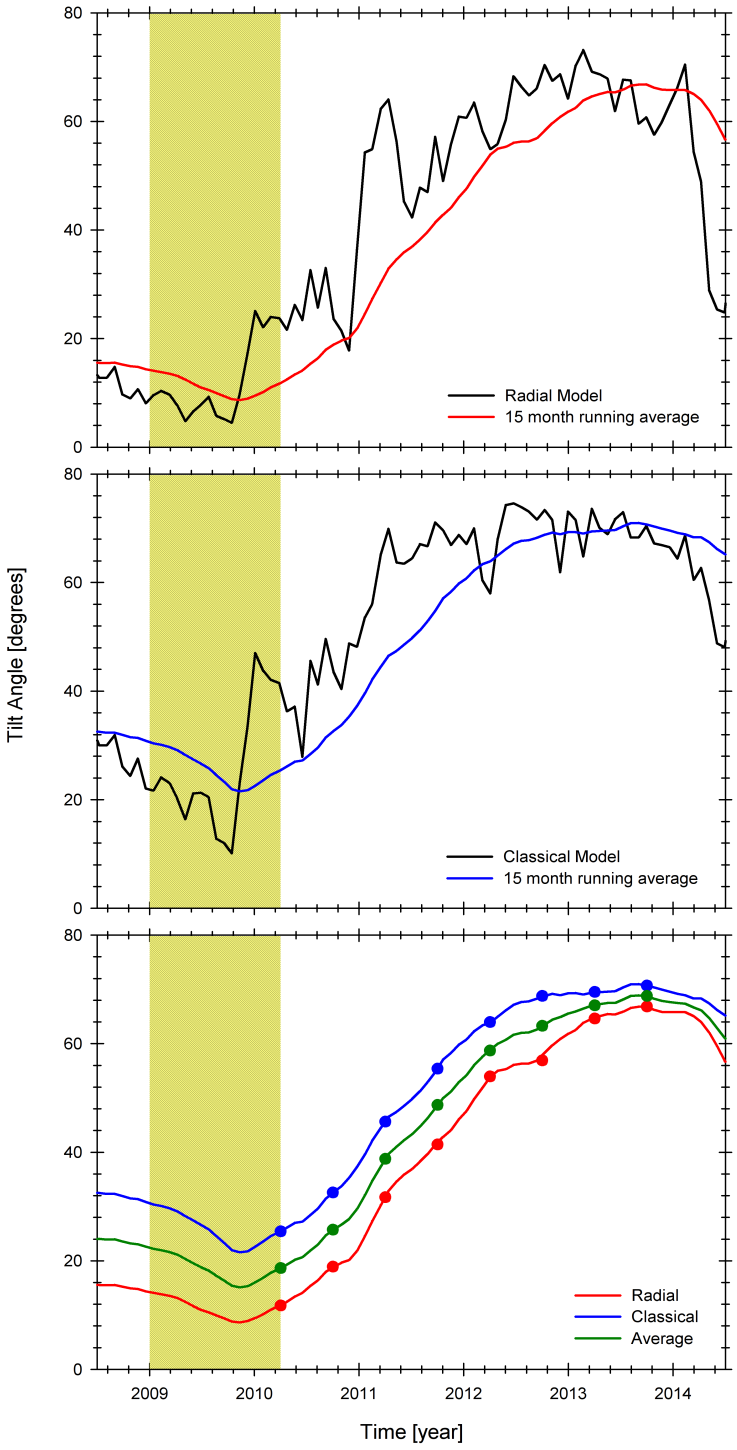


Fig. 3.9 *The top and middle panels show the tilt angles calculated by the Radial and Classic models respectively (black lines), together with the 15 month running averages (red and blue lines respectively). The bottom panel shows only the 15 month running averages for each model (red and blue lines), and now also shows the 15 month running average for the average of the tilt angles predicted by the Radial and Classic models (green line). In each panel, the 15 months over which the average for 2010a was calculated is indicated by the shaded region. The red, blue and green dots show the averages in each case at each of the times that are selected for the six-month averaged spectra, i.e. 2010a/b, 2011a/b, 2012a/b, and 2013a/b. All data obtained from* `http://wso.stanford.edu/Tilts.html`.

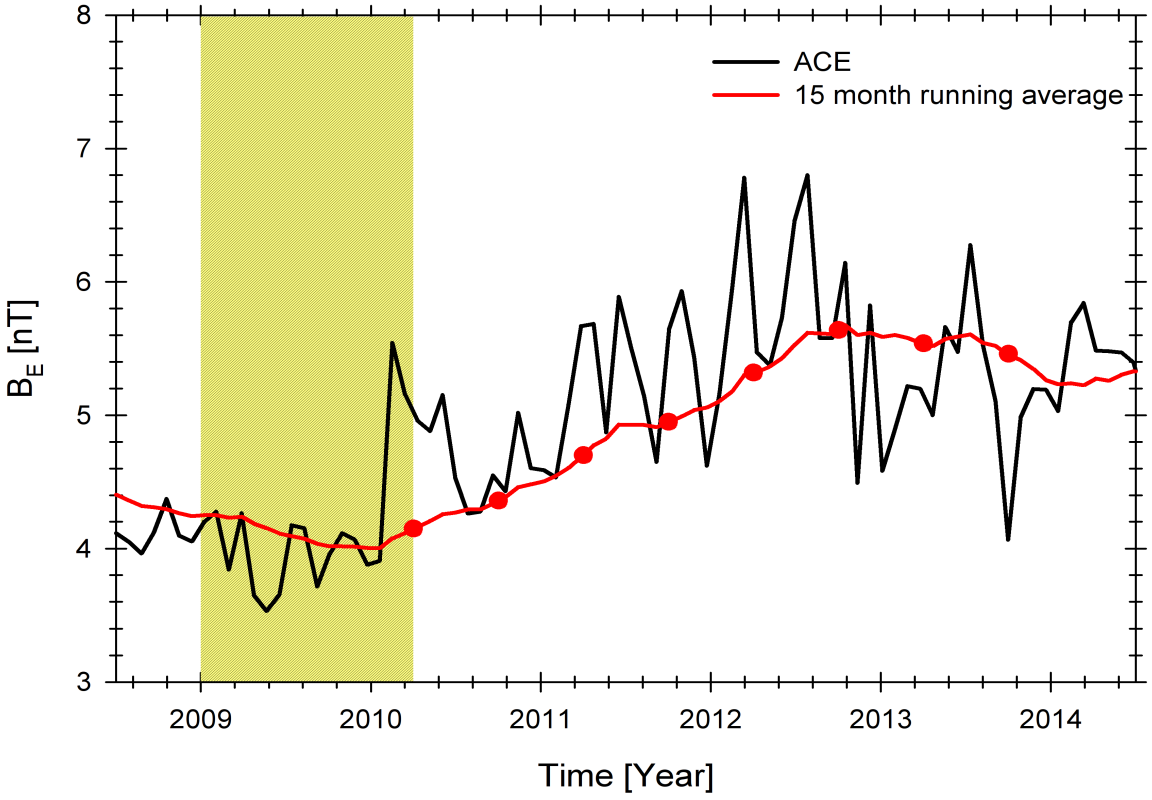


Fig. 3.10 *The HMF magnitude at Earth as measured by ACE (black line); this data was obtained from* `https://omniweb.gsfc.nasa.gov` *and was averaged over one Carrington Rotation ∼27 days. It is overlaid by the 15-month running average (red line) and the red dots show the times at which the average was taken to use in the calculation of the spectra, i.e. 2010a/b, 2011a/b, 2012a/b, and 2013a/b.*

Section 3.4. Figure 3.10 shows this data (black line) together with the 15-month running average (red line); the values for each of the half-yearly averaged spectra are shown by the red dots and the first 15-month period over which the first of these averages were calculated is again indicated by the shaded region. The average values of the HMF magnitude at Earth for each of the half-yearly spectra from January 2010 to December 2013 are shown in Table 3.3. From 2010a to 2012b the B_{E} value increases gradually by 0.21, 0.34, 0.25, 0.37, and 0.32 nT over each of the six-month intervals respectively, as solar activity conditions progress towards solar maximum. The value of B_{E} then decreases from 2012b to 2013a by 0.10 nT and again from 2013a to 2013b by 0.08 nT; it may therefore be clear that the B_{E} value had settled around its maximum values by 2012b.

Although the radial distance r_{TS} at which the solar wind termination shock (TS) occurs is also a function of time, the value of this parameter was kept fixed at $r_{\mathrm{TS}} = 90$ AU for the purposes of the current study. Manuel et al. [2015] has shown that the effect of a dynamic inner heliosheath thickness becomes less significant at smaller radial distances and, consequently, the effect on spectra solutions at Earth would be small.

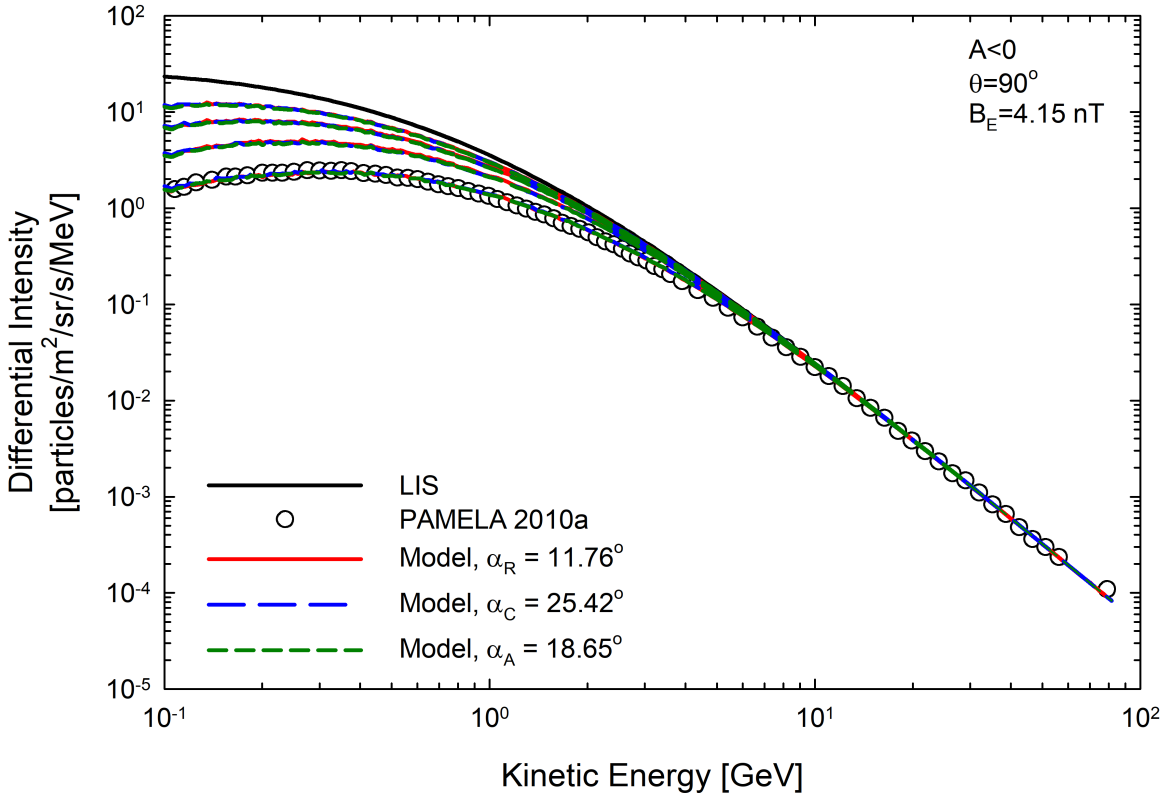


Fig. 3.11 *Data from PAMELA for 2010a (white circles) together with model reproductions using the Radial model α_R (solid red line), Classic model α_C (long dashed blue line) and the average tilt angle α_A (short dashed green line) respectively. The LIS is shown by the solid black line. Spectra are also shown at intermittent distances from Earth 90, 60 and 30 AU (descending solutions) for each of the tilt angle models, making use of the same colour scheme applied at 1 AU. These spectra are shown over the energy range ∼100 MeV to ∼80 GeV. Solutions are calculated for the $A < 0$ polarity cycle.*

3.5.2 Numerically Reproduced Spectra: Results

In this section, the parameters calculated in Section 3.5.1, i.e. α and B_E, were incorporated into the numerical modulation model after which the transport coefficients (diffusion in particular) were adjusted in order to obtain reproductions of the eight half-yearly averaged spectra calculated from the PAMELA data. The assumptions for these coefficients were similar to those of Martucci et al. [2018], i.e. as described in Chapter 2, so that they were scaled as $1/B$ and therefore changing with the solar cycle. However, no additional scaling down of drift effects towards solar maximum was included, except where explicitly stated otherwise; see Chapter 4 for more on this topic.

The proton energy spectrum for the first of the half-yearly averaged spectra, i.e. 2010a, is shown in Figure 3.11, using $N = 1000$ pseudo-particles for the model computed solution (this value of N is also used for all subsequent model reproductions of spectra in this chapter). The PAMELA data are indicated by the white circles; these are overlaid by the

$A < 0$ model solutions using α_R (red line), α_C (blue line) and α_A (green line) respectively, as given in Table 3.3. The value of B_E was also as given in Table 3.3. The corresponding spectra at 30 AU, 60 AU and 90 AU in the equatorial plane are also shown, being the highest at 90 AU and descending to 30 AU. The LIS is indicated by the solid black line. The values of the parameters for the transport coefficients, i.e. $\kappa_{||,0}$ and a in Equation (2.45), that were obtained for the model reproduction using the average tilt angle α_A are indicated in Table 3.3, i.e. $\kappa_{||,0} = 19.60$ in units of 1×10^{22} cm^2/s (all subsequent values for $\kappa_{||,0}$ are in these units) and the dimensionless constant $a = 0.95$. The values of $\kappa_{||,0}$ in the case of the model reproductions assuming α_R and α_C are not indicated in Table 3.3, but were found to be $\kappa_{||,0} = 18.90$ and $\kappa_{||,0} = 20.00$ respectively; the value of a was the same as the case assuming α_A.

Figure 3.12 presents a zoomed in version of Figure 3.11, with the focus on energies between 100 MeV and 10 GeV, and shows only the reproductions that assume the average tilt angle α_A. All subsequent results will consider only the reproductions obtained using α_A. Figures 3.13 to 3.19 are similar to Figure 3.12, but for each of the cases 2010b, 2011a/b, 2012a/b, and 2013a/b respectively. The values of the tilt angle α_A in each case as well as the value for B_E are listed in Table 3.3. Also listed in Table 3.3 are the values of $\kappa_{||,0}$ and a that were obtained for each model reproduction.

The MFPs (diffusion) required to reproduce each spectrum are shown graphically in Figure 3.20, where the parallel MFPs are shown as function of rigidity. The MFPs for 2010a to 2012a are presented by the red lines and are for an $A < 0$ polarity cycle. The six-month time intervals for the cases 2012b and 2013a/b overlap with the transition region discussed in Section 3.4 and the solar polarity cycle was therefore uncertain. The model reproductions were consequently obtained for the zero-drift scenario, providing spectra independent of drifts; the motivation for using zero-drift was the suppression of drifts towards solar maximum (e.g. Ferreira [2002], Ferreira and Potgieter [2004], Ndiitwani et al. [2005], Manuel et al. [2011], Siluszyk et al. [2011]). The MFPs for 2012b to 2013b are indicated by the blue lines in Figure 3.20.

More results are shown in Tables 3.4 and 3.5, pertaining to the energy at which the peak in intensity had occurred and also the intensities at 100 MeV and how these had evolved over the time period 01/2010 to 01/2014. These figures are discussed for their qualitative significance in the next section.

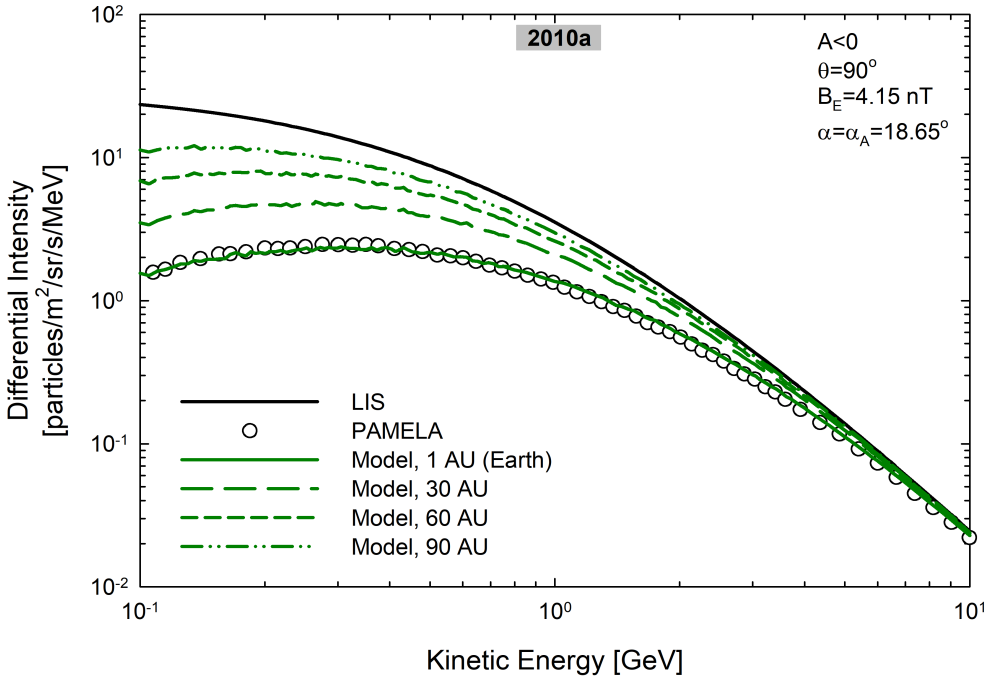


Fig. 3.12 *Similar to Figure 3.11, i.e. showing the 2010a spectrum from PAMELA (white circles) together with the model reproductions (green lines), but only showing intensities for energies 100 MeV to 10 GeV and only for the case using* α_{A}.

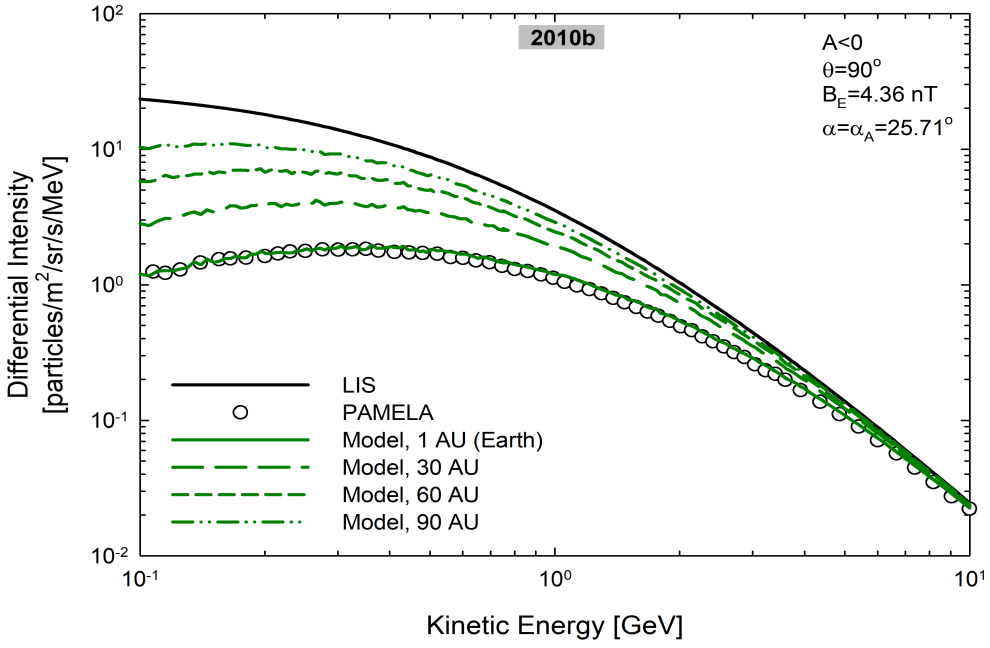


Fig. 3.13 *Similar to Figure 3.12, but for the 2010b PAMELA spectrum and model reproductions.*

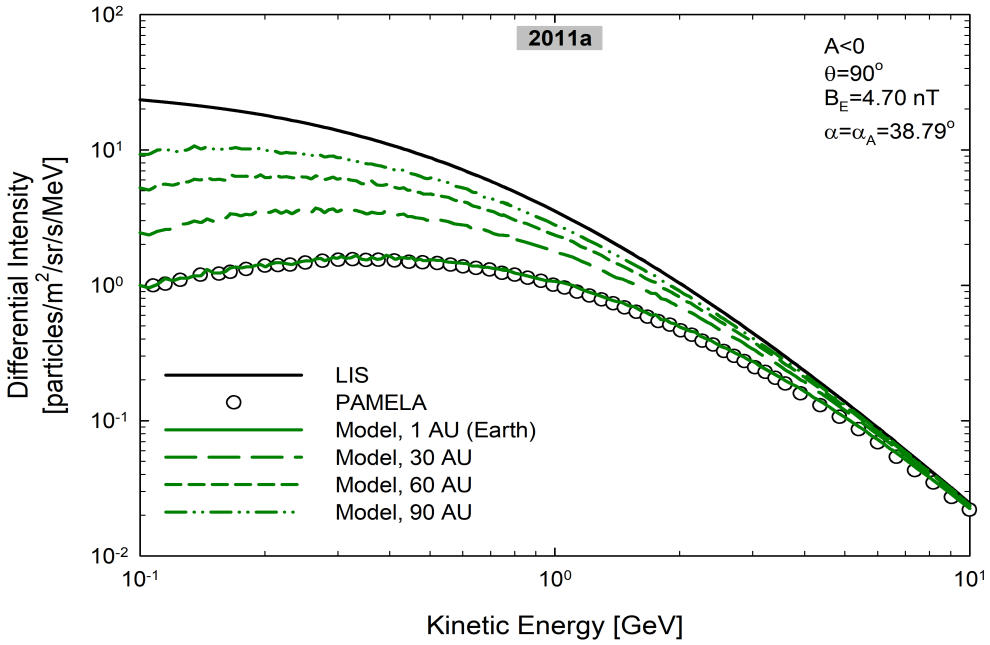


Fig. 3.14 *Similar to Figures 3.12 and 3.13, but for the 2011a PAMELA spectra together with model reproductions.*

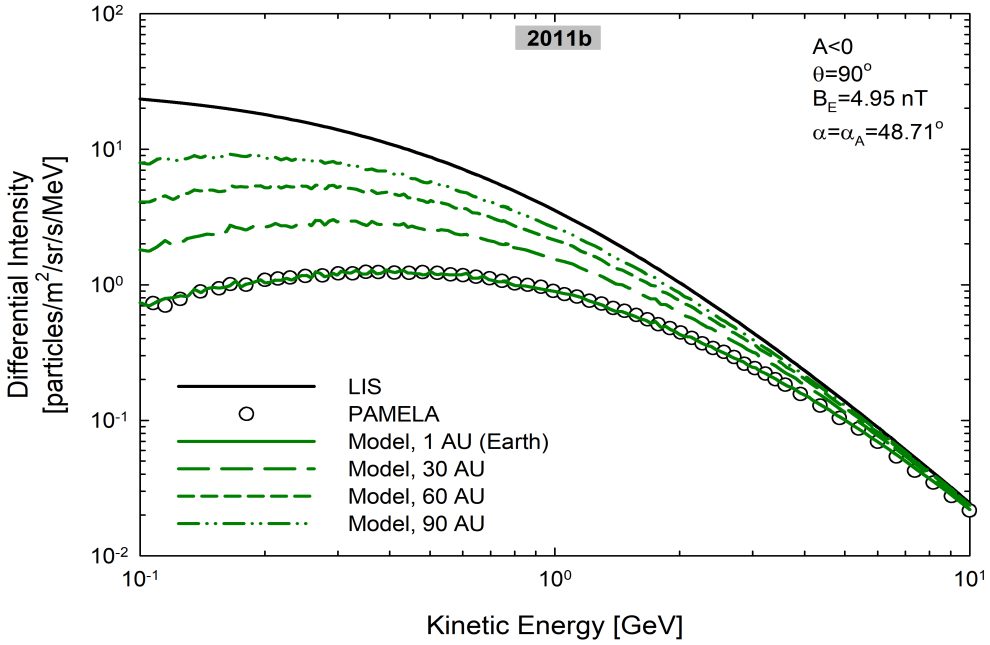


Fig. 3.15 *Similar to Figures 3.12 to 3.14, but for the 2011b PAMELA spectra together with model reproductions.*

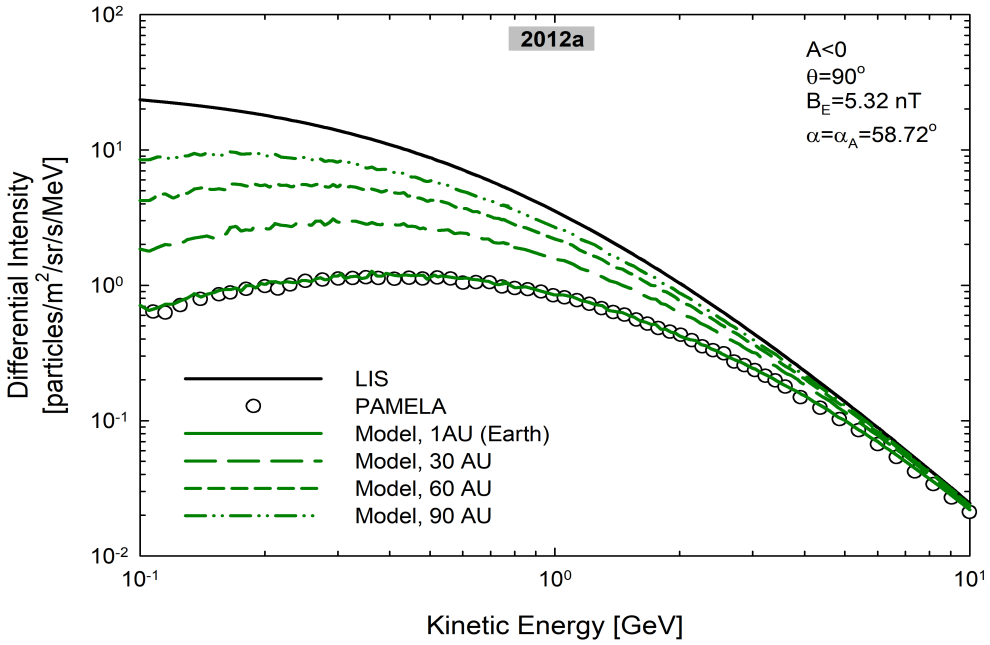


Fig. 3.16 *Similar to Figures 3.12 to 3.15, but for the 2012a PAMELA spectra together with model reproductions.*

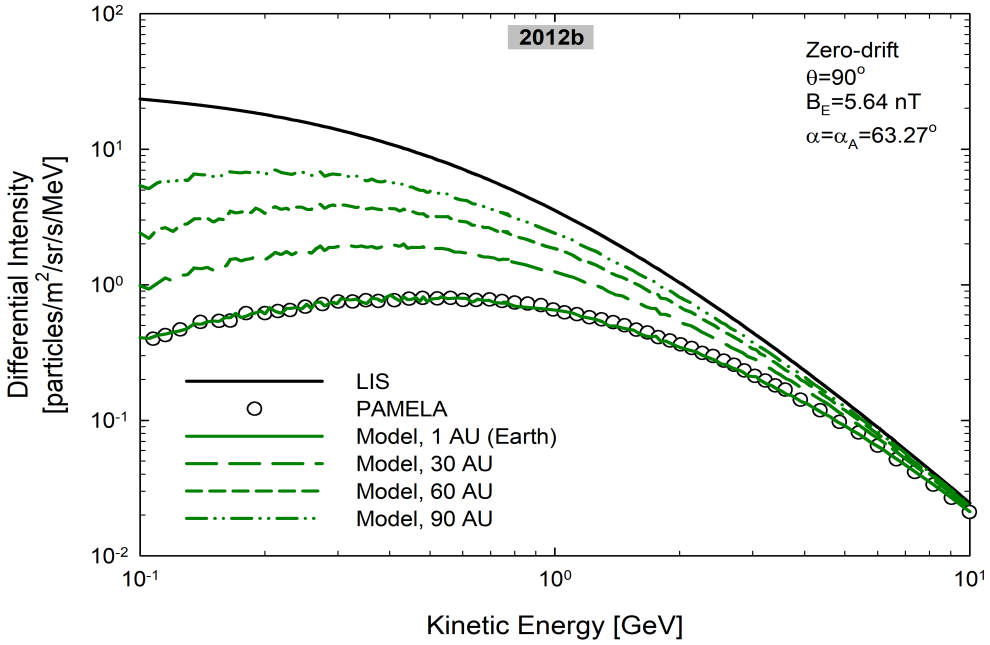


Fig. 3.17 *Similar to Figures 3.12 to 3.16, but for the 2012b PAMELA spectra together with model reproductions. Drifts were assumed to be zero.*

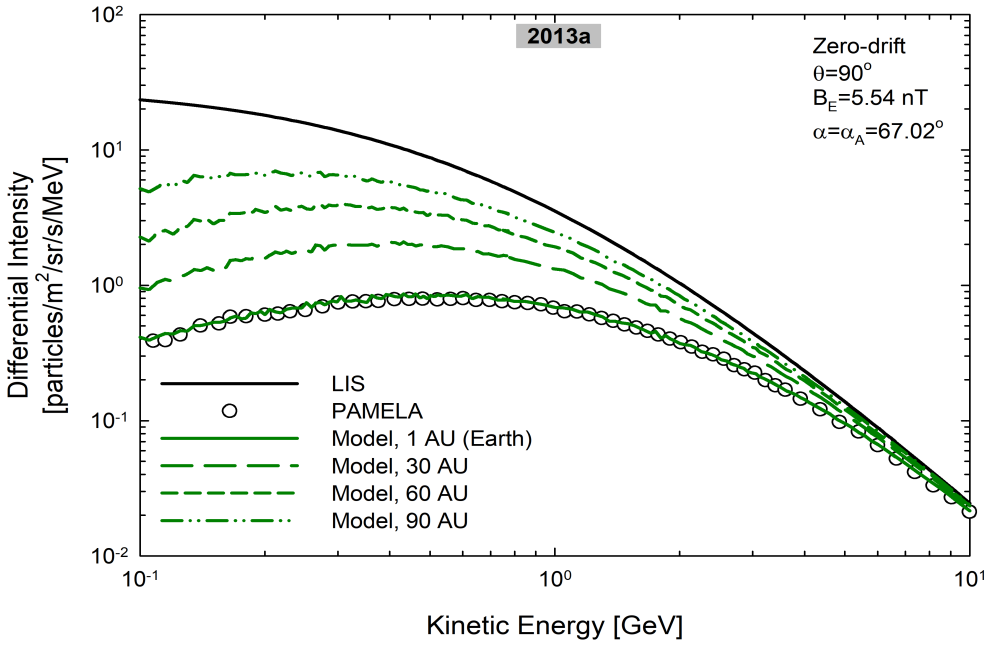


Fig. 3.18 *Similar to Figure 3.17, but for the 2013a PAMELA spectra together with model reproductions.*

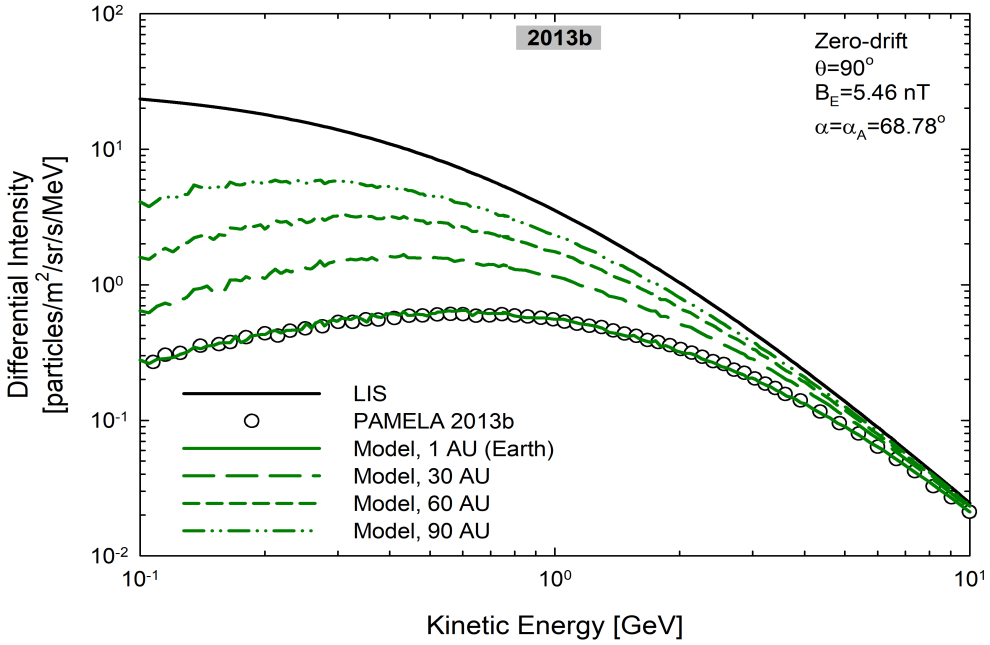


Fig. 3.19 *Similar to Figures 3.17 and 3.18, but for the 2013b PAMELA spectra together with model reproductions.*

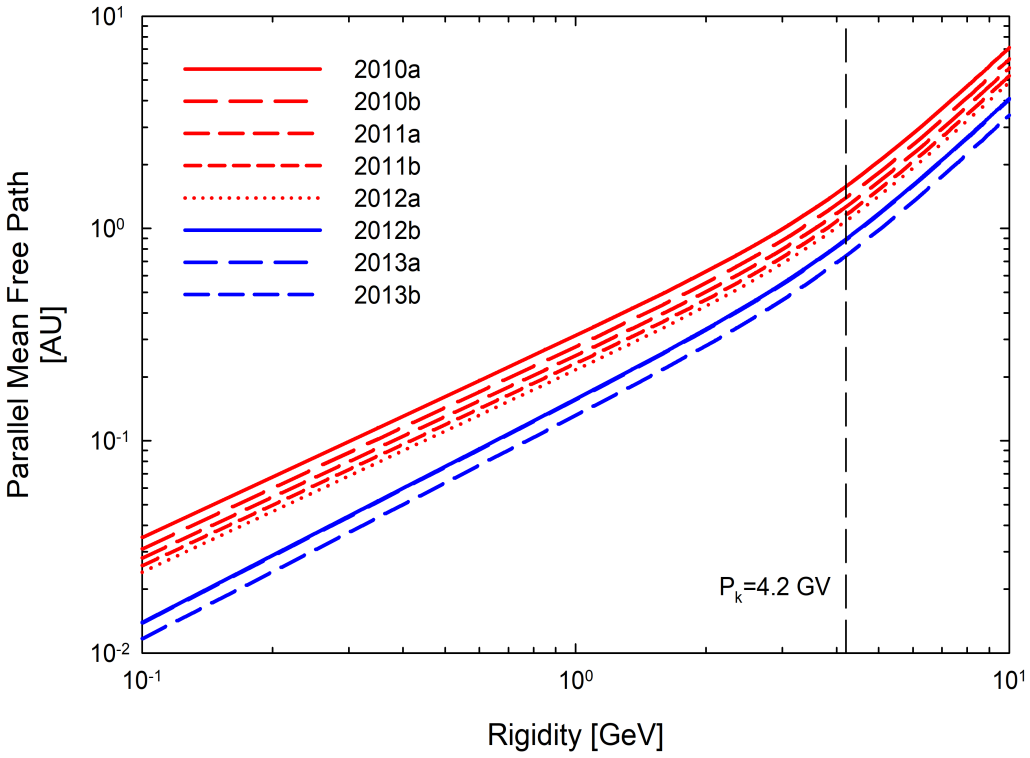


Fig. 3.20 *The evolution of the parallel MFP rigidity profile during 2010a to 2012a (red lines) and during 2012b to 2013b (blue lines). The vertical line is drawn at* $P_{\rm k} = 4.2$ *GV where* $P_{\rm k}$ *is as given in Equation (2.45). The parameter values for each of these profiles are as given in Table 3.3.*

3.5.3 Numerically Reproduced Spectra: Discussion

From Figures 3.11 and 3.12 it is clear that the model computes negligible modulation above ∼10 GeV and that, below ∼10 GeV, computed intensities drop below the LIS where the modulated spectra deviate from the -2.7 spectral index; this result is similar to results obtained by Strauss and Potgieter [2014*b*] where modulation was indicated to be negligible above ∼30 GeV. The computed spectra at Earth give compatible reproductions of the PAMELA observations at all energies. In all cases, the spectra peak at a certain energy $E_{\rm peak}$ with intensity $I_{\rm peak}$, after which they bend into the characteristic adiabatic slope. In the discussion that follows, references to $I_{\rm peak}$ and $E_{\rm peak}$ pertain to Table 3.4, while Table 3.5 should be consulted when mention of intensities at 100 MeV, i.e. I_{100}, is made. Throughout the rest of this chapter, $I_{\rm peak}$, $E_{\rm peak}$ and I_{100} refer to the model computed values.

Figure 3.12 shows the $A < 0$ spectrum for 2010a, using only $\alpha_{\rm A}$, and with the focus on energies between 100 MeV and 10 GeV. The peak in intensity was $I_{\rm peak}(2010{\rm a}) \approx 2.36$, in units of particles/m^2/s/sr/MeV at around $E_{\rm peak}(2010{\rm a}) \approx 332$ MeV. In the remainder of this chapter, whenever the value of intensity is referred to, the units are assumed to be as

given above; these units are therefore not indicated in the text to follow. At Earth, the intensity at 100 MeV was $I_{100}(2010a) \approx 1.56$. From Table 3.3, the value of the magnetic field magnitude at Earth was $B_E = 4.15$ nT and the average tilt angle was $\alpha_A = 18.65°$. The values of $\kappa_{||,0}$ and a required in the model to obtain the 2010a reproduction were $\kappa_{||,0} = 19.60$ and $a = 0.95$.

Using the smaller tilt angle of the Radial model, $\alpha_R = 11.76°$ required a lower diffusion $\kappa_{||,0} = 18.90$ (not indicated in Table 3.3); the value of $a = 0.95$ was unchanged. Because the tilt angle was now smaller, the extent or waviness of the HCS was smaller so that it would disrupt the inward contribution from the diffusion of protons to a lesser extent so that intensities would increase if the value of $\kappa_{||,0}$ was left unchanged. Therefore, to obtain the same intensities with the model, the value of $\kappa_{||,0}$ must decrease. Note that the inward contribution from diffusion is henceforth referred to as 'inward diffusion'; the diffusive process, however, has no preferred direction.

When using the larger tilt angle of the Classic model, $\alpha_C = 25.42°$, diffusion had to be increased to $\kappa_{||,0} = 20.00$ (not listed in Table 3.3); the value of a was still fixed at 0.95. A larger tilt angle means a larger HCS extent which would disrupt inward diffusion to a larger extent so that intensities would decrease if the value of $\kappa_{||,0}$ was left unchanged; in order to still reproduce the spectrum, the value of $\kappa_{||,0}$ in the model must increase.

In this way, the HCS extent does have an effect on the diffusive process even though the diffusion coefficients defined by Equations (2.45) and (2.46) to (2.50) are not explicit functions of α. This explanation also serves as a clear indication that the scenario is dominated by diffusion over drift, since - if it were drift dominated - intensities would increase with an expanding HCS: as the HCS grows it would pick up more and more particles and drift them inward to increase intensities at Earth.

For the 2010b to 2013b spectra, only the average tilt angle α_A is considered, since the effect of a difference in tilt angle, as computed by the Radial and Classic models, was illustrated sufficiently in the above paragraphs, i.e. in the case for 2010a. The dependence of intensity on the tilt angle, at various levels of solar activity, is considered in more detail in Chapters 4 and 5.

The $A < 0$ 2010b spectrum, i.e. averaged over the period starting on the 1st of July 2010 and ending on the 31st of December 2010, is shown in Figure 3.13. The peak in intensity now shifted to $E_{peak}(2010b) \approx 362$ MeV, where intensities reached levels of $I_{peak}(2010b) \approx 1.96$; this is 83% of the value at the peak of 2010a, i.e. $I_{peak}(2010a)$. At Earth, I_{100} decreased to $I_{100}(2010b) = 1.20$, which is 77% of the corresponding intensity in 2010a, $I_{100}(2010a)$. The $I_{100}(2010b)$ intensity at Earth was therefore clearly lower than that of 2010a.

Table 3.3 This table shows the tilt angle values for the Radial and Classic models (α_{R} and α_{C} respectively) as well as the average tilt angle α_{A}. It also shows the values of B_{E} for each of the half-yearly averaged spectra. The last two lines show the parameters that were obtained for the model reproductions of each of the spectra, i.e. $\kappa_{||,0}$ and a, assuming only α_{A}. Note that the values of the parameters which are not shown in the table, are b=1.95, c=3.00, d=3.00, $P_{A,0} = 0.16$ GV, and $P_{\mathrm{k}} = 4.2$ GV as they occur in Equations (2.32), (2.45) and (2.46) to (2.50).

	$A < 0$					zero-drift		
Parameter	**2010a**	**2010b**	**2011a**	**2011b**	**2012a**	**2012b**	**2013a**	**2013b**
α_{R} [deg]	11.76	18.93	31.73	41.41	53.94	56.91	64.64	66.85
α_{C} [deg]	25.42	32.55	45.62	55.41	64.00	68.78	69.51	70.70
α_{A} [deg]	18.65	25.71	38.79	48.71	58.72	63.27	67.02	68.78
B_{E} [nT]	4.15	4.36	4.70	4.95	5.32	5.64	5.54	5.46
$\kappa_{||,0}$ [1×10^{22} cm^2/s]	19.60	18.20	17.80	17.20	17.20	12.05	11.70	9.75
a	0.95	0.95	0.95	0.95	0.95	1.05	1.05	1.05

Table 3.4 Shift in the energy E_{peak} (MeV) at which the maximum intensity I_{peak} (particles/m^2/s/sr/MeV) occurs and the value of I_{peak} at E_{peak}. The ratio of each value of I_{peak} relative to the preceding value is given in the third line.

	2010a	**2010b**	**2011a**	**2011b**	**2012a**	**2012b**	**2013a**	**2013b**
E_{peak}	332	362	332	392	392	402	392	592
I_{peak}	2.36	1.96	1.67	1.28	1.23	0.84	0.86	0.65
I_{peak} ratio	N/A	0.83	0.85	0.77	0.96	0.68	1.02	0.76

Table 3.5 The 100 MeV intensity I_{100} of each of the spectra 2010b to 2013b as ratio of I_{100} for the preceding spectrum; indicated at 1 AU.

	2010b	**2011a**	**2011b**	**2012a**	**2012b**	**2013a**	**2013b**
1 AU	0.77	0.83	0.74	0.96	0.58	1.00	0.68

From 2010a to 2010b, the HMF magnitude at Earth increased by 0.21 nT, changing from $B_{\rm E} = 4.15$ nT to $B_{\rm E} = 4.36$ nT. The average HCS tilt angle increased by 7.06° from its values for 2010a, so that $\alpha_{\rm A} = 25.71°$. With a larger magnetic field, while employing a diffusion coefficient scaling as $1/B$, as well as a larger tilt angle, the value of $\kappa_{||,0}$ would have to increase to maintain the same intensities as in 2010a. However, the intensities shown by the 2010b data are lower to such an extent that the diffusion had to be decreased from its value in 2010a to $\kappa_{||,0} = 18.20$ in 2010b; the value of $a = 0.95$ was unchanged.

The $A < 0$ 2011a spectrum, i.e. averaged over the period starting on the 1st of January 2011 and ending on the 30th of June 2011, is shown in Figure 3.14. The peak in intensity now shifted back to $E_{\rm peak}(2011{\rm a}) \approx 332$ MeV, where intensities reached levels of $I_{\rm peak}(2011{\rm a}) \approx 1.67$; this corresponds to 85% of the intensity at the peak of 2010b, $I_{\rm peak}(2010{\rm b})$. At Earth and at 100 MeV, the intensity decreased to $I_{100}(2011{\rm a}) \approx 1.00$, which is at about 83% of $I_{100}(2010{\rm b})$. The $I_{100}(2011{\rm a})$ intensity at Earth was therefore notably lower than that of 2010b, $I_{100}(2010{\rm b})$.

From 2010b to 2011a, the HMF magnitude at Earth increased by 0.34 nT, changing from $B_{\rm E} = 4.36$ nT to $B_{\rm E} = 4.70$ nT. The average HCS tilt angle increased by 13.08° from its value in 2010b, so that $\alpha_{\rm A} = 38.79°$ in 2011a. With a larger magnetic field, as well as a larger tilt angle, the value of $\kappa_{||,0}$ would have to increase in order to maintain the same intensities as in 2010b. However, intensities shown by the 2011a data are lower to such an extent that the diffusion had to be decreased to $\kappa_{||,0} = 17.80$, still using $a = 0.95$.

The $A < 0$ 2011b spectrum, i.e. averaged over the period starting on the 1st of July 2011 and ending on the 31st of December 2011, is shown in Figure 3.15. The peak in the intensity now shifted to $E_{\rm peak}(2011{\rm b}) = 392$ MeV where intensities reached levels of $I_{\rm peak}(2011{\rm b}) \approx 1.28$; this is 77% of $I_{\rm peak}(2011{\rm a})$. At Earth, I_{100} decreased to $I_{100}(2011{\rm b}) = 0.74$, which is 74% of $I_{100}(2011{\rm a})$. The intensity $I_{100}(2011{\rm b})$ at Earth was therefore markedly lower than that of 2011a.

The HMF magnitude at Earth $B_{\rm E}$ increased by 0.25 nT from $B_{\rm E} = 4.70$ nT to $B_{\rm E} = 4.95$ nT for 2011b, while the average tilt angle increased by 9.92° from $\alpha_{\rm A} = 38.79°$ in 2011a to $\alpha_{\rm A} = 48.71°$ in 2011b. To match significantly lower intensities in the data, the value of $\kappa_{||,0}$ had to be decreased to $\kappa_{||,0} = 17.20$ in 2011b; the rigidity dependence remained fixed at $a = 0.95$.

The $A < 0$ 2012a spectrum, i.e. averaged over the period starting on the 1st of January 2012 and ending on the 30th of June 2012, is shown in Figure 3.16. The peak in the intensity remained at $E_{\rm peak}(2012{\rm a}) \approx 392$ MeV, where intensities reached levels of $I_{\rm peak}(2012{\rm a}) \approx 1.23$; this is almost identical to the intensity at the peak of 2011b,

being about 96% of $I_{\text{peak}}(2011\text{b})$. At Earth, and at 100 MeV, the intensity dropped to $I_{100}(2012\text{a}) = 0.71$, which is about 96% of $I_{100}(2011\text{b})$, so that the decrease was less significant than in the previous cases.

The intensities at $I_{\text{peak}}(2011\text{b})$ and $I_{\text{peak}}(2012\text{a})$ were almost identical with the latter being only about 4% lower; the spectra at Earth show that the intensity at 100 MeV had decreased by the same amount from 2011b to 2012a. The intensity had only decreased very slightly, but the value of B_{E} showed an increase by an amount of 0.37 nT from 4.95 nT to 5.32 nT. If the model was to reproduce the same intensities in 2012a as in 2011b, the value of $\kappa_{||,0}$ would have to be increased. The data was, however, slightly lower and this could be reproduced using the same value of $\kappa_{||,0} = 17.20$. The value of $a = 0.95$ was still unchanged.

The zero-drift 2012b spectrum, i.e. averaged over the period starting on the 1st of July 2012 and ending on the 31st of December 2012, is shown in Figure 3.17. The peak in the intensity shifted to $E_{\text{peak}}(2012\text{b}) \approx 402$ MeV, where intensities were at levels of $I_{\text{peak}}(2012\text{b}) \approx 0.84$; this is about 68% of the intensity at the peak of 2012a. At Earth, and at 100 MeV, the intensity dropped to $I_{100}(2012\text{b}) \approx 0.41$, which is 58% of $I_{100}(2012\text{a})$. It is clear, from the data, that intensities in 2012b have decreased from those in 2012a and, as such, the diffusion coefficient had to be decreased to $\kappa_{||,0} = 12.05$. In addition to the decrease in the magnitude of the diffusion coefficient, the rigidity dependence below $P_{\text{k}} = 4.2$ GV had to be changed as well so that $a = 1.05$. The larger $B_{\text{E}} = 5.64$ nT (an increase of 0.32 nT) and slightly larger $\alpha = 63.27°$ (an increase of only 4.55°) together with the switch in solar magnetic polarity from $A < 0$ to zero-drift were evidently not enough to account for the difference in modulation without introducing these additional changes in the diffusion coefficient.

The zero-drift 2013a spectrum, i.e. averaged over the period starting on the 1st of January 2013 and ending on the 30th of June 2013, is shown in Figure 3.18. The peak in the intensity was at $E_{\text{peak}}(2013\text{a}) \approx 392$ MeV, where intensities were at levels of $I_{\text{peak}}(2013\text{a}) \approx 0.86$; this is 102% of $I_{\text{peak}}(2012\text{b})$ and, taking into account the uncertainties in the model solutions, these intensities are essentially identical. At Earth, and at 100 MeV, the intensity was also identical and remained at $I_{100}(2013\text{a}) \approx 0.41$. Therefore, the differences in the 2012b and 2013a intensities at Earth were clearly minor and it is a good approximation to say that intensities remained the same. However, $B_{\text{E}} = 5.54$ had decreased by 0.10 nT and $\alpha = 67.02°$ had only slightly increased. For intensities to remain the same, the lower B_{E} would require a smaller $\kappa_{||,0}$ and this value is found to be $\kappa_{||,0} = 11.70$; the rigidity dependence remained fixed at $a = 1.05$.

The zero-drift 2013b spectrum, i.e. averaged over the period starting on the 1st of June 2013 and ending on the 31st of December 2013, is shown in Figure 3.19. The peak in the intensity now shifted to $E_{\text{peak}}(2013\text{b}) \approx 592$ MeV, where intensities were at levels of $I_{\text{peak}}(2013\text{b}) \approx 0.65$; this is about 76% of $I_{\text{peak}}(2013\text{a})$. At Earth, I_{100} decreased to $I_{100}(2013\text{b}) \approx 0.28$, which was 68% of $I_{100}(2013\text{a})$. Therefore, differences in the 2013b

and 2013a intensities at Earth were clearly evident. The differences in both B_{E} and α were small, with the first decreasing by only 0.08 nT to $B_{\mathrm{E}} = 5.46$ nT and the latter increasing by less than 2.00° to $\alpha = 68.78°$. If the model were to produce intensities on the same level as in 2013a, $\kappa_{||,0}$ would have to decrease; now, however, the PAMELA data was significantly lower and therefore $\kappa_{||,0}$ had to be even smaller so that $\kappa_{||,0} = 9.75$ with $a = 1.05$ yielded a good reproduction.

Figure 3.20 presents a graphic summary of the evolution of the parallel MFP (and thus of the diffusion coefficients through Equation (2.43)) that was required to reproduce the 2010a to 2013b PAMELA proton spectra. It showed a diffusion coefficient (or MFP) systematically decreasing from $\kappa_{||,0} = 19.60$ to $\kappa_{||,0} = 9.75$, as well as a change in the rigidity dependence below $P_{\mathrm{k}} = 4.2$ GV from $P^{0.95}$ to $P^{1.05}$. The change in rigidity dependence coincided with the switch from an $A < 0$ polarity cycle to the zero-drift scenario, i.e. where the MFP profiles switch from red to blue lines at 2012b.

3.6 Summary

Chapter 3 presented an investigation of the solar modulation of galactic protons during the time period January 2010 (solar minimum) to January 2014 (solar maximum). The chapter started off with a discussion of the local interstellar spectrum (LIS) for galactic protons in Section 3.2. This is an important aspect of modulation studies, since the LIS is used as primary input or boundary condition in most numerical modulation models. The proton LIS used in this work was given by Equation (3.1) and was illustrated in Figure 3.1 together with some earlier estimations.

The proton data from PAMELA was presented in Figure 3.2 of Section 3.3; these spectra were averaged over one Carrington Rotation. The modulation over time was illustrated in more detail in Figure 3.3, showing the ratios of each spectrum with respect to the January 2010 spectrum. It was clear that intensities decreased from January 2010 to 2014 as solar activity progressed from minimum to maximum conditions. The Carrington Rotation numbers (CRNs) corresponding to January of each year were indicated in Table 3.1. The focus of this section was on the overall modulation over the entire period and, as such, the spectra of January 2010 and 2014 were shown together with their model reproductions in Figure 3.4; some of these results were also presented in Martucci et al. [2018]. It was shown that the model could reproduce these spectra well and the parameter values required to obtain these reproductions were indicated in Table 3.2. It was an important conclusion that the difference in the modulation between the January 2010 and 2014 spectra could not be accounted for by merely changing the values of the magnetic field magnitude and the tilt angle, i.e. additional changes in the magnitude of the diffusion coefficient as well as its rigidity dependence were necessary; this was illustrated further in Figure 3.5.

In order to investigate solar modulation in between January 2010 and January 2014, Section 3.4 considered the solar activity or conditions during this time period. The three panels of Figure 3.6 showed the evolution of Solar Cycle 24 from solar minimum conditions in January 2010 to solar maximum conditions in January 2014. The top, middle and bottom panels showed the evolution of the tilt angle α, magnetic field magnitude at Earth B_{E}, and neutron monitor count rate respectively. An important aspect of this section is that it was not exactly clear when (or whether) the switch in solar polarity cycle, i.e. from an $A < 0$ to an $A > 0$ cycle, had occurred and that a 'transition period' was therefore defined in which drifts were assumed to be zero; this is illustrated in Figure 3.7. It was also noted that if similarly defined transition periods were defined for earlier solar cycles, they would be shorter in duration.

In Section 3.5.1 a number of eight half-yearly averaged spectra were calculated from the PAMELA proton data and shown in Figure 3.8. These were calculated for the first and second halves of each of the years 2010 to 2013, i.e. January 1st to June 30th and July 1st to December 31st respectively. The spectra thus obtained were denoted by the year number followed by an 'a' or 'b' for the first and second halves respectively so that the first and last spectra were denoted 2010a and 2013b, respectively. In order to numerically reproduce the eight spectra, 15-month averaged values for α and B_{E} were calculated for each spectrum; the procedure for these calculations was illustrated in Figures 3.9 and 3.10. These average values were listed in Table 3.3.

In Sections 3.5.2 and 3.5.3 the average values of α and B_{E} that were calculated in Section 3.5.1 were incorporated into the numerical model after which the half-yearly averaged spectra 2010a to 2013b were reproduced by obtaining suitable values for the transport coefficients. These values were listed in Table 3.3 and the numerical reproductions of the spectra, together with the PAMELA data were shown in Figures 3.11 to 3.19. Table 3.3 showed that the diffusion coefficient had to be decreased systematically from solar minimum conditions in 2010a to maximum conditions in 2013b. The rigidity dependence of this coefficient below 4.2 GV also had to be adjusted for the last three of the spectra, i.e. 2012b, 2013a and 2013b; these three spectra assumed zero drift conditions because of the uncertainty as to the actual status of the polarity cycle during this time. It was once again pointed out that to merely change α and B_{E} as function of solar activity was not enough to account for the difference in modulation between the successive half-yearly averaged spectra. In Figure 3.20 the evolution of the diffusion coefficient required to reproduce these spectra was illustrated in terms of the rigidity profiles of the parallel mean free path (MFP) for each of the 2010a to 2013b spectra.

The results listed in Table 3.4 showed, on a qualitative level, that the energy E_{peak} at which the peak in intensity I_{peak} had occured shifted from lower to higher values as the solar cycle progressed from minimum to maximum conditions. It also showed that the decreases in the intensity I_{peak} from one spectrum to the next were significant for all but two of the spectra, these being the 2012a and 2013a cases. Table 3.5 showed that

intensities I_{100} around 100 MeV at 1 AU indicated similar significant decreases in all but the mentioned two cases.

Chapter 4

The Properties of Drifts and its Effect on Cosmic Rays in the Heliosphere

4.1 Introduction

The scaling down of drift effects towards solar maximum conditions forms the central topic of this chapter. As indicated before, if realistic charge-sign dependent modulation is to be computed at extreme solar maximum conditions, drifts need to be scaled down even to zero at such levels of solar activity (Ferreira [2002], Ndiitwani et al. [2005]). To accommodate this reduction in drift, a function is introduced in the model to scale down drift as function of increasing tilt angle. This approach is purely phenomenological and the proposed function together with its effect on modulation are illustrated and discussed. The reproductions of the PAMELA proton data (Martucci et al. [2018]) that were obtained in Chapter 3 are reconsidered so that a new set of parameters is obtained to account for the additional scaling down of drifts towards solar maximum. A large part of this chapter is also devoted to a discussion of the drift properties of the model. The illustrative capabilities of models based on the stochastic differential equation (SDE) approach provide much advantage to understanding physical modulation processes (e.g. Strauss and Effenberger [2017]) and, in this chapter, such capabilities are exploited to yield some valuable insights into the mechanisms of modulation and drifts in particular. Different ways in which drifts can be scaled down, as well as the energy dependence of drift effects, are illustrated and discussed.

4.2 Cosmic Ray Drift over a Solar Cycle

This section considers computed proton intensities as function of increasing solar activity without any scaling down of drifts as explicit function of the tilt angle α, i.e. for similar

conditions under which the results presented in Chapter 3 were produced. The changes that do occur in intensity as α is increased are rather a consequence of the expanding/increasing neutral heliospheric current sheet (HCS), as was explained in Chapter 3 and will be explained further below.

Drift effects in computed cosmic ray (CR) intensities can be studied effectively through model generated profiles of intensity versus tilt angle. Such profiles are shown in the top panel of Figure 4.1 for 500 MeV protons during the zero-drift scenario (green line) and during both the $A > 0$ (red line) and $A < 0$ (blue line) polarity cycles. The values of all modulation parameters, including $\kappa_{||,0}$ in Equation (2.45) and the magnitude of the HMF at Earth B_{E}, were chosen so as to be of the same order of magnitude as those obtained for the spectra reproductions in Chapter 3; $\kappa_{\mathrm{A},0} = 1.0$ in Equation (2.32). Since the average tilt angles, calculated in Chapter 3, are all larger than about 12.00°, a lower value of $\alpha = 10.00°$ was selected for these illustrations. The interest is mainly on the behaviour of the profile towards solar maximum conditions and $\alpha = 75°$ was selected to represent extreme solar maximum, since neither the Radial nor the Classic models for tilt angles calculate values $\alpha > 75°$ (see Chapter 3). At $\alpha = 75°$, solar maximum conditions are assumed to be present over the whole heliosphere.

For the explanation of Figure 4.1, the $A > 0$ and $A < 0$ solutions are each considered relative to the zero-drift solution. The reason why the zero-drift solution is chosen as reference is the following: when drift effects decrease, it cannot be readily deduced whether intensities will increase or decrease in response (at any given position in the heliosphere), but what is readily apparent is that both the $A > 0$ and $A < 0$ solutions must approach the zero-drift solution - this can either mean an increase or a decrease in intensities, depending on the parameters assumed in the model. Figure 4.1 then gives information as to whether the intensity has to increase/decrease at Earth in order to approach the zero-drift solution.

In Figure 4.1, the $A > 0$ solution starts off higher than the zero-drift solution. This can be understood through the following explanation. When $A > 0$ drift is switched on in the model, protons drift inward over the polar regions and out along the HCS in the equatorial regions. There is now easy access over the polar regions because, in these regions, particles both drift inward as well as experience diffusion more effectively towards the inner heliosphere. This more effective status of diffusion in the polar regions can be understood by considering that parallel diffusion is much larger than perpendicular diffusion $\kappa_{||} \gg \kappa_{\perp}$, according to Equation (2.46). Over the polar regions, there are mainly open magnetic filed lines and $\kappa_{||}$ is very effective in diffusing particles towards the inner heliosphere; in the equatorial regions, on the other hand, the geometry of the field does not allow for $\kappa_{||}$ to be as effective; rather, $\kappa_{\perp}$ will now play a more important role, but $\kappa_{\perp} \ll \kappa_{||}$. Furthermore, in the equatorial regions, diffusion inward will be opposed by the outward drift, so that diffusion is even more effective in tranporting protons inward over the polar regions as compared to the equatorial regions. Therefore, the $A > 0$ solution is higher than the zero-drift solution at all values of α.

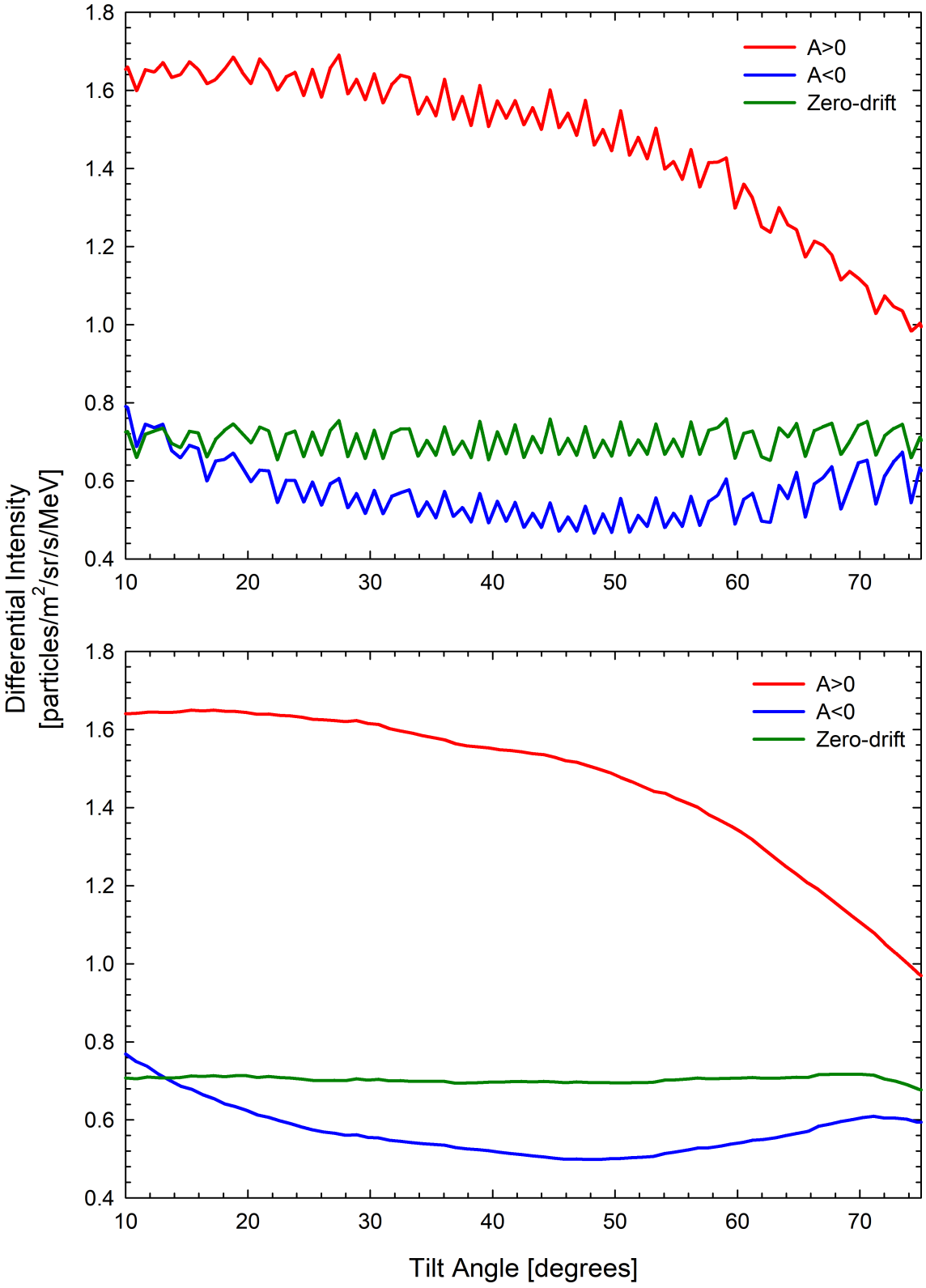


Fig. 4.1 *Computed intensity versus tilt angle profiles at Earth for 500 MeV protons during the $A > 0$ polarity cycle (red curve), the $A < 0$ polarity cycle (blue curve), and the zero-drift scenario (green curve) with $\kappa_{A,0} = 1.0$ in Equation (2.32). The top and bottom panels show the unsmoothed and smoothed solutions, respectively.*

The $A > 0$ solution initially does not respond significantly to an increase in α and remains at a more or less constant level above the zero-drift solution. This is because, during the $A > 0$ polarity cycle, intensities are strongly influenced by inward drift over the polar regions and consequently a change in α (while α is still small and occurs in the equatorial regions) will not affect the polar regions. However, at $\alpha \gtrsim 20°$, the $A > 0$ solution does start to decrease as a function of increasing α. To understand this, note that an increase in α will render the global drift pattern (see Chapter 2) less effective because more particles are scattered off the HCS so that less particles can drift outwards. This therefore results in a reduced global drift pattern, i.e. the drift pattern is interrupted to such an extent that the $A > 0$ solution has to approach the zero-drift solution, i.e. at Earth it has to decrease. As the HCS enters progressively higher latitudinal regions, this disruption of the global drift pattern gets increasingly pronounced, because the HCS now starts directly affecting inward diffusion and drifts over the polar regions, and $A > 0$ intensities keep on decreasing towards the zero-drift solution.

The $A < 0$ solution, on the other hand, reacts immediately to an increase in the value of α. When $A < 0$ drift is switched on in the model, protons drift in along the current sheet to increase intensities above the zero-drift levels. It does so, however, only at smaller values of α where the extent of the HCS is small. When the HCS is this small, protons flow in very effectively by means of diffusion over the polar regions and by means of drifts along the HCS in the equatorial regions to increase the intensities. However, at a relatively small value of $\alpha \approx 14°$, the effect of $A < 0$ drift is to reduce proton intensities below that of the zero-drift solution: the larger HCS is not as effective in drifting particles inward because particles are now scattered off it by diffusion before it can reach Earth; the inward diffusion is rendered less effective by outward drift in the polar regions so that the intensities are below the zero-drift level. Intensities then keep on decreasing up to about $\alpha \approx 50°$ where it starts increasing with any further increase in α because it has to approach the zero-drift solution when the HCS starts entering into the higher latitudinal regions to disrupt the global drift pattern, reducing drift effects.

The bottom panel of Figure 4.1 shows the smoothed versions of the solutions in the top panel. It is clear that these profiles sketch the same qualitative picture as the unsmoothed solutions and, in the rest of this chapter, profiles of intensity versus tilt angle are smoothed likewise. The very slight downward trend of the zero-drift solution at the highest values of α is insignificant and ascribed to restrictions imposed by the numerical model, as it is clear that the zero-drift solution has to stay constant with α. Likewise, nothing can be made of the slight decrease in the $A < 0$ solution at these large α.

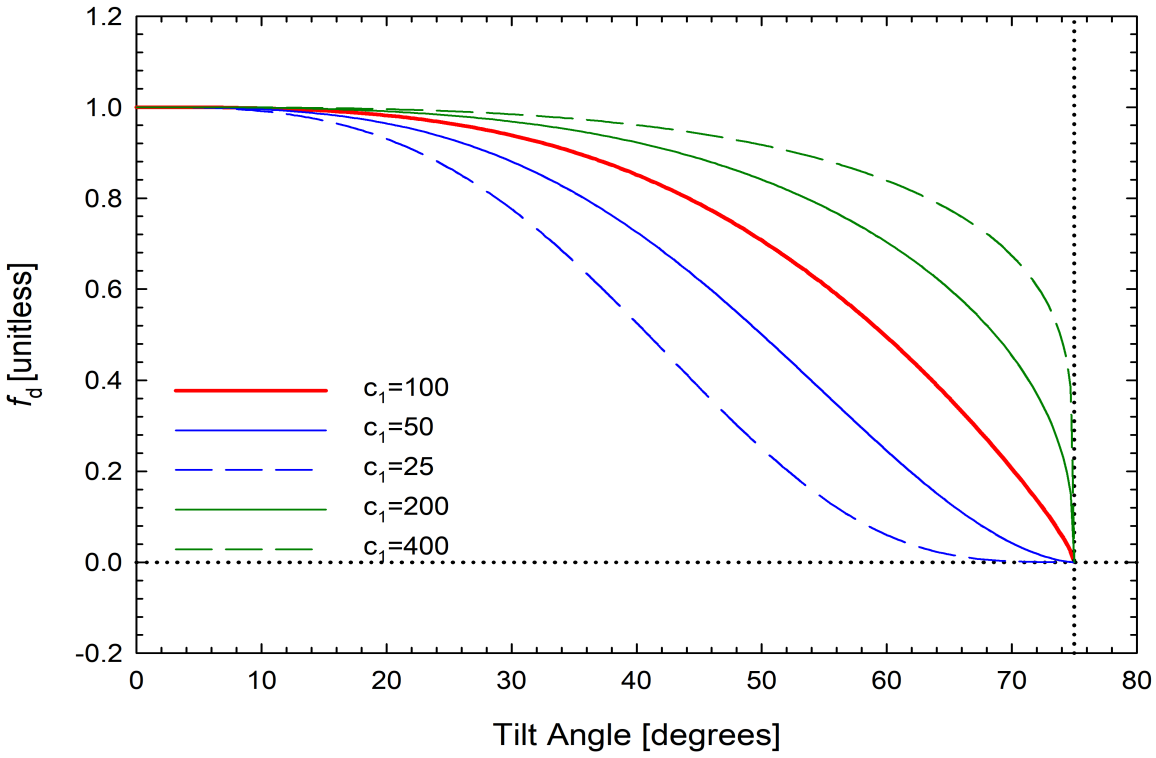


Fig. 4.2 *The drift scaling function* $f_{\mathrm{d}}(\alpha)$ *is shown for different values of the constant* c_1 *in Equation (4.1). The red curve shows the function as used in this study, i.e. with* $c_1 = 100$. *The solid and dashed blue curves show* $f_{\mathrm{d}}(\alpha)$ *for two successively lower values* $c_1 = 50$ *and* $c_1 = 25$, *while the green solid and dashed curves do so for two successively higher values* $c_1 = 200$ *and* $c_1 = 400$ *respectively.*

.

4.3 The Drift Scaling Function

In Chapter 2, it was explained that drifts are reduced in the presence of turbulence. It was emphasised that the exact form of this suppression is not yet known. Earlier phenomenological studies in which the scaling down of drifts towards solar maximum was accounted for include Ferreira [2002], Ferreira and Potgieter [2004], Ndiitwani et al. [2005]; see also Potgieter et al. [2001], Manuel et al. [2011] and Siluszyk et al. [2011]. The solar cycle dependence of heliospheric transport parameters, including drifts, was also disussed by Nel [2015].

In this study, a simple function is introduced with the aim of reducing drifts towards solar maximum so that it scales down drifts to zero at $\alpha = 75°$. The function is defined in terms of the tilt angle α by

$$f_{\mathrm{d}}(\alpha) = \left[\cos\left(\frac{\pi}{150}\alpha\right)\right]^{\frac{\alpha}{c_1}}, \tag{4.1}$$

where c_1 is a constant measured in degrees (these units are not indicated in the text to follow). The function $f_d(\alpha)$ does not change the global features of the intensity versus tilt angle profiles for small α, but closes the loop in the $A > 0$ and $A < 0$ intensity versus α solutions at $\alpha = 75°$. The scaling down function is implemented by setting $\kappa_{A,0}$ in Equation (2.32) equal to $\kappa_{A,0} = f_d(\alpha)$.

Figure 4.2 shows the function $f_d(\alpha)$, given by Equation (4.1), for different values of the constant c_1. The red line shows the case for $c_1 = 100$, which is the value for c_1 that is used in this study. The solid and dashed blue curves show $f_d(\alpha)$ upon decreasing the value of c_1 to $c_1 = 50$ and $c_1 = 25$ respectively. The solid and dashed green curves show how $f_d(\alpha)$ is influenced when larger values for c_1 are used, i.e. $c_1 = 200$ and $c_1 = 400$ respectively. The function $f_d(\alpha)$ decreases to zero in all cases to ensure that no drifts are present at solar maximum. For $c_1 = 100$, $f_d(\alpha)$ does not differ significantly from unity up to about $\alpha \approx 20°$ and then decreases steadily to zero at $\alpha = 75°$. Upon increasing the value of c_1 a steeper decrease to zero at $\alpha = 75°$ is found and upon decreasing the value of c_1, $f_d(\alpha)$ can decrease to zero for values $\alpha < 75°$.

Figure 4.3 shows the computed intensity profiles similar to those of Figure 4.1, but with $f_d(\alpha)$ now applied for the different values of c_1. The case where $f_d = 1.0$, i.e. where drift was not scaled down as function of α, is shown as reference by the thick black lines. The thick red lines show the profiles that result from employing $f_d(\alpha)$ as in Equation (4.1) with $c_1 = 100$; these are the profiles that will be of interest further on in this chapter. The form of $f_d(\alpha)$ is clearly visible in these spectra with the profiles not differing significantly from the unmodified case at small tilt angles, but then gradually decreasing with increasing α to close the loop at the intensity levels of the zero-drift solution. Using a larger value of $c_1 = 400$ (green lines), the smoothed loop does not seem to close at $\alpha = 75°$. This is, however, simply because the value of $f_d(75°)$ is not uniquely defined when using such large values of c_1. Using a smaller value of $c_1 = 25$ (blue lines), the loop can be closed even for smaller $\alpha < 75°$.

4.4 PAMELA Proton Spectra

In this section, the 2010 to 2013 PAMELA proton spectra that were reproduced in Chapter 3 are revisited, this time employing the scaling function $f_d(\alpha)$ of Equation (4.1) to scale down drifts towards solar maximum. The same half-yearly averaged spectra are used, i.e. 2010a/b, 2011a/b, 2012a/b and 2013a/b, where "a" and "b" respectively indicate the first and second six-month periods of each year. The results are presented and discussed in two parts: first, considering the 2010a to 2012a spectra which were during an $A < 0$ polarity cycle; second, considering the 2012b to 2013b spectra where both $A < 0$ and $A > 0$ drift were assumed due to the uncertainty of the polarity cycle over this period, as discussed in Chapter 3. Note that the computed spectra and the compatibility with

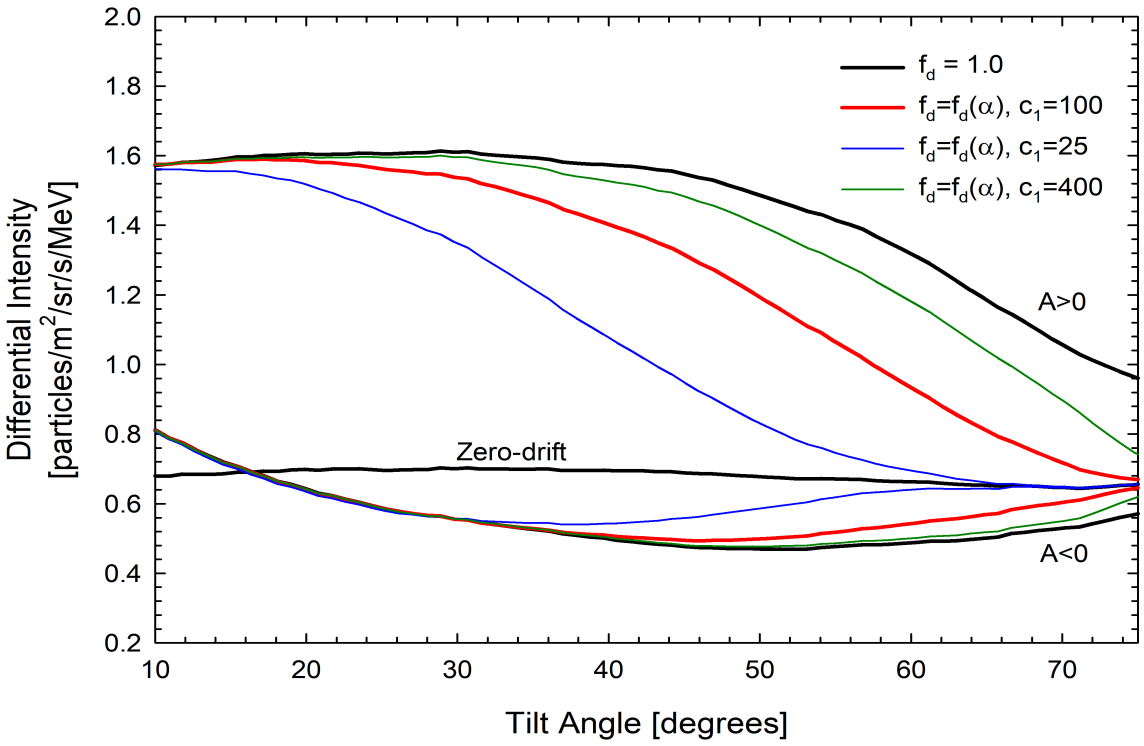


Fig. 4.3 *The effect of the scaling down function $f_{\rm d}(\alpha)$ on computed intensity profiles is illustrated. The thick black lines show the unmodified intensities as reference, while the thick red lines show the scaled down case that will be used in this study, i.e. $c_1 = 100$. The thin blue lines show the case where $c_1 = 25$, while the thin green lines show the case where $c_1 = 400$. For each value of c_1 the higher and lower solutions represent the $A > 0$ and $A < 0$ polarity cycle respetively.*

.

the PAMELA observations were very similar to what was found in Chapter 3 and are therefore not repeated here.

The inclusion of the function $f_{\rm d}(\alpha)$ had an impact on the values of $\kappa_{||,0}$ that were required to reproduce the 2010a to 2012a spectra. These values are indicated in the last row of Table 4.1 and are now denoted by $\left(\kappa_{||,0}\right)_f$. The values of $\kappa_{||,0}$ that were determined in Chapter 3, i.e. for the reproductions without the inclusion of $f_{\rm d}(\alpha)$, are included in the third row of Table 4.1 for reference. The averaged values for the tilt angle $\alpha_{\rm A}$, i.e. averaged between the Radial and Classic models, as well as the magnetic field magnitude at Earth $B_{\rm E}$ are shown in the first and second rows of the table respectively. The values of the parameters not indicated in the table are $a = 0.95$, $b = 1.95$, $c = 3.00$, $d = 3.00$, $P_{A,0} = 0.16$ GV, and $P_{\rm k} = 4.2$ GV as they occur in Equations (2.32), (2.45) and (2.46) to (2.50). These parameters were also unchanged from their values in Chapter 3.

For 2010a to 2011a, with $\alpha_{\rm A}$ varying between 18.65° and 38.79°, the inclusion of $f_{\rm d}(\alpha)$ had no significant effect on model reproductions and the value of $\kappa_{||,0}$ did not have to be modified so that $\left(\kappa_{||,0}\right)_f = \kappa_{||,0}$ in Table 4.1. From Figure 4.2, it is clear that $f_{\rm d}(\alpha)$ had

Table 4.1 This table shows the parameter values that were used for the model reproductions of the 2010a to 2012a PAMELA proton spectra, with and without the inclusion of the scaling down function $f_{\mathrm{d}}(\alpha)$ defined in Equation (4.1). The values for the diffusion coefficient where $f_{\mathrm{d}}(\alpha)$ was not included are indicated by $\kappa_{||,0}$, as in Chapter 3; in the case where $f_{\mathrm{d}}(\alpha)$ was included, the diffusion coefficients are denoted by $\left(\kappa_{||,0}\right)_f$.

	$A<0$				
Parameter	**2010a**	**2010b**	**2011a**	**2011b**	**2012a**
α_{A} [degrees]	18.65	25.71	38.79	48.71	58.72
B_{E} [nT]	4.15	4.36	4.70	4.95	5.32
$\kappa_{\|\|,0}$ $[1\times10^{22}$ cm^2/s]	19.60	18.20	17.80	17.20	17.20
$\left(\kappa_{\|\|,0}\right)_f$ $[1\times10^{22}$ cm^2/s]	19.60	18.20	17.80	16.85	15.70

Table 4.2 This table shows the parameter values that were applicable for the model reproductions of the 2012b to 2013b PAMELA proton spectra, with and without the inclusion of the scaling down function $f_{\mathrm{d}}(\alpha)$ defined in Equation (4.1). The values for the diffusion coefficient where $f_{\mathrm{d}}(\alpha)$ was not included are indicated by $\kappa_{||,0}$, as in Chapter 3; in the case where $f_{\mathrm{d}}(\alpha)$ was included, the diffusion coefficients are denoted by $\left(\kappa_{||,0}\right)_f$.

Parameter	**2012b**	**2013a**	**2013b**
α_A [degrees]	63.27	67.02	68.78
B_{E} [nT]	5.64	5.54	5.46
$\kappa_{\|\|,0}$, zero-drift $[1\times10^{22}$ cm^2/s]	12.05	11.70	9.75
$\left(\kappa_{\|\|,0}\right)_f$, $A<0$ $[1\times10^{22}$ cm^2/s]	13.35	13.00	11.15
$\left(\kappa_{\|\|,0}\right)_f$, $A>0$ $[1\times10^{22}$ cm^2/s]	9.40	10.70	9.30

only decreased slightly from unity at these tilt angles. For 2011b, however, $\alpha_{\mathrm{A}}=48.71°$ and the decrease from unity was sufficiently large to require a change in the magnitude of diffusion so that the value of $\kappa_{||,0}$ had to be modified from $\kappa_{||,0}=17.20$ to $\left(\kappa_{||,0}\right)_f=16.85$ in the case where $f_{\mathrm{d}}(\alpha)$ is included. For 2012a, $f_{\mathrm{d}}(\alpha)$ had decreased even further from unity and required that the diffusion coefficient decreased from $\kappa_{||,0}=17.20$ to $\left(\kappa_{||,0}\right)_f=15.70$ which is a larger decrease than in the 2011b case. The value of $a=0.95$ remained fixed.

Because drift effects are now scaled down towards solar maximum, it is not necessary to assume zero-drift for the 2012b to 2013b spectra. Rather, $A<0$ and $A>0$ drifts are assumed respectively where each is scaled down as function of solar activity through $f_{\mathrm{d}}(\alpha)$. The values of $\kappa_{||,0}$ that were required to obtain these $A>0$ and $A<0$ reproductions are indicated in the fourth and fifth rows of Table 4.2 respectively; these values are once again denoted by $\left(\kappa_{||,0}\right)_f$. The values of $\kappa_{||,0}$ that were found in Chapter 3, i.e. for the zero-drift case, are given in the third row of the table for reference. The values of α_{A} and B_{E} are again given in the first two rows. With the exception of the parameter a having changed from $a=0.95$ to $a=1.05$, all parameters were the same as those specified for Table 4.1. These values were therefore unchanged from their values in Chapter 3.

From Table 4.2 it is clear that all values of diffusion are higher in the case of the $A < 0$ fit than in the zero-drift case, i.e. $\left(\kappa_{||,0}\right)_f > \kappa_{||,0}$. This implies that, at these tilt angles and at Earth, the effect of $A < 0$ drift is to lower the computed intensities so that larger diffusion is necessary to reproduce the data. All values of diffusion in the $A > 0$ case are lower than the zero-drift values, i.e. $\left(\kappa_{||,0}\right)_f < \kappa_{||,0}$, implying that at these tilt angles and at Earth, the effect of $A > 0$ drift is to increase the computed intensities with respect to the zero-drift solutions, so that smaller diffusion is required to reproduce the data.

4.5 Drift Properties of the Model

This section illustrates some of the basic drift properties of the model. It considers how drift effects can be influenced either directly by changing the drift coefficient through $\kappa_{A,0}$ in Equation (2.32), or indirectly by altering the intensity gradient. Last mentioned changes in the intensity gradient are initiated by altering the diffusion coefficient: larger diffusion will generally lead to smaller gradients as it has the effect of 'wiping out' these gradients; conversely, smaller diffusion will instigate larger gradients. The energy dependent effects of drifts are also considered in this section.

4.5.1 Altering of Drift Effects towards Solar Maximum

The use of the scaling down function $f_d(\alpha)$ represents a scaling down of drift effects by means of directly altering the value of the drift coefficient κ_A, setting $\kappa_{A,0} = f_d(\alpha)$ in Equation (2.32). To illustrate the effect of this direct reduction of drift effects more clearly, the top panel of Figure 4.4 shows intensity versus tilt angle profiles for 500 MeV protons at Earth, assuming the 2013b parameters, and using $\kappa_{A,0} = 0.75 f_d(\alpha)$ (blue lines) and $\kappa_{A,0} = 0.50 f_d(\alpha)$ (green lines) in addition to the case for $\kappa_{A,0} = 1.00 f_d(\alpha)$ (red lines); the black line shows the zero-drift solution. In each case, the upper solution represents the $A > 0$ polarity cycle while the lower solution represents the $A < 0$ polarity cycle. The loop formed between the $A > 0$ and $A < 0$ solutions covers the largest area in the case of $\kappa_{A,0} = 1.00 f_d(\alpha)$, decreasing successively as $\kappa_{A,0}$ is decreased; this is indicative of the drift effects that become successively smaller.

The bottom panel of Figure 4.4 shows the corresponding $A > 0$ to $A < 0$ ratios of each of the scaled down profiles in the top panel. For the purposes of this work, such ratios provide an indication of the extent of drift effects. Note, however, that care should be taken when interpreting these ratios as such an indication: when the $A < 0$ solution rises above the zero-drift levels of intensity - this happens at small values of α - the $A > 0$ to $A < 0$ ratio will decrease, while $A < 0$ drift effects would, in fact, be increasing. However, when interpreting the $A > 0$ to $A < 0$ ratios as an indication of the extent of drift effects, from the bottom panel, it is also clear that drift effects become successively smaller as $\kappa_{A,0}$ is decreased. The largest difference between the $A > 0$ and $A < 0$ cycles occurs between

$\alpha \approx 30°$ and $\alpha \approx 40°$, where the ratio decreases by about 40% from the $\kappa_{A,0} = 1.00 f_d(\alpha)$ to the $\kappa_{A,0} = 0.50 f_d(\alpha)$ case.

The scaling down of drifts, via the value of $\kappa_{A,0}$ in Equation (2.32), can also be illustrated by constructing contour plots of exit positions and exit energies, i.e. the positions where pseudo-particles leave the modulation space and the energy with which they do so. The reader is reminded of the fact that the modulation model works in a time backward fashion so that these exit positions and energies should rather, inversely, be interpreted as entry positions and energies. In the rest of this work, whenever it is referred to as exit energies or positions, it is to be understood from a modelling perspective, i.e. according to the dynamics of the numerical model and its treatment of pseudo-particles; when it is referred to as entry energies or positions, it is understood from a physical point of view, i.e. from the viewpoint of actual protons and their modulation in the heliosphere. It is important to point out that the value of the exit energy compared to the energy at Earth will then give an indication of particle energy losses suffered during the modulation from the HP to the Earth.

Figure 4.5 shows a scatter plot of such exit positions (latitudes) and energies in the case of 500 MeV protons, using a sufficiently large number (1×10^4) of pseudo-particles, during a zero-drift scenario, i.e. where drift has been directly scaled down to zero by setting $\kappa_{A,0} = 0.00$ in Equation (2.32). The diffusion was set to a small value $\kappa_{||,0} = 5.00$ so that, for illustrative purposes, drift effects were not overly suppressed (see Section 4.5.2 for more on this effect). The exit latitudes $|\theta - 90°|$ are indicated on the horizontal axis and the exit energies on the vertical axis. Particles exiting in the equatorial regions will show up at smaller values of $|\theta - 90°|$, with the equator at $|\theta - 90°| = 0°$; particles exiting over the polar regions will register at larger values of $|\theta - 90°|$ with the poles at $|\theta - 90°| = 90°$.

The model output presented in Figure 4.5 needs to be processed further in order to be of more informative value. It is therefore binned into bins of 2.5° and 333 MeV (indicated by the grey grid lines in Figure 4.5) so that each bin contains the number of particles exiting at the latitudes and energies ascribed to the paticular bin. This number of particles is influenced by the statistical processes of the stochastic model so that any contour plot subsequently constructed will not be smooth. Such contours are presented primarily for their qualitative significance and, as such, no colour bar is presented.

The first contour plot constructed as described above is shown in the top panel of Figure 4.6, and corresponds to the setup of Figure 4.5, i.e. zero-drift. The middle and bottom panels show the exit positions and exit energies for the $A > 0$ and $A < 0$ polarity cycles respectively, assuming a tilt angle of $\alpha = 15°$ and $\kappa_{A,0} = 1.00 f_d(\alpha)$. In all of these simulations the diffusion was set to $\kappa_{||,0} = 5.00$. The exit energies are once again shown on the vertical axis, while the exit latitudes $|\theta - 90°|$ are shown on the horizontal axis. All contour plots are normalised individually so that the colour scale ascends from the lowest intensities (dark blue) to highest intensities (red).

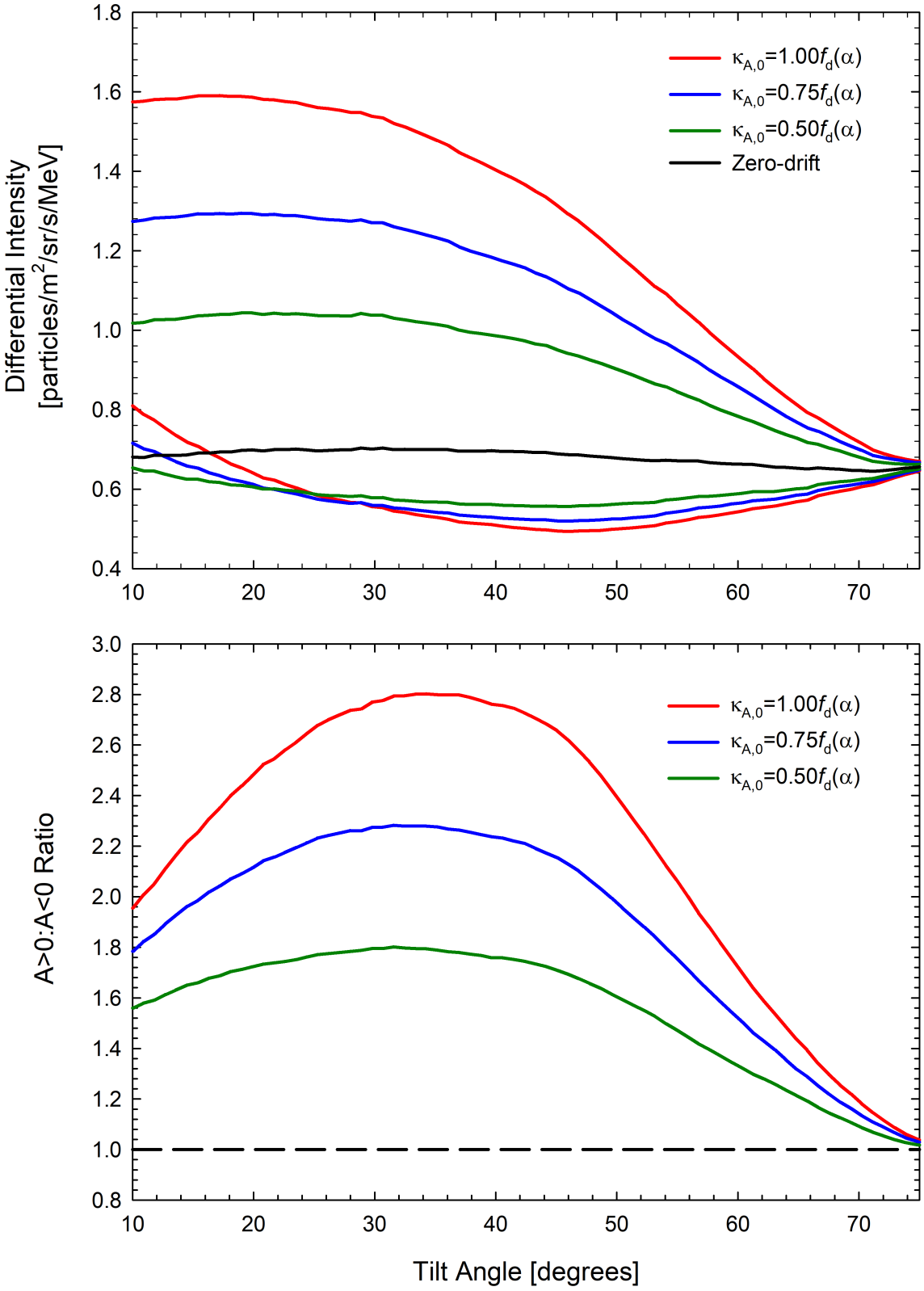


Fig. 4.4 *The direct scaling down of drifts towards solar maximum is illustrated on the hand of intensity versus tilt angle profiles for 500 MeV protons at Earth. The top panel shows these profiles where the value of* $\kappa_{A,0}$ *is changed from* $\kappa_{A,0} = 1.00$ *(red lines) to* $\kappa_{A,0} = 0.75$ *(blue lines) and 0.50 (green lines) respectively; for each of these cases, the upper line presents the* $A > 0$ *solution, while the lower line represents the* $A < 0$ *solution. The bottom panel shows the corresponding* $A > 0$ *to* $A < 0$ *ratios.*

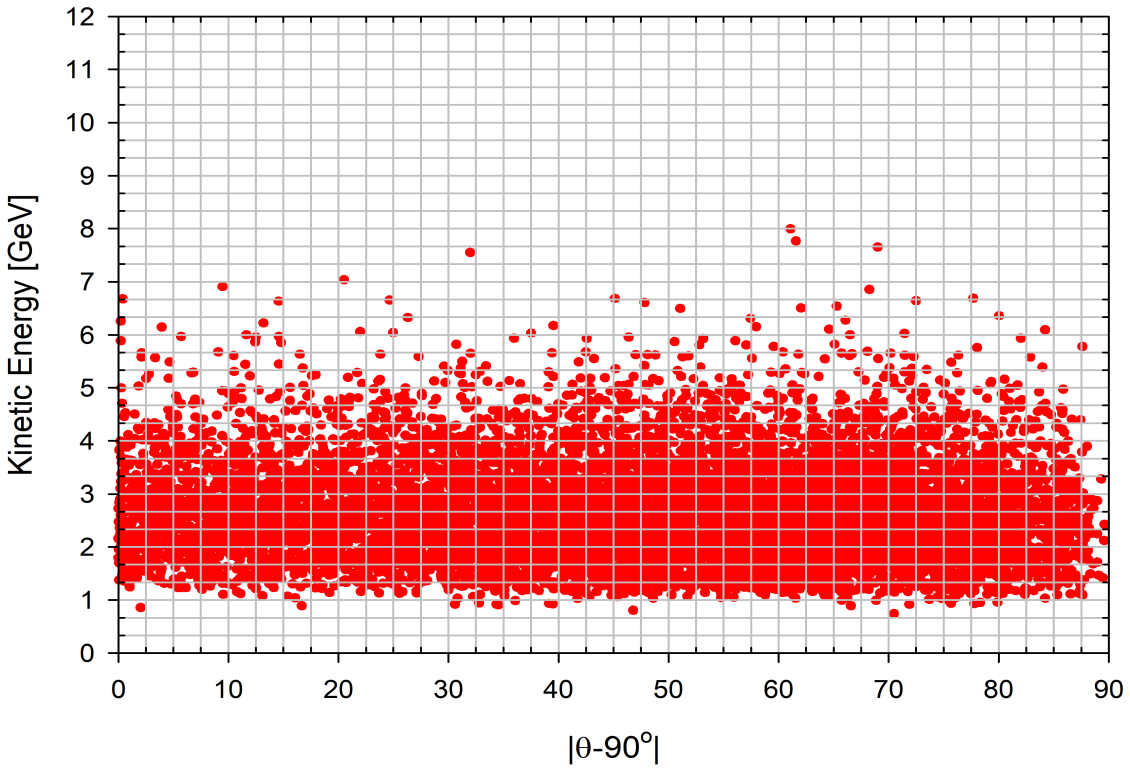


Fig. 4.5 *The exit positions (latitudes) and exit energies of* 1×10^4 *pseudo-particles in the case of 500 MeV protons for the zero-drift scenario. Diffusion was set to* $\kappa_{||,0} = 5.00$ *to ensure significant drift effects for the purposes of illustration.*

.

Considering the top panel, which shows the scenario for zero-drift, there is a preference for protons to enter at intermediate to high latitudes between ∼45° and ∼75° (as indicated by the red and yellow filled regions). Indicated by the light blue regions, significant amounts of particles enter over all latitudes, but the preference for higher latitudes is clear and the reason for this can only be the fact that parallel diffusion $\kappa_{||}$ is so much larger than perpendicular diffusion $\kappa_{\perp}$ so that particles will more easily diffuse inwards via the progressively more open magnetic field lines at higher latitudes rather than across closed field lines at lower latitudes. It is then interesting to note that the maximum amount of particles do not enter at the highest latitudes closest to the poles, but rather about 15° to 45° removed from the poles. This is the effect of the Smith-Bieber modification to the magnetic field, which is illustrated later on in Section 4.5.3. It is therefore evident that the Smith-Bieber modification influences modulation in the polar regions, even without the presence of drifts.

The effects of drifts are illustrated in the second and third panels of Figure 4.6 where the exit positions and exit energies for the $A > 0$ and $A < 0$ polarity cycles are considered respectively. Compared to the zero-drift case, the $A > 0$ case indicates that the turning on

of drifts in the model has caused exit positions to shift to higher latitudes. There are still some pseudo-particles that exit at lower latitudes, but the vast majority (considering the red and yellow filled regions) now leave modulation space in the higher latitudinal regions between ∼50° and ∼90° from the equator. From a physical point of view, this is to be expected since $A > 0$ drift will cause particles to drift inward over the polar regions, and hence more particles will enter in these regions. Far less particles now enter at latitudes below ∼ 15°, because the HCS will drift protons outwards in these regions.

Considering the $A < 0$ polarity cycle, significant amounts of particles enter in the region occupied by the HCS, i.e. at latitudes below 15°. Because the extent of the HCS is relatively small with the selected value $\alpha = 15°$, there is still a majority of particles entering at intermediate latitudes, as explained for the zero-drift scenario.

The effects of drifts are also evident in the exit energies of the pseudo-particles. In the zero-drift case, the exit energy is centered around ∼ 2.30 GeV and the significant fraction of particles (considering the colour scale down to the light blue filled regions) are distributed very roughly over ∼ 1.10 GeV above and below this value. There is a slight asymmetry in the distribution, above and below the central value: exit energies are spread out slightly more above than below the central value; this should be due to the energy dependence of the energy loss term in Equation (2.69). In all cases to follow, the indicated spread can be viewed as a 'minimum spread' in the sense that it is chosen so as to include at least the energies spread out below the central value. The above mentioned values correspond to an energy loss of $\sim 1.80 \pm 1.10$ GeV where $\pm$ is used simply to indicate the spread in energy, i.e. not to be confused with a range of error.

Comparing the second panel, where $A > 0$ drift was turned on, the exit energy was now centered around ∼ 5.25 GeV and spread out over ∼ 3.75 GeV above and below this value so that the energy loss was $\sim 4.75 \pm 3.75$ GeV; it was therefore spread out wider around the center value than in the zero-drift case. Also, the spread becomes wider with increasing latitude. Considering the third panel, where $A < 0$ drift was turned on, the exit energy was centered around $\sim 5.00 \pm 3.00$ GeV, corresponding to an energy loss of $\sim 4.5 \pm 3.00$ GeV. It is therefore clear that the effect of including drifts was to increase the energy losses and also to spread out the distribution over energy.

The reason why turning on drifts has the effect of increasing exit energies, and consequently the energy losses, is illustrated by the three panels of Figure 4.7. These panels were compiled from the trajectories of 50 pseudo-particles (due to limited resources) in each of the cases for zero-drift (top panel), $A > 0$ drift (middle panel), and $A < 0$ drift (bottom panel); it shows where pseudo-particles spend most time before exiting modulation space at the modulation boundary. It is important to point out that particles will spend most time in regions where they experience the most 'difficulty' in propagating; these regions will show up as high activity regions in Figure 4.7. Regions where particles spend the least amount of time are the regions where propagation is the most effortless and these regions will not show up in Figure 4.7 or in any similar figures that will follow. It is

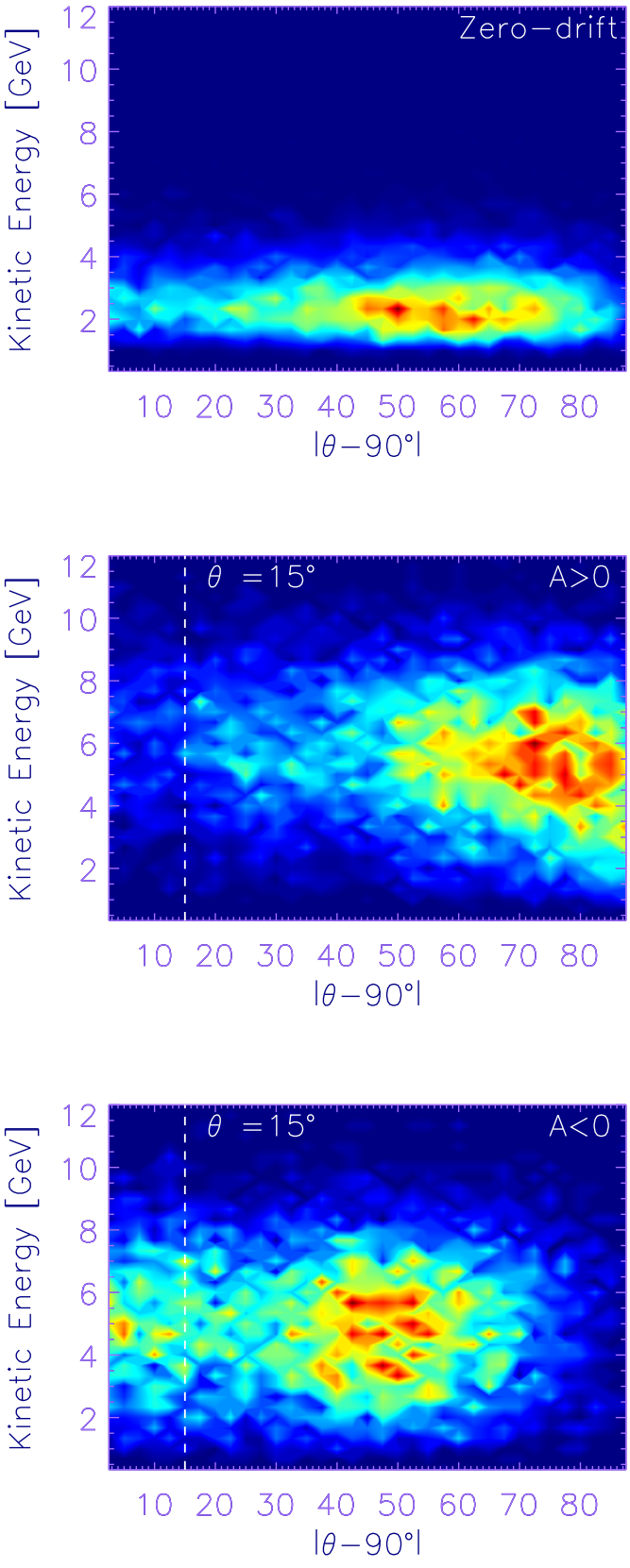


Fig. 4.6 Exit positions (latitudes) and exit energies for 1×10^4 pseudo-particles in the case of 500 MeV protons. The top, middle and bottom panels show these positions and energies in the case of zero-drift, $A > 0$ and $A < 0$ respectively. Diffusion was set to $\kappa_{||,0} = 5.00$. The colour scale ascends from blue to red according to intensity.

also important to point out that figures such as Figure 4.7 are by no means an indication of the exit positions - there is no obvious direct correlation. All these contour plots have been normalised in a fashion likewise to the panels of Figure 4.6. In this case, the darkest colour on the scale (red) corresponds to the largest fraction of total modulation time.

For the zero-drift case, the majority of modulation time is spent at radial distances of less than ~ 20 AU and latitudes less than $\sim 25°$, but a significant amount of activity is also spread out over larger radial distances and latitudes: light blue filled regions are found up to almost 110 AU and 70° latitude. The reason for the larger amount of time spent at smaller radial distances is the fact that the HMF magnitude becomes very large at such small values of r, since $B \propto 1/r$, or even $B \propto 1/r^2$ for very small radial distances, according to Equation (1.9); both the processes of diffusion and drift will then be small because both coefficients scale as $1/B$ according to Equations (2.32) and (2.45) to (2.50).

The second panel shows the effect on these high activity regions when $A > 0$ drift is turned on. The distribution is now much less spread out with both radial distance and latitude, showing that the majority of modulation time is spent at very small radial distances of less than ~ 5 AU. This explains the increased energy loss in the $A > 0$ case, since the energy loss term in Equation (2.69) is particularly large at small values of r. With such a large amount of time spent at very small radial distances, the energy losses are larger than in the zero-drift case. Considering what happens physically when $A > 0$ drift is turned on, this difference between the zero-drift and $A > 0$ cases can be explained as follows: the $A > 0$ drift cycle will drift in particles over the poles so that these particles now easily travel towards Earth with the aid of both diffusion and drift, only encountering difficulties at small radial distances when the HMF magnitude is very large so that both the diffusion and drift coefficients, scaled as $1/B$, are small. It is noticeable that this high activity region is also limited to latitudes $\theta < \alpha = 15°$, i.e. it occurs on the HCS - the HCS drift now contributes to the difficulty of inward propagation towards Earth by drifting particles outward, in opposition to the inward diffusion.

Considering the $A < 0$ case, most time is spent at small radial distances of less than ~ 20 AU and away from the HCS. This is understood in the sense that, close to the HCS, particles will now both diffuse and drift inward so that they reach Earth quickly and these regions are therefore not lighted up on the plot. However, when the particles have traveled inwards down to ~ 20 AU, and then happen to leave the HCS, they encounter outward drift and inward diffusion so that these two processes oppose each other; hence, most of the modulation time is spent at radial distances less than ~ 20 AU and off the HCS. Therefore, in this case, the energy losses are also much higher than in the zero-drift case.

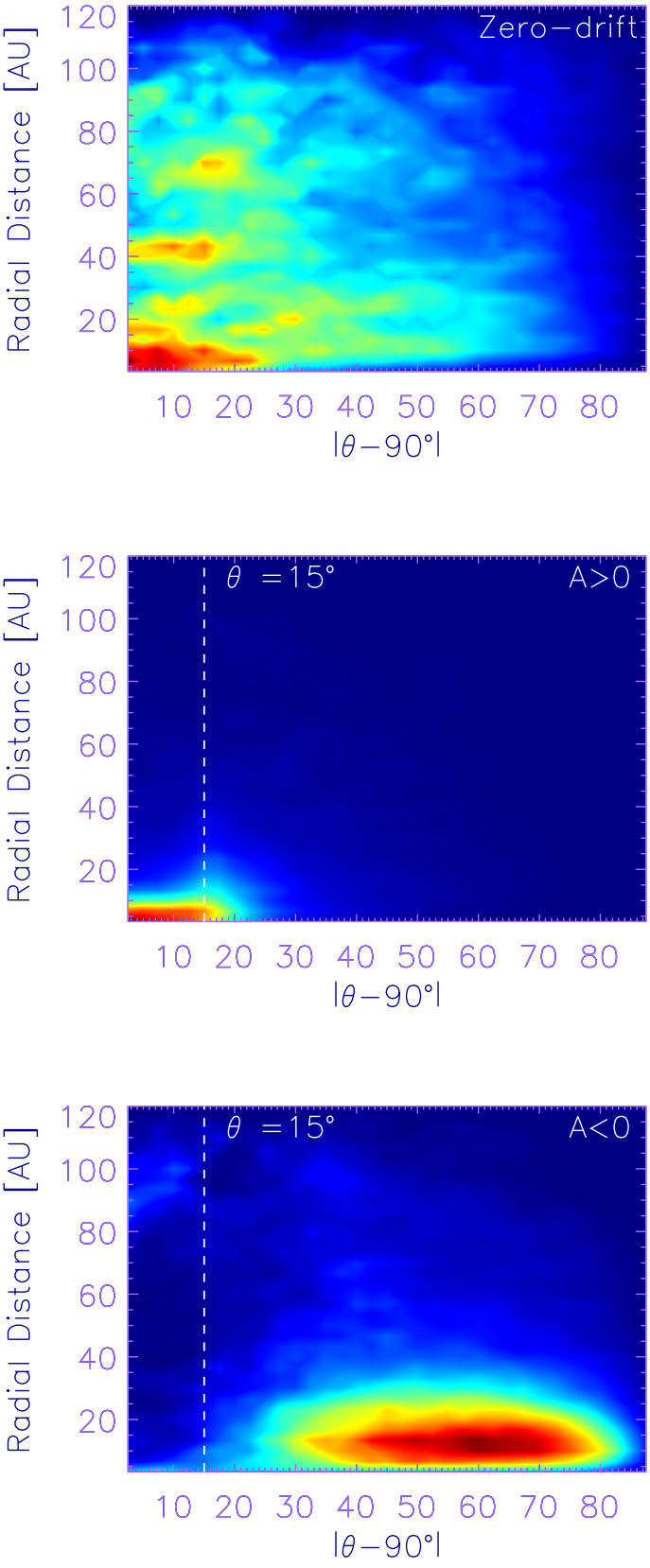


Fig. 4.7 This figure shows the high activity regions, i.e. the regions where pseudo-particles spend most time during the modulation process. The top panel shows the result for the zero-drift situation, while the middle and bottom panels do so for the $A > 0$ and $A < 0$ polarity cycles respectively. These panels were constructed from the trajectories of 50 pseudo-particles. The value of diffusion was set at $\kappa_{||,0} = 5.00$. The colour scale, once again, ascends from blue to red.

4.5.2 Diffusion and Drift Effects

Drift effects can also be influenced by altering the amount of diffusion during the modulation process. When diffusion is increased (decreased), the intensity gradients of cosmic ray particles will decrease (increase) and this will, through the TPE given in Equation (2.1), decrease (increase) the extent of drift effects experienced by these particles. This is illustrated in Figure 4.8, where the top panel shows zero-drift, $A > 0$ and $A < 0$ solutions of intensity versus tilt angle for three different values of diffusion in the case of 500 MeV protons at Earth. These solutions are for large diffusion $\kappa_{||,0} = 20.00$ (red lines), intermediate diffusion $\kappa_{||,0} = 10.00$ (blue lines) and small diffusion $\kappa_{||,0} = 5.00$ (green lines); drift was set to $\kappa_{\mathrm{A},0} = 1.0 f_{\mathrm{d}}(\alpha)$. In each of these cases (colours) the line running at the top shows the $A > 0$ solution, while the line at the bottom shows the $A < 0$ solution; the line that essentially runs in the middle of the $A > 0$ and $A < 0$ solution is, in each case, the zero-drift solution. It is clear that the area covered by the loop that is formed between the $A > 0$ and $A < 0$ solutions gets smaller as the value of diffusion is increased and so it is implied that the drift effect gets smaller as the value of diffusion is increased. This is illustrated more clearly in the bottom panel, which shows the corresponding $A > 0$ to $A < 0$ ratios for each of the cases $\kappa_{||,0} = 20.00$, $\kappa_{||,0} = 10.00$ and $\kappa_{||,0} = 5.00$.

The intersection of the $A < 0$ and zero-drift solutions shifts towards larger values of α as the diffusion is decreased, i.e. as the drift effect becomes larger. This means that the larger the drift effect (and the smaller the diffusion), the longer (up to higher values of α) protons will be able to stick to the HCS and be drifted on a more direct route to Earth without being scattered away by diffusion. For such smaller diffusion, the intensities are still lower than for higher diffusion - it only stays higher relative to the particular zero-drift solution.

This indirect scaling of drift effects can also be illustrated with the help of contour plots similar to those shown in Figures 4.6 and 4.7. Figure 4.9 is similar to Figure 4.6, but for diffusion increased to $\kappa_{||,0} = 20.00$. The first panel shows the zero-drift result, while the middle and bottom panels show the $A > 0$ and $A < 0$ results respectively. The scale of these panels, to be directly comparable to Figure 4.6, reaches all the way up to 12 GeV. This scale, therefore, does not lean itself to sufficient comparison of the cases for $\kappa_{||,0} = 20.00$ and $\kappa_{||,0} = 5.00$ in terms of distribution with latitude. The panels of Figure 4.10 present zoomed in versions of the top, middle and bottom panels of Figure 4.9, restricting the range of the vertical axis to only 3 GeV. This enables more effective comparison with Figure 4.6, i.e. the case for $\kappa_{||,0} = 5.00$.

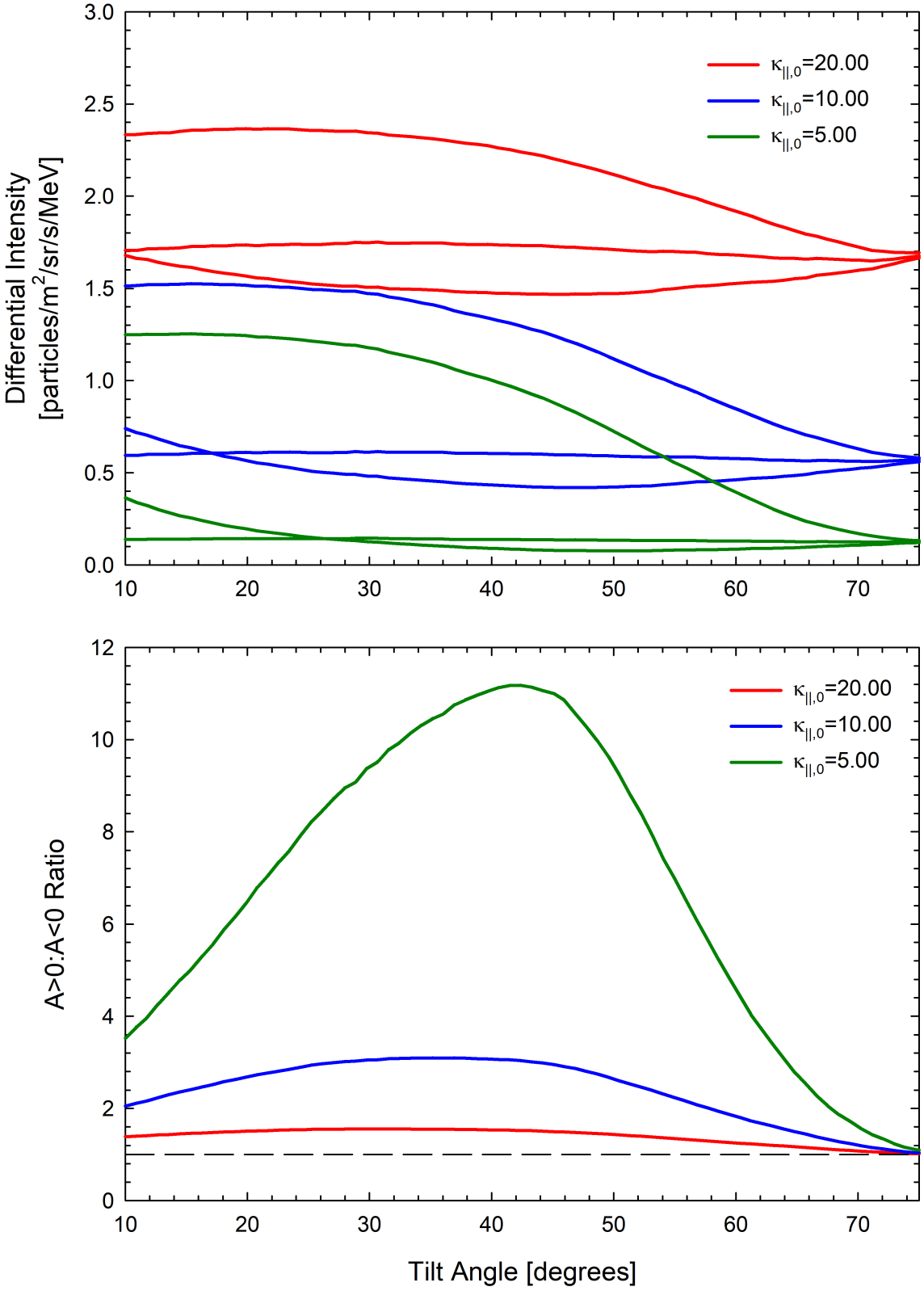


Fig. 4.8 *The indirect scaling down of drifts is illustrated on the hand of intensity versus tilt angle profiles for 500 MeV protons at Earth. The top panel shows such profiles where* $\kappa_{||,0} = 20.00$ *(red lines), 10.00 (blue lines), and 5.00 (green lines) respectively. The upper line of each colour shows the* $A > 0$ *solution, while the lower line shows the* $A < 0$ *solution; the line that runs essentially in the middle of the* $A > 0$ *and* $A < 0$ *solutions is, in each case, the zero-drift solution. The bottom panel shows the corresponding* $A > 0$ *to* $A < 0$ *ratios. Parameters for 2013b were used.*

.

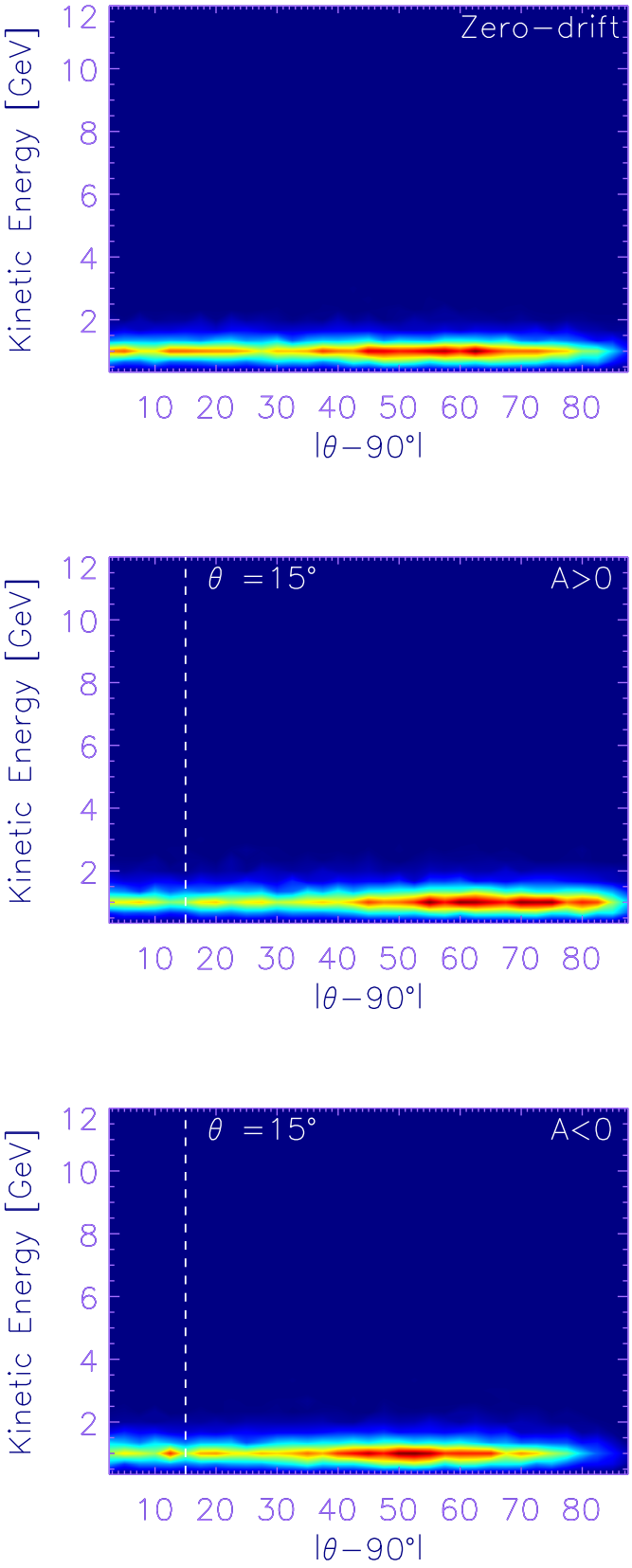


Fig. 4.9 Exit positions (latitudes) and exit energies for 1×10^4 pseudo-particles in the case of 500 MeV protons. The top, middle and bottom panels show these exit positions and energies in the case for zero-drift, $A > 0$ and $A < 0$ drifts respectively. Diffusion was set to $\kappa_{||,0}$=20.00. These figures are presented on this scale to accomodate comparison with Figure 4.6. See Figure 4.10 for a zoomed in version of these panels.

Figure 4.10 indicates that these exit positions are more spread out over latitude in the $\kappa_{||,0} = 20.00$ case and also that a significant amount of particles now enter modulation space all the way down to the equatorial regions. There is, however, still a preference for the intermediate to higher latitudinal regions due to $\kappa_{||} > \kappa_{\perp}$, as explained earlier. The highest latitude exit positions still do not go up to the poles, due to the Smith-Bieber modification (discussed in Section 4.5.3).

The second panel shows the case for the $A > 0$ polarity cycle and there is a significant preference for the higher latitudinal regions when compared to the zero-drift case. This is, of course, due to the $A > 0$ drift bringing in particles over the polar regions, as explained in the case of Figure 4.6. The preference is, however, less pronounced than in the case for $\kappa_{||,0} = 5.00$, when considering that significant amounts of pseudo-particles now also leave modulation space at the lower latitudes and especially below the extent of the HCS $\theta = 15°$. This clearly indicates the weaker relative effect of drifts in the high diffusion case, i.e. the global drift pattern is less pronounced. Looking at the $A < 0$ case, where protons now come drifting inwards along the HCS, there is not much difference in the distribution with latitude between the $\kappa_{||,0} = 20.00$ and $\kappa_{||,0} = 5.00$ cases; this is most probably due to the small extent of the HCS.

Regarding the energy losses, it is already clear from comparison of the top panels from Figures 4.6 and 4.9 that particles have lost notably less energy in the case for increased diffusion $\kappa_{||,0} = 20.00$. It is also evident that the distribution of these exit energies were less spread out than in the lower diffusion case. The top panel of Figure 4.10 shows a narrow band of intensity around $\sim 1.00 \pm 0.50$ GeV in the zero-drift case, including the light blue regions. This corresponds to an energy loss of 0.50 ± 0.50 GeV, which is now notably less than in the low diffusion case considered earlier. This result is as expected, since larger diffusion will more effectively transport protons inwards to the Earth so that they spend less time in modulation space, hence being modulated to a lesser extent. However, the amount of modulation is not only determined by how much time particles spend in modulation space, but also by *where* in modulation space they spend this time, as was apparent from the discussion of Figure 4.7. Figure 4.11 is analogous to Figure 4.7, but for increased diffusion $\kappa_{||,0} = 20.00$. If the top panels of Figures 4.7 and 4.11 are compared, i.e. the zero-drift cases, it is evident that the activity is much more spread out in the radial dimension for the high diffusion case so that a less *disproportionate* amount of time is spent at the smallest radial distances where most energy is lost. In all cases to follow, the word "disproportionate" is used to indicate the contrast between time spent at larger radial distances and time spent at smaller radial distances, i.e. a disproportionate amount of time spent at smaller radial distances would indicate more time spent at smaller radial distances *relative* to larger distances.

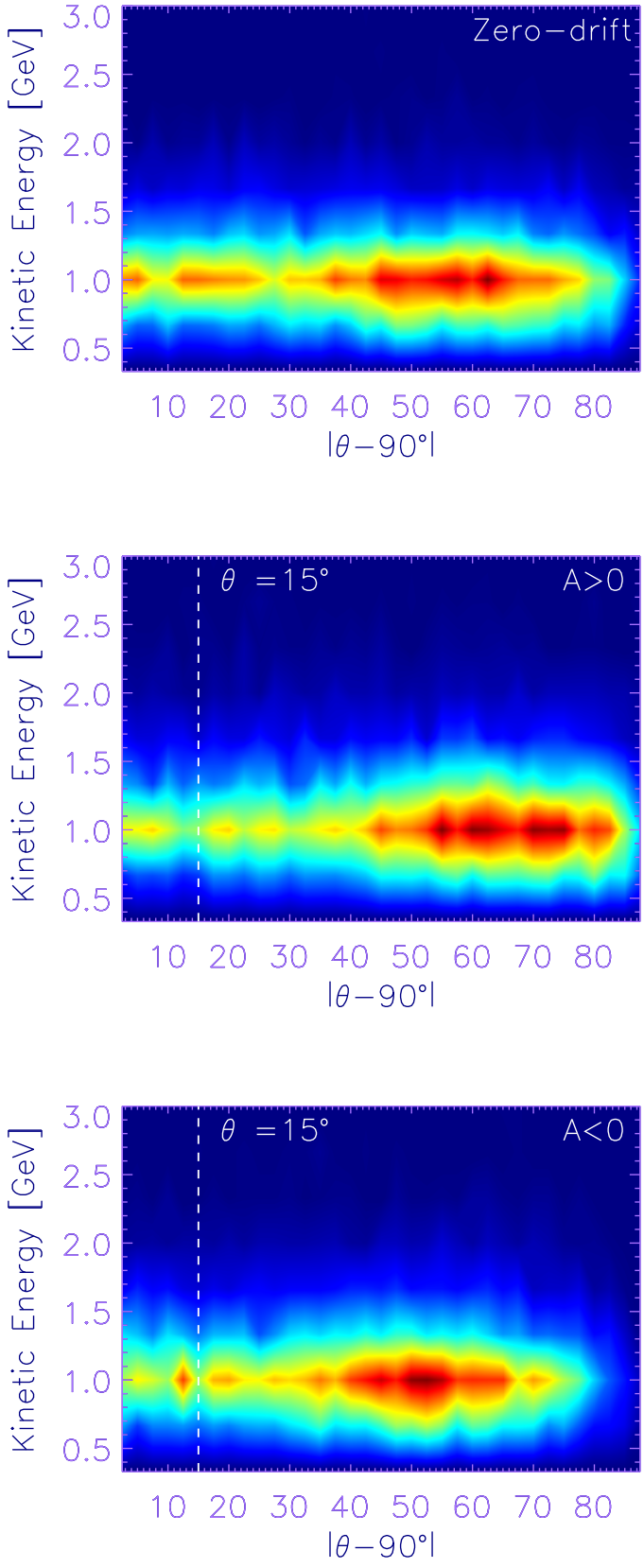


Fig. 4.10 Similar to Figure 4.9, here zoomed in over 3 GeV.

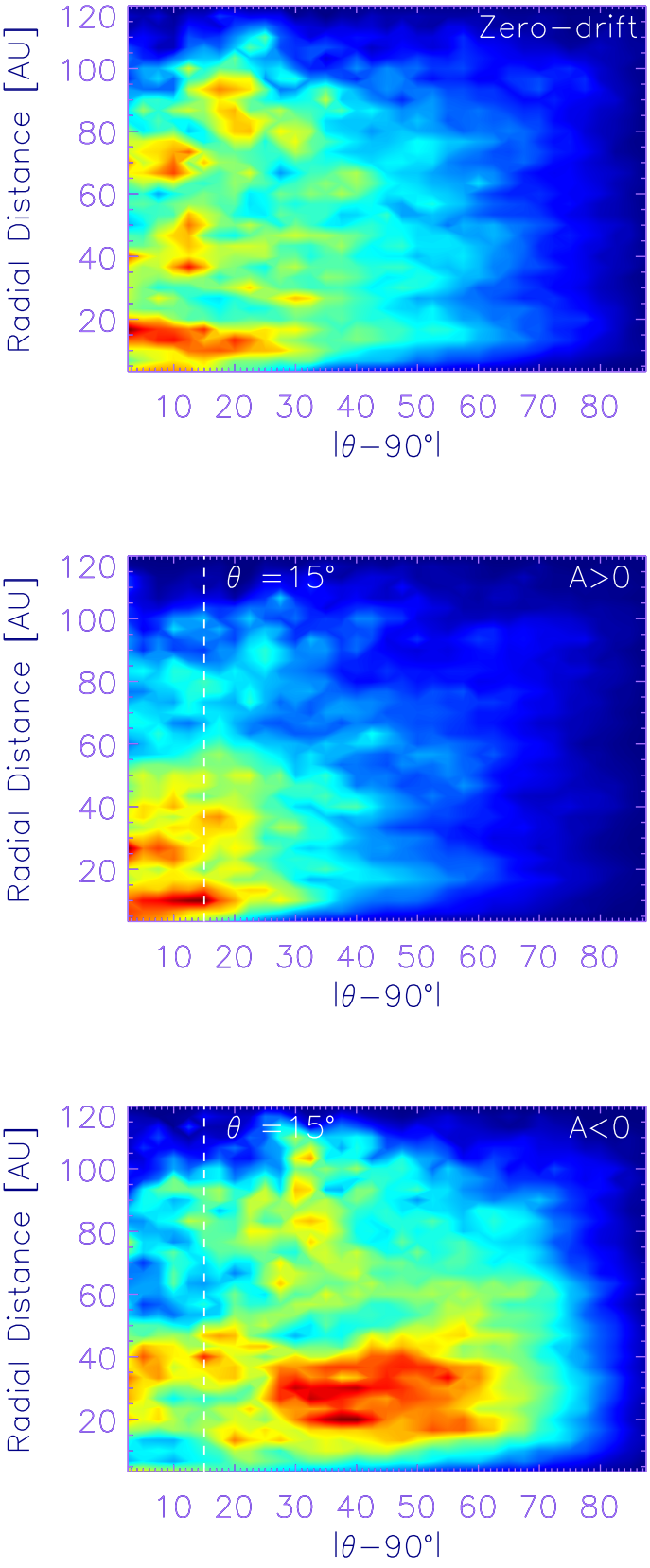


Fig. 4.11 This figure is similar to Figure 4.7 and shows the high activity regions, i.e. the regions where pseudo-particles spend most time during the modulation process. The top panel shows the result for the zero-drift situation, while the middle and bottom panels do so for the $A > 0$ and $A < 0$ polarity cycles respectively. The value of diffusion was set at $\kappa_{||,0} = 20.00$.

This is even more clear from comparing the second panels of Figures 4.7 and 4.11, i.e. the $A > 0$ polarity cycles. In the case for small diffusion $\kappa_{||,0} = 5.00$, the high activity regions were limited to radial distances smaller than about 5 AU and also below the HCS extent at $\theta = 15°$. For larger diffusion, $\kappa_{||,0} = 20.00$, the distribution is significantly more spread out in both the radial and latitudinal directions with the majority of time now being spent (considering the red to yellow/green filled regions) at radial distances as high as ~ 60 AU or even 80 AU and at latitudes of up to $\sim 20°$ above the extent of the HCS; a clear majority of time is still, however, spent on the HCS. Overall, a less disproportionate amount of time is spent at small radial distances where energy losses are the largest; the result is that less energy is lost in the higher diffusion case. The second panel of Figure 4.10 shows a narrow band of intensity around $\sim 1.00 \pm 0.50$, similar to the zero-drift case. This again corresponds to an energy loss of 0.50 ± 0.50 GeV, which is less than in the low diffusion case.

Very much the same conclusions are drawn from comparing the third panels of Figures 4.7 and 4.11, i.e. the $A < 0$ polarity cycles. In the case for small diffusion $\kappa_{||,0} = 5.00$, the activity was limited to smaller radial distances below ~ 25 AU and latitudes off the HCS. In the high diffusion case $\kappa_{||,0} = 20.00$, the activity is significantly more spread out over both the radial and latitudinal dimensions, so that less time is spent in the regions where most energy is lost. The result of this more spread out distribution is that less energy is lost and the third panel of Figure 4.10 shows an energy loss of $\sim 0.50 \pm 0.50$, similar to the zero-drift and $A > 0$ cases. Furthermore, for the high diffusion case, the energy losses did not increase when drifts were turned on; this can only be interpreted as further indication of the reduced effect of drifts when diffusion is increased.

When comparing the panels of Figures 4.7 and 4.11, it must be kept in mind that each of these panels was normalised so that the colour filled regions give indication of the amount of time spent relative to the total modulation time in that particular case. The consequence of this is that the panels of Figure 4.11, i.e. the high diffusion case, show a lot more red filled regions, even though the total amount of time spent by pseudo-particles in modulation space is less than in the low diffusion case of Figure 4.7. All contours showing these high activity regions must be interpreted in this way.

4.5.3 Drift Effects as Function of Energy

The top panel of Figure 4.12 illustrates the energy dependence of drift effects in terms of profiles of intensity versus tilt angle for protons of two different energies, at Earth. The zero-drift, $A > 0$ and $A < 0$ solutions for 1 GeV (red lines) and 250 MeV (green lines) protons are shown. Diffusion was set to $\kappa_{||,0} = 5.00$ again for the same reasons as explained earlier. As in Figure 4.3, for each colour, the upper and lower lines represent the $A > 0$ and $A < 0$ solutions respectively, while the line that essentially runs in the middle represents the zero-drift solution. From this figure, it is clear that the area enclosed by the

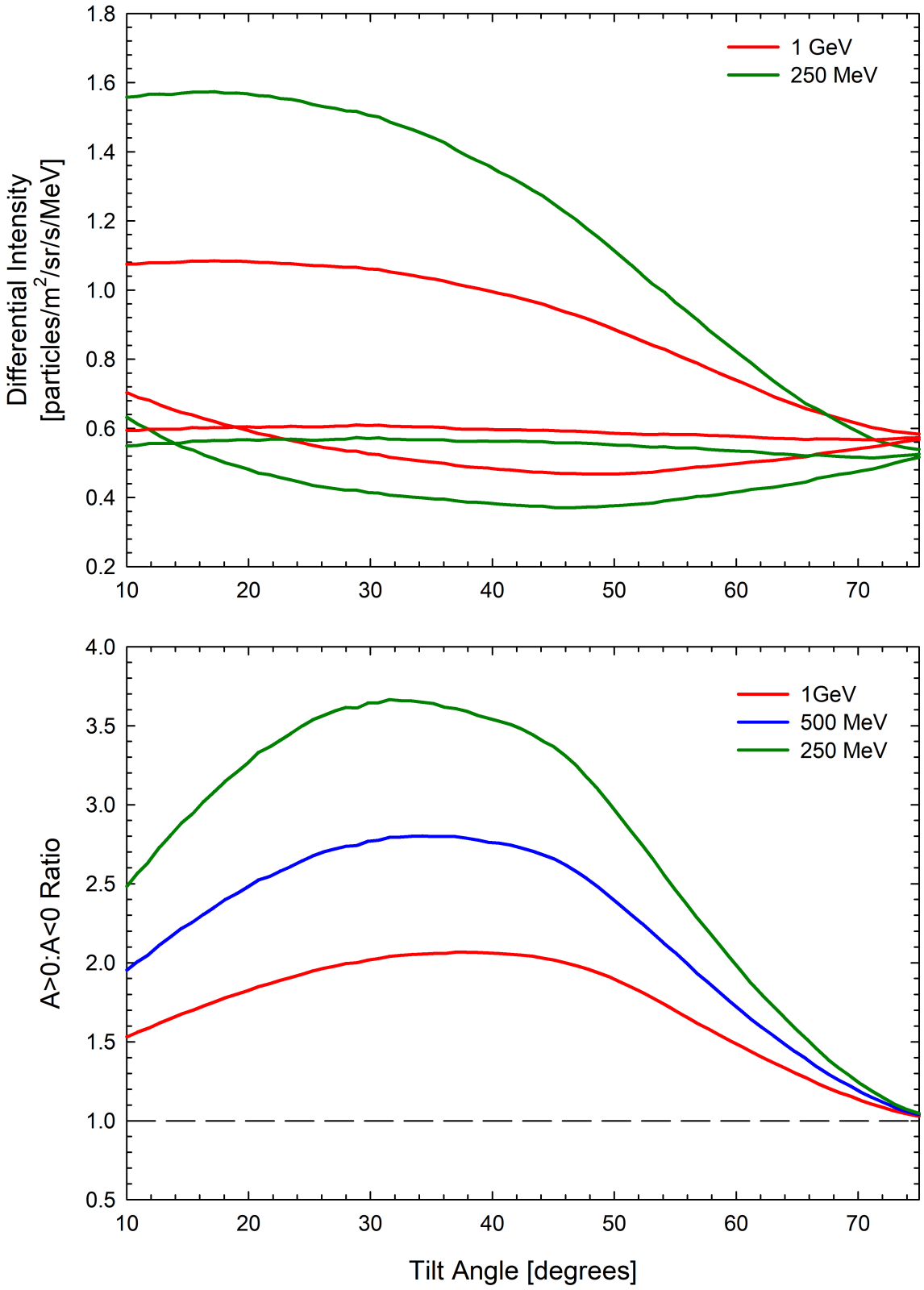


Fig. 4.12 *The energy dependence of drift effects is illustrated. In the top panel, the zero-drift, $A > 0$ and $A < 0$ solutions are shown for each of two selected energies 1 GeV (red lines), and 250 MeV (green lines). For each colour (energy) the upper and lower lines represent the $A > 0$ and $A < 0$ solutions respectively, while the line that for most part runs in between these two solutions represents the zero-drift solution. The bottom panel shows the $A > 0$ to $A < 0$ ratios for each of these energies as well as for 500 MeV (blue line). The parameters in the case of 2013b were used.*

.

$A > 0$ and $A < 0$ solutions become larger as the energy is decreased, which can be interpreted as increasing drift effects. This is understood by considering that even though the graph of λ_A versus P (Figure 2.1) shows that the drift coefficient will increase as function of energy (rigidity), the diffusion coefficient also increases with increasing energy and will therefore progressively suppress drift effects through smaller gradients in CR intensity (as explained before) for higher energies. From physical considerations, the more effective diffusion at higher energies will ensure that particles reach the Earth in smaller amounts of time, thus having less opportunity to experience drift motion. The bottom panel of Figure 4.12 shows the $A > 0$ to $A < 0$ ratio in each of the cases for 1 GeV (red line) and 250 MeV (green line) as well as for 500 MeV (blue line); while this ratio is interpreted as an indication of the drift effect, it confirms the decrease with increasing energy.

The energy dependence can also be illustrated using contour plots. Figure 4.13 shows exit positions and exit energies of pseudo-particles in the case for 100 MeV protons, while Figure 4.14 does so in the case of 5 GeV protons; diffusion was set to $\kappa_{||,0} = 5.00$. The first panel in each of these figures shows the zero-drift case. Comparing the cases for 100 MeV and 5 GeV, there is not much difference in the distribution with latitude - both show the preference for intermediate to higher latitudes that can be ascribed to $\kappa_{||} \gg \kappa_{\perp}$ and the effect of the Smith-Bieber modification over the polar regions. Figure 4.15 shows the exit positions and exit energies for 100 MeV protons in the case of the unmodified Parker field, and it is clear that most particles do indeed exit at the highest latitudes closest to the poles in this case.

Though the distribution with latitude does not show much difference, the distribution of the exit energies is more spread out in the case for 100 MeV. The exit energies in the 100 MeV case were centered around $\sim 2.25 \pm 1.50$ GeV, implying an energy loss of $\sim 2.15 \pm 1.50$ GeV; this is a fractional energy loss of between ~ 0.87 and ~ 0.97, i.e. protons that arrive at Earth with an energy of 100 MeV have lost between $\sim 87\%$ and $\sim 97\%$ of the energy with which they had entered the heliosphere at the modulation boundary. The exit energies in the 5 GeV case were centered around $\sim 6.00 \pm 0.50$ GeV, implying an energy loss of $\sim 1.00 \pm 0.50$ GeV; this is a fractional energy loss of only between ~ 0.09 and ~ 0.23 so that protons that arrive at Earth with an energy of 5 GeV have lost only about $\sim 9\%$ to $\sim 23\%$ of the energy with which they had originally entered modulation space at the modulation boundary. Keep in mind that these numbers indicate the minimum spread, as explained earlier. In this instance, it is important to point out that the spread above the central value may actually reach up to ~ 7.50 GeV. This would imply an energy loss of up to $\sim 33\%$, which is still significantly less than in the 100 MeV case. This result is as expected, since particles of higher energy must experience less modualtion because of the increased effect of inward diffusion.

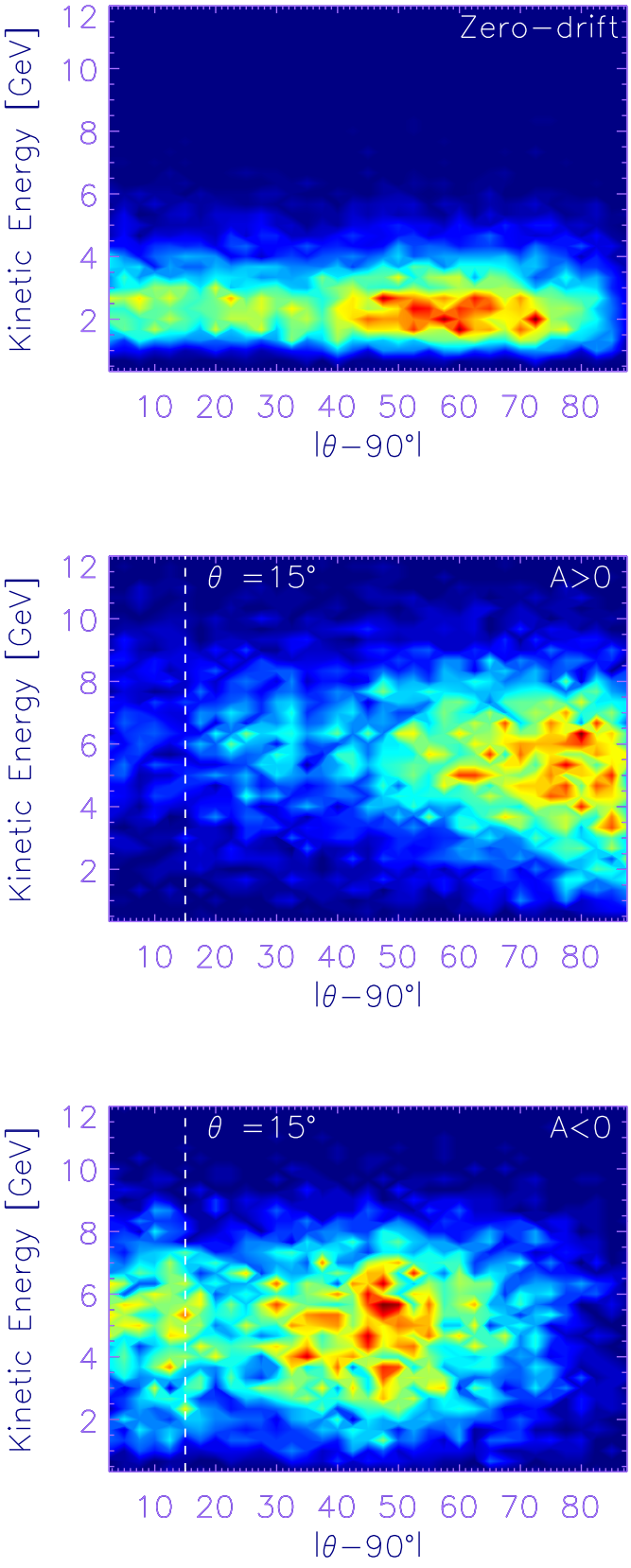


Fig. 4.13 Exit positions and exit energies of pseudo-particles in the case of 100 MeV protons, using $\kappa_{||,0} = 5.00$.

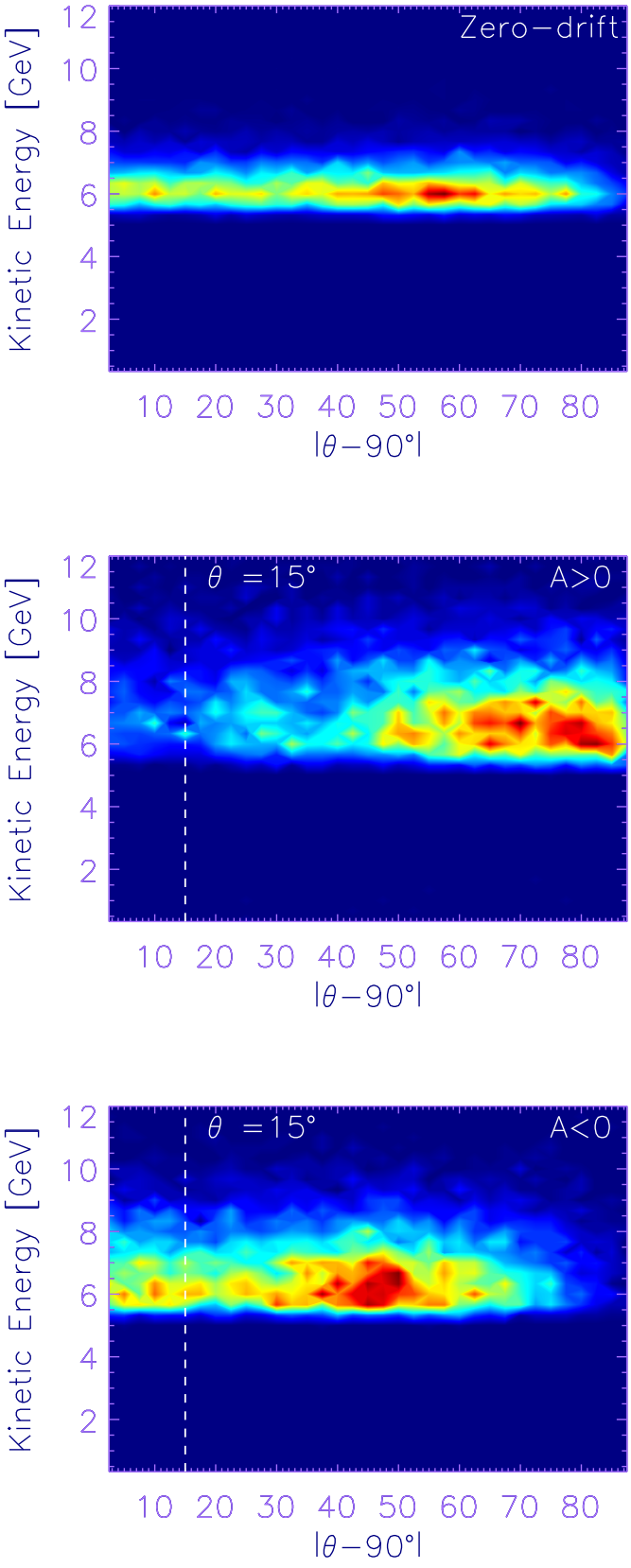


Fig. 4.14 The exit positions and energies of pseudo-particles in the case of 5 GeV protons, using $\kappa_{||,0} = 5.00$.

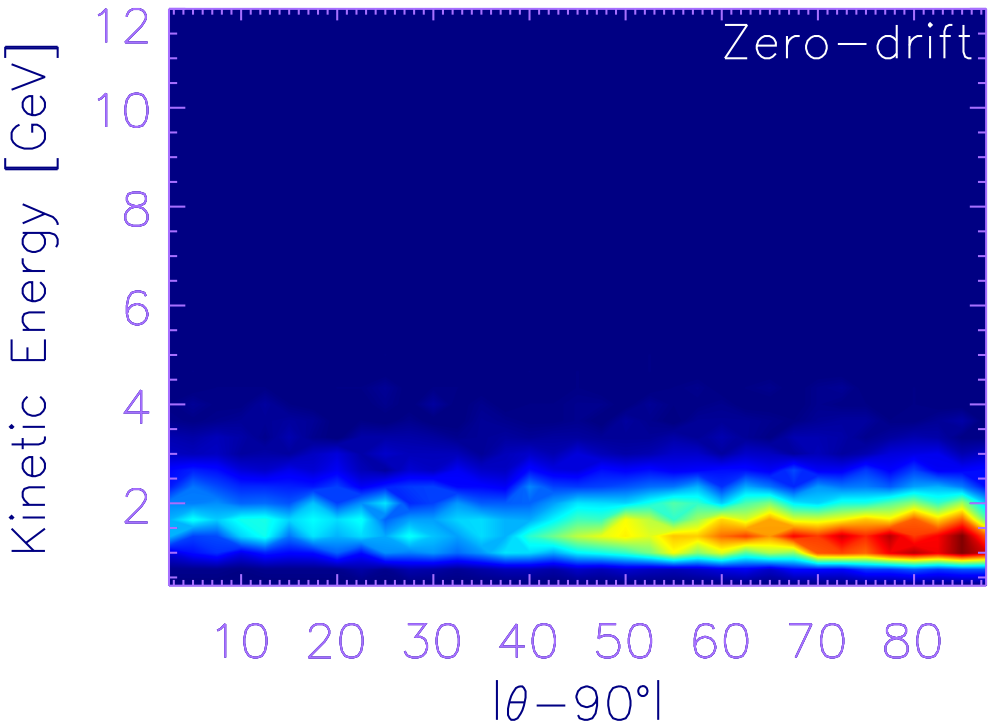


Fig. 4.15 The exit positions and exit energies of 1×10^4 pseudo-particles in the case of 100 MeV protons for the zero-drift scenario, using the unmodified Parker field.

Consider now the effect of turning on $A > 0$ drifts in each of the 100 MeV and 5 GeV cases, i.e. the second panels of Figures 4.13 and 4.14. The exit positions in both the cases for 100 MeV and 5 GeV now shift towards higher latitudes, following the global drift pattern. The exit positions in the case of 5 GeV are, however, slightly more spread out over latitude than in the case for 100 MeV; this can be seen by comparing e.g. the red to yellow regions and indicates that the shift of exit positions towards higher latitudes was slightly weaker in the 5 GeV case, i.e. the effect of the globally imposed drift pattern was weaker. Much the same conclusions can be reached from comparing the $A < 0$ drift cases, i.e. the third panels of Figures 4.13 and 4.14, but it is less clear due to the small latitudinal extent of the HCS.

The difference in the drift effect between the 100 MeV and 5 GeV cases is best illustrated by looking at the respective exit energies. It was illustrated earlier, in the case for 500 MeV, that when drift effects were turned on, the energy losses would increase. In the case for 100 MeV, the energy losses were increased from $\sim 2.15 \pm 1.50$ GeV in the zero-drift case to $\sim 4.90 \pm 3.50$ GeV for the $A > 0$ polarity cycle; this is an increase in the energy losses of $\sim 128\%$, using only the values around which these energy losses are centered. In the case of 5 GeV, the energy losses were increased from $\sim 1.00 \pm 0.50$ GeV in the

zero-drift case to $\sim 1.50 \pm 1.50$ GeV for the $A > 0$ polarity cycle; this is an increase in the energy losses of $\sim 50\%$, once again using only the values around which these energy losses are centered. The relative increase in the energy loss from the zero-drift case to the $A > 0$ case is therefore significantly smaller in the 5 GeV than in the 100 MeV case, clearly illustrating the weaker drift effects for the higher energy scenario. The same argument can be constructed for the $A < 0$ polarity cycle. It was found, on the scale of the contour plots at least, that there was no significant difference between the energy losses for the $A > 0$ and $A < 0$ cycles and, therefore, the same conclusions are reached from comparing the $A < 0$ cycles of the 100 MeV and 5 GeV cases.

Some insights can also be obtained from the contour plots constructed from particle trajectories. Figures 4.16 and 4.17 are analogeous to Figure 4.7, but for 100 MeV and 5 GeV respectively. Comparing these figures yields some additional insights.

First comparing the top panels, i.e. the zero-drift scenarios, as the energy is increased, the contrast between time spent at larger radial distances and the time spent at smaller radial distances becomes less pronounced, i.e. a less disproportionate amount of time is spent at smaller radial distances. In the case for 100 MeV, the majority of activity (red to yellow/green filled regions) is restricted to below radial distances of ~ 15 AU, with little to no significant activity (light blue filled regions) occuring above about ~ 100 AU. In the case for 500 MeV, the majority of activity is found up to radial distances of ~ 100 AU, while significant activity occurs up to ~ 120 AU. In the 5 GeV case, the highest activity regions are found up to radial distances of ~ 110 AU, while significant activity now occurs over all values of r. The consequence, as indicated earlier, is successively smaller energy losses (relative to the energy at the modulation boundary) because of the $1/r$ dependence of the energy loss term in Equation (2.69).

The same conclusions are drawn from comparing the second panels of Figures 4.16 and 4.17, i.e. the $A > 0$ solutions. For the 100 MeV case, the majority of activity (red to yellow/green regions) is restricted to radial distances below ~ 10 AU, while, in the case for 5 GeV, this majority of activity was found to reach up to ~ 35 AU or even ~ 45 AU. In the case for 100 MeV, significant activity (light blue regions) did not reach higher than about ~ 15 AU, while in the case for 5 GeV it reached all the way up to about ~ 60 AU. This would again account for the larger energy losses in the case for 100 MeV, since those particles had spent more time at the smallest radial distances. The same conclusions are drawn for considering the $A < 0$ solutions: the activity regions are much more spread out over higher radial distances in the case for 5 GeV, leading to smaller energy losses.

The reason why the activity regions spread out over r with an increasing energy can be understood as follows. When the energy is low, at 100 MeV, the inward diffusion is weakest. This will cause particles to spend a large disproportionate amount of time at the smallest values of r where the HMF is strongest; it can be stated that particles 'get caught' or 'held up' at these smaller radial distances due to the strong HMF. When the energy is increased to 500 MeV in Figure 4.7, diffusion is larger and particles can now more easily

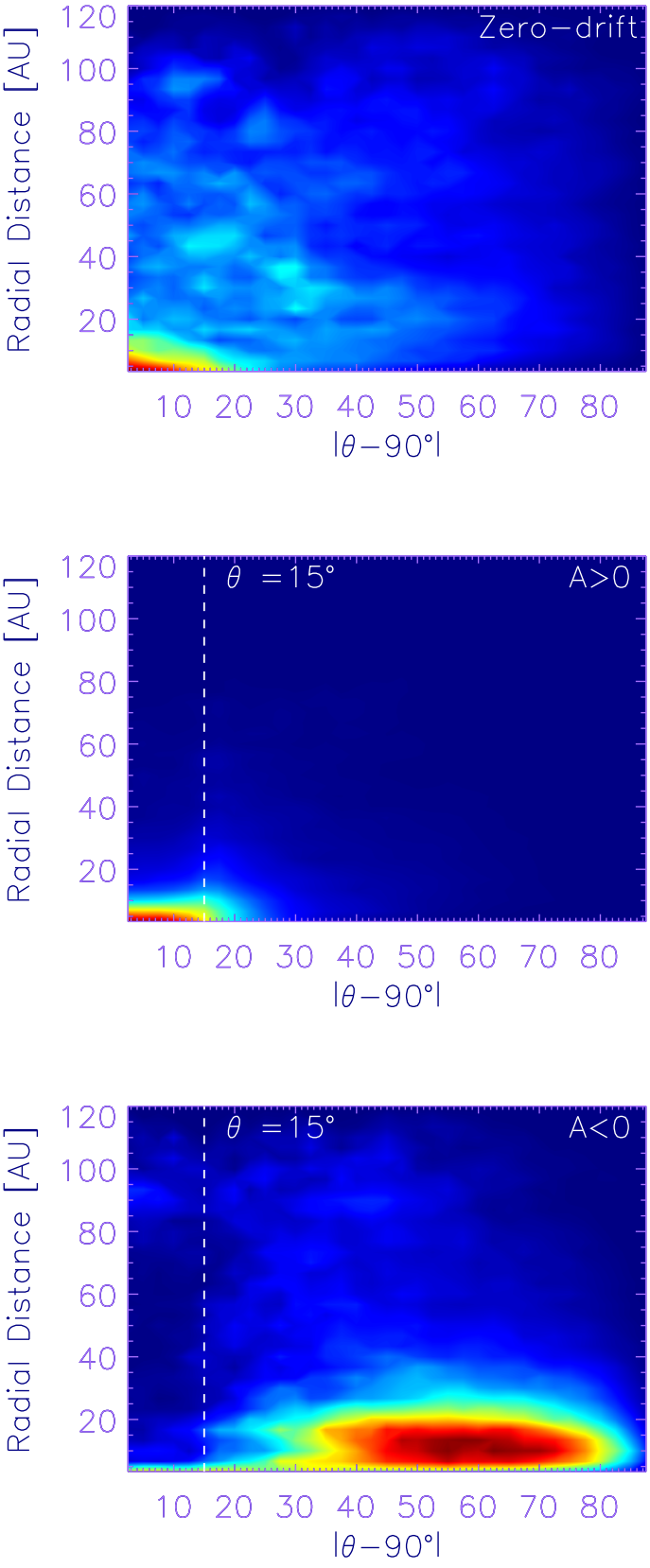


Fig. 4.16 The most sampled regions for pseudo-particles in the case of 100 MeV protons. The top panel shows the zero-drift scenario, while the middle and bottom panels show the $A > 0$ and $A < 0$ scenarios respectively.

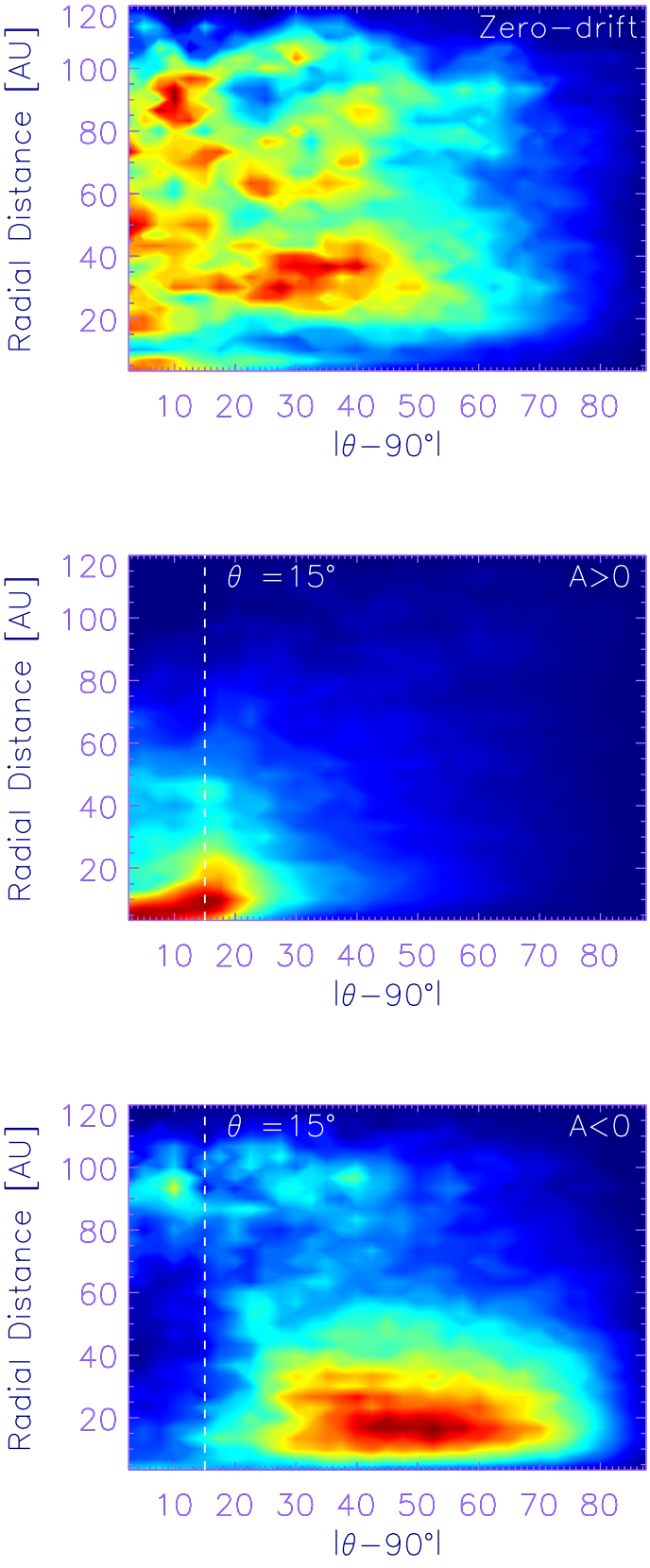


Fig. 4.17 The most sampled regions for pseudo-particles in the case of 5 GeV protons. The top panel shows the zero-drift scenario, while the middle and bottom panels show the $A > 0$ and $A < 0$ scenarios respectively.

diffuse inward, including at the smallest values of r, and the amount of modulation time spent in these regions is now less disproportionate; hence, the distribution spreads out with r. When the energy is increased to 5 GeV in Figure 4.17 - by the same reasoning - the distribution over r spreads out even more so that the relative energy loss decreases even further.

4.6 Summary

This chapter considered the scaling down of drift effects towards extreme solar maximum conditions and the consequent effects on modulation were compared to the modulation results of Chapter 3, where the scaling down of drifts as explicit function of the tilt angle was not applied. Other phenomenological studies in which drifts were scaled down towards solar maximum were performed by e.g. Ferreira [2002] and Ndiitwani et al. [2005]. Making use of the illustrative capabilities of the modulation model, the chapter also provided significant insights into the mechanisms of modulation and especially the drift process in the heliosphere.

Section 4.2 described drift over the course of the solar cycle with no additional scaling down of drift effects towards solar maximum, i.e. there was no scaling down as explicit function of the tilt angle α. The solar cycle related changes that did occur in the drift effects were rather established through the corresponding values of the magnetic field that occur in the expression for the drift coefficient, Equation (2.32), as well as through effects imposed on the propagation of (pseudo-)particles by the expanding neutral heliospheric current sheet (HCS). The top panel of Figure 4.1 showed proton differential intensities as function of the tilt angle α in the case of 500 MeV protons. The behaviour of each profile was explained relative to the zero-drift solution. In the bottom panel of Figure 4.1, the solutions of the top panel were smoothed and it was indicated that it did not influence the conclusions based on the qualitative results. The smoothing process was then applied throughout the rest of this chapter.

Section 4.3 introduced the scaling function $f_{\mathrm{d}}(\alpha)$ in Equation (4.1) that would be used to scale down drift effects as function of increasing solar activity through the tilt angle α. Figure 4.2 showed this function for several different settings of its parameters, in order to illustrate its properties and show in which way it could be used to scale down drift effects. In Figure 4.3, intensity versus α plots were shown to illustrate the effect of $f_{\mathrm{d}}(\alpha)$ on these profiles. The function was shown to be easily adaptable in terms of the value of α at which it reduces drift effects to zero.

In Section 4.4, the parameters that were obtained for reproducing the PAMELA proton spectra, with the inclusion of the scaling function $f_{\mathrm{d}}(\alpha)$, were presented. These were compared to the parameters obtained in Chapter 3, i.e. without the inclusion of $f_{\mathrm{d}}(\alpha)$. It was indicated that, for the spectra ranging from 1 January 2010 to 30 June 2011 (spectra 2010a to 2011a), no changes in the $A < 0$ parameters were required because of $f_{\mathrm{d}}(\alpha)$ being

close to unity and therefore having minimal impact. However, for the spectrum ranging from 1 July 2011 to 31 December 2011 (spectrum 2011b during the $A < 0$ polarity cycle), a change in the diffusion was necessary so that the parameter $\kappa_{||,0}$ in Equation (2.45) was required to decrease. A reduction in drift via $f_{\mathrm{d}}(\alpha)$ therefore had the effect of increasing the intensities computed by the model at Earth so that smaller diffusion was necessary to reproduce the data. The relevant parameters were indicated in Table 4.1. For the spectra ranging from 1 July 2012 to 31 December 2013 (spectra 2012b to 2013b), where in Chapter 3 only zero-drift reproductions were obtained, Chapter 4 obtained reproductions asuming $A > 0$ and $A < 0$ drift respectively; in each case the drift was scaled according to the function $f_{\mathrm{d}}(\alpha)$. For the $A < 0$ reproductions, the inclusion of drift had as consequence that decreased intensities were calculated by the model so that larger values of diffusion were necessary to reproduce the data. Switching on $A > 0$ drift had the opposite effect, increasing computed intensities, so that smaller values of diffusion were required. The parameters for the 2012b to 2013b reproductions were indicated in Table 4.2.

Section 4.5 presented an investigation into the drift properties of the model. In Section 4.5.1, the focus was on the alteration of drifts by direct means, i.e. changing the value of the drift coefficient κ_{A} by multiplying it with a certain factor of the scaling function $f_{\mathrm{d}}(\alpha)$. This was illustrated in the top and bottom panels of Figure 4.4, showing solutions of intensity versus α and $A > 0$ to $A < 0$ ratios respectively. The reduction that occurred in drift effects, upon reducing the drift coefficient to $0.75 f_{\mathrm{d}}(\alpha)$ and $0.50 f_{\mathrm{d}}(\alpha)$ respectively, was clearly evident.

The first contour plots of particle exit positions (latitudes) and exit energies were presented in Section 4.5.1 after the binning process by means of which these contours are produced was explained with the help of Figure 4.5; this figure showed a scatter plot of particle exit latitudes and energies. Figure 4.6 presented the corresponding contour plot in the first panel where drift was scaled down directly to zero by setting $\kappa_{\mathrm{A},0} = 0.00 f_{\mathrm{d}}(\alpha)$. The effect of this direct scaling down of drift was clearly illustrated when comparing it to the second and third panels of Figure 4.6 which showed the exit positions and exit energies in the cases of $A > 0$ and $A < 0$ polarity cycles respectively, i.e. where $\kappa_{\mathrm{A},0} = 1.00 f_{\mathrm{d}}(\alpha)$. It was found that turning on drifts in the model led to larger energy losses and this was explained with the help of Figure 4.7, showing the regions in the heliosphere where pseudo-particles spend the most time during modulation; these regions were referred to as high activity regions. It was explained that turning on drifts led to different distributions of these high-activity regions over both radial distance and latitude and that this was a crucial factor when determining energy losses.

Section 4.5.2 explained how the extent of drift effects could be influenced indirectly through changing the amount of diffusion that occurs during the modulation process. The top panel of Figure 4.8 illustrated this through model solutions of differential intensity versus α in the case of three different values of the diffusion coefficient, corresponding to relatively high, intermediate and relatively low diffusion; the bottom panel showed the

$A > 0$ to $A < 0$ ratios in each of these cases. It was clearly evident from both these panels that an increase in diffusion led to a suppression or reduction in drift effects. This was again illustrated with the aid of contour plots and Figure 4.9 was similar to Figure 4.6, but using an increased value for diffusion; Figure 4.10 presented a zoomed in version of Figure 4.9 so that comparisons with the case for smaller diffusion could be made more effectively. Additional insight into the modulation process and effects of drifts were once again obtained through a contour plot showing the distribution of the high-activity regions over modualtion space in Figure 4.11.

Drift effects were considered as function of energy in Section 4.5.3. The top panel of Figure 4.12 illustrated this dependence on energy by means of intensity versus tilt angle profiles, comparing cases for 1 GeV and 250 MeV. It was clear from these profiles that drift effects were reduced with increasing energy. This was confirmed in the bottom panel, showing the $A > 0$ to $A < 0$ ratios for both energies 1 GeV and 250 MeV as well as for an intermediate energy 500 MeV. The energy dependence was then illustrated with the help of contour plots of exit positions and exit energies in Figures 4.13 and 4.14 which showed the cases for 100 MeV and 5 GeV respectively. Contour plots of the high activity regions were once again produced in order to yield additional insights and these were shown in Figures 4.16 and 4.17 for 100 MeV and 5 GeV respectively.

Chapter 5

Charge-Sign Dependent Modulation

5.1 Introduction

In this chapter, particle drift effects are illustrated in terms of the charge-sign dependent modulation of cosmic ray (CR) positrons e^+ and electrons e^-. The modulation of these species is first discussed briefly by providing only the essential background information. The energy dependence of the e^+ fraction, $e^+/(e^+ + e^-)$, calculated by the model employed in this study is presented and the results are shown to be in agreement with the qualitative picture provided by observations from the PAMELA spacecraft (Galper and Spillantini [2018]). The e^+ to e^- ratio, e^+/e^-, is then considered as function of solar activity and it is again illustrated that the model yields results that are in qualitative agreement with the work of other authors (e.g. Burger and Potgieter [1999]). New in this chapter is that cases with and without the inclusion of the drift scaling function $f_{\mathrm{d}}(\alpha)$ from Equation (4.1) are considered.

The final section of this chapter is devoted to providing a glimpse of research that can be done in future, using this model, to investigate drift effects. Specifically, it is illustrated how different scaling functions $f_{\mathrm{d}}(\alpha)$ can influence the e^+/e^- ratio as a function of solar activity and also how the inclusion of a time dependent magnetic field magnitude can affect the intensity versus solar activity profiles. Though the aim of this chapter is not to reproduce data, it is motivated that the model should be ideally suited to reproduce observations such as e^+/e^- ratios and the e^+ fraction in future studies.

5.2 Positron and Electron Modulation

For the purposes of this chapter, only the very basics of CR e^+ and e^- modulation are discussed. Because the focus is on the ratio, e^+/e^-, rather than on the modulation specifics for each of these species individually, such as e^+ or e^- energy spectra, this discussion is presented only in the most general terms.

As mentioned in Chapter 2, CRs that reach Earth are mainly composed of $\sim 98\%$ atomic nuclei (most of which are protons) and $\sim 2\%$ electrons, positrons and anti-protons, along with small abundances of heavier nuclei (e.g. Longair [1990], Simpson [1992]). Together, positrons and electrons constitute only about 1% of the proton intensity at 10 GeV (e.g. du Vernois et al. [2001]). Positrons and electrons are therefore exceedingly rare, but remain important because their propagation through the Galaxy is governed by energy-loss processes that are different from those of CR nuclei of the same energy; measurement of this CR component therefore provides additional information about the physical conditions and the propagation of CRs in interstellar space that are not accessible from the study of CR nuclear components alone (Boezio et al. [2000]). In addition, precise measurements of the e^+ and e^- spectra over a wide range of energy can be used to obtain information on the charge sign dependence of solar modulation.

Observed CR positrons and electrons may consist of a mixture of primary and secondary particles. Primary particles are accelerated in CR sources, such as supernova remnants, while secondary particles are produced mainly by the interactions of CR nuclei with the interstellar gas (see e.g. Boezio et al. [2000], Büsching et al. [2005], Serpico [2009], Hooper et al. [2009]). However, at the top of the atmosphere, the observed positron fraction, $e^+/(e^+ + e^-)$, is about $\sim 10\%$ at a few GeV (e.g. Golden et al. [1996]) and hence a large majority of electrons has to be of primary origin (Boezio et al. [2000]). See also Fanselow et al. [1969] and Buffington et al. [1975] for earlier measurements of the positron fraction in the 1 - 10 GeV range.

To calculate the energy spectra of positrons and electrons and to study their charge-sign dependent modulation, the local interstellar spectra (LISs) of these species need to be defined at the modulation boundary. The e^+ LIS used in this model was used by Vos [2016] (private communication) and is given by the expression

$$j_{\mathrm{LIS,e^+}} = j_{\mathrm{base}} + j_{\mathrm{excess}} \tag{5.1}$$

with

$$j_{\mathrm{base}} = 0.0335\xi^{-0.07}\left[\frac{\xi^{1.64} + 0.194^{1.64}}{1 + 0.194^{1.64}}\right]^{\frac{-3.39}{1.64}} \tag{5.2}$$

and

$$j_{\mathrm{excess}} = 11.7 \times 10^{-7}\xi^{15.00}\left[\frac{\xi^{1.5} + 0.84^{1.5}}{1 + 0.84^{1.5}}\right]^{\frac{-17.42}{1.5}} . \tag{5.3}$$

in units of particles/m^2/sr/s/MeV. As in Equation (3.1), $\xi = E/1\mathrm{GeV}$ where the energy E is given in GeV and divided by 1 GeV in order to obtain the dimensionless quantity ξ.

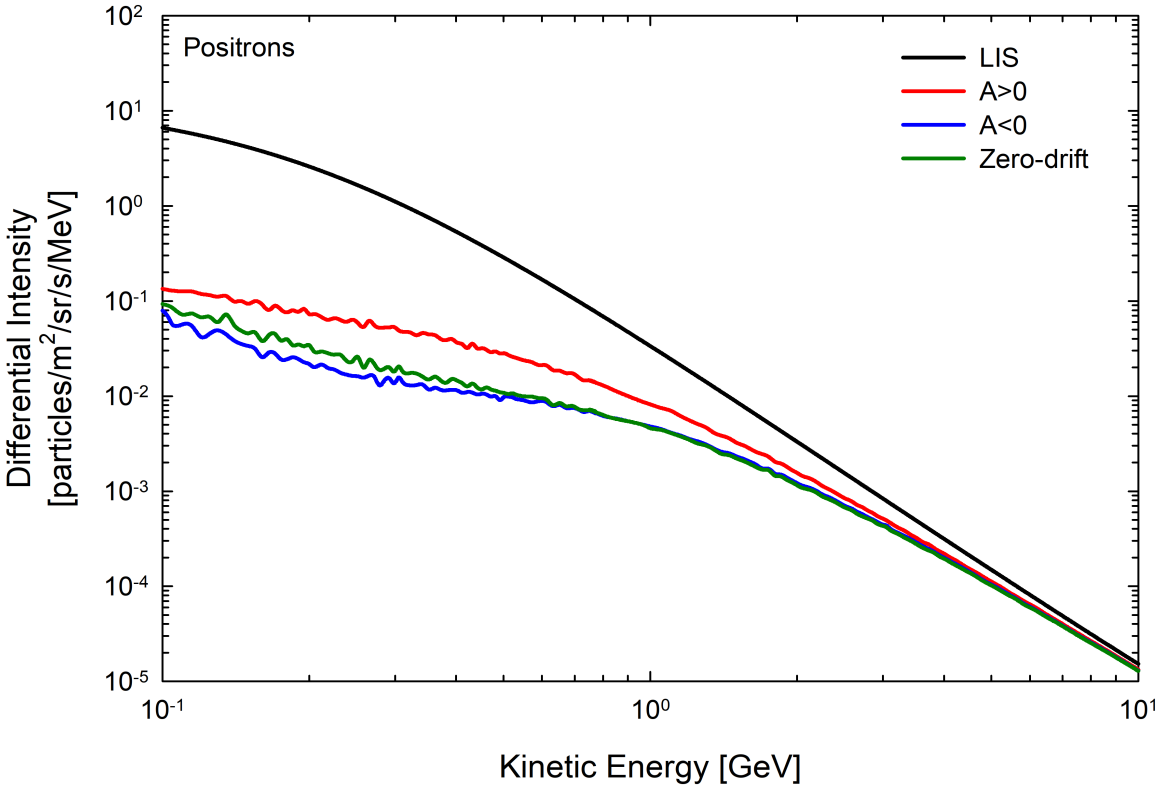


Fig. 5.1 *Positron spectra for 2009 solar minumum conditions. The black line shows the LIS, while the red, blue and green lines respectively represent the* $A > 0$*,* $A < 0$ *and zero-drift spectra at Earth.*

Figure 5.1 shows this e^+ LIS, together with modulated spectra at Earth for the zero-drift scenario (green line), as well as for each of the $A > 0$ (red line), and $A < 0$ (blue line) polarity cycles. The modulation parameters are those of the 2009 solar minimum determined for electrons by Vos [2011], but using the scaling function $f_{\mathrm{d}}(\alpha)$ of Equation (4.1); these parameters are indicated in Table 5.1. The actual polarity cycle of the 2009 solar minimum, i.e. $A < 0$, was unimportant in the context of this section and therefore $A > 0$ and zero-drift solutions were calculated using the same parameters. The $A > 0$ solution, during which positrons drift inwards over the poles, is higher than the zero-drift solution over the energy range 100 MeV to ~ 4 GeV. The $A < 0$ solution, during which positrons drift inward along the HCS, is lower than the zero-drift solution at energies 100 MeV to ~600 MeV. Compared to protons, the e^+ spectra do not assume the characteristic adiabatic slope at lower energies. This is because of the much smaller rest-mass of positrons, implying that these particles remain relativistic down to lower energies.

Table 5.1 This table shows the parameter values that were employed for the production of both the e^+ spectra in Figure 5.1 and the e^- spectra in Figure 5.2; these parameters were determined by Vos [2011]. All quantities are as defined in previous chapters.

Parameter	**2009**
α_{A} [degrees]	10.00
B_{E} [nT]	3.94
$\kappa_{\|\|,0}$ $[1 \times 10^{22}\mathrm{cm}^2/\mathrm{s}]$	13.70
$\kappa^0_{\perp r}$, $\kappa^0_{\perp\theta}$	0.02
$\kappa_{\mathrm{A},0} = f_{\mathrm{d}}(10°)$ with $c_1 = 100$	1.00
a	0.00
b	1.23
c	2.70
d	3.00
$P_{\mathrm{A},0}$ [GV]	0.16
P_{k} [GV]	0.45

The e^- LIS that was employed in this work is the LIS used by Vos [2016], given by the expression

$$j_{\mathrm{LIS,e^-}} = \frac{0.21\xi^{-1.35}}{\beta_c^2}\left[\frac{\xi^{1.65}+0.6920}{1.6920}\right]^{-1.1515} + j_{\mathrm{bump}} \tag{5.4}$$

with $\beta_c = v/c$ as defined by Equation (2.8); here

$$j_{\mathrm{bump}} = 1.73\exp\left[4.19 - 5.40\log\xi - 8.9\xi^{-0.64}\right], \tag{5.5}$$

where j_{bump} is as explained in more detail by e.g. Potgieter et al. [2015]. For more on the LIS for electrons, see also Potgieter and Nndanganeni [2013] and Potgieter [2014].

Figure 5.2 shows the e^- LIS, together with the modulated spectra at Earth for the zero-drift case (green line), as well as the $A > 0$ (red line) and $A < 0$ (blue line) polarity cycles. The modulation parameters were the same as in the case for positrons in Figure 5.1, i.e. those indicated in Table 5.1. The $A > 0$ solution, during which electrons drift inwards via the HCS, is lower than the zero-drift solution starting from 100 MeV to ∼600 MeV. The $A < 0$ solution, during which electrons drift inwards over the poles, is higher than the zero-drift solution at energies 100 MeV to ∼ 4 GeV. The behaviour of the spectra at lower energies is similar to that of positrons, since the rest-masses for these two species are the same.

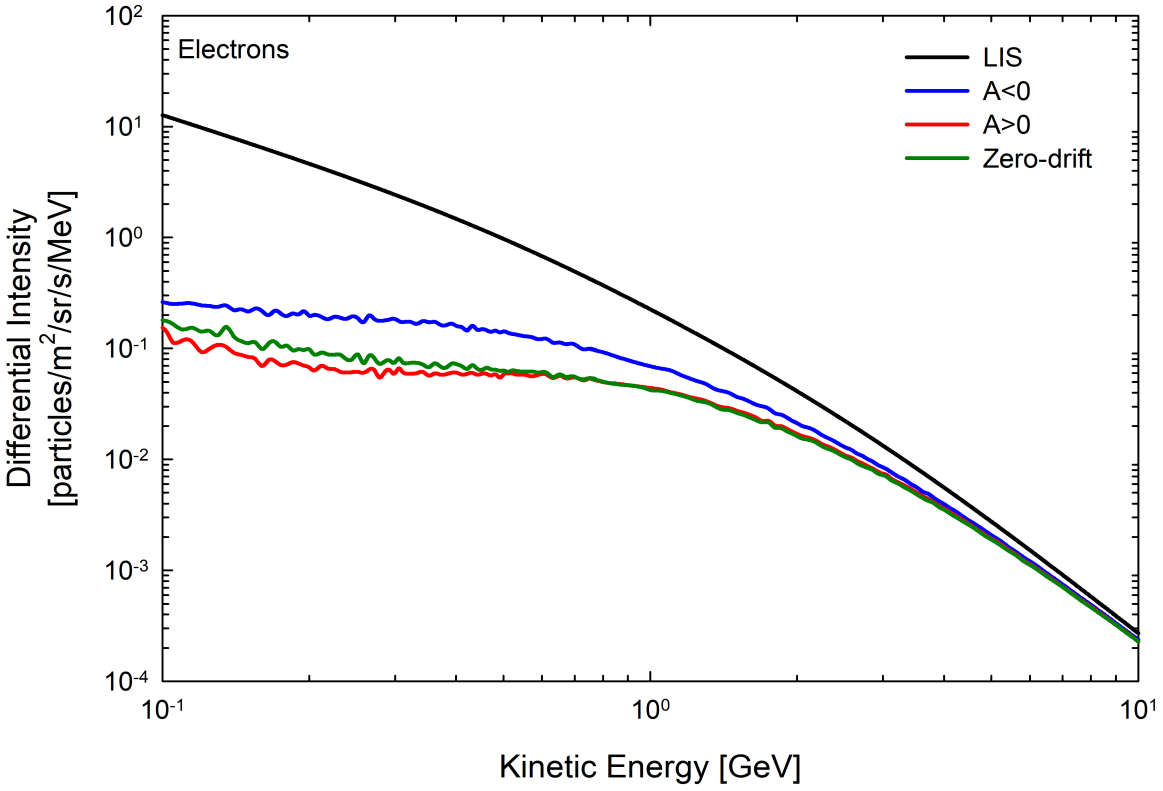


Fig. 5.2 *Electron spectra for 2009 solar minimum conditions. The black line shows the LIS, while the red, blue and green lines respectively represent the $A > 0$, $A < 0$ and zero-drift spectra at Earth.*

5.3 Positron Fraction as Function of Energy

The solution shown by the green line in Figure 5.3 is the e^+ fraction, i.e. $e^+/(e^+ + e^-)$, for the zero-drift case. At 100 MeV the e^+ fraction shows that just more than 30% of the combined e^+ and e^- intensities actually consists of positrons. This percentage then gradually decreases down to about 5% at 5 or 6 GeV, where it flattens off briefly and starts to increase shortly before reaching 10 GeV. For the zero-drift solution, this variation with energy must be entirely due to the difference in the e^+ and e^- LISs, considering that the same transport parameters were assumed in the model.

The red line shows the e^+ fraction in the case of $A > 0$ drift. In this case, the e^+ fraction starts off at about 50% at 100 MeV, stays more or less constant up to ∼200 MeV and then starts to decrease towards the zero-drift solution as energies are increased and the drift effect gets correspondingly smaller; at ∼10 GeV, it joins with the zero-drift solution, where drift effects become small to negligible. The e^+ fraction for the $A > 0$ polarity cycle is higher than the zero-drift values at lower energies because the $A > 0$ cycle will drift

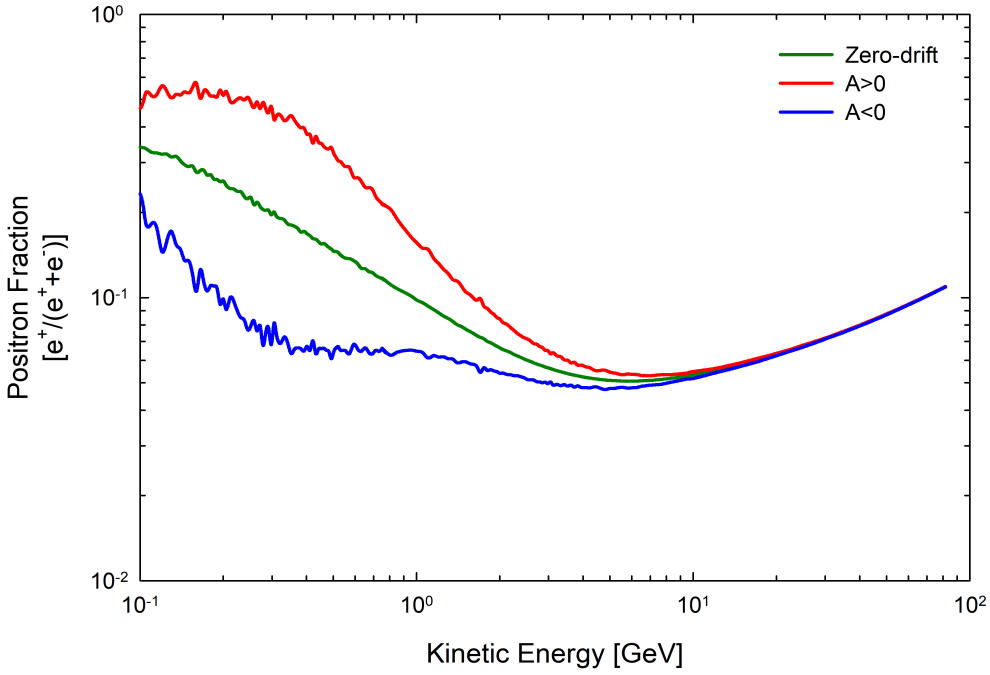


Fig. 5.3 *The positron fraction $e^+/(e^+ + e^-)$ as function of energy as calculated by the model featured in this work. The zero-drift solution is shown by the green line, the $A < 0$ solution by the blue line, and the $A > 0$ solution by the red line.*

positrons inward over the polar regions, while electrons will drift out over the polar regions - this will increase the e^+ intensities relative to those of electrons.

In the case of $A < 0$ drift, the e^+ fraction starts out between 20% and 30% and immediately starts decreasing. It also joins the zero-drift solution at about 10 GeV where drift effects have decreased to negligible levels. The e^+ fraction in this case is lower than for the zero-drift scenario because positrons will drift out over the polar regions while electrons will drift inward, leading to decreased e^+ intensities relative to those of electrons.

It is notable that the model used in this study shows that a significant increase occurs in the e^+ fraction at higher energies above $\sim$ 10 GeV. This is in agreement with measurements by both PAMELA (e.g. Adriani et al. [2009]; Galper and Spillantini [2018]) and AMS-02 (Feng et al. [2014]). This behaviour is due to the use of the e^+ LIS that includes the so-called positron excess. Figure 5.4 was taken from Galper and Spillantini [2018] and shows the data from PAMELA (red circles), as well as the calculation of Moskalenko and Strong [1998] using a model that assumes mainly secondary production of positrons. The data from PAMELA clearly shows a significant increase above $\sim$ 10 GeV, while the secondary production model predicts a continued decrease.

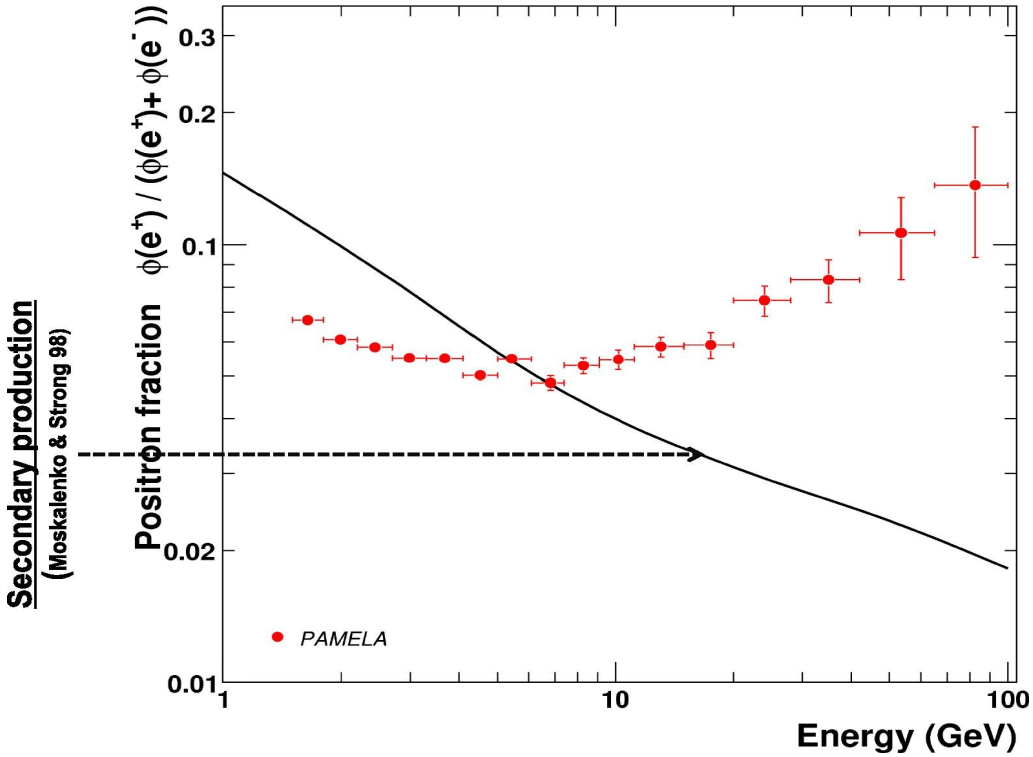


Fig. 5.4 *The positron fraction $e^+/(e^+ + e^-)$ as measured by PAMELA is indicated by the red circles, while the calculation by the secondary production model of Moskalenko and Strong [1998] is shown by the black line. This figure was taken from Galper and Spillantini [2018].*

This is, however, a topic of astrophysics and is not discussed in detail in this work, other than pointing out that such an increase may suggest a primary source of positrons such as pulsars (see e.g. Hooper et al. [2009]; Serpico [2009]; Venter et al. [2015]; Aguilar et al. [2019]). Earlier measurements also reported this increase, e.g. Müller and Tang [1987], Golden et al. [1987, 1994], Barwick et al. [1995], Barbiellini et al. [1996], and Barwick et al. [1997]; a study by Golden et al. [1996] could not confirm this increase. Authors such as Adriani et al. [2009] have concluded that a primary source such as an astrophysical object or even dark matter annihilation was necessary to explain such an increase. Cholis and Hooper [2013] point out that, while some dark matter models are no longer able to accommodate data measured by AMS, similar models may still explain this phenomenon. Adriani et al. [2014] also indicated that propagation models may need to be revisited in terms of dark matter annihilation or a pulsar contribution. For a discussion of this matter, see eg. Boudaud et al. [2015].

5.4 Positron to Electron Ratios as Function of Solar Activity

In this section, e^+/e^- ratios are calculated as function of tilt angle, i.e. solar activity. It is done with and without the inclusion of the drift scaling function $f_\mathrm{d}(\alpha)$ of Equation

(4.1), respectively. The results are indicated to be in agreement with work done by other authors such as Burger and Potgieter [1999].

Figure 5.5 shows the intensity versus tilt angle profiles at Earth for 750 MeV positrons (top panel) and electrons (bottom panel) for both the $A > 0$ (solid lines) and $A < 0$ (dashed lines) polarity cycles. The drift scaling function $f_{\mathrm{d}}(\alpha)$ is not used. The behaviour of the e^+ intensity is qualitative similar to that in the case of protons; since this was described in detail in Chapter 4, only a brief discussion is presented here.

During the $A > 0$ polarity cycle, in which positrons drift inwards over the polar regions, the intensity initially does not react much to an increase in α because, while α is small, such changes will primarily affect the equatorial regions. When α becomes large enough, outward drift along the HCS will interrupt inward diffusion significantly over larger parts of the heliosphere so that intensities decrease. Intensities will decrease especially once the HCS starts entering the higher latitudinal regions where it will oppose or interrupt both inward diffusion and inward drift over the polar regions.

During the $A < 0$ polarity cycle, a change in α is immediately reflected in the intensity because positrons now drift inward via the HCS in the equatorial regions: the intensity decreases as α is increased because the HCS becomes more wavy and more particles are scattered off it via diffusion before they can drift inward to reach Earth. At a certain value of α, this effect attains its maximum impact so that intensities do not decrease further, but flatten off. Intensities increase slightly at the highest values of α as the HCS interrupts the global drift pattern in the higher latitudinal regions and the intensities have to approach those of the zero-drift solution. The behaviour of electrons, having an opposite charge, is reversed, with respect to the $A > 0$ and $A < 0$ polarity cycles.

Figure 5.6 shows the intensities in the top and bottom panels of Figure 5.5 folded open over consecutive $A < 0$ and $A > 0$ polarity cycles. The results show the well known sharp peak during $qA < 0$ and flattened peak during $qA > 0$ cycles (Kóta and Jokipii [1983]), where q is the sign of the particle charge. Note that e^+ intensities are scaled by the red vertical axis, while e^- intensities are scaled by the blue vertical axis so that the abundance of electrons over positrons is evident.

Figure 5.7 shows the e^+/e^- ratio, also over the consecutive $A < 0$ and $A > 0$ polarity cycles; this was calculated directly from the results of Figure 5.6. The e^+/e^- ratio assumes the well-known 'W' and 'M' shapes during the $A < 0$ and $A > 0$ polarity cycles respectively, such as those shown by Burger and Potgieter [1999] where the e^- to proton and e^- to helium ratios were computed for a hypothetical solar activity cycle. These results are reprinted in Figure 5.8 at energies ∼3 GeV, ∼1 GeV and ∼0.3 GeV, normalised with respect to the minimum value for each ratio. The 'W' and 'M' shapes now occur during the $A > 0$ and $A < 0$ polarity cycles, respectively, because e^-/Helium and e^-/proton ratios were calculated rather than e^+/e^- ratios. Except for this reversal with respect to

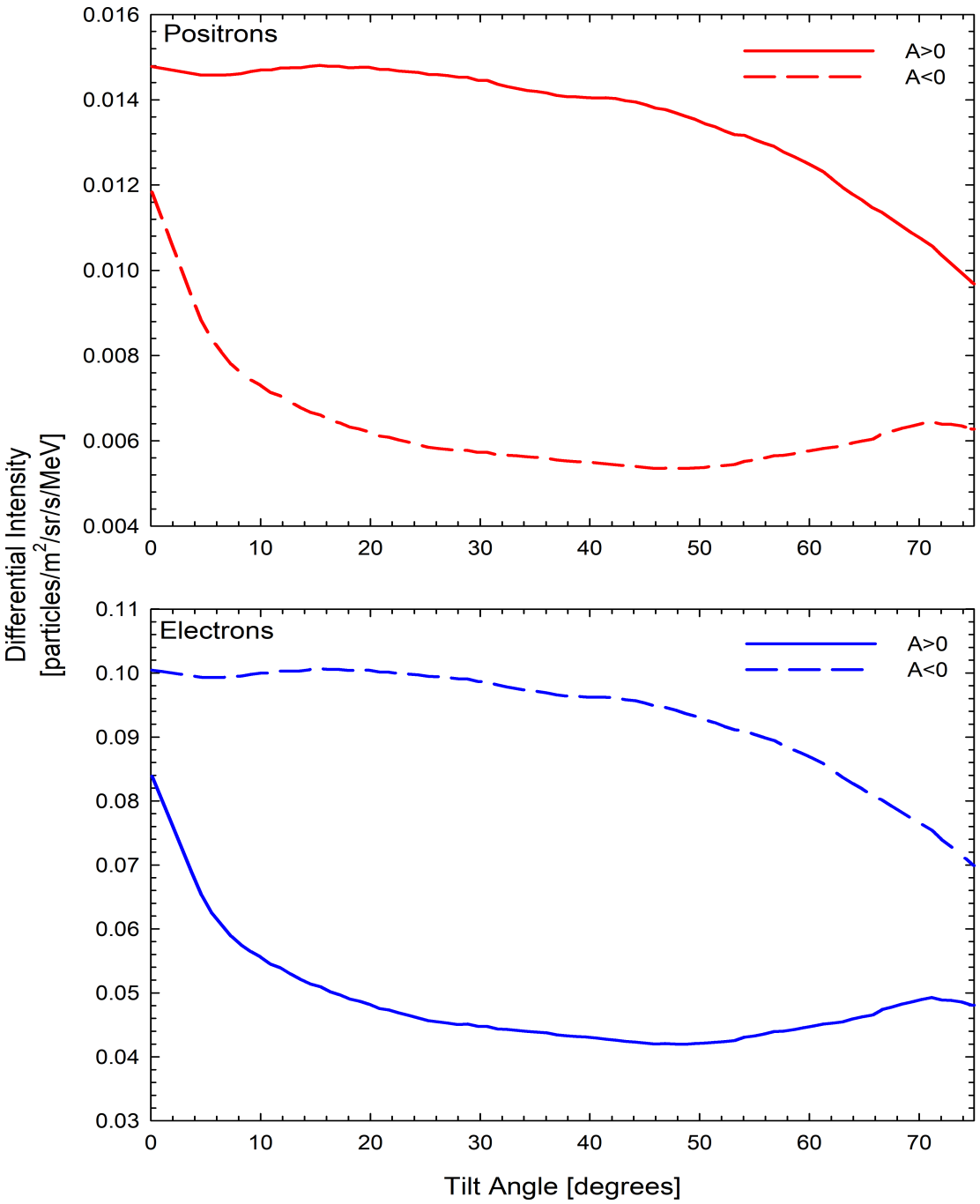


Fig. 5.5 *This figure illustrates drift effects without the inclusion of the drift scaling function* $f_{\mathrm{d}}(\alpha)$. *The top panel shows the computed intensity versus tilt angle profiles for 750 MeV positrons, while the bottom panel shows the solutions for electrons of the same energy; the* $A > 0$ *and* $A < 0$ *polarity cycles are indicated by the solid and dashed lines, respectively.*

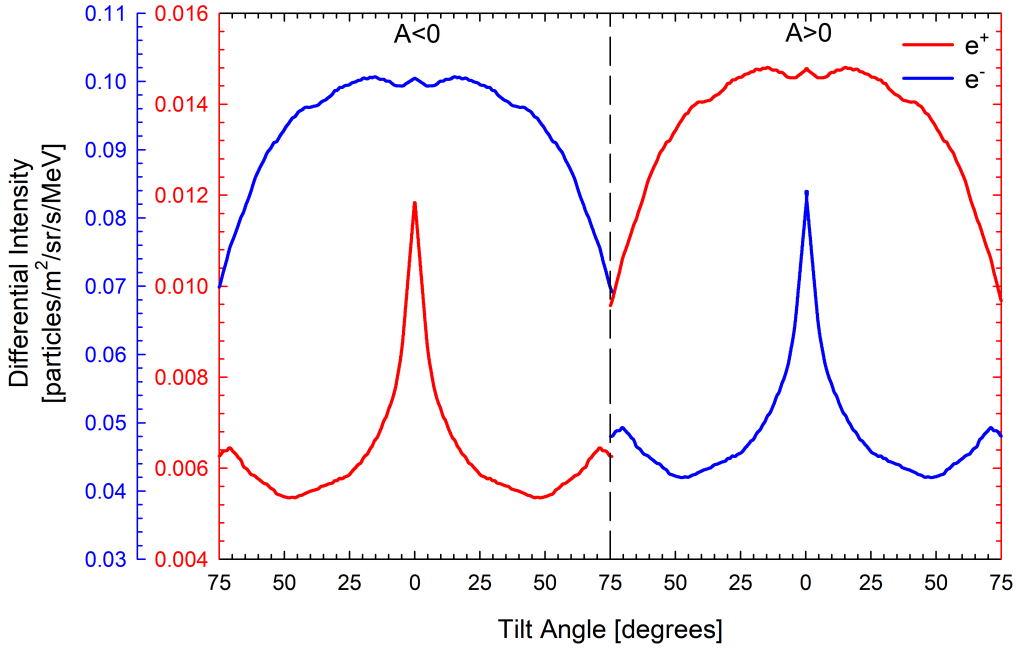


Fig. 5.6 *This figure shows the e^+ (red lines) and e^- (blue lines) profiles of Figure 5.5 folded open over consecutive $A < 0$ and $A > 0$ polarity cycles.*

the polarity cycle, the ratios possess the same qualitative behaviour as the e^+/e^- ratios. The solution in Figure 5.7 shows a jump in intensity at solar maximum $\alpha = 75°$, while this is not present in the Figure 5.8; this discrepancy can be traced back to Figure 5.5 where the loop formed by the $A > 0$ and $A < 0$ solutions was not closed at $\alpha = 75°$ because the drift was not scaled down. These results also agree qualitatively with observations (e.g. Bieber et al. [1999]).

Although the results of Figure 5.7 follow directly from the drift picture that was described in Figure 5.6, some additional insights can be obtained by explaining this figure in more detail. The e^+/e^- ratio is smaller during the $A < 0$ polarity cycle than during the $A > 0$ polarity cycle because positrons (electrons) now drift outward (inward) over the polar regions and therefore decreasing the amount of positrons compared to electrons. The results of this figure are explained, starting at solar minimum conditions $\alpha = 0°$ during the $A < 0$ polarity cycle and moving toward the right - since the profile is, per construction, symmetric around solar minimum, the part to the left of 0° is not described. In the following explanation, the profiles shown in Figure 5.6 have to be kept in mind, especially the slopes of these profiles.

At this point, i.e. $\alpha = 0°$ during $A < 0$ conditions, the ratio is about ∼0.120; note that these values are only mentioned so as to illustrate the relative variation of the profile with solar activity. The ratio decreases immediately when the tilt angle is increased because e^+ intensities, with poitrons drifting inwards along the HCS, will immediately decrease sharply (strong negative slope in Figure 5.6) with an increase in the waviness of the HCS,

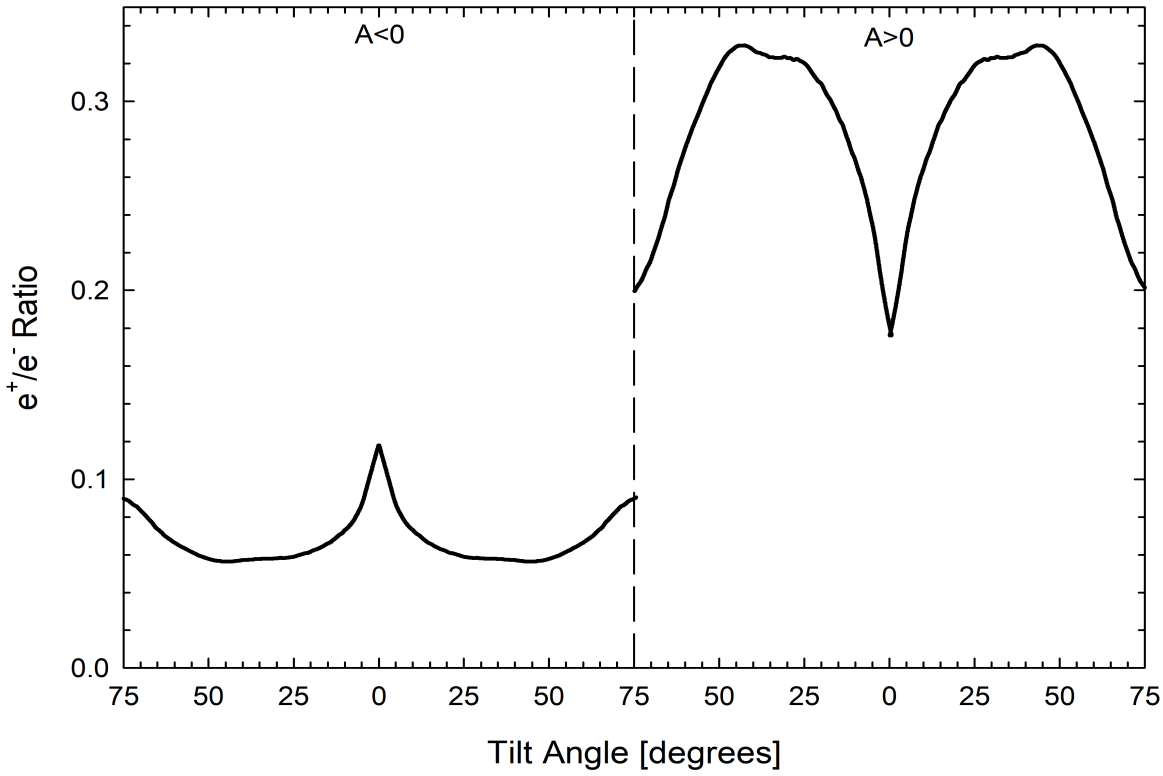


Fig. 5.7 *The e^+/e^- ratio as function of solar activity or tilt angle over the course of two successive $A < 0$ and $A > 0$ polarity cycles; this is without including the drift scaling function $f_{\mathrm{d}}(\alpha)$. The vertical dashed line shows the division between the $A < 0$ and $A > 0$ polarity cycles.*

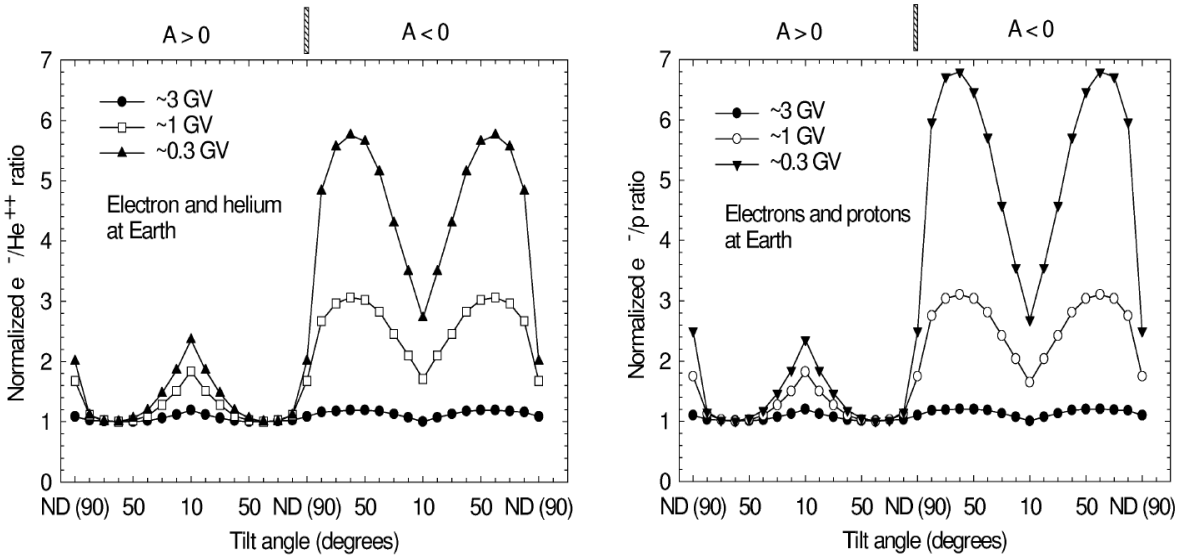


Fig. 5.8 *Tilt angle and solar polarity dependence of the electron/Helium (left) and electron/proton (right) ratios. These ratios are normalised with respect to the minimum value for each ratio. This figure was obtained from Burger and Potgieter [1999].*

while e^- intensities will remain largely unaffected (negligible slope). Ratios decrease down to about ∼0.060 at $\alpha \approx 20°$, where it flattens off when any further increase in the HCS is no longer effective in reducing e^+ intensities relative to those of electrons (the intensity profiles in Figure 5.6 show negative slopes of comparable magnitude). When the HCS enters higher latitudinal regions, e^- intensities decrease sharply (strong negative slope), while e^+ intensities now show an increase (weaker, but positive slope). This causes the e^+/e^- ratio to start increasing at $\alpha \approx 50°$ to reach ∼0.095 at $\alpha = 75°$, i.e. at solar maximum.

At this point, the jump that is seen in the intensities at solar maximum comes into effect so that a corresponding jump occurs in the ratio: the ratio increases from ∼0.095 for the $A < 0$ polarity cycle to about 0.200 for the $A > 0$ polarity cycle. From here, the ratio increases sharply up to about ∼0.325 at $\alpha \approx 45°$. The reason for this sharp increase is obvious when comparing Figure 5.6: between $\alpha \approx 75°$ and $\alpha \approx 45°$, e^+ intensities increase sharply (strong positive slope), while e^- intensities show a slight decrease (weaker negative slope); when solar activity decreases from $\alpha = 75°$, e^+ intensities increase immediately, because the HCS is now removed/withdrawn from the polar regions so that positrons can drift inwards. Intensities flatten off slightly between $\alpha \approx 45°$ and $\alpha \approx 25°$ as any further decrease in the HCS waviness is not as effective in increasing e^+ intensities over those of electrons; both e^+ and e^- intensities now show positive slopes of comparable magnitude and hence the ratio flattens off. The ratio then drops rapidly to levels of ∼0.180, as the decreasing HCS allows more electrons to drift inwards along the HCS without being scattered; this is seen in the sharp increase in e^- intensities (strong positive slope), while the e^+ intensities flatten off (weak to negligible slope).

Figure 5.9 is similar to Figure 5.5, but this time employing the drift scaling function $f_\mathrm{d}(\alpha)$ of Equation (4.1) with $c_1 = 100$. The important difference is therefore that the loop formed by the $A < 0$ and $A > 0$ solutions is now closed at $\alpha = 75°$ (not fully closed due to smoothing of the results). Figure 5.10 is similar to Figure 5.6, where the intensities of Figure 5.9 are once again folded open over consecutive polarity cycles. The jump in intensities at the transition between solar minimum and maximum conditions is now largely removed. From these results, the e^+/e^- ratio is again calculated and shown in Figure 5.11. This illustrates the removal of the jump that occurs across solar maximum in Figure 5.7, with the inclusion of $f_\mathrm{d}(\alpha)$, so that the results are in even better agreement with those of Burger and Potgieter [1999]. The small jump that still occurs at the transition between solar minimum and maximum is, once again, ascribed to the smoothing process; this jump has a magnitude of only about 0.01 which is small on the scale of this graph, i.e. only about 4% of the difference between the lowest and highest points on this graph.

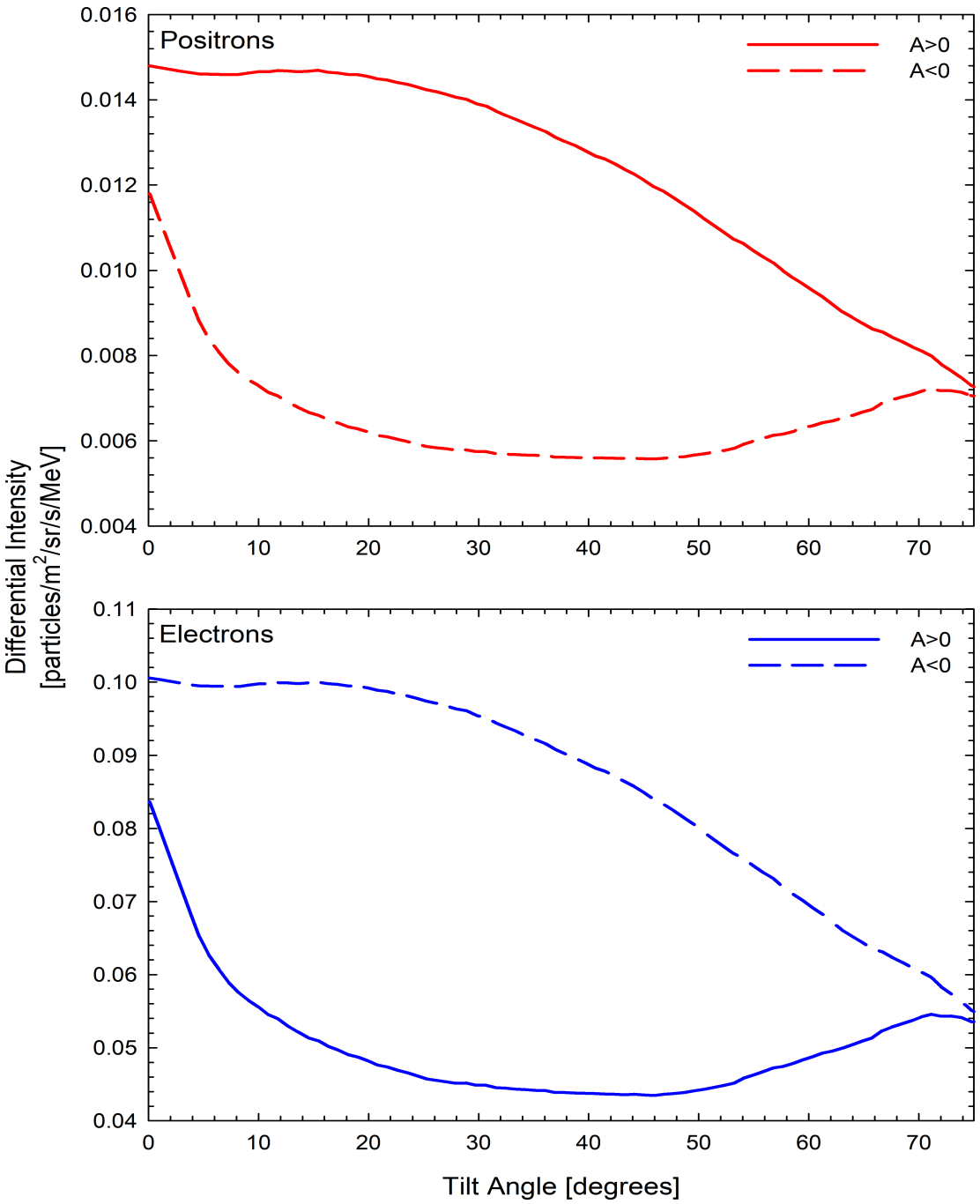


Fig. 5.9 *This figure illustrates drift effects with the inclusion of the drift scaling function* $f_{\mathrm{d}}(\alpha)$. *The top panel shows the computed intensity versus tilt angle profiles for 750 MeV positrons, while the bottom panel shows the solutions for electrons of the same energy; the* $A > 0$ *and* $A < 0$ *polarity cycles are indicated by the solid and dashed lines respectively.*

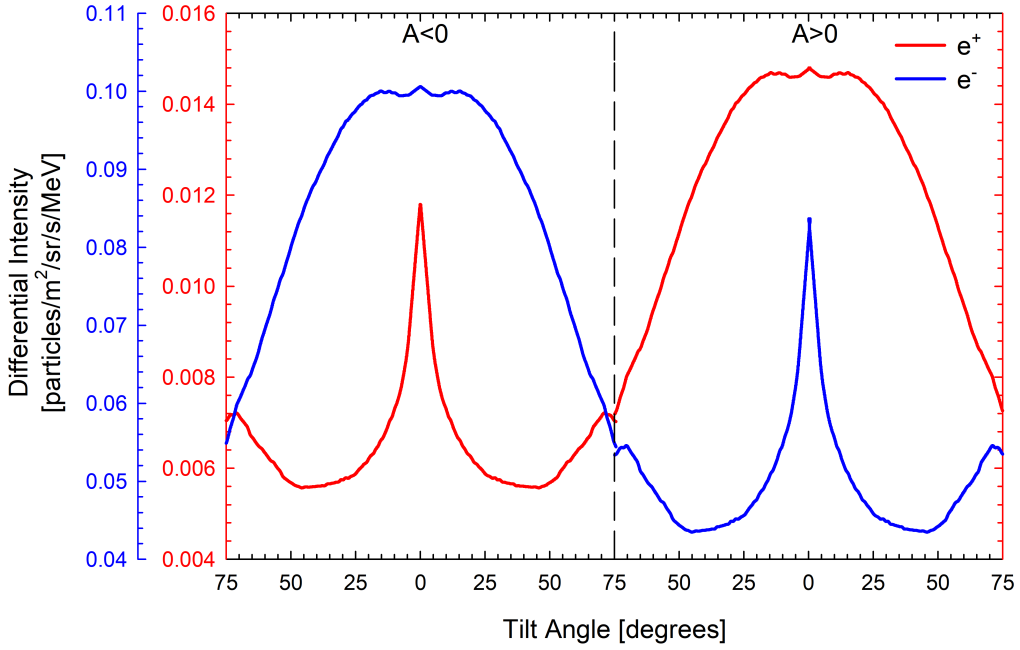


Fig. 5.10 *The e^+ (red lines) and e^- (blue lines) profiles of Figure 5.9 folded open over consecutive $A < 0$ and $A > 0$ polarity cycles.*

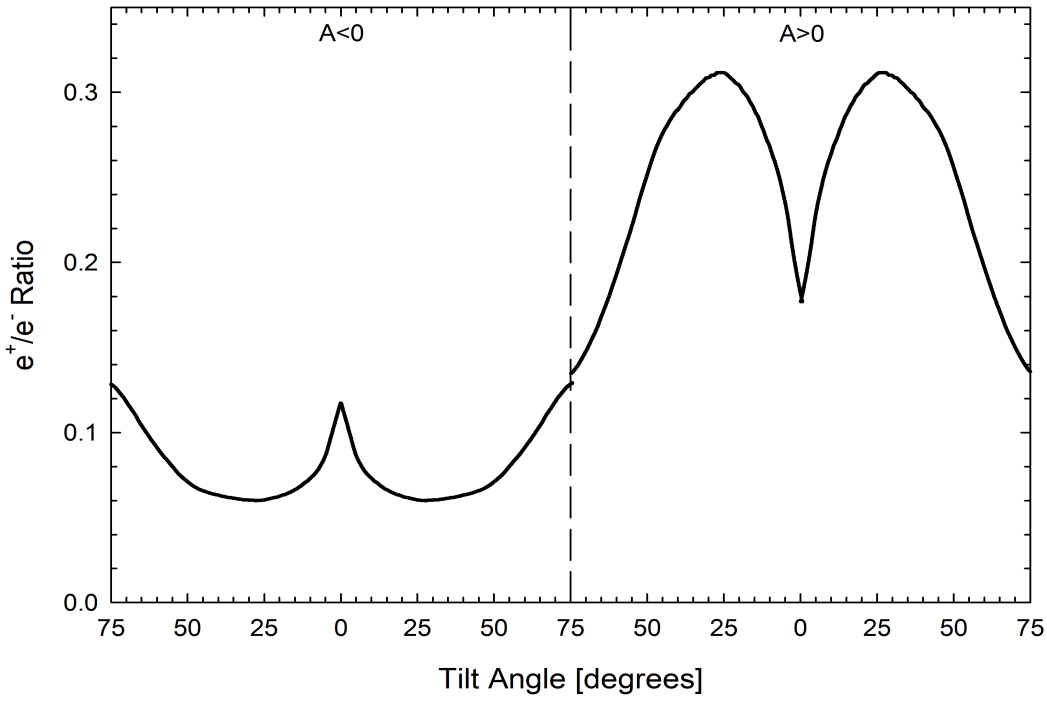


Fig. 5.11 *The e^+/e^- ratio as function of solar activity or tilt angle over the course of two successive $A < 0$ and $A > 0$ polarity cycles; this is with inclusion of the drift sacling function $f_{\mathrm{d}}(\alpha)$. The vertical dashed line shows the division between the $A < 0$ and $A > 0$ polarity cycles.*

5.5 Future Research

This section provides a view of research that may be done in future, consisting of three parts: the first shows how the e^+/e^- ratio profile can be manipulated via different settings for the drift scaling function $f_{\mathrm{d}}(\alpha)$ in Equation (4.1); the second part shows how more realistic profiles could be obtained by including a time-dependent magnetic field magnitude; part three of this section considers a small selection of relevant satellite observations. The results presented in this section are not meant to be complete or final and can, as such, be improved upon. These results are therefore presented in a very general sense, only serving so as to give a glimpse of what can be done in future by applying a modulation model such as the model featured in this work.

5.5.1 The Drift Scaling Down Function

The top panel of Figure 5.12 shows the effect that reducing the value of c_1 has on the profile of $f_{\mathrm{d}}(\alpha)$ in Equation (4.1). The cases for c_1 =100, 50, 40, 30 and 10 are represented by the red, blue, green, magenta and dark red lines, respectively. In all cases $f_{\mathrm{d}}(0^\circ) = 1.0$, while $f_{\mathrm{d}}(75^\circ) = 0.0$, so that drifts are decreased from full drift at $\alpha = 0^\circ$ to zero drift at $\alpha = 75^\circ$. As the value of c_1 is reduced, the decrease of $f_{\mathrm{d}}(\alpha)$ towards zero starts at successively smaller values of α and the function reaches zero at successively smaller values of α. Comparing the cases for $c_1 = 100$ and $c_1 = 10$, $f_{\mathrm{d}}(\alpha)$ remains very close to 1.0 even up to 15° in the former case, while in the latter case it is already well below this level; in the former case, $f_{\mathrm{d}}(\alpha)$ decreases to 0.0 only at $\alpha = 75^\circ$, while in the latter case it decreases to 0.0 as early as $\alpha \approx 55^\circ$.

The bottom panel shows the corresponding effect that decreasing the value of c_1 has on the e^+/e^- ratio at Earth and at 750 MeV, as function of α. All modulation parameters are still of the same order of magnitude as those used by Vos [2011], although their exact values are not important for the purposes of this section. This panel is described starting at $\alpha = 0^\circ$ during the $A < 0$ polarity cycle, then moving to the right along the horizontal axis, and ending at $\alpha = 0^\circ$ during the $A > 0$ polarity cycle; solutions are symmetric around $\alpha = 0^\circ$ in both polarity cycles and the description of the figure is therefore limited to this range of α.

For all values of c_1, starting at $\alpha = 0^\circ$ during the $A < 0$ polarity cycle and moving towards the right on the horizontal axis, the solutions start out at the same level of intensity because $f_{\mathrm{d}}(\alpha) \approx 1.0$ for $\alpha \in [0^\circ, 6^\circ]$. For all values of c_1, the e^+/e^- ratio immediately decreases with an increase in α. All of these solutions, i.e. for all values of c_1, reach a value of α where they stop decreasing and start to flatten off; this value of α is smaller for smaller c_1, while the level of intensity at which this occurs is higher for smaller c_1. After this flattening off in intensities, all solutions start to increase again and do so at smaller

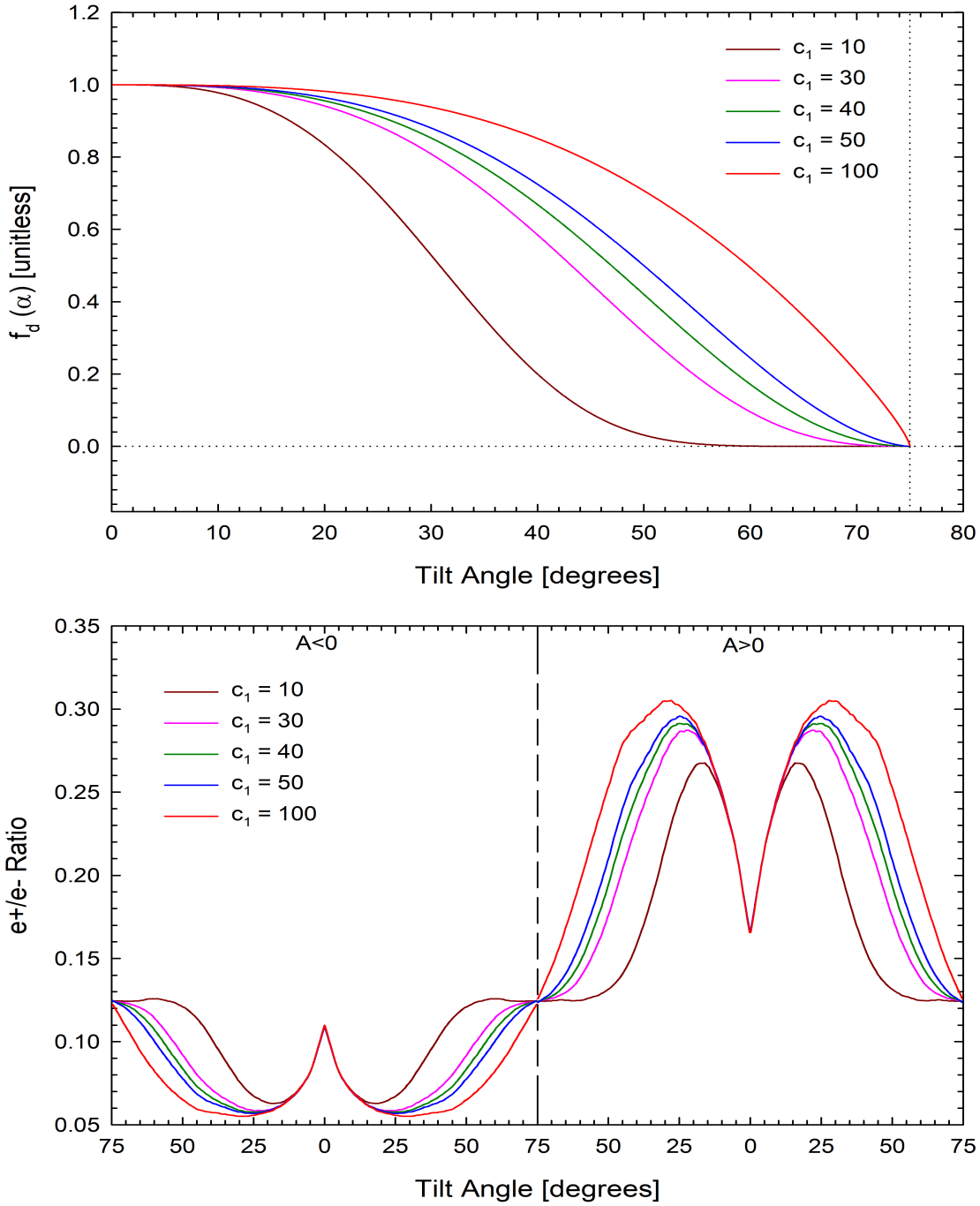


Fig. 5.12 *The top panel shows the drift scaling function* $f_{\mathrm{d}}(\alpha)$ *for different choices of the parameter* c_1*. The bottom panel shows the* e^+/e^- *ratios at 750 MeV, resulting from each of these choices, over two consecutive* $A < 0$ *and* $A > 0$ *polarity cycles. In both panels, the cases for* $c_1 = 10, 30, 40, 50,$ *and* 100 *are presented by the dark red, magenta, green, blue and red lines, respectively.*

values of α for smaller values of c_1. In each case, intensities increase towards the same value at $\alpha = 75°$, because $f_d(75°) = 0.0$; for smaller c_1, this value is reached at $\alpha < 75°$ because $f_d(\alpha) = 0.0$ for successively smaller values of α as c_1 is decreased. After the flattening, all solutions start increasing again and this increase occurs at smaller α for smaller c_1. The result is a flattening in the ratio around $\alpha = 75°$ in all cases but the case for $c_1 = 100$, and starting at successively smaller values of α for smaller values of c_1. All intensities increase towards a maximum value at an α which is successively smaller for smaller values of c_1; this maximum is also smaller for smaller values of c_1. After the maximum in each case, the solutions start to decrease towards the same value at $\alpha = 0°$, because $f_d(\alpha) = 1.0$ for all values of α up to 6° removed from solar minimum.

It is therefore evident that, during the $A < 0$ polarity cycle, e^+/e^- ratios are higher for smaller c_1 over the range of α for which the solutions are not equal. This implies that smaller drift effects lead to higher e^+/e^- ratios during much of the $A < 0$ polarity cycle. During the $A > 0$ polarity cycle, on the other hand, the e^+/e^- ratios are lower for smaller values of c_1. This implies that smaller drift effects lead to lower e^+/e^- ratios over much of the $A > 0$ polarity cycle.

5.5.2 A More Realistic Time Dependence

A way to improve future model solutions, is to not change α linearly, but to read into the model actual values of α, each coupled to a particular Carrington Rotation number (CRN), together with the corresponding B_E, i.e. the value of the observed magnetic field at Earth; see Raath and Potgieter [2017] for an example of this. This will effectively include a more realistic time-dependent component into model solutions.

As an example, this was done for CRNs 2024 to 2176, corresponding to the time period December 2004 to April 2016, which overlaps with the period of time over which the PAMELA spectra were reproduced in Chapters 3 and 4. The values of α for this period are shown in the top panel of Figure 5.13; the black line shows the calculations according to the radial model (data obtained from `http://wso.stanford.edu/Tilts.html`), while the red lines show the nonlinear regressions yielding the values of α to be used in the model. The corresponding values for B_E are shown in the bottom panel of Figure 5.13 where the black line indicates the data from ACE, averaged over one Carrington Rotation (`https://omniweb.gsfc.nasa.gov`), and the red lines once again show the nonlinear regressions. The α and B_E values according to the regressions were then read into the model and the solutions calculated.

In both the cases for α and B_E the period ranging from CRN 2024 to 2176 was divided into three regions, indicated by the vertical dashed lines, and a regression was performed for each region. This division into three regions was merely to enable suitable regressions and the CRNs at which the vertical lines are drawn have no other significance. Furthermore, the ranges of these regions did not need to be correlated for α and B_E: in the case of α the regression regions were separated at CRNs 2088 and 2135, while in the case of B_E they

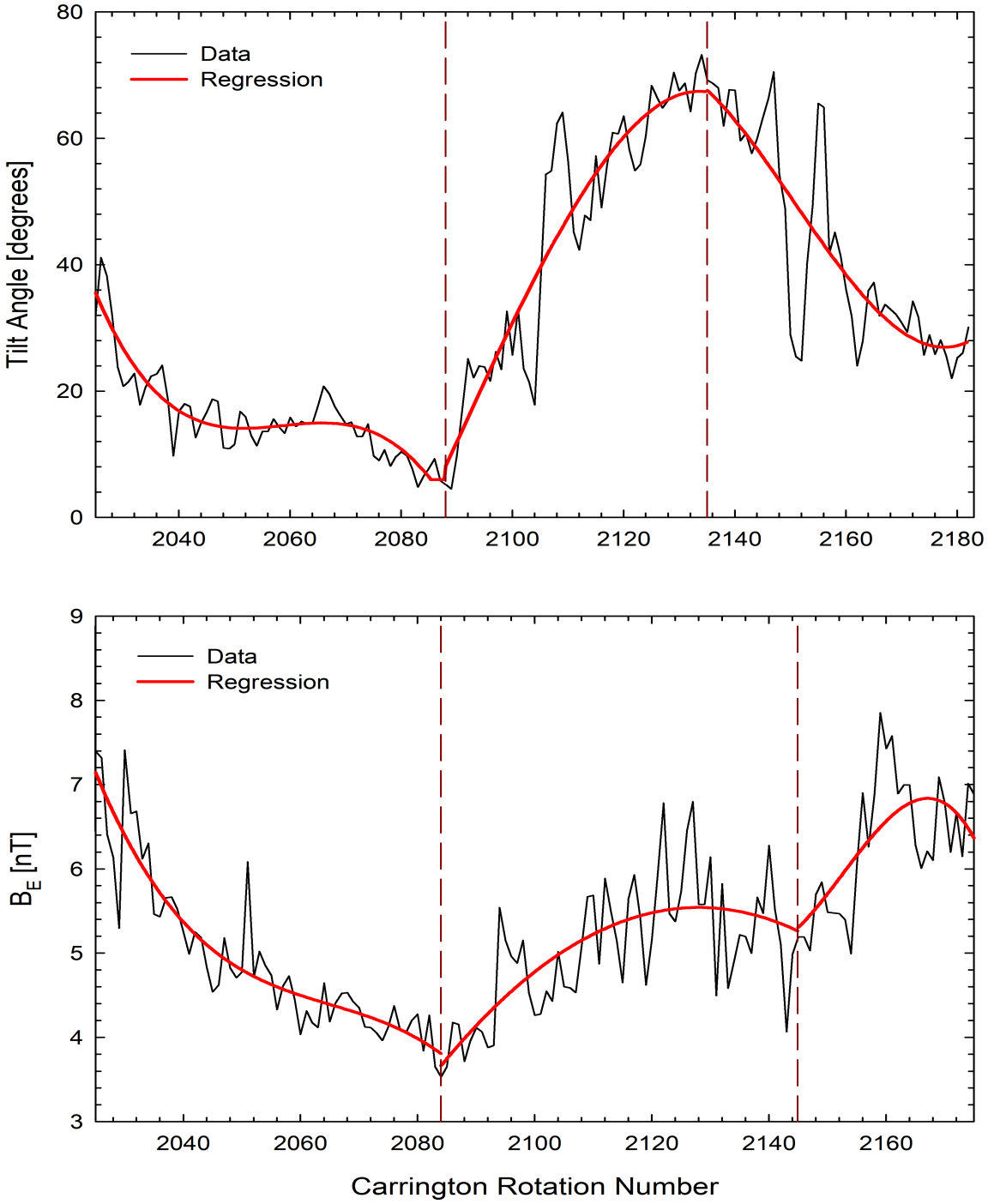


Fig. 5.13 *The top panel shows the tilt angle over Carrington Rotations 2024 to 2176. The black lines are as calculated by the radial model (*`http://wso.stanford.edu/Tilts.html`*), while the red lines show the various regressions fitted through these values. In the bottom panel, the black line shows the magnetic field magnitude at Earth* B_{E} *as measured by ACE (*`https://omniweb.gsfc.nasa.gov`*), while the red line again shows the regressions. In both panels, the vertical dashed lines separate the respective regression regions.*

were separated at CRNs 2084 and 2145. The procedure followed here is only preliminary and can certainly be improved upon in future by using more advanced regression methods; the discontinuities that occur in the regressions at the boundaries of the regression regions, i.e. at the vertical dashed lines, should also be removed in future. For the purposes of this work, however, the current procedure proved sufficient.

The solutions computed this way for 750 MeV positrons at Earth are shown in Figure 5.14 where the red lines represent the $A < 0$ polarity cycle (CRNs 2024 to 2148) and the blue lines represent the $A > 0$ polarity cycle (CRNs 2128 to 2176). The $A < 0$ and $A > 0$ polarity cycles therefore overlap during the transition period between CRNs 2127/8 and 2147/8, as discussed in Chapters 3 and 4. The top panel shows computations obtained only changing α without changes in B_{E}, while the bottom panel shows the solutions where the changes in B_{E} were taken into account. It is clear that the inclusion of such changes in the magnetic field magnitude notably changes the computed solutions. All modulation parameters, except α and B_{E} were still set to values similar to those of Vos [2011]. This is sufficient for the current purposes, since the interest here is not on reproducing any data, but rather on the dependence of the solutions on α and B_{E}.

The results of Figure 5.14 are best explained considering the bottom panel first, i.e. the case where the changes in B_{E} were also accounted for, and then referring back to the top panel. The figure is explained starting at the point on the graph labeled 2024, indicating CRN 2024, and following the arrows along the computed solutions; only the CRNs most essential to the explanation of this graph are indicated so as to ensure the readability of the graph. Looking at the top panel of Figure 5.13, tilt angles are seen to decrease starting at CRN $\sim$ 2024 up to about CRN $\sim$ 2050, while the bottom panel shows that B_{E} is decreasing over this range of CRNs. Therefore, the intensity versus tilt angle profile is traced towards the left, while increasing. The top panel of Figure 5.13 shows α staying constant in the range CRN $\sim$ 2050 to CRN $\sim$ 2070, while the bottom panel shows that B_{E} is still decreasing. The result is a vertical ascent of the intensity versus α profile over these ranges of CRNs. From CRN $\sim$ 2070 to CRN $\sim$ 2088, α again decreases and the red line proceeds towards smaller α; B_{E} is still decreasing up to CRN $\sim$ 2084 and the intensities are therefore still increasing, eventually reaching the point labeled 2088. The jump that occurs in the regression at CRN 2084 (bottom panel of Figure 5.13) is also evident in the bottom panel of Figure 5.14 between CRN $\sim$ 2084 and $\sim$ 2088. At this point, i.e. CRN $\sim$ 2088, α starts increasing, while B_{E} is now also increasing. The resulting intensity versus α profile therefore goes to the right of the figure while decreasing. The tilt angle now increases all the way up to CRN $\sim$ 2135, while B_{E} is only increasing up to about CRN $\sim$ 2128 and the intensity versus α profile decreases up to this point. It then flattens off as B_{E} flattens off and even increases slightly when B_{E} starts decreasing at CRN $\sim$ 2130 (not indicated on the graph). At CRN $\sim$ 2135, α starts decreasing again and therefore the red line turns around and starts going back to the left in the case that the polarity cycle is still assumed to be $A < 0$; it then stays at more or less the same levels up

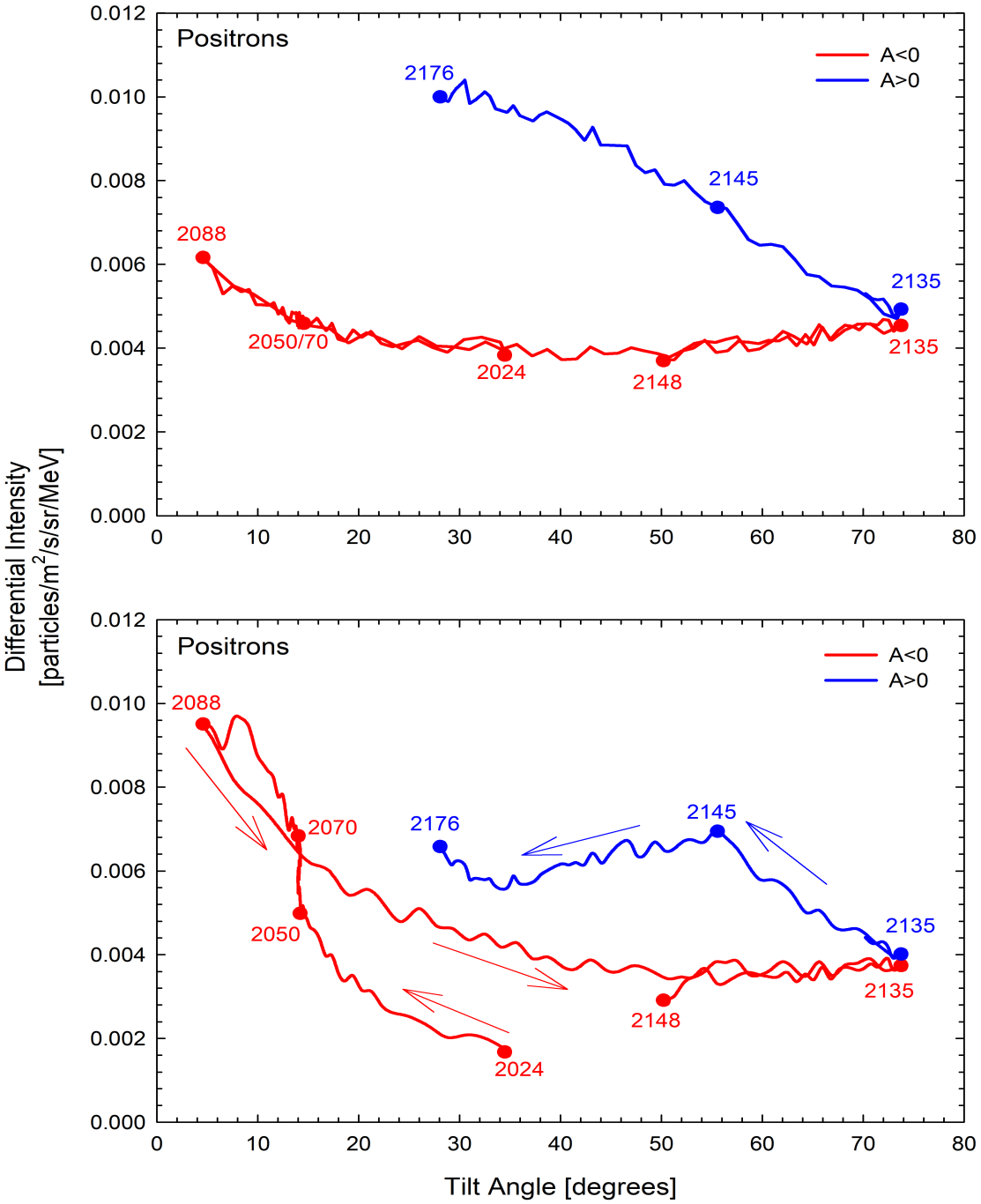


Fig. 5.14 *These panels show the intensity versus tilt angle (solar activity) profiles for 750 MeV positrons at Earth where the value of the tilt angle α was not changed linearly, but followed a profile corresponding to the period of CRN 2024 to 2176. The top panel shows these profiles with no temporal change in the HMF magnitude at Earth B_{E}, while the bottom panel shows these profiles where B_{E} follows the time dependent profile shown in the bottom panel of Figure 5.13. In both the top and bottom panels, the $A < 0$ polarity cycle is indicated by the red lines, while the $A > 0$ polarity cycle is indicated by the blue lines. The corresponding CRNs are also indicated and the arrows provide an indication of how to interpret these figures.*

to CRN $\sim$ 2145 because the change in B_{E} is very small up to this point. When followed to the end of the transition period at CRN 2148, it is clear that the intensity has started to decrease again, in response to the increasing value of B_{E}.

If an $A > 0$ polarity cycle (blue line) is assumed at the start of the transition period, i.e. CRN 2127/8 (not indicated on the graph), the intensity is traced towards the right at CRN 2135, where it turns around and proceeds to the left because α is now decreasing. The intensity is increasing between CRN 2135 and 2145 because B_{E} is decreasing. Note that this increase is much more pronounced that in the $A < 0$ case; the reason for this is clear: α is decreasing and so the HCS is removed from the higher latitudinal regions so that more particles can drift inward over the polar regions during the $A > 0$ polarity cycle. At CRN 2145, B_{E} starts increasing, with α still decreasing, and the result is the blue line traced to the left while decreasing. Between CRN 2168 (not shown on the graph) and 2176 B_{E} decreases so that the intensity increases again.

It is now easy to interpret the top panel of Figure 5.14 by merely neglecting the changes that occur in the value of B_{E}. With this change neglected, intensities stay close enough to each other so that the only difference can be ascribed to stochastic considerations inherent in the model.

Related studies, i.e. studies of intensity versus tilt angle loops, were performed by Moloto [2015] and such investigations present perfect opportunity for comparative studies. Moloto [2015] used the concept of an effective tilt angle, i.e. a tilt angle value calculated from the average of the tilt angles over the previous 18 months, to emulate time dependence. This is similar to what was done in Chapters 3 and 4 of this study. Moloto et al. [2018] applied an improved simulated time dependence into an their modulation model and this approach can also, in future, be incorporated into the model featured in this study.

5.5.3 Observations

This section presents a small selection of relevant data which is available from various spacecraft, focusing on the e^+ fraction and e^+/e^- ratios as a mean to investigate charge-sign dependent modulation. The data is not discussed in detail, but merely presented as an indication of possible future applications for the model featured in this work. Earlier in this chapter, it was indicated that the model yielded results consistent with expectations based on existing research and, furthermore, that it could be improved upon by including a more realistic time dependence. These considerations render the model particularly well suited for studying data such as the samples that are provided in this section.

Figure 5.15 presents a selection of $e^+/(e^+ + e^-)$ data, compiled by Munini et al. [2017] for various spacecraft and periods of time. Observations from PAMELA are shown for July 2006 to December 2009 (solar minimum as in Adriani et al. [2013]), May 2011 to November 2013, and January to December 2015. Other measurements, referring to the previous $A > 0$ polarity cycle, are also shown: HEAT94+95 (Barwick et al. [1997]), CAPRICE94

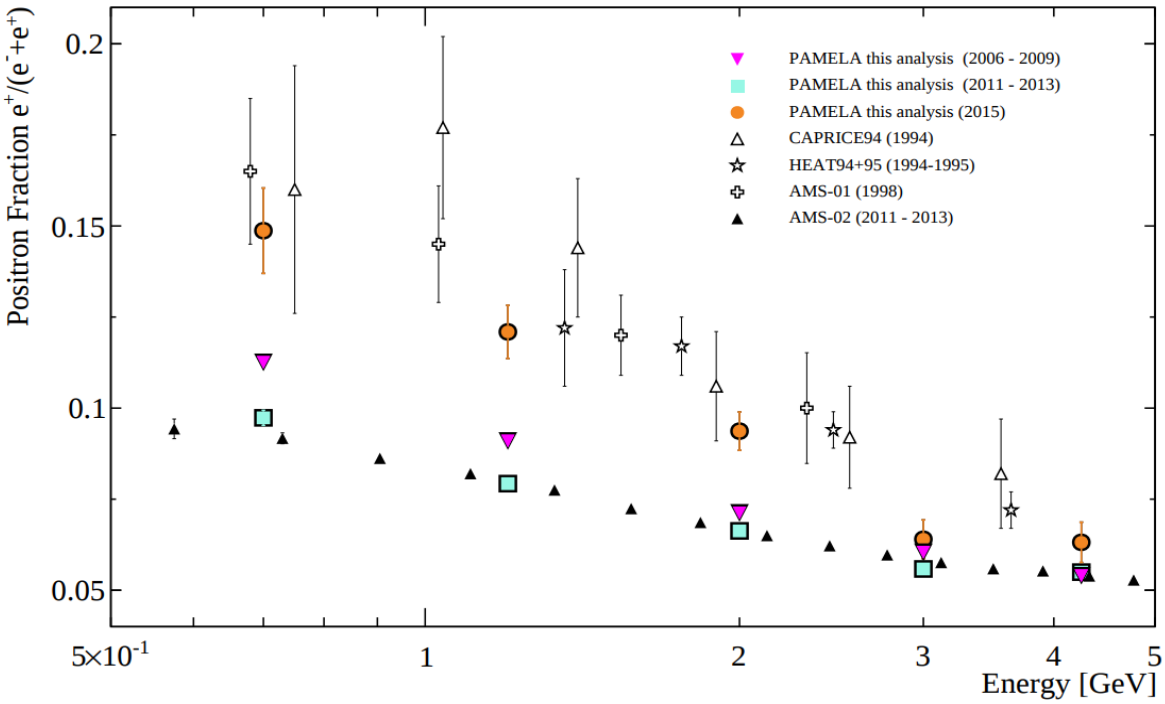


Fig. 5.15 *The positron fraction $e^+/(e^+ + e^-)$ derived by Munini et al. [2017] for three time periods: July 2006 to December 2009 (magenta inverted triangles), May 2011 to November 2013 (blue squares), and January to December 2015 (orange circles). Other measurements are also shown: HEAT94+95 (empty stars), CAPRICE94 (empty triangles), AMS-01 (empty crosses) and AMS-02 (black triangles). This figure was taken from Munini et al. [2017].*

(Boezio et al. [2000]), and AMS-01 (Alcaraz et al. [2000]). Results from AMS-02 (Accardo et al. [2014]) for 2011 to 2013 are shown as well. Except for the variation as function of energy, this data also shows a dependence on time which will need to be reproduced sufficiently.

Figure 5.16, adapted from Munini et al. [2017], shows the e^+/e^- ratio as normalised to the July to December 2006 time period and measured at Earth by PAMELA for three different intervals of energy, i.e. 0.5 GeV to 1.0 GeV (top panel), 1.0 GeV to 2.5 GeV (middle panel) and 2.5 GeV to 5.0 GeV (bottom panel). The shaded region on the graph indicates a transition period, i.e. a period where the HMF polarity is not known, which is similar to the transition period defined in (Sun et al. [2015]). The variation of the e^+/e^- ratio with time as well as its dependence on energy should provide further opportunity for the application of the model. For an example of a study where a numerical modulation model was applied extensively to model the e^+/e^- ratio, see e.g. Tomassetti et al. [2017].

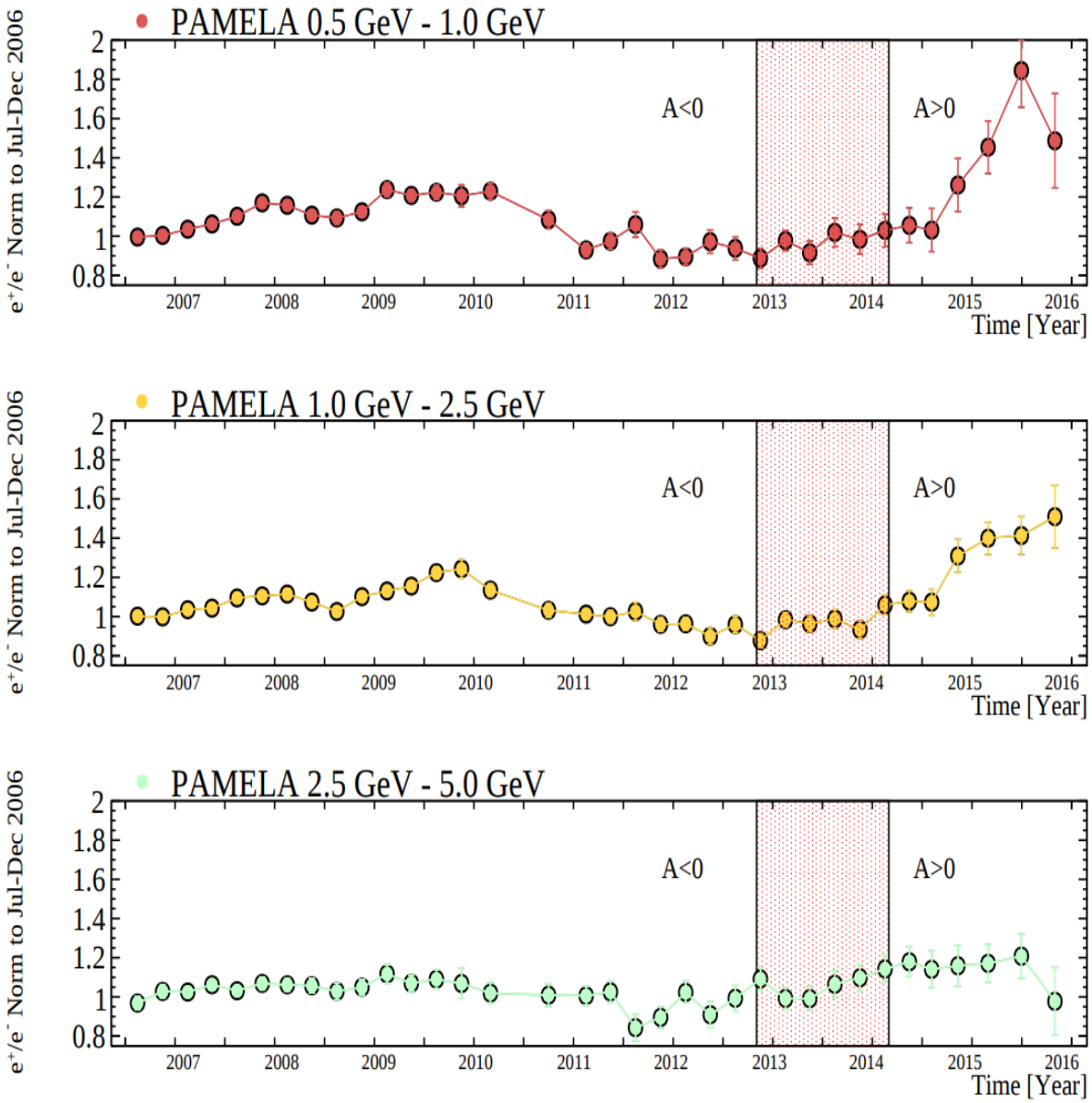


Fig. 5.16 *The e^+/e^- ratio as normalised to the July to December 2006 time period, measured at Earth by PAMELA for three different intervals of energy, i.e. 0.5 GeV to 1.0 GeV in the top panel, 1.0 GeV to 2.5 GeV in the middle panel, and 2.5 GeV to 5.0 GeV in the bottom panel. The shaded region indicates a transition period between $A < 0$ and $A > 0$ polarities. This figure was adapted from Munini et al. [2017].*

These two examples of $e^+/(e^+ + e^-)$ and e^+/e^- conclude this section and is necessarily not an exhaustive account of the relevant data available. For other recent publications pertaining to such observations and studies of the charge-sign dependent modulation of cosmic rays in the heliosphere, see e.g. Adriani et al. [2014], Adriani et al. [2016] and di Felice et al. [2017] (PAMELA), as well as Aguilar et al. [2016] (AMS).

5.6 Summary

The first section, after the introduction to this chapter, was devoted to a brief discussion of positron e^+ and electron e^- modulation. It was motivated why the study of this component of cosmic rays (CRs) is important, even though it is extremely rare. Distinction was made briefly between primary and secondary particles, refering to their source. The local interstellar spectrum (LIS), as used in this study, was presented for each of these species and examples of both e^+ and e^- spectra at Earth were shown in Figures 5.1 and 5.2, respectively. The important difference between the modulation of these species and the modulation of CR protons, viz. the modulation associated with adiabatic cooling at lower energies, was pointed out. Drift solutions of both species were compared to the respective zero-drift solutions so that the dependence of modulation on the charge-sign of particles was clearly illustrated.

Section (5.3) was devoted to a discussion of the e^+ fraction, $e^+/(e^+ + e^-)$, as function of energy. This fraction was shown for the zero-drift case as well as for each of the $A > 0$ and $A < 0$ polarity cycles in Figure 5.3. At energies below ~ 10 GeV, the e^+ fraction of the $A > 0$ polarity cycle was higher than that for the zero-drift scenario at all energies, while the e^+ fraction in the case of the $A < 0$ polarity cycle was lower; this could be explained sufficiently from consideration of the global drift pattern. It was also shown that the model used in this study correctly reproduces the increase in $e^+/(e^+ + e^-)$ at higher energies above $\sim$10 GeV, comparing it with some of the latest results from PAMELA in Figure 5.4. This can be obtained through the implementation of a e^+ LIS that includes the so-called positron excess which occurs because of sources such as pulsars or the annihilation of dark matter.

In the next section, the focus was on the e^+/e^- ratio as function of solar activity via the tilt angle α. The section started off showing intensity versus α profiles for both positrons and electrons and during both the $A > 0$ and $A < 0$ polarity cycles without applying the drift scaling down function $f_{\mathrm{d}}(\alpha)$ of Equation (4.1); see Figures 5.5 and 5.6. From these results the e^+/e^- ratio in Figure 5.7 were calculated from which the familiar 'M' and 'W' profiles were obtained, in agreement with earlier work done by other authors as illustrated in Figure 5.8. The intensity versus α profiles, this time with the inclusion of the drift scaling function, were shown in Figures 5.9 and 5.10, leading to the e^+/e^- ratio shown in Figure 5.11 where the jump that occurs at the transition between the $A < 0$ and $A > 0$ polarity cycles was now largely eliminated.

The last section of this chapter was aimed at providing a glimpse on future research, following from the work presented in this thesis. It was shown that the function $f_{\mathrm{d}}(\alpha)$ could be used effectively to alter the e^+/e^- profile as function of solar activity, depending on the values of the parameters of this function; see Figure 5.12. It was pointed out that this model could be improved by incorporating a more realistic time dependence via the magnetic field magnitude; such values for the magnetic field magnitude were shown in the bottom panel of Figure 5.13, while corresponding values for the tilt angle were shown

in the top panel of this figure. The effect that the inclusion of such a time dependent magnetic field profile can have on the intensity versus α (solar activity) profiles were illustrated in Figure 5.14 and discussed. Considering such possible improvements to the model, it was stated that the model should be able to reproduce observations of the e^+ fraction and e^+/e^- ratio in future studies; such observations from various spacecraft were shown in Figures 5.15 and 5.16.

Chapter 6

Summary and Conclusions

This chapter summarises the most important aspects of this work, emphasising the most significant conclusions. References in this chapter are limited to only those most relevant and necessary.

The first chapter served as an introduction to this thesis and considered basic background information like the heliosphere, cosmic rays (CRs), the solar wind (SW), the heliospheric magnetic field (HMF) and the neutral heliospheric current sheet (HCS). It also gave a brief outline of the chapter division of the thesis.

Chapter 2 was concerned primarily with the theoretical groundwork that was essential for the research presented in Chapters 3 to 5. The Parker transport equation (TPE) was introduced and indicated to account for all of the relevant transport phenomena, i.e. physical modulation processes, in the heliosphere. All the relations needed for the implementation of the TPE were explained, including relations between particle energy and rigidity, and between the omnidirectional distribution function and particle density. The diffusion tensor $\mathbf{K}$ was defined in field-aligned coordinates with elements giving the diffusion coefficients parallel and perpendicular to the HMF as well as the drift coefficient. The TPE as well as the tensor $\mathbf{K}$ were cast into spherical coordinates and the set of stochastic differential equations (SDEs) corresponding to the TPE was derived to establish the basis of the numerical modulation model.

As one of the major physical modulation processes in the heliosphere - and one that is of particular interest in this study - particle drifts were discussed. The drift coefficient was defined and much emphasis was placed on the suppression of drift effects due to turbulence. Gradient and curvature drift velocities were defined in terms of the drift coefficient, while expressions for the drift velocity along the neutral heliospheric current sheet were also indicated. The global drift pattern established by these drift processes was illustrated, since it would become an important topic of discussion in later chapters.

Particle diffusion was discussed, and it was indicated that the diffusion coefficient depends on the turbulence model and theory which is adopted. A simplified approach was followed for the diffusion coefficient in this study with the spatial dependence of both the parallel and perpendicular diffusion coefficients scaling as $1/B$ where B is the HMF

magnitude. The rigidity dependence of these coefficients was assumed to be a combination of two power laws. Perpendicular diffusion was scaled by 2% of the parallel diffusion. The perpendicular diffusion in the polar direction was scaled as function of the polar angle.

Chapter 3 presented an investigation into the solar modulation of galactic protons during the time period January 2010 to January 2014. The Chapter started off with a discussion of the local interstellar spectrum (LIS) for galactic protons and emphasis was placed on the importance of such a spectrum as boundary condition or input spectrum in modulation models. The galactic proton spectra measured by PAMELA from January 2010 to January 2014, averaged over one Carrington Rotation, were presented. It was clear that intensities decreased from January 2010 to 2014 as solar activity progressed from minimum to maximum conditions. The focus was first on the overall modulation over the entire period as discussed in Martucci et al. [2018], i.e. on the difference between the January 2010 and January 2014 spectra. It was shown that the model could reproduce these spectra well and the parameter values required to do so were obtained. It was an important conclusion that this difference in modulation could not be accounted for by merely changing the values of the magnetic field magnitude and the tilt angle, i.e. additional changes in the magnitude of the diffusion coefficient as well as its rigidity dependence were necessary.

Next, the solar modulation in between January 2010 and January 2014 was considered in increments of six months. For this purpose, a number of eight half-yearly averaged spectra were calculated from the PAMELA proton data. In order to numerically reproduce these eight spectra, 15-month averaged values for the tilt angle α and HMF magnitude at earth B_{E} were calculated for each spectrum. The period of 15 months was selected, since this is the approximate time that it takes for these quantities to propagate from the Earth to the HP, assuming a SW velocity of 430 km/s. An important consideration was that it was not exactly clear when (or if) the switch in solar polarity cycle, i.e. from an $A < 0$ to an $A > 0$ cycle, had occurred and hence a 'transition period' was defined in which drifts were assumed to be zero due to suppression by turbulence towards solar maximum conditions. It was also noted that, if similarly defined transition periods were defined for earlier solar cycles, they would be shorter in duration.

The 15-month averages were then incorporated into the model after which the eight half-yearly averaged spectra were reproduced, obtaining suitable values for the transport coefficients. From these values, it was clear that the diffusion coefficient had to be decreased systematically from solar minimum to solar maximum conditions. The rigidity dependence of this coefficient below 4.2 GV also had to be adjusted for the last three spectra; these three spectra assumed zero drift conditions, falling within the transition period defined earlier. It was once again pointed out that to merely change α and B_{E} as function of solar activity was not enough to account for the difference in modulation between the successive half-yearly spectra.

On a qualitative level, the results showed that the energy E_{peak} at which the peak in intensity I_{peak} occurs shifted from lower to higher values as the solar cycle progressed from minimum to maximum conditions. It also showed that the decreases in the intensity I_{peak} from one spectrum to the next were significant in all but two cases. It was indicated that intensities I_{100} around 100 MeV at 1 AU showed similar significant decreases over the successive spectra in all but the mentioned two cases.

Chapter 4 introduced the scaling function $f_{\text{d}}(\alpha)$ that would be used later in the chapter to scale down drift effects as function of increasing solar activity via the tilt angle α. The function was examined for several different settings of it parameters in order to illustrate its properties and show in which way it could be used to scale down drift effects. Its effect on modulation was illustrated in terms of intensity versus tilt angle profiles and the function was shown to be easily adaptable in terms of the value of α at which it reduces drift effects to zero.

The parameters that were obtained for reproducing the PAMELA proton spectra, with the inclusion of the scaling function $f_{\text{d}}(\alpha)$, were presented. These were compared to the parameters obtained in Chapter 3, i.e. without the inclusion of $f_{\text{d}}(\alpha)$. It was indicated that, for the spectra ranging from 1 January 2010 to 30 June 2011, no changes in the $A < 0$ parameters were required because of $f_{\text{d}}(\alpha)$ being close to unity and therefore having minimal impact. However, for the spectrum ranging from 1 July 2011 to 31 December 2011 during the $A < 0$ polarity cycle, a change in the diffusion was necessary so that the diffusion was required to decrease. A reduction in drift via $f_{\text{d}}(\alpha)$ during the $A < 0$ polarity cycle therefore had the effect of increasing the intensities computed by the model at Earth so that smaller diffusion was necessary to reproduce the data. For the spectra ranging from 1 July 2012 to 31 December 2013, where in Chapter 3 only zero-drift reproductions were obtained, Chapter 4 obtained reproductions asuming $A > 0$ and $A < 0$ polarity cycles respectively; in each case the drift was scaled according to the function $f_{\text{d}}(\alpha)$. For the $A < 0$ reproductions, the inclusion of drifts had as consequence that decreased intensities were calculated by the model relative to the zero-drift solutions, so that larger values of diffusion were necessary to reproduce the data. Switching on $A > 0$ drift had the opposite effect, increasing computed intensities relative to those of the zero-drift scenario, so that smaller values of diffusion were required to reproduce the data.

A large part of Chapter 4 was devoted to an investigation of the drift properties of the model. The focus was first on the alteration of drifts by direct means, i.e. changing the value of the drift coefficient by multiplying it with a certain factor of the scaling function $f_{\text{d}}(\alpha)$. This was illustrated in solutions of intensity versus α for $A > 0$ to $A < 0$ ratios respectively. The reduction that occurred in drift effects, upon reducing the drift coefficient to three successively smaller values was clearly evident.

The illustrative properties of the model were then utilised so that contour plots of exit positions and exit energies were presented. It showed contour plots where drifts were full $A > 0$ and $A < 0$ and where drifts were set to zero, respectively. The effect of this scaling

down of drift was clearly illustrated when comparing the zero-drift case to the $A > 0$ and $A < 0$ cases. It was found that turning on drifts in the model led to larger energy losses and this was explained with the help contour plots showing the regions in the heliosphere where pseudo-particles spend the most time during modulation, i.e. 'high activity' regions. It was explained that, under different circumstances, turning on drifts led to different distributions of these high-activity regions over both radial distance and latitude and that this was a crucial factor when determining energy losses.

Next, the focus was on how the extent of drift effects could be influenced indirectly through changing the amount of diffusion that occurs during the modulation process. This was once again illustrated through model solutions of differential intensity versus tilt angle as well as through contour plots of exit positions and exit energies. This was done for different values of the diffusion coefficient corresponding to high, intermediate and low diffusion respectively. It was clearly evident that an increase in diffusion led to a suppression or reduction of drift effects. Additional insight into the modulation process and effects of drifts were once again obtained through a contour plot showing the distribution of the high-activity regions over modualtion space.

Finally, drift effects were considered as function of energy. This was done showing solutions of differential intensitiy versus tilt angle for cases using 1 GeV and 250 MeV respectively. It was clear, from these profiles, that drift effects were reduced with increasing energy. The energy dependence was then illustrated with the help of contour plots of exit positions and exit energies showing the cases for 100 MeV and 5 GeV respectively. Contour plots of the high activity regions were once again produced in order to yield additional insights.

Chapter 5 focused on charge-sign dependent modulation of CR positrons and electrons. The first section was devoted to a brief discussion of positron e^+ and electron e^- modulation in general and it was motivated why the study of this component of CRs was important, even though it is extremely rare. Distinction was made briefly between primary and secondary particles, refering to their source. The local interstellar spectra (LISs), as used in this study, were presented for each of these species and examples of both e^+ and e^- spectra calculated at Earth were shown. The important difference between the modulation of these species and the modulation of CR protons, viz. the modulation associated with adiabatic cooling at lower energies, was pointed out. Drift solutions of both species were compared to the respective zero-drift solutions so that the dependence of modulation on the charge-sign of particles was clearly illustrated.

A discussion of the e^+ fraction, $e^+/(e^+ + e^-)$, as function of energy was presented. This fraction was shown for the zero-drift case as well as for each of the $A > 0$ and $A < 0$ polarity cycles and, from these results, it was clear that the effect of drifts became very small to negligible at higher energies. At lower energies, the e^+ fraction of the $A > 0$ polarity cycle was higher than that for the zero-drift scenario at all energies, while the e^+ fraction in the case of the $A < 0$ polarity cycle was lower; this could be explained

sufficiently from consideration of the global drift pattern. It was also shown that the model used in this study correctly simulates the increase in $e^+/(e^+ + e^-)$ at higher energies above ~ 10 GeV, comparing it with some of the latest results from PAMELA. This was indicated to be attributable to the use of a e^+ LIS that includes the so-called positron excess which occurs because of sources such as pulsars or the annihilation of dark matter.

In the next section, the focus was on the e^+/e^- ratio as function of solar activity, i.e. as function of tilt angle α. The section started off showing intensity versus α profiles for both positrons and electrons and during both the $A > 0$ and $A < 0$ polarity cycles without applying the drift scaling down function $f_{\mathrm{d}}(\alpha)$. From these results were calculated the e^+/e^- ratio and the familiar 'M' and 'W' profiles were obtained, in agreement with earlier work done by other authors. The intensity versus α profiles, this time with the inclusion of the drift scaling function, were also shown, leading to the e^+/e^- ratio where the jump that occurs at the transition between the $A < 0$ and $A > 0$ polarity cycles was largely eliminated.

The last section of this chapter was aimed at providing a glimpse on future research, following from the work presented in this thesis. It was shown that the function $f_{\mathrm{d}}(\alpha)$ could be used effectively to alter the e^+/e^- profile, depending on the values of the parameters of this function. It was pointed out that this model could be improved by incorporating of a more realistic time dependence via the magnetic field magnitude. The effect that the inclusion of such a time dependent magnetic field profile can have on the intensity versus α (solar activity) profiles were illustrated and discussed. Considering such possible improvements to the model, it was stated that the model should be able to reproduce observations of the e^+ fraction and e^+/e^- ratio in future studies.

References

Accardo, L., M. Aguilar, D. Aisa, A. Alvino, G. Ambrosi, K. Andeen, L. Arruda, N. Attig et al., High statistics measurement of the positron fraction in primary cosmic rays of 0.5-500 GeV with the Alpha Magnetic Spectrometer on the International Space Station, *Phys. Rev. Lett.*, *113*, 121101, 2014.

Adriani, O., G. C. Barbarino, G. A. Bazilevskaya, R. Bellotti, M. Boezio, E. A. Bogomolov, L. Bonechi, M. Bongi et al., An anomalous positron abundance in cosmic rays with energies 1.5 to 100 GeV, *Nature*, *458*, 607, 2009.

Adriani, O., G. C. Barbarino, G. A. Bazilevskaya, R. Bellotti, A. Bianco, M. Boezio, E. A. Bogomolov, M. Bongi et al., Cosmic-ray positron energy spectrum measured by PAMELA, *Phys. Rev. Lett.*, *111*, 081102, 2013.

Adriani, O., G. C. Barbarino, G. A. Bazilevskaya, R. Bellotti, M. Boezio, E. A. Bogomolov, M. Bongi, V. Bonvicini et al., The PAMELA mission: Heralding a new era in precision cosmic ray physics, *Phys. Rep.*, *544*, 323, 2014.

Adriani, O., G. C. Barbarino, G. A. Bazilevskaya, R. Bellotti, M. Boezio, E. A. Bogomolov, M. Bongi, V. Bonvicini et al., Time dependence of the electron and positron components of the cosmic radiation measured by the PAMELA experiment between July 2006 and December 2015, *Phys. Rev. Lett.*, *116*, 241105, 2016.

Aguilar, M., L. Ali Cavasonza, B. Alpat, G. Ambrosi, L. Arruda, N. Attig, S. Aupetit, P. Azzarello et al., Antiproton flux, antiproton-to-proton flux ratio, and properties of elementary particle fluxes in primary cosmic rays measured with the Alpha Magnetic Spectrometer on the International Space Station, *Phys. Rev. Lett.*, *117*, 091103, 2016.

Aguilar, M., L. Ali Cavasonza, B. Alpat, G. Ambrosi, L. Arruda, N. Attig, S. Aupetit, P. Azzarello et al., Observation of fine time structures in the cosmic proton and helium

fluxes with the Alpha Magnetic Spectrometer on the International Space Station, *Phys. Rev. Lett.*, *121*, 051101, 2018.

Aguilar, M., L. Ali Cavasonza, G. Ambrosi, L. Arruda, N. Attig, P. Azzarello, A. Bachlechner, F. Barão et al., Towards understanding the origin of cosmic-ray positrons, *Phys. Rev. Lett.*, *122*, 041102, 2019.

Alania, M. V., Stochastic variations of galactic cosmic rays, *Acta Physica Polonica B*, *33*, 1149, 2002.

Alania, M. V., and T. V. Dzapiashvili, The expected features of cosmic ray anisotropy due to Hall-type diffusion and the comparison with experiment, *Int. Cosmic Ray Conf. Proc.*, *3*, 19, 1979.

Alanko-Huotari, K., I. G. Usoskin, K. Marsula, and G. A. Kovaltsov, Stochastic simulation of cosmic ray modulation including a wavy heliospheric current sheet, *JGR*, *112*, A08101, 2007.

Alcaraz, J., B. Alpat, G. Ambrosi, H. Anderhub, L. Ao, A. Arefiev, P. Azzarello, E. Babucci et al., Leptons in near earth orbit, *Phys. Lett. B*, *484*, 10, 2000.

Aslam, O. P. M., and Badruddin, Study of cosmic-ray modulation during the recent unusual minimum and mini-maximum of solar cycle 24, *Solar Phys.*, *290*, 2333, 2015.

Ball, B., M. Zhang, H. Rassoul, and T. Linde, Galactic cosmic-ray modulation using a solar minimum MHD heliosphere: A stochastic particle approach, *ApJ*, *634*, 1116, 2005.

Barbiellini, G., G. Basini, R. Bellotti, M. Bocciolini, M. Boezio, F. Massimo-Brancaccio, U. Bravar, F. Cafagna et al., The cosmic ray positron to electron ratio in the energy range 0.85 to 14 GeV, *Astron. and Astrophys.*, *309*, L15, 1996.

Barwick, S. W., J. J. Beatty, C. R. Bower, C. Chaput, S. Coutu, G. de Nolfu, D. Ficenec, J. Knapp et al., Cosmic ray positrons at high energies: a new measurement, *Phys. Rev. Lett.*, *75*, 390, 1995.

Barwick, S. W., J. J. Beatty, A. Bhattacharyua, C. R. Bower, C. J. Chaput, S. Coutu, G. A. de Nolfu, J. Knapp, and etal, Measurements of the cosmic-ray positron fraction from 1 to 50 GeV, *ApJ*, *482*, L191, 1997.

Bieber, J. W., W. H. Matthaeus, C. W. Smith, W. Wanner, M. B. Kallenrode, and G. Wibberenz, Proton and electron mean free paths: the Palmer consensus revisited, *ApJ*, *420*, 294, 1994.

Bieber, J. W., R. A. Burger, R. Engel, T. K. Gaisser, S. Roesler, and T. Stanev, Antiprotons at solar maximum, *Phys. Rev. Lett.*, *83*, 674, 1999.

Bieber, J. W., W. H. Matthaeus, A. Shalchi, and G. Qin, Nonlinear guiding center theory of perpendicular diffusion: general properties and comparison with observation, *Geophys. Res. Lett.*, *31*, L10805, 2004.

Bieber, J. W., and W. H. Matthaeus, Cosmic ray pitch angle scattering in dynamical magnetic turbulence, *Int. Cosmic Ray Conf. Proc.*, *3*, 248, 1991.

Bieber, J. W., and W. H. Matthaeus, Perpendicular diffusion and drift at intermediate cosmicy-ray energies, *ApJ*, *485*, 655, 1997.

Bisschoff, D., M. S. Potgieter, and O. P. M. Aslam, New very local interstellar spectra for electrons, positrons, protons, and light cosmic ray nuclei, *ApJ*, *878*, 59, 2019.

Bisschoff, D., and M. S. Potgieter, New local interstellar spectra for protons, helium and carbon derived from PAMELA and Voyager 1 observations, *Astrophys. Space Sci.*, *361*, 48, 2016.

Bobik, P., M. Kudela, M. Boschini, D. Grandi, M. Gervasi, and P. G. Rancoita, Solar modulation model with reentrant particles, *Adv. Space Res.*, *41*, 339, 2008.

Bobik, P., G. Boella, M. J. Boschini, C. Consolandi, S. Della Torre, M. Gervasi, D. Grandi, M. Elmo et al., Energy loss for electrons in the heliosphere and local interstellar spectrum for solar modulation, in *Cosmic Rays for Particle and Astroparticle Physics*, edited by S. Giani, C. Leroy„ and P. G. Rancoita, 2011.

Bobik, P., G. Boella, M. J. Boschini, C. Consolandi, S. Della Torre, M. Gervasi, D. Grandi, K. Kudela et al., Systematic investigation of solar modulation of galactic protons for solar cycle 23 using a Monte Carlo approach with particle drift effects and latitudinal dependence, *ApJ*, *745*, 132, 2012.

Bobik, P., M. J. Boschini, S. D. Torre, M. Gervasi, D. Grandi, G. L. Vacca, S. Pensotti, M. Putis et al., On the forward-backward-in-time approach for Monte Carlo solutions of Parker's transport equation: 1-dimensional case, *JGR*, *121*, 3920, 2016.

Boezio, M., P. Carlson, T. Francke, N. Weber, M. Suffert, M. Hof, W. Menn, M. Simon et al., The cosmic-ray electron and positron spectra measured at 1 AU during solar minimum activity, *ApJ*, *532*, 653, 2000.

Boschini, M. S., S. Della Torre, M. Gervasi, D. Grandi, G. Johannesson, M. Kachelriess, G. La Vacca, N. Masi et al., Solution of heliospheric propagation: unveiling the local interstellar spectra of cosmic-ray species, *ApJ*, *840*, 115, 2017.

Boudaud, M., S. Aupetit, S. Caroff, A. Putze, G. Belanger, Y. Genolini, C. Goy, V. Poireau et al., A new look at the cosmic ray positron fraction, *Astron. and Astrophys*, *575*, A67, 2015.

Buffington, A., C. D. Orth, and G. F. Smoot, Measurement of primary cosmic-ray electrons and positrons from 4 to 50 GeV, *ApJ*, *199*, 669, 1975.

Burger, R. A., On the theory and application of drift motion of charged particles in inhomogeneous magnetic fields, Ph.D. thesis, Potchefstroom University for CHE, Potchefstroom, South Africa, 1987.

Burger, R. A., *Physics of the outer heliosphere*, edited by S. Grzedzielski, and D. E. Page. Oxford Pergamon, 1990.

Burger, R. A., Modelling drift along the heliospheric wavy neutral current sheet, *ApJ*, *760*, 60, 2012.

Burger, R. A., H. Moraal, and G. M. Webb, Drift theory of charged particles in electric and magnetic fields, *Astrophys. Space Sci.*, *116*, 107, 1985.

Burger, R. A., M. S. Potgieter, and B. Heber, Rigidity dependence of cosmic ray proton latitudinal gradients measured by the Ulysses spacecraft: implications for the diffusion tensor, *JGR*, *105*, 27447, 2000.

Burger, R. A., T. P. J. Krüger, M. Hitge, and N. E. Engelbrecht, A Fisk-Parker hybrid heliospheric magnetic field with a solar-cycle dependence, *ApJ*, *674*, 511, 2008.

Burger, R. A., and M. Hattingh, Toward a realistic diffusion tensor for galactic cosmic rays, *ApJ*, *505*, 244, 1998.

Burger, R. A., and M. Hattingh, Effect of Fisk-type heliospheric magnetic fields on the latitudinal transport of cosmic rays, *Int. Cosmic Ray Conf. Proc.*, *9*, 3698, 2001.

Burger, R. A., and M. Hitge, The effect of a Fisk-type heliospheric magnetic field on cosmic-ray modulation, *ApJ*, *617*, L73, 2004.

Burger, R. A., and M. S. Potgieter, The calculation of neutral sheet drift in two-dimensional cosmic-ray modulation models, *ApJ*, *339*, 501, 1989.

Burger, R. A., and M. S. Potgieter, The effect of large heliospheric current sheet tilt angles in numerical modulation models: A theoretical assessment, *Int. Cosmic Ray Conf. Proc.*, *7*, 13, 1999.

Burger, R. A., and D. J. Visser, Reduction of drift effects due to solar wind turbulence, *ApJ*, *725*, 1366, 2010.

Burlaga, L. F., and N. F. Ness, Large-scale distant heliospehric magnetic field: Voyager 1 and 2 observations from 1986 through 1989, *JGR*, *98*, 17451, 1993.

Büsching, I., A. Kopp, M. Pohl, R. Schlickeiser, C. Perrot, and I. Grenier, Cosmic-ray propagation properties for an origin in supernova remnants, *ApJ*, *619*, 314, 2005.

Candia, J., and E. Roulet, Diffusion and drift of cosmic rays in highly turbulent magnetic fields, *J. Cosmology Astroparticle Phys.*, *10*, 007, 2004.

Casolino, M., P. Picozza, and PAMELA Collaboration, The PAMELA experiment: A space-borne observatory for heliospheric phenomena, *Adv. Space Res.*, *41*, 2043, 2008.

Chalov, S. V., H. J. Fahr, and V. Izmodenov, Spectra of energized pick-up ions upstream of the heliospheric termination shock I. the role of Alfvenic turbulences, *Astron. Astrophys.*, *304*, 609, 1995.

Chenette, D. L., T. F. Conlon, and J. A. Simpson, Burst of relativistic electrons from jupiter observed in interplanetary space with the time variation of the planetary rotation period, *JGR*, *79*, 3551, 1974.

Cholis, I., and D. Hooper, Dark matter and pulsar origins of the rising cosmic ray positron fraction in light of new data from the AMS, *Phys. Rev. D*, *88*, 2013.

Chowdhury, P., K. Kudela, and Y. J. Moon, A study of heliospheric modulation and periodicities of galactic cosmic rays during cycle 24, *Sol. Phys.*, *291*, 581, 2016.

Cliver, E. W., Solar energetic particles: Acceleration and transport, *Int. Cosmic Ray Conf. Proc.*, *516*, 103, 2000.

Corti, C., M. S. Potgieter, V. Bindi, C. Consolandi, C. Light, M. Palermo, and A. Popkow, Numerical modeling of galactic cosmic-ray proton and helium observed by AMS-02 during the solar maximum of solar cycle 24, *ApJ*, *871*, 253, 2019.

Dalla, S., M. S. Marsh, J. Kelly, and T. Laitinen, Solar energetic particle drifts in the parker spiral, *JGR*, *118*, 5979, 2013.

de Simone, N., V. di Felice, J. Gieseler, M. Boezio, M. Casolino, P. Picozza, B. Heber, and PAMELA Collaboration, Latitudinal and radial gradients of galactic cosmic ray protons in the inner heliosphere - PAMELA and Ulysses observations, *ASTRA*, *7*, 425, 2011.

Decker, R. B., S. M. Krimigis, E. C. Roelof, M. E. Hill, T. P. Armstrong, G. Gloeckler, D. C. Hamilton, and L. J. Lanzerotti, A study of heliospheric modulation and periodicities of galactic cosmic rays during cycle 24, *Sci.*, *309*, 2020, 2005.

Della Torre, S., P. Bobik, M. J. Boschini, C. Consolandi, M. Gervasi, D. Grandi, K. Kudela, S. Pensotti et al., Effects of solar modulation on the cosmic ray positron fraction, *Adv. Space Res.*, *49*, 1587, 2012.

di Felice, V., R. Munini, E. E. Vos, and M. S. Potgieter, New evidence for charge-sign-dependent modulation during the solar minimum of 2006 to 2009, *ApJ*, *834*, 89, 2017.

Dialynas, K., S. M. Krimigis, R. B. Decker, and D. G. Mitchell, Plasma pressures in the heliosheath from Cassini ENA and Voyager 2 measurements: Validation by the Voyager 2 heliopause crossing, *Geophys. Res. Lett.*, *46*, 7911, 2019.

Dresing, N., R. Gómez-Herrero, A. Klassen, B. Heber, Y. Kartavykh, and W. Dröge, The large longitudinal spread of solar energetic particles during the 17 January 2010 solar event, *Sol. Phys.*, *281*, 281, 2012.

Dröge, W., Y. Y. Kartavykh, B. Klecker, and G. A. Kovaltsov, Anisotropic three-dimensional focused transport of solar energetic particles in the inner heliosphere, *ApJ*, *709*, 912, 2010.

Dröge, W., Y. Y. Kartavykh, N. Dresing, B. Heber, and A. Klassen, Wide longitudinal distribution of interplanetary electrons following the 7 February 2010 solar event: Observations and transport modeling, *JGR*, *119*, 6074, 2014.

Dröge, W., Y. Y. Kartavykh, N. Dresing, and A. Klassen, Multi-spacecraft observations and transport modeling of energetic electrons for a series of solar particle events in August 2010, *ApJ*, *826*, 134, 2016.

Dröge, W., Y. Y. Kartavykh, L. Wang, D. Telloni, and R. Bruno, Transport modeling of interplanetary electrons in the 2002 October 20 solar particle event, *ApJ*, *869*, 168, 2018.

du Vernois, M. A., S. W. Barwick, J. J. Beatty, A. Bhattacharyua, C. R. Bower, C. J. Chaput, S. Coutu, and G. A. de Nolfu, Cosmic-ray electrons and positrons from 1 to 100 GeV: Measurements with HEAT and their interpretation, *ApJ*, *559*, 296, 2001.

Dunzlaff, P., B. Heber, A. Kopp, O. Rother, R. Müller-Mellin, A. Klassen, R. Gómez-Herrero, and R. Wimmer Schweingruber, Observations of recurrent cosmic ray decreases during solar cycles 22 and 23, *Annales Geophysicae*, *26*, 3127, 2008.

Dunzlaff, P., R. D. Strauss, and M. S. Potgieter, A stochastic differential equation code for multidimensional Fokker-Planck type problems, *Comp. Phys. Comm.*, *192*, 156, 2015.

Engelbrecht, N. E., 2008. On the heliospheric diffusion tensor and its effect on the 26-day recurrent cosmic ray variations. Master's thesis, North-West University, Potchefstroom, South Africa.

Engelbrecht, N. E., On the development and applications of a three-dimensional *ab initio* cosmic-ray modulation model, Ph.D. thesis, North-West University, Potchefstroom, South Africa, 2012.

Engelbrecht, N. E., and R. A. Burger, Effect of various dissipation range onset models on the 26-day variation of low-energy galactic cosmic-ray electrons, *Adv. Space Res.*, *45*, 1015, 2010.

Engelbrecht, N. E., and R. A. Burger, An ab initio model for cosmic-ray modulation, *ApJ*, *772*, 46, 2013*a*.

Engelbrecht, N. E., and R. A. Burger, An *ab initio* model for the modulation of galactic cosmic-ray electrons, *ApJ*, *779*, 158, 2013*b*.

Engelbrecht, N. E., and R. A. Burger, A comparison of turbulence-reduced drift coefficients of importance for the modulation of galactic cosmic-ray protons in the supersonic solar wind, *Adv. Space Res.*, *55*, 390, 2015*a*.

Engelbrecht, N. E., and R. A. Burger, Sensitivity of cosmic-ray proton spectra to the low-wavenumber behavior of the 2D turbulence power spectrum, *ApJ*, *814*, 152, 2015*b*.

Engelbrecht, N. E., R. D. Strauss, J. A. le Roux, and R. A. Burger, Toward a greater understanding of the reduction of drift coefficients in the presence of turbulence, *ApJ*, *841*, 107, 2017.

Engelbrecht, N. E., S. T. Mohlolo, and S. E. S. Ferreira, An improved treatment of neutral sheet drift in the inner heliosphere, *ApJ*, *884*, L54, 2019.

Fahr, H. J., T. Kausch, and K. Scherer, A 5-fluid hydrodynamic approach to model the solar system-interstellar medium interaction, *Astron. Astrophys.*, *357*, 268, 2000.

Fanselow, J. L., R. C. Hartman, R. H. Hilderbrand, and P. Meyer, Charge composition and energy spectrum of primary cosmic-ray electrons, *ApJ*, *158*, 771, 1969.

Feng, L., R. Z. Yang, H. N. He, T. K. Donk, Y. Fan, and J. Chang, AMS-02 positron excess: new bounds on dark matter models and hint for primary electron spectrum hardening, *Phys. Lett. B*, *728*, 250, 2014.

Ferreira, S. E. S., The heliospheric transport of galactic cosmic rays and Jovian electrons, Ph.D. thesis, North-West University, Potchefstroom, South Africa, 2002.

Ferreira, S. E. S., M. S. Potgieter, R. A. Burger, and B. Heber, Modulation effects of anisotropic perpendicular diffusion on cosmic ray electron intensities in the heliosphere, *JGR*, *105*, 18305, 2000.

Ferreira, S. E. S., M. S. Potgieter, R. A. Burger, B. Heber, and H. Fichtner, Modulation of Jovian and galactic electrons in the heliosphere: 1. Latitudinal transport of a few-MeV electrons, *JGR*, *106*, 24979, 2001*a*.

Ferreira, S. E. S., M. S. Potgieter, B. Heber, H. Fichtner, R. A. Burger, and P. Ferrando, A study of the compatibility between observations and model simulations for Jovian and galactic electrons, *Adv. Space Res.*, *27*, 553, 2001*b*.

Ferreira, S. E. S., and M. S. Potgieter, Long term cosmic ray modulation in the heliosphere, *ApJ*, *603*, 744, 2004.

Ferreira, S. E. S., and K. Scherer, The heliomagnetic and solar-cycle related variation of the cosmic ray flux modeled with the BoPo-hybrid code, *Astron. Astrophys.*, *442*, L11, 2005.

Fichtner, H., Anomalous cosmic rays: Messengers from the outer heliosphere, *Space Sci. Rev.*, *95*, 639, 2001.

Fichtner, H., J. A. le Roux, U. Mall, and D. Rucinski, On the transport of pick-up ions in the heliosphere, *Astron. Astrophys.*, *314*, 650, 1996.

Fichtner, H., and K. Scherer, The heliosphere: A brief overview, in *The outer heliosphere: Beyond the planets*, edited by K. Scherer, H. Fichtner„ and E. Marsch, Copernicus Publications, Katlenburg-Lindau, 2000.

Fisk, L. A., Motion of the footprints of heliospheric magnetic field lines at the sun: Implications for recurrent energetic particle events at high heliographic latitudes, *JGR*, *101*, 15547, 1996.

Fisk, L. A., An overview of the transport of galactic and anomalous cosmic rays in the heliosphere: theory, *Adv. Space Res.*, *23*, 415, 1999.

Fisk, L. A., and N. A. Schwadron, The influence of intermediate-scale variations in the heliospheric magnetic field on the transport of galactic cosmic rays, *JGR*, *100*, 7865, 1995.

Florinski, V., On the transport of cosmic rays in the distant heliosheath, *Adv. Space Res.*, *48*, 308–313, 2011.

Florinski, V., S. E. S. Ferreira, and N. V. Pogorelov, Galactic cosmic rays in the outer heliosphere: theory and models, *Space Sci. Rev.*, *176*, 147, 2013.

Florinski, V., and N. V. Pogorelov, Four-dimensional transport of galactic cosmic rays in the outer heliosphere and heliosheath, *ApJ*, *701*, 642, 2009.

Forbush, S. E., Three unusual cosmic-ray increases possibly due to charged particles from the sun, *Phys. Rev.*, *70*, 771, 1946.

Forman, M. A., J. R. Jokipii, and A. J. Owens, Cosmic-ray streaming perpendicular to the mean magnetic field, *ApJ*, *192*, 535, 1974.

Galper, A., and P. Spillantini, Ten years of cosmic ray physics with PAMELA, *Adv. Space Res.*, *62*, 2892, 2018.

Gardiner, C. W., *Handbook of stochastic methods for physics, chemistry and the natural sciences*. Springer, Berlin, 1983.

Gardiner, C. W., *Stochastic methods: a handbook for the natural and social sciences*. Springer, Berlin, 2009.

Gervasi, M., I. G. Rancoita, I. G. Usoskin, and G. A. Kovaltsov, Monte-Carlo approach to galactic cosmic ray propagation in the heliosphere, *Nuclear Physics*, *78*, 26, 1999.

Giacalone, J., and J. R. Jokipii, The transport of cosmic rays across a turbulent magnetic field, *ApJ*, *520*, 204, 1999.

Ginzburg, V. L., and S. I. Syrovatskii, *The origin of cosmic rays*. Gordon and Breach, New York, 1969.

Gleeson, L. J., The equations describing the cosmic-ray gas in the interplanetary region, *Planet. Space Sci.*, *17*, 31, 1969.

Gleeson, L. J., and W. I. Axford, Cosmic rays in the interplanetary medium, *ApJ Lett.*, *149*, L115, 1967.

Gleeson, L. J., and W. I. Axford, The Compton-getting effect, *Astrophys. Space Sci.*, *2*, 431, 1968.

Golden, R. L., B. G. Mauger, S. Horan, S. A. Stephens, R. R. Daniel, G. D. Badhwar, J. L. Lacy, and J. E. Zipse, Observation of cosmic ray positrons in the region from 5 to 50 GeV, *Astron. Astrophys.*, *188*, 145, 1987.

Golden, R. L., C. Grimani, B. L. Kimbell, S. A. Stephens, S. J. Stochaj, W. R. Webber, G. Basini, F. Bongiorno et al., Observations of cosmic-ray electrons and positrons using an imaging calorimeter, *ApJ*, *436*, 769, 1994.

Golden, R. L., S. J. Stochaj, S. A. Stephens, F. Aversa, G. Barbiellini, M. Boezio, U. Bravar, A. Colavita et al., Measurement of the positron to electron ratio in cosmic rays above 5 GeV, *ApJ Lett.*, *457*, L103, 1996.

Guo, X., and V. Florinski, Corotating interaction regions and the 27 day variation of galactic cosmic rays intensity at 1 AU during the cycle 23/24 solar minimum, *JGR*, *119*, 2411, 2014*a*.

Guo, X., and V. Florinski, Galactic cosmic-ray modulation near the heliopause, *ApJ*, *793*, 18, 2014*b*.

Gurnett, D. A., W. S. Kurth, L. F. Burlaga, and N. F. Ness, In situ observations of interstellar plasma with Voyager 1, *Sci.*, *341*, 1489, 2013.

Haasbroek, L. J., 1993. Modulation of cosmic rays in the heliosphere: a model study for the Ulysses spacecraft. Master's thesis, Potchefstroom University for CHE, Potchefstroom, South Africa.

Haasbroek, L. J., and M. S. Potgieter, The modulation of cosmic rays in the high latitude heliosphere: A computer simulation, *Space Sci. Rev.*, *72*, 385, 1995.

Hattingh, M., The modulation of galactic cosmic rays in a three-dimensional heliosphere, Ph.D. thesis, Potchefstroom University for CHE, Potchefstroom, South Africa, 1998.

Hattingh, M., and R. A. Burger, A new simulated wavy neutral sheet drift model, *Adv. Space Res.*, *16*, 213, 1995.

Heber, B., W. Dröge, and P. Ferrando, Spatial variation of >400 MeV/n nuclei fluxes observed during the Ulysses rapid latitude scan, *Astron. Astrophys.*, *316*, 538, 1996.

Heber, B., A. Kopp, J. Gieseler, R. Müller-Mellin, H. Fichtner, K. Scherer, M. Potgieter, and S. Ferreira, Modulation of galactic cosmic ray protons and electrons during an unusual solar minimum, *ApJ*, *699*, 1956, 2009.

Heber, B., and M. S. Potgieter, Cosmic rays at high heliolatitudes, *Space Sci. Rev.*, *127*, 117, 2006.

Herbst, K., B. Heber, A. Kopp, O. Sternal, and F. Steinhilber, The local interstellar spectrum beyond the heliopause: what can be learned from Voyager in the inner heliosheath?, *ApJ*, *761*, 17, 2012.

Hoeksema, J. T., Large-scale structure of the heliospheric magnetic field - 1976-1991, in *Solar Wind 7 Colloquium*, edited by E. Marsch, and R. Schwenn, Pergamon Press, Oxford, New York, Seoul, Tokyo, 1992.

Hooper, D., P. Blasi, and P. D. Serpico, Pulsars as the sources of high energy cosmic ray positrons, *J. Cosmology Astroparticle Phys.*, *01*, 025, 2009.

Iskra, K., M. Siluszyk, M. Alania, and W. Wozniak, Experimental investigation of the delay time in galactic cosmic ray flux in different epochs of solar magnetic cycles: 1959 - 2014, *Sol. Phys.*, *249*, 115, 2019.

Johnson, L. W., R. D. Reiss, and J. T. Arnold, *Introduction to linear algebra*. Addison Wesley, USA, 5 edition, 2002.

Jokipii, J. R., Cosmic ray propagation. I. Charged particles in a random magnetic field, *ApJ*, *146*, 480, 1966.

Jokipii, J. R., Particle drifts for a finite scattering rate, *Int. Cosmic Ray Conf. Proc.*, *3*, 497, 1993.

Jokipii, J. R., Latitudinal heliospheric magnetic field: stochastic and causal components, *JGR*, *106*, 15841, 2001.

Jokipii, J. R., E. H. Levy, and W. B. Hubbard, Effects of particle drift on cosmic-ray transport. I - General properties, application to solar modulation, *ApJ*, *213*, 861, 1977.

Jokipii, J. R., J. Kóta, J. Giacalone, T. S. Horbury, and E. J. Smith, Interpretation and consequences of large-scale magnetic variances observed at high heliospheric latitude, *Geophys. Res. Lett.*, *22*, 3385, 1995.

Jokipii, J. R., and D. A. Kopriva, Effects of particle drift on the transport of cosmic rays. III - Numerical models of galactic cosmic-ray modulation, *ApJ*, *234*, 384, 1979.

Jokipii, J. R., and J. Kóta, The polar heliospheric magnetic field, *Geophys. Res. Lett.*, *16*, 1, 1989.

Jokipii, J. R., and E. H. Levy, Effects of particle drifts on the solar modulation of galactic cosmic rays, *ApJ Lett.*, *213*, L85, 1977.

Jokipii, J. R., and E. N. Parker, On the convection, diffusion, and adiabatic deceleration of cosmic rays in the solar wind, *ApJ*, *160*, 735, 1970.

Jokipii, J. R., and B. Thomas, Effects of drifts on the transport of cosmic rays. IV - Modulation by a wavy interplanetary current sheet, *ApJ*, *243*, 1115, 1981.

Kalinin, M. S., G. A. Bazilevskaya, M. B. Krainev, A. K. Svirzhevskaya, N. S. Svirzhevsky, and S. A. Starodubtsev, Modulation of galactic cosmic rays in solar cycles 22-24: Analysis and physical interpretation, *Geomagnetism Aeronomy*, *57*, 549, 2017.

Kloeden, P. E., E. Platen, and H. Schurz, *Numerical solution of SDE through computer experiments*. Springer, Berlin, 1994.

Kloeden, P. E., and E. Platen, *Numerical solutions of stochastic differential equations*. Springer, Berlin, 1999.

Kobylinski, Z., Comparison of the Fisk magnetic field with the standard Parker IMF: Consequences for diffusion coefficients, *Adv. Space Res.*, *27*, 541, 2001.

Kopp, A., I. Büsching, R. D. Strauss, and M. S. Potgieter, A stochastic differential equation code for multidimensional Fokker-Planck type problems, *Comp. Phys. Comm.*, *183*, 530, 2012.

Kopp, A., T. Wiengarten, H. Fichtner, F. Effenberger, P. Kühl, B. Heber, J. L. Raath, and M. S. Potgieter, Cosmic-ray transport in heliospheric magnetic structures. II. Modelling particle transport through corotating interaction regions, *ApJ*, *837*, 37, 2017.

Kóta, J., The role of particle drifts in the heliosphere, *J. Phys. Conf. Series*, *767*, 012014, 2016.

Kóta, J., and J. R. Jokipii, Effects of drift on the transport of cosmic rays. VI. A three-dimensional model including diffusion, *ApJ*, *265*, 573, 1983.

Kóta, J., and J. R. Jokipii, 3-D distribution of cosmic rays in the outer heliosphere, *Int. Cosmic Ray Conf. Proc.*, *4*, 680, 1995.

Kóta, J., and J. R. Jokipii, 3-D simulations of heliospheric transport: A comparison of models, *Int. Cosmic Ray Conf. Proc.*, *2*, 25, 1997.

Kóta, J., and J. R. Jokipii, Are cosmic rays modulated beyond the heliopause?, *ApJ*, *782*, 24, 2014.

Koyama, K., R. Petre, E. V. Gotthelf, U. Hwang, M. Matsuura, M. Ozati, and S. S. Holt, Evidence for shock acceleration of high-energy electrons in the supernova remnant SN1006, *Nauture*, *378*, 255, 1995.

Krimigis, S. M., E. C. Roelof, R. B. Decker, and M. E. Hill, Zero ouflow velocity for a plasma in a heliosheath transition layer, *Nature*, *474*, 359, 2013.

Krüger, T. P. J., 2005. The effect of a Fisk-Parker hybrid magnetic field on cosmic rays in the heliosphere. Master's thesis, North-West University, Potchefstroom, South Africa.

Laitinen, T., S. Dalla, and M. S. Marsh, Energetic particle cross-field propagation early in a solar event, *ApJ Lett.*, *773*, L29, 2013.

Laitinen, T., A. Kopp, F. Effenberger, S. Dalla, and M. S. Marsh, Solar energetic particle access to distant longitudes via turbulent field-line meandering, *Astron. Astrophys.*, *591*, A18, 2016.

Laitinen, T., F. Effenberger, A. Kopp, and S. Dalla, The effect of turbulence strength on meandering field lines and solar energetic particle event extents, *J. Space Weather Space Climate*, *8*, A13, 2018.

Langner, U. W., 2000. Effects of different local interstellar spectra on the heliospheric modulation of cosmic rays. Master's thesis, Potchefstroom University for CHE, Potchefstroom, South Africa.

Langner, U. W., Effects of termination shock acceleration on cosmic rays in the heliosphere, Ph.D. thesis, Potchefstroom University for CHE, Potchefstroom, South Africa, 2004.

Langner, U. W., M. S. Potgieter, H. Fichtner, and T. Borrmann, Effects of different solar wind speed profiles in the heliosheath on the modulation of cosmic-ray protons, *ApJ*, *640*, 1119, 2006.

Langner, U. W., and M. S. Potgieter, Solar wind termination shock and heliosheath effects on the modulation of protons and antiprotons, *JGR*, *109*, A01103, 2004.

le Roux, J. A., M. S. Potgieter, and V. S. Ptuskin, A transport model for the diffusive shock acceleration and modulation of anomalous cosmic rays in the heliosphere, *JGR*, *101*, 4791, 1996.

Li, H., C. Wang, and J. D. Richardson, Properties of the termination shock observed by Voyager 2, *Geophys. Res. Lett.*, *35*, L19107, 2008.

Lockwood, J. A., and W. R. Webber, Intensities of galactic cosmic rays of ∼1.5 GV rigidity at Earth versus the heliospheric current sheet tilt, *JGR*, *110*, A04102, 2005.

Longair, M. S., Cosmic rays and galactic radio background emission, in *Low frequency astrophysics from space*, edited by N. E. Kassim, and K. W. Weiler, 227, Springer-Verlag, Berlin, 1990.

Luo, X., M. Zhang, H. K. Rassoul, and N. V. Pogorelov, Cosmic-ray modulation by the global merged interaction region in the heliosheath, *ApJ*, *730*, 13, 2011.

Luo, X., M. Zhang, H. K. Rassoul, N. V. Pogorelov, and J. Heerikhuisen, Galactic cosmic-ray modulation in a realistic global magnetohydrodynamic heliosphere, *ApJ*, *764*, 85, 2013.

Luo, X., M. Zhang, M. Potgieter, X. Feng, and N. V. Pogorelov, A numerical simulation of cosmic-ray modulation near the heliopause, *ApJ*, *808*, 82, 2015.

Maccione, L., Low energy cosmic ray positron fraction explained by charge-sign dependent solar modulation, *Phys. Rev. Lett.*, *110*, 081101, 2013.

Manuel, R., Time-dependent modulation of cosmic rays in the outer helisphere, Ph.D. thesis, North-West University, Potchefstroom, South Africa, 2013.

Manuel, R., S. E. S. Ferreira, M. S. Potgieter, R. D. Strauss, and N. E. Engelbrecht, Time-dependent cosmic ray modulation, *Adv. Space Res.*, *47*, 1529, 2011.

Manuel, R., S. E. S. Ferreira, and M. S. Potgieter, Time-dependent modulation of cosmic rays in the heliosphere, *Sol. Phys.*, *289*, 2207, 2013.

Manuel, R., S. E. S. Ferreira, and M. S. Potgieter, The effect of a dynamic inner heliosheath thickness on cosmic-ray modulation, *ApJ*, *799*, 223, 2015.

Marsch, E., W. I. Axford, and J. F. McKenzie, Solar wind, in *Dynamic Sun*, edited by B. N. Dwivedi, Cambridge University Press, Cambridge, United Kingdom, 2003.

Martucci, M., R. Munini, M. Boezio, V. di Felice, O. Adriani, G. C. Barbarino, G. A. Bazilevskaya, R. Bellotti et al., Proton fluxes measured by the PAMELA experiment from the minimum to the maximum solar activity for solar cycle 24, *ApJ Lett.*, *854*, L2, 2018.

Maruyama, G., Continuous Markov processes and stochastic equations, *Rend. Circ. Mat. Palermo*, *4*, 48, 1955.

Matthaeus, W. H., G. Qin, J. W. Bieber, and G. P. Zank, Nonlinear collisionless perpendicular diffusion of charged particles, *ApJ Lett.*, *590*, L53, 2003.

Menn, W., M. Hof, O. Reimer, M. Simon, A. J. Davis, A. W. Labrador, R. A. Mewaldt, S. M. Schindler et al., The absolute flux of protons and helium at the top of the atmosphere using IMAX, *ApJ*, *533*, 281, 2000.

Mewaldt, R. A., A. J. Davis, K. A. Lave, R. A. Leske, E. C. Stone, M. E. Wiedenbeck, W. R. Binns, E. R. Christian et al., Record-setting cosmic-ray intensities in 2009 and 2010, *ApJ Lett.*, *723*, L1, 2010.

Minnie, J., 2002. Observational constraints on the heliospheric diffusion tensor for galactic cosmic rays. Master's thesis, Potchefstroom University for CHE, Potchefstroom, South Africa.

Minnie, J., An ab-initio approach to the heliospheric modulation of galactic cosmic rays, Ph.D. thesis, North-West University, Potchefstroom, South Africa, 2006.

Minnie, J., J. W. Bieber, W. H. Matthaeus, and R. A. Burger, Suppression of particle drifts by turbulence, *670*, 1149, 2007.

Miyake, S., and S. Yanagita, Effects of the tilted and wavy current sheet on the solar modulation of galactic cosmic rays, *Int. Cosmic Ray Conf. Proc.*, *2*, 203, 2005.

Moeketsi, D. M., 2004. Modelling of galactic and Jovian electrons in the heliosphere. Master's thesis, North-West University, Potchefstroom, South Africa.

Mohlolo, S. T., 2016. The modulation of galactic cosmic rays over a solar cycle. Master's thesis, North-West University, Potchefstroom, South Africa.

Moloto, K. D., 2015. The effect of the heliospheric current sheet on cosmic ray modulation. Master's thesis, North-West University, Potchefstroom, South Africa.

Moloto, K. D., N. E. Engelbrecht, and R. A. Burger, A simplified *ab initio* cosmic-ray modulation model with simulated time dependence and predictive capability, *ApJ*, *859*, 107, 2018.

Moloto, K. D., N. E. Engelbrecht, R. D. Strauss, D. M. Moeketsi, and J. P. van den Berg, Numerical integration of stochastic differential equations: A parallel cosmic ray modulation implementation of Africa's fastest computer, *Adv. Space Res.*, *63*, 626, 2019.

Moraal, H., Proton modulation during solar minimum periods in consecutive solar cycles, *Int. Cosmic Ray Conf. Proc.*, *6*, 140, 1990.

Moskalenko, I. V., A. W. Strong, J. F. Ormes, and M. S. Potgieter, Secondary antiprotons and propagation of cosmic rays in the Galaxy and heliosphere, *ApJ*, *565*, 280, 2002.

Moskalenko, I. V., and A. W. Strong, Production and propagation of cosmic-ray positrons and electrons, *ApJ*, *493*, 694, 1998.

Müller, D., and K. K. Tang, Cosmic-ray positrons from 10 GeV to 20 GeV: A balloon-borne measurement using the geomagnetic east-west asymmetry, *ApJ*, *312*, 183, 1987.

Munini, R., V. di Felice, M. Boezio, O. Adriani, G. C. Barbarino, G. A. Bazilevskaya, R. Bellotti, E. A. Bogomolov et al., Ten years of positron and electron solar modulation measured by the PAMELA experiment, *Proc. Int. Cosmic Ray Conf.*, *301*, 12, 2017.

Ndiitwani, D. C., S. E. S. Ferreira, M. S. Potgieter, and B. Heber, Modelling cosmic ray intensities along the Ulysses trajectory, *Annales Geophysicae*, *23*, 1061, 2005.

Nel, A. E., 2015. The solar-cycle dependence of the heliospheric diffusion tensor. Master's thesis, North-West University, Potchefstroom, South Africa.

Ngobeni, D. C., and M. S. Potgieter, Modelling the effects of scattering parameters on particle drift in the solar modulation of galactic cosmic rays, *Adv. Space Res.*, *56*, 1525, 2015.

Øksendal, B., *Stochastic differential equations: an introduction with applications*. Springer, Berlin, 2003.

Parker, E. N., Dynamics of the interplanetary gas and magnetic fields, *ApJ*, *128*, 664, 1958.

Parker, E. N., The passage of energetic charged particles through interplanetary space, *Planetary and Space Sci.*, *13*, 9, 1965.

Pei, C., J. Bieber, R. A. Burger, and J. Clem, A general time-dependent stochastic method for solving Parker's equation in spherical coordinates, *JGR*, *115*, A12107, 2010.

Pei, C., J. W. Bieber, and R. A. Burger, Three-dimensional wavy current sheet drifts, *ApJ*, *744*, 170, 2012.

Pesses, M. E., J. R. Jokipii, and D. Eichler, Cosmic ray drift, shock wave acceleration, and the anomalous component of cosmic rays, *ApJ*, *246*, L85, 1981.

Phillips, J. L. et al., Ulysses solar wind plasma observations from pole to pole, *Geophys. Res. Lett.*, *22*, 3301, 1995.

Picozza, P., A. M. Galper, G. Castellini, O. Adriani, F. Altamura, M. Ambriola, G. C. Barbarino, A. Basili et al., PAMELA: A payload for antimatter matter exploration and light-nuclei astrophysics, *Astroparticle Phys.*, *27*, 296, 2007.

Pogorelov, N. V., E. C. Stone, and V. Florinski, Termination shock asymmetries as seen by the Voyager spacecraft: the role of the interstellar magnetic field and neutral hydrogen, *ApJ*, *668*, 611, 2007.

Potgieter, M. S., The modulation of galactic cosmic rays as described by a three-dimensional drift model, Ph.D. thesis, Potchefstroom University for CHE, Potchefstroom, South Africa, 1984.

Potgieter, M. S., Heliospheric modulation of galactic electrons: consequences of new calculations for the mean free path of electrons between 1 MeV and ∼10 GeV, *JGR*, *101*, 24411, 1996.

Potgieter, M. S., The modulation of galactic cosmic rays in the heliosphere: theory and models, *Space Sci. Rev.*, *83*, 147, 1998.

Potgieter, M. S., Heliospheric modulation of cosmic ray protons: role of enhanced perpendicular diffusion during periods of minimum solar modulation, *JGR*, *105*, 18295, 2000.

Potgieter, M. S., Solar cycle variations and cosmic rays, *JASP*, *70*, 207, 2008.

Potgieter, M. S., Cosmic rays in the inner heliosphere: insights from observations, theory and models, *Space Sci. Rev.*, *176*, 165, 2011.

Potgieter, M. S., Solar modulation of cosmic rays, *Liv. Rev. Sol. Phys.*, *10*, 3, 2013.

Potgieter, M. S., Very local interstellar spectra for galactic electrons, protons and helium, *Braz. J. Phys.*, *44*, 581, 2014.

Potgieter, M. S., J. A. leRoux, and R. A. Burger, Interplanetary cosmic ray radial gradients with steady state modulation models, *JGR*, *94*, 2323, 1989.

Potgieter, M. S., R. A. Burger, and S. E. S. Ferreira, Modulation of cosmic rays in the heliosphere from solar minimum to maximum: a theoretical perspective, *Space Sci. Rev.*, *97*, 295, 2001.

Potgieter, M. S., E. E. Vos, M. Boezio, N. de Simone, V. di Felice, and V. Formato, Modulation of galactic protons in the heliosphere during the unusual solar minimum of 2006 to 2009, *Sol. Phys.*, *289*, 391, 2014.

Potgieter, M. S., E. E. Vos, R. Munini, M. Boezio, and V. di Felice, Modulation of galactic electrons in the heliosphere during the unusual solar minimum of 2006 - 2009: A modeling approach, *ApJ*, *810*, 141, 2015.

Potgieter, M. S., and S. E. S. Ferreira, The importance of perpendicular diffusion in the heliospheric modulation of cosmic ray electrons, *Adv. Space Res.*, *23*, 463, 1999.

Potgieter, M. S., and L. J. Haasbroek, The simulation of base-line cosmic-ray modulation for the Ulysses trajectory, *Int. Cosmic Ray Conf. Proc.*, *3*, 457, 1993.

Potgieter, M. S., and H. Moraal, A drift model for the modulation of galactic cosmic rays, *ApJ*, *294*, 425, 1985.

Potgieter, M. S., and R. R. Nndanganeni, A local interstellar spectrum for galactic electrons, *Astroparticle Phys.*, *48*, 25, 2013.

Potgieter, M. S., and E. E. Vos, Difference in the heliospheric modulation of cosmic-ray protons and electrons during the solar minimum period of 2006 to 2009, *601*, A23, 2017.

Prinsloo, P. L., 2016. Acceleration of cosmic rays in the outer heliosphere. Master's thesis, North-West University, Potchefstroom, South Africa.

Ptuskin, V. S., Origin of galactic cosmic rays: sources, acceleration and propagation, *Int. Cosmic Ray Conf. Proc.*, *10*, 317, 2005.

Qin, G., and Z. N. Shen, Modulation of galactic cosmic rays in the inner heliosphere, comparing with PAMELA measurements, *ApJ*, *846*, 56, 2017.

Raath, J. L., 2015. A comparative study of cosmic ray modulation models. Master's thesis, North-West University, Potchefstroom, South Africa.

Raath, J. L., R. D. Strauss, and M. S. Potgieter, New insights from modeling the neutral heliospheric current sheet, *Astrophys. Space Sci.*, *360*, 24, 2015.

Raath, J. L., M. S. Potgieter, R. D. Strauss, and A. Kopp, The effects of magnetic field modifications on the solar modulation of cosmic rays with a SDE-based model, *Adv. Space Res.*, *57*, 1965, 2016.

Raath, J. L., and M. S. Potgieter, Charge-sign dependent modulation of cosmic ray electrons and positrons up to extreme solar maximum conditions, *Proc. Int. Cosmic Ray Conf.*, *301*, 39, 2017.

Reames, D. V., The two sources of solar energetic particles, *Space Sci. Rev.*, *75*, 53, 2013.

Scherer, K., H. Fichtner, and E. Marsch, *The outer heliosphere: beyond the planets, Copernicus-Gesellschaft*. 2000.

Scherer, K., H. Fichtner, R. D. Strauss, S. E. S. Ferreira, M. S. Potgieter, and H. J. Fahr, On cosmic ray modulation beyond the heliopause: Where is the modulation boundary, *ApJ*, *735*, 128, 2011.

Schlickeiser, R., On the interplanetary transport of solar cosmic rays, *JGR*, *93*, 2725, 1988.

Schlickeiser, R., *Cosmic Ray Astrophysics*. Springer, Berlin, 2002.

Schröder, K. P., M. Mittag, J. H. M. M. Schmitt, D. Jack, A. Hempelman, and J. N. GonzálezPérez, Carrington cycle 24: the solar chromospheric emission in a historical and stellar perspective, *Monthly Notices of the Royal Astronomical Society*, *470*, 276, 2017.

Serpico, P. D., Possible causes of a rise with energy of the cosmic ray positron fraction, *Phys. Rev. D*, *79*, 021302, 2009.

Shalchi, A., Extended nonlinear guiding center theory of perpendicular diffusion, *Astron. and Astrophys.*, *453*, L43, 2006.

Shalchi, A., *Nonlinear cosmic ray diffusion theories*. Springer-Verlag, Berlin, 2009.

Shalchi, A., J. W. Bieber, and W. H. Matthaeus, Analytic forms of the perpendicular diffusion coefficient in magnetostatic turbulence, *ApJ*, *604*, 675, 2004.

Shalchi, A., and R. Schlickeiser, The parallel mean free path of heliospheric cosmic rays in composite slab/two-dimensional geometry. I. The damping model of dynamical turbulence, *ApJ*, *604*, 861, 2004.

Sheeley, N. R., Y. M. Wang, S. H. Hawley, G. E. Brueckner, K. P. Dere, R. A. Howard, M. J. Koomen, and C. M. Korendyke, Measurements of flow speeds in the corona between 2 and 30 $r_{\rm sun}$, *ApJ*, *484*, 472, 1997.

Siluszyk, M., A. Wawrzynczak, and M. V. Alania, A model of the long period galactic cosmic ray variations, *JASP*, *73*, 1923, 2011.

Simpson, J. A., Cosmic radiation: Particle astrophysics in the heliosphere, in *Frontiers in Cosmic Ray Physics: Symposium in memory of Serge Korff*, edited by R. D. Mendell, and A. J. Mincer, New York Academy of Sciences, New York, 1992.

Simpson, J. A., The cosmic radiation: Reviewing the present and future, *Int. Cosmic Ray Conf. Proc., Invited Rapporteur and Highlighted Papers*, 4, 1998.

Simpson, J. A., D. Hamilton, G. Lentz, R. B. McKinnem, A. Mogro Campero, M. Perkins, K. R. Pyle, A. Tuzzolino et al., Protons and electrons in Jupiter's magnetic field: Results from the University of Chicago Experiment on Pioneer 10, *Sci.*, *183*, 306, 1974.

Smith, C. W., and J. W. Bieber, Solar cycle variation of the interplanetary magnetic field spiral, *ApJ*, *370*, 435, 1991.

Smith, E. J., Interplanetary magnetic field over two solar cycles and out to 20 AU, *Adv. Space Res.*, *9*, 159, 1989.

Smith, E. J., The heliospheric current sheet, *JGR*, *106*, 15819, 2001.

Snodgrass, H. B., Magnetic rotation of the solar photosphere, *ApJ*, *270*, 288, 1983.

Stawicki, O., On solar wind magnetic fluctuations on their influence on their influence on the transport of charged particles in the heliosphere, Ph.D. thesis, Ruhr Universität, Bochum, Germany, 2003.

Sternal, O., N. E. Engelbrecht, R. A. Burger, S. E. S. Ferreira, H. Fichtner, B. Heber, A. Kopp, M. S. Potgieter et al., Possible evidence for a Fisk-type heliospheric magnetic field. I. Analyzing Ulysses/KET electron observations, *ApJ*, *741*, 23, 2011.

Steyn, P. J., 2016. An investigation into a generalized Fisk-type heliospheric magnetic field. Master's thesis, North-West University, Potchefstroom, South Africa.

Stone, E. C., A. C. Cummings, F. B. McDonald, B. C. Heikkila, N. Lal, and W. R. Webber, Voyager 1 explores the termination shock region and the heliosheath beyond, *Sci.*, *309*, 2017, 2005.

Stone, E. C., A. C. Cummings, and F. B. McDonald, Voyager 1 observes low-energy galactic cosmic rays in a region depleted of heliospheric ions, *Sci.*, *341*, 150, 2013.

Strauss, R. D., 2010. Modelling of anomalous cosmic rays. Master's thesis, North-West University, Potchefstroom, South Africa.

Strauss, R. D., Modelling of cosmic rays in the heliosphere by stochastic processes, Ph.D. thesis, North-West University, Potchefstroom, South Africa, 2013.

Strauss, R. D., and F. Effenberger, A hitch-hiker's guide to stochastic differential equations. Solution methods for energetic particle transport in space physics and astrophysics, *Space Sci. Rev.*, *212*, 151, 2017.

Strauss, R. D., M. S. Potgieter, I. Büsching, and A. Kopp, Modelling the modulation of galactic and Jovian electrons by stochastic processes, *ApJ*, *735*, 83, 2011*a*.

Strauss, R. D., M. S. Potgieter, I. Büsching, and A. Kopp, On the propagation times and energy losses of cosmic rays in the heliosphere, *JGR*, *116*, A12105, 2011*b*.

Strauss, R. D., M. S. Potgieter, I. Büsching, and A. Kopp, Modeling heliospheric current sheet drift in stochastic cosmic ray transport models, *Astrophys. Space Sci.*, *339*, 223, 2012.

Strauss, R. D., M. S. Potgieter, S. E. S. Ferreira, H. Fichtner, and K. Scherer, Cosmic ray modulation beyond the heliopause: a hybrid modelling approach, *ApJ Lett.*, *765*, L18, 2013.

Strauss, R. D., J. A. le Roux, N. E. Engelbrecht, D. Ruffolo, and P. Dunzlaff, Non-axisymmetric perpendicular diffusion of charged particles and their transport across tangential magnetic discontinuities, *ApJ*, *825*, 43, 2016.

Strauss, R. D., and M. S. Potgieter, Is the highest cosmic-ray flux yet to come?, *Sol. Phys.*, *289*, 3197, 2014*a*.

Strauss, R. D., and M. S. Potgieter, Where does the heliospheric modulation of galactic cosmic rays start?, *Adv. Space Res.*, *53*, 1015, 2014*b*.

Sun, X., J. T. Hoeksema, Y. Liu, and J. Zhao, On polar magnetic field reversal and surface flux transport during solar cycle 24, *ApJ*, *798*, 114, 2015.

Tanimori, T., Discovery of TeV gamma rays from SN1006: Further evidence for the supernova remnant region of cosmic rays, *ApJ Lett.*, *497*, L25, 1998.

Tautz, R. C., and A. Shalchi, Drift coefficients of charged particles in turbulent magnetic fields, *ApJ*, *744*, 125, 2012.

Teufel, A., and R. Schlickeiser, Analytic calculation of the parallel mean free path of heliospheric cosmic rays. II. Dynamical magnetic slab turbulence and random sweeping turbulence with finite wave power at small wavenumbers, *Astron. Astrophys.*, *397*, 15, 2003.

Tomassetti, N., M. Orcinha, F. Barão, and B. Bertucci, Evidence for a time lag in solar modulation of galactic cosmic rays, *ApJ*, *849*, L32, 2017.

Tomassetti, N., F. Barão, B. Bertucci, E. Fiandrini, J. L. Figueiredo, J. B. Lousada, and M. Orcinha, Testing diffusion of cosmic rays in the heliosphere with proton and helium data from AMS, *Phys. Rev. Lett.*, *121*, 251104, 2018.

Venter, C., A. Kopp, A. K. Harding, P. L. Gonthier, and I. Büsching, Cosmic-ray positrons from millisecond pulsars, *ApJ*, *807*, 130, 2015.

Visser, D. J., 2009. The effect of turbulence-modified drift on the modulation of cosmic rays in the heliosphere. Master's thesis, North-West University, Potchefstroom, South Africa.

Vogt, A., P. Dunzlaff, B. Heber, A. Kopp, P. Kühl, and R. D. Strauss, Jovian electrons in the inner heliosphere: A parameter study on intensity profiles near Earth, *Int. Cosmic Ray Conf. Proc.*, *34*, 207, 2015.

Vos, E. E., 2011. Cosmic ray modulation processes in the heliosphere. Master's thesis, North-West University, Potchefstroom, South Africa.

Vos, E. E., Modelling charge-sign dependent modulation of cosmic rays in the heliosphere, Ph.D. thesis, North-West University, Potchefstroom, South Africa, 2016.

Vos, E. E., and M. S. Potgieter, New modeling of galactic proton modulation during the minimum of solar cycle 23/24, *ApJ*, *815*, 119, 2015.

Wawrzynczak, A., R. Modzelewska, and M. Kluczek, Numerical methods for solution of the stochastic differential equations equivalent to the non-stationary parker's transport equation, *J. Phys.: Conf. Series*, *633*, 012058, 2015*a*.

Wawrzynczak, A., R. Modzelewska, and A. Gil, Stochastic approach to the numerical solution of the non-stationary parker's transport equation, *J. Phys.: Conf. Series*, *574*, 012078, 2015*b*.

Wawrzynczak, A., and R. Modzelewska, The stochastic modeling of the short-time variations of the galactic cosmic rays, *J. Phys.: Conf. Series*, *738*, 012001, 2016.

Webb, G. M., and L. J. Gleeson, Green's theorem and green's function for the steady-state cosmic-ray equation of transport, *Astrophys. Space Sci.*, *50*, 205, 1977.

Webber, W. R., M. S. Potgieter, and R. A. Burger, A comparison of predictions of a wavy neutral sheet drift model with cosmic-ray data over a whole modulation cycle - 1976-1987, *ApJ*, *349*, 634, 1990.

Webber, W. R., B. Heber, and J. A. Lockwood, Time variations of cosmic ray electrons and nuclei between 1978 and 2004: Evidence for charge-dependent modulation organized by changes in solar magnetic polarity and curent sheet tilt, *JGR Space Phys.*, *110*, A12107, 2005.

Webber, W. R., F. B. McDonald, A. C. Cummings, E. C. Stone, N. Heikkila, and N. Lal, At Voyager 1 starting on about August 25, 2012 at a distance of 121.7 AU from the Sun, a sudden disappearance of anomalous cosmic rays and an unusually large sudden increase of galactic cosmic ray H and He nuclei and electrons occurred, *ArXiv*, *1212*, 0883, 2012.

Webber, W. R., and F. B. McDonald, Recent Voyager 1 data indicate that on August 25, 2012 at a distance of 121.7 AU from the Sun, sudden and unprecedented intensity changes were observed in anomalous and galactic cosmic rays, *Geophys. Res. Lett.*, *40*, 1665, 2013.

Yamada, Y., S. Yanagita, and T. Yoshida, A stochastic view of the solar modulation phenomena of cosmic rays, *Geophys. Res. Lett.*, *25*, 2353, 1998.

Yamada, Y., S. Yanagita, and T. Yoshida, A stochastic simulation method for the solar cycle modulation of cosmic rays, *Geophys. Res. Lett.*, *25*, 2353, 1999.

Zank, G., G. Li, V. Florinski, W. Matthaeus, and J. leRoux, Perpendicular diffusion coefficient for charged particles of arbitrary energy, *JGR*, *109*, A04107, 2004.

Zhang, M., A linear relationship between the latitude gradient and 26 day recurrent variation in the fluxes of galactic cosmic rays and anomalous nuclear components. I. Observations, *ApJ*, *488*, 841, 1997.

Zhang, M., A Markov stochastic process theory of cosmic-ray modulation, *ApJ*, *513*, 409, 1999.

Zhang, M., X. Luo, and N. Pogorelov, Where is the cosmic-ray modulation boundary of the heliosphere?, *Phys. Plasmas*, *22*, 091501, 2015.

Zhao, L.-L., G. Qin, M. Zhang, and B. Heber, Modulation of galactic cosmic rays during the unusual solar minimum between cycles 23 and 24, *JGR*, *119*, 1493, 2014.

Zhao, L. L., L. Adhikari, G. P. Zank, Q. Hu, and X. S. Feng, Influence of the solar cycle on turbulence properties and cosmic-ray diffusion, *ApJ*, *856*, 94, 2018.

Acknowledgements

- My supervisor, Prof. S.E.S. Ferreira, for essential guidance and support both professional and personal.
- My co-supervisor Dr. A. Kopp for his dedicated work and various late night discussions.
- Prof. M.S. Potgieter for guiding me through the first years of my PhD.
- Prof N.E. Engelbrecht for relevant discussions and helpful suggestions.
- Dr. D. Bisschoff for his help pertaining to the LIS for positrons.
- Dr. O.P.M. Aslam for modelling related discussions.
- Mr. P.L. Prinsloo and S.T. Mohlolo for help on more than one occasion.
- Mrs. M.P. Sieberhagen, for assistance with financial and other administrative matters.
- Mrs. E. van Rooyen for administrative work and always doing more than what is expected.
- Mrs. L. van Wyk for handling administrative/financial matters.
- Mr. M. Holleran, for his help with computer related problems and for various insightful discussions.
- Mrs. R.M. Steffen for proof reading this work.
- My mother, family and friends for their love and support throughout the duration of this study.
- The Centre for Space Research at the North-West University, the National Research Foundation, and the South African National Space Agency for financial support throughout this study.

Jan Louis Raath

Centre for Space Research, North-West University

November 2019